

**MINERAL EXPLORATION  
IN  
THE PARANÁ BASIN AREA,  
THE FEDERATIVE REPUBLIC  
OF  
BRAZIL  
FINAL REPORT**

**MARCH 2003**

**METAL MINING AGENCY OF JAPAN**  
**JAPAN INTERNATIONAL COOPERATION AGENCY**

<b>MPN</b>
<b>JR</b>
<b>03-067</b>

## PREFACE

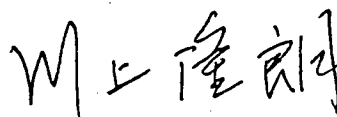
In responding to the request of the government of the Federative Republic of Brazil, the Government of Japan decided to conduct mineral exploration including satellite image analysis and geological survey to identify the possibility of existence of nonferrous mineral resources in the Paraná basin area and entrusted the survey works to Japan International Cooperation Agency (JICA). JICA, considering the technical nature of geology and mineral resources, entrusted the survey works to the Metal Mining Agency of Japan (MMAJ).

The survey works was commenced by two years schedule from FY 2001, and the survey in FY 2002 is the final stage. MMAJ organized a mission consisting of four members and dispatched the mission to the site of the survey for the period from July 12 to September 27, 2002. The field survey was completed as scheduled thanks to cooperation of the Brazilian government offices.

This report is the final report that summarizes the results of the survey works carried out in two years.

We would like to express our sincere gratitude to the Brazilian government and its associated organizations. We are also grateful to the officials concerned of the Ministry of Foreign Affairs of Japan, the Ministry of Economy, Trade and Industry of Japan, and the Japanese Embassy in the Federative Republic of Brazil for their helpful supports to conduct the survey works.

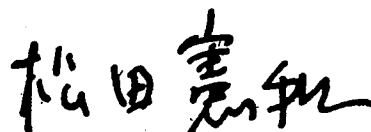
March, 2003



Takao Kawakami

President

Japan International Cooperation Agency

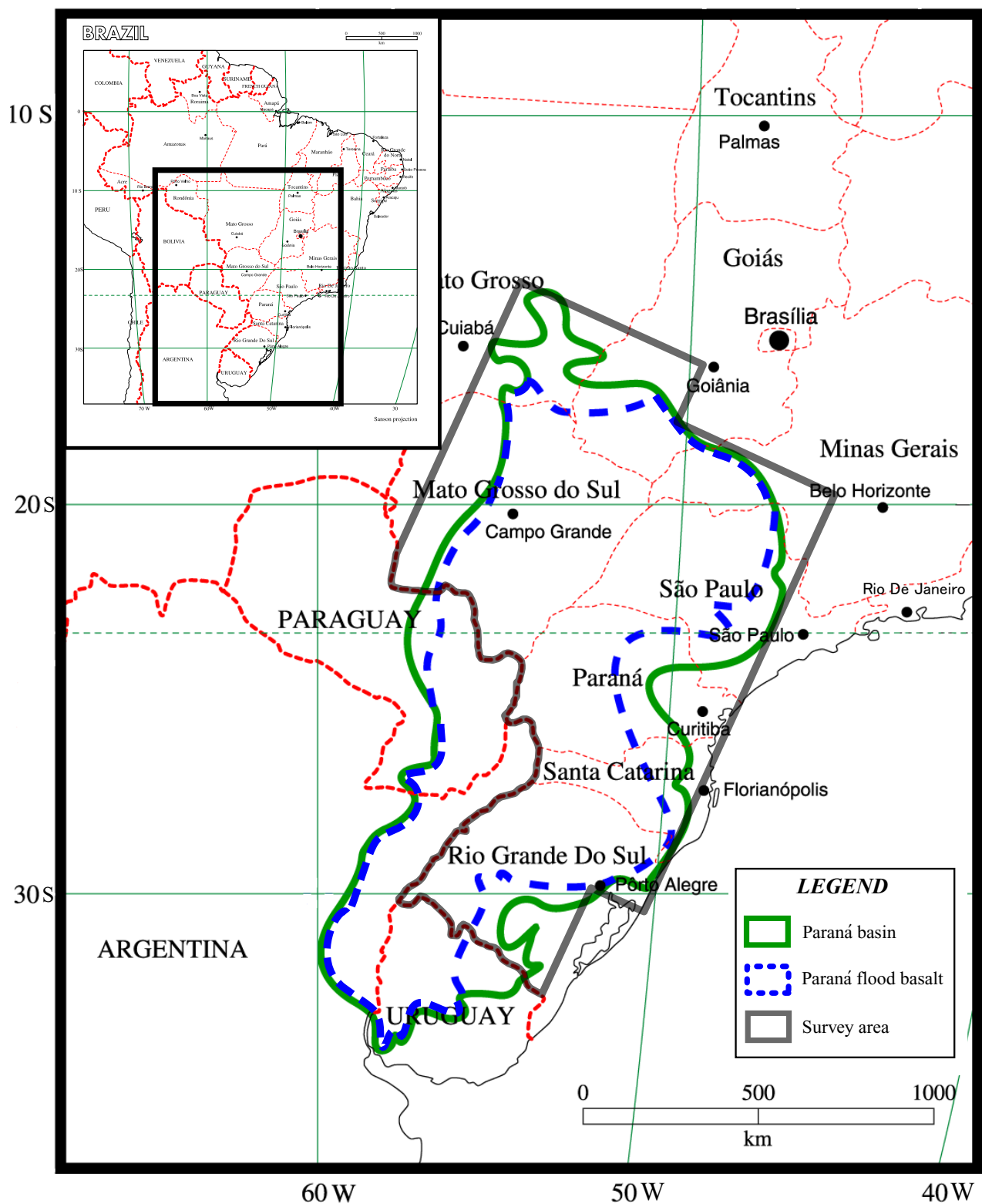


Norikazu Matsuda

President

Metal Mining Agency of Japan





**Location of the Paraná Basin Area, Brazil**

## SUMMARY

Based on the Scope of Work concluded between the Governments of Japan and Brazil on the 30<sup>th</sup> May, 2001, the present survey of nonferrous metal resources was carried out for two years with the purpose of regional exploration of Noril'sk type Ni-Cu-PGE ore deposit in the Paraná area situated in the southeastern part of Brazil.

In the survey, existing data and satellite images, geophysical data were analyzed and geological survey on the surface ground was conducted. In the existing data analysis, the Noril'sk ore deposit, and the geological structure of flood basalt and basement rock were analyzed. In the satellite images analysis, JERS-1 SAR images and TM image were used. In the geological survey, whole rock analysis, trace elements analysis, isotope analyses and so on of Paraná flood basalt were conducted.

### 1. Exploration Criteria

Considering the forming environment of the Noril'sk ore deposits from the view point of the condition of orthomagmatic sulfide ore deposit forming, the follows are presented as the exploration criteria for orthomagmatic ore deposit accompanied with flood basalt:

- (1) The existence of sulfur undersaturated PGE rich magmas as lavas or intrusions.
- (2) The existence of magmas showing the signatures of crustal contamination and sulfide segregation associated with above PGE rich magmas as lavas or intrusions.
- (3) It is desirable that the magmas are high temperature picritic to basaltic composition that easily contaminates the crust materials.
- (4) The center of the magmatic activity where the large volume of silicate magmas are supplied through crustal suture zone.

### 2. Geological Structure and Promising areas of Emplacement of Ore deposit

A comprehensive explanation of Precambrian basement rocks, sedimentary rocks and flood basalts in Post- Early Paleozoic, faults, gravity anomalies and aeromagnetic anomalies in the Paraná Basin resulted in promising areas of emplacement of Noril'sk-type Ni-Cu-PGE ore deposit were selected.

A large low anomaly zone in the central part of the pseudogravity anomaly map overlaps with a zone where sedimentary sequence and flood basalt lava are thicker, with a zone where a large quantity of sills and dykes intruded, with a high residual gravity anomaly zone, and with a high attenuation factor zone. Based on these facts, it is concluded that the large low anomaly

zone was rift zone associated with flood basalt magmatism.

The direction of the rift zone extends in the N-S directions in the northern Basin; in the NE-SW directions the central Basin, and branches into the NE-SW and NW-SE directions in the southern Rio Alfonzo fault. The inside of the rift zone has repetitions of high anomaly zones and low anomaly zones in the NE-SW direction. These anomaly zones in the NE-SW directions were formed by stair-step normal faults (vertical direction: maximum compressive principal stress axis  $\sigma_1$ ) in the extensional stress in the NW-SE directions field (minimum compressive principal stress axis  $\sigma_3$ ).

Many magnetic lineaments which represent faults in the NW-SE direction are recognized on the pseudogravity anomaly map. For example, Rio Alfonzo fault on the geological map are represented by several magnetic lineaments on the pseudogravity anomaly map. The faults in the NW-SE directions are estimated to be sinistral transcurrent faults because they have sharp boundaries and are accompanied with many secondary shear faults in E-W directions. In the Duluth ore deposit, many secondary shear fractures occurred in the form of Cymoid Loop-like tensional fractures in areas where the rift zone and transcurrent faults cross. The Duluth Complex intruded there and formed the ore deposit. The Noril'sk ore deposit was also formed in the volcano-center where magma extruded most intensely in the Gydansk-Omsk rift zone (Tamrazyan, 1962).

As the results mentioned above, we propose the following four promising areas, which rift zone and transcurrent faults cross, of emplacements of Ni-Cu-PGE ore deposits.

- (1) The area where the Tiete structural line in the NW-SE direction crosses through Paraná River
- (2) The area where the Guapiara fault in the NW-SE direction crosses through Paraná River.
- (3) The area where Rio Alfonzo fault in the NW-SE direction crosses through Paraná River.
- (4) The western part of Torres - Posadas fault in the southern region of Paraná Basin

All of these areas are estimated to have been the volcano-center of flood basalt magmas. The largest volcano-center is found in the area (3) where the Rio Alfonzo fault crosses through Paraná River. Among four areas, it is concluded that areas where the Guapiara fault and the Rio Alfonzo fault in the NW-SE directions cross through Paraná River are the most promising area of emplacements of Ni-Cu-PGE ore deposits.

### 3. Geochemical Characteristics of Paraná Flood Basalts

Pitanga, High-Ti type, is distributed from the northern to the central part of the Paraná Basin. This magma type shows the smallest degree of partial melting. It is thought to have

been generated in relatively deeper portion in the upper mantle. Paranapanera-Ribeira, the Intermediate type, is distributed in the central area of the Paraná Basin. The degree of partial melting of this type is shown larger than that of Pitanga. This means that it has been generated in a shallower portion than Pitanga was generated. The effect of the crustal contamination is considered limited in these two types of magma because of poor contents of U and Th that concentrate in the crust. Mantovani et al. (2000) described that the two types above were generated from a similar magma source with different degrees of partial melting. The large quantities of the two magma types above erupted and were piled with a thickness of approximately 1,800 meters along the Paraná River in the central part of the Paraná Basin, which is thought to be the center of the magmatic activity.

The Low-Ti type magmas (Gramado and Esmeralda) show relatively large degree of partial melting. They are thought to have been generated in relatively shallower portions compared to the other magma types. The increases of LIL elements such as Th, U and the likes that concentrate in crust, and Sr isotopic ratio are observed in both magma types. It is thought to be the effect of crustal contamination. The effect is particularly marked in Gramado. Esmeralda is considered to be the most primitive magma among all the magma types because of its low contents of light rare earth elements and a relatively high Nd isotopic ratio.

As regards the Low-Ti types of magma, the following three points are thought to have a close relationship. The first is that the magma was generated in a shallow portion. The second is that the magma was highly affected by crustal contamination, and the third is the existence of acidic rocks, which are considered to be the products of lower crust melting, in the southern part of the Paraná Basin. More specifically, the following process is thought to have occurred. That is, the acidic magma was generated from the melt of the lower crust by the mantle plume heating. After generating the acidic magma, this magma and the magma generated by the melting of the mantle plume itself mixed and yielded Gramado type magma. Finally, just after the commencement of expanding the Atlantic, Esmeralda type magma is thought to have been generated that is less influenced by crustal contamination although the origin is the same as Gramado.

The original magmas of the Paraná flood basalts are thought to be PGE rich as a whole, particularly Pd rich although there are some differences among the magma types. The most PGE enriched magma is Paranapanema-Ribeira. The average content of Pt and Pd summing is approximately the same as that of the Tuklonsky lava, the most PGE enriched lava in the Noril'sk region. Paranapanema-Ribeira is also rich in Cu. The magma of this type as lavas is distributed along the Paraná River in the central part of the Paraná Basin, and much native copper is observed in the cavities. The geochemical anomaly in PGE, Ni, Cu, and other elements that is observed in the western part of the state of Paraná (by the stream sediment geochemical survey carried out by MINEROPAR) possibly shows the distribution of

Paranápanema-Ribeira that has high PGE contents. Paranápanema-Riberia as intrusions is distributed in the Ponta Grossa Arch intermingled with Pitanga of High-Ti type. The magma type of the higher PGE content next to Pitanga is Esmeralda that has the most primitive chemical composition. The PGE depletion by sulfur saturation is rarely observed in Paranápanema-Ribeira and Esmeralda.

Regarding Gramado and Pitanga, there are two populations of samples, PGE enriched and depleted. These two types are thought to have been initially PGE enriched. The depletion of PGE, however, is thought to have occurred due to sulfur saturation in a part of the magma. As the cause of sulfur saturation, the crustal contamination in Gramado, and the crystallization differentiation in Pitanga are both thought to have occurred.

In the Noril'sk region, the majority of the lava and intrusion is basaltic, however, the sills which embed ore deposits contain picritic parts and the assimilation of country rock on a large scale in the picritic sill is observed. Picritic magma, however, is rarely observed in the Paraná flood basalts, and the basalts are more differentiated than in the Noril'sk region. The magma temperature of the Paraná flood basalts is thought to be lower than that of the Noril'sk region. It is thought to be possible that this low temperature obstruct the assimilation of country rock and the large scale segregation of immiscible sulfides.

The segregation of sulfides in a large scale magma chamber like the Skaergaard intrusion under the high R factor is necessary to generate sulfide ore deposit from basaltic magma with high PGE contents. The location with the highest possibility of generating sulfide ore deposit is thought to be the eruption center of Paranápanema-Ribeira and Pitanga types, which have the largest quantities of magmas among the Paraná flood basalts. The eruption center is thought to be located in the central area of the Paraná Basin along the Paraná River where the lava piles are the thickest. Based on the existing data analysis, the strong shrinkage of lithosphere by the ascension of the asthenosphere is observed in this area, and magma intrusion is estimated to be the most active in this area.

# CONTENTS

**Preface**

**Location Map of the Paraná Basin area, Brazil**

**Summary**

**Contents**

**List of Figures and Tables**

## **Part I GENERAL DISCUSSION**

Chapter 1: Introduction .....	1
1-1 Circumstances for Starting the Survey .....	1
1-2 Summary of the Survey .....	2
1-2-1 Purpose of the Survey .....	2
1-2-2 Survey Area .....	2
1-2-3 Survey Method .....	2
1-2-4 Configuration of the Survey Mission .....	3
1-2-5 Period and Quantity of the Survey .....	4
Chapter 2: Geography of the Survey Area .....	5
2-1 Location .....	5
2-2 Topography .....	5
2-3 Drainage Systems .....	5
2-4 Climate .....	7
2-5 Plantation .....	7
Chapter 3: Geology, Mineral Deposits, and Mining of the Survey Area .....	8
3-1 Recent Mining Situation .....	8
3-1-1 Mining Production .....	8
3-1-2 Mining Policy .....	10
3-1-3 Exploration and Development .....	12
3-1-4 Recent Mining Situation .....	12
3-1-5 Mining Related Regulations .....	14
3-2 Summary of Geology and Ore Deposits in Brazil .....	15
3-2-1 Summary of Geology .....	15
3-2-2 Outline of Ore Deposits .....	26
3-2-3 Mines, Ore Deposits, and Ore Showings .....	29
3-3 PGE National Program of the CPRM .....	36
3-3-1 Histories .....	36

3-3-2	Overview of CPRM's Platinum Project	38
Chapter 4:	Summary of Investigation Results, Conclusion, and Proposal	48
4-1	Summary of Investigation Results	48
4-1-1	Genesis of Flood Basalt and PGE Sulfide Ore Deposit	48
4-1-2	Exploration Criteria of the Noril'sk style Deposit	49
4-1-3	Geology and Geological Structure of the Paraná Basin	50
4-1-4	Promising Areas of Emplacement of Ni-Cu-PGE Deposits Estimated from Geological Structure	51
4-1-5	Geochemical Characteristics of the Paraná Flood Basalts	52
4-1-6	Mineralization Potential of the Paraná Flood Basalts	55
4-2	Conclusion and Proposal	56

## **Part II DETAILED DISCUSSION**

Chapter 1:	Analysis of the Existing Data	57
1-1	Summary of the Collected Data	57
1-1-1	Scientific Documents and Research/Survey Materials	57
1-1-2	Collected Data and Materials	58
1-2	The Feature and Origin of the Flood Basalt around the World	65
1-2-1	Introduction	65
1-2-2	Characteristics of the Flood Basalt	65
1-2-3	Genesis of the Flood Basalt	72
1-2-4	Activity of the Flood Basalt and PGE Mineralization	89
1-3	Noril'sk Cu-Ni-PGE Deposits and Key Factors in their Exploration	92
1-3-1	Introduction	92
1-3-2	Outline of Geology	92
1-3-3	Siberian Flood Basalts	97
1-3-4	Intrusions	102
1-3-5	Genetic Model of the Noril'sk Deposits	110
1-3-6	Genetic Model of the Orthomagmatic Sulfide Deposits and Key Factors in the Exploration of the Noril'sk Style Deposits	116
1-4	Geology and Geological Structure of Paraná Basin	124
1-4-1	Tectonic Province of the South American Plate	124
1-4-2	Geology and Geological Structure of Basement Rock	129
1-4-3	Geology and Geological Structure of Basin	134
1-4-4	Basement Structure Analyzed by Geophysical Data	147
1-5	Geology and Geological Structure of Central Paraná Basin	173
1-5-1	Geology and Geological Structure	173
1-5-2	Aeromagnetic Anomaly Maps	181

1-5-3	Measuring the Magnetism of Rocks	195
1-5-4	Analysis of Magnetic Anomaly Maps	200
1-5-5	TM image Analysis	203
1-6	Tectonics of Ni-Cu-PGE Ore Deposit associated with Flood Basalt	205
1-6-1	Tectonics of Duluth Ore Deposit	205
1-6-2	Tectonics of Noril'sk Ore Deposit	213
1-6-3	Tectonics of Paraná Flood Basalt and Emplacement of Ni-Cu-PGE Ore Deposit	218
Chapter 2:	Satellite Image Analysis	224
2-1	Objectives	224
2-2	Processing and Production of JERS-1/SAR Image	224
2-2-1	Outline of the Survey Area	224
2-2-2	Satellite Data Used	224
2-2-3	Processing and Production of Image	227
2-3	Interpretation and Analysis of the Image	228
2-3-1	JERS-1/SAR Image	228
2-3-2	Landsat TM Image	233
Chapter 3:	Geological Survey	237
3-1	Overview of the Geology	237
3-1-1	Overview of the Geology in the Paraná Basin	237
3-1-2	Paraná Flood Basalts	242
3-2	Contents of the Study	255
3-2-1	Sampling	255
3-2-2	Laboratory Test	255
3-2-3	Occurrences of the Paraná Flood Basalts	260
3-2-4	Microscopic Observation of the Paraná Basaltic Lava and Intrusion	264
3-3	Geochemical Feature and Volcanism of the Paraná Flood Basalts	266
3-3-1	Review of Geochemical Feature of the Paraná Flood Basalts	266
3-3-2	Geochemical Characteristics of the Paraná Flood Basalts	275
3-3-3	Ar-Ar Age of the Paraná Flood Basalts	326
3-3-4	Geochemical Feature and Magmatism of the Paraná Flood Basalts	335
3-4	Intrusions Distributed in the Eastern Margin of the Paraná Basin	339
3-4-1	Overview of the Cooperative Survey Program of Canada and Brazil	339
3-4-2	Distribution of Intrusions in the Eastern Rim of the Paraná Basin	341
3-4-3	Collecting Samples	341
3-4-4	Petrochemistry of Intrusions	360
3-4-5	Sulfur Isotopic Ratio	381
3-5	PGE Geochemistry of the Paraná Flood Basalts	383
3-5-1	PGE Contents of the Paraná Flood Basalts	383



3-5-2	Relationship between Degree of Partial Melting and PGE Content	392
3-5-3	Relationship between Sulfur Saturation and PGE Content	394
3-5-4	Potential of Cu-Ni-PGE Sulfide Deposit Accompanied with Paraná Flood Basalts	398
3-6	Study of the Stream Sediment Geochemical Anomaly by MINEROPAR	401
3-6-1	Review of the Stream Sediment Geochemical Survey by MINEROPAR	401
3-6-2	Origin of the Geochemical Anomaly	401
3-7	Metallic Minerals in the Paraná Flood Basalts	404
3-8	Geochemical Survey with Stream Sediments	409
3-8-1	Introduction	409
3-8-2	Geochemical Interpretation	410
3-8-3	Survey Results	410
3-8-4	Summary of the Survey	421
Chapter 4:	Considering the Survey Results	422
4-1	Genesis of Flood Basalt and PGE Sulfide Ore Deposit	422
4-2	Exploration Criteria of the Noril'sk style Deposit	423
4-3	Geology and Geological Structure of the Paraná Basin	424
4-4	Promising Areas of Emplacement of Ni-Cu-PGE Deposits Estimated from Geological Structure	425
4-5	Geochemical Characteristics of the Paraná Flood Basalts	426
4-6	Mineralization Potential of the Paraná Flood Basalts	429
4-7	Subjects and Survey Methods in the Future	430

### **Part III CONCLUSION AND PROPOSAL**

Chapter 1:	Conclusion	431
1-1	Genesis of Flood Basalt and PGE Sulfide Ore Deposit	431
1-2	Exploration Criteria of the Noril'sk style Deposit	432
1-3	Geology and Geological Structure of the Paraná Basin	433
1-4	Promising Areas of Emplacement of Ni-Cu-PGE Deposits Estimated from Geological Structure	434
1-5	Geochemical Characteristics of the Paraná Flood Basalts	435
1-6	Mineralization Potential of the Paraná Flood Basalts	438
Chapter 2:	Proposal	439
<b>References</b>		441

### **Appendix**

## LIST OF FIGURES AND TABLES

**Frontispiece** Location of the Paraná basin area, Brazil

### Figures

Figure I-2-1-1	Location of the Paraná basin area, Brazil	6
Figure I-3-2-1	Ages of major tectonic movements and igneous activities in Brazil	17
Figure I-3-2-2	Major old stable continental blocks in Precambrian age of South America	18
Figure I-3-2-3	Directions of orogenic belts in orogenic cycles in Brazil	18
Figure I-3-2-4	Major geological structure sections in Precambrian age in Brazil	20
Figure I-3-2-5	Distribution of sedimentary basins in the Phanerozoic eons in Brazil	21
Figure I-3-2-6	Mesozoic mafic igneous activity in eastern South America (compiled from Rezende, 1972; Bigarella, 1973; McConnell, 1975; Zamborano & Urien, 1974; Cordani et al., 1967)	24
Figure I-3-2-7	Distribution of aluminum ore deposits and smelting factories	30
Figure I-3-2-8	Distribution of tin ore deposits	31
Figure I-3-2-9	Distribution of Fe/Mn/Cr/Ni/Nb ore deposits	32
33Figure I-3-2-10	Distribution of gold and gem stone deposits	33
Figure I-3-2-11	Principal mineral provinces of Brazil	34
Figure I-3-3-1	Geological map of Paraná basalt region	37
Figure I-3-3-2	Target areas and bodies for PGE prospecting by CPRM	43
Figure II-1-1-1	Index map of the topographic maps on a scale of 1/250,000 in the survey area	59
Figure II-1-1-2	Index map of the geological maps on a scale of 1/100,000 made by CPRM	60
Figure II-1-1-3	Index map of the airborne magnetic survey	61
Figure II-1-1-4	Index map of the GIS data set	63
Figure II-1-1-5	Index map of PETROBRAS's drill log	64
Figure II-1-2-1	Global distribution of the major Large Igneous Province (LIP)	67
Figure II-1-2-2	Relationship of the continental breakup and the flood basalts	70
Figure II-1-2-3	Panoramic view of the lava flow in the Deccan Trap (Takahashi and Nakajima, 1997, The photographer: T. Fujii)	71
Figure II-1-2-4	Plots of SiO <sub>2</sub> vs. MgO, Al <sub>2</sub> O <sub>3</sub> vs. MgO, CaO vs. MgO and Al <sub>2</sub> O <sub>3</sub> /CaO ratio vs. MgO for Hawaiian lavas (Frey et al., 1994)	75
Figure II-1-2-5	Schematic model of a zoned mantle plume beneath Hawaii (Hauri, 1996)	75
Figure II-1-2-6	Experimentally determined melting characteristics of core (Fe, FeO) and lower mantle material (MgSiO <sub>3</sub> : perovskite)	76
Figure II-1-2-7	A schematic model of the convection in the mantle	78
Figure II-1-2-8	A schematic model of homogeneous plume head for magma generation through study of the Columbia River flood basalts	79
Figure II-1-2-9	Volume of plume heads calculated on the basis of McKenzie's model (McKenzie and Bickle, 1988)	79

Figure II-1-2-10	Magma types generated by adiabatic decompressional melting of peridotite (Takahashi, 1996) .....	81
Figure II-1-2-11	Distribution of the Columbia River basalts and track of the Yellowstone hot spot ..	83
Figure II-1-2-12	Feature of geochemical composition of the Columbia River flood basalts .....	83
Figure II-1-2-13	Melting phase relations on the Columbia River basalts listed Table II-1-2-3 (Takahashi et al., 1998) .....	85
Figure II-1-2-14	Liquidus and solidus for a fertile peridotite (data: Takahashi, 1986) and primitive MORB (data: Yasuda, et al., 1994; Takahashi et al., 1998) under dry 86condition .....	86
Figure II-1-2-15	A model for heterogeneous mantle plume head for the initial stage of the Yellowstone hot spot (Takahashi et al., 1998) .....	86
Figure II-1-3-1	Grades versus production + reserves for major Ni sulfide deposits of the world ..	94
Figure II-1-3-2	Simplified geologic map of the Noril'sk-Talnakh district (Czamanske et al., 1995) .....	95
Figure II-1-3-3	Main structural elements of the northwest corner of the Siberian platform (Naldrett, 1992) .....	96
Figure II-1-3-4	Geologic cross sections of the Noril'sk-Talnakh district platform (Naldrett, 1992) .....	98
Figure II-1-3-5	Correlation chart relating flood basalt stratigraphy of the Noril'sk region (Czamanske et al., 1995) .....	99
Figure II-1-3-6	Relation between La/Sm versus Gd/Yb for basalts of the Noril'sk region (Naldrett, 1992) .....	101
Figure II-1-3-7	Vertical variation in La/Sm, Ni, Cu, Pt for basalts of the Noril'sk region (Naldrett, 1999) .....	101
Figure II-1-3-8	Generalized stratigraphic column for Silurian to Permian formations based on typical stratigraphic thickness for the Tanlakh ore junction (Czamanske et al., 1995) .....	103
Figure II-1-3-9	Generalized lithologic section for the "fully differentiated" main body of the ore-forming intrusions (Czamanske et al., 1995) .....	104
Figure II-1-3-10	Plan and cross section of the ore body of Talnakh intrusion .....	105
Figure II-1-3-11	Cross section through the east branch of Noril'sk I intrusion (Naldrett, 1999) ...	107
Figure II-1-3-12	Composite lithologic section of the Talnakh intrusion (Czamanske et al., 1995) ..	108
Figure II-1-3-13	Vertical variations in major and trace element for the Talnakh intrusion (Czamanske et al., 1995) .....	109
Figure II-1-3-14	Evolution of the magmas parental to the Lower Talnakh type and the Noril'sk type ore-bearing intrusions .....	111
Figure II-1-3-15 (a), (b), (c)	Formation of the Noril'sk type ore-bearing intrusion .....	112
Figure II-1-3-16	Ni-Cu correlation in lavas from the Noril'sk region .....	119
Figure II-1-3-17	Ni-Au correlation in lavas from the Noril'sk region .....	119
Figure II-1-3-18	Ni-Pd correlation in lavas from the Noril'sk region .....	121

Figure II-1-3-19	Ni-Pt correlation in lavas from the Noril'sk region	121
Figure II-1-3-20	Cu vs. Pd discriminant diagram for lavas from the Noril'sk region between the field of rocks formed by sulfur-saturated magmas and the field of rocks formed by sulfur-undersaturated magmas	122
Figure II-1-4-1	World data set regression line (solid) and the standard deviation (dashed curves) of the calculated $T_e$ for 36 stations (M.S.M. Mantvani et al., 2001)	125
Figure II-1-4-2	Effective elastic thickness ( $T_e$ ) pattern of the South American Plate	126
Figure II-1-4-3	South America effective elastic thickness pattern in correspondence with tectonic provinces, seismic activity and the age provinces map of Condie (1982)	128
Figure II-1-4-4	Schematic map of basement and tectonic framework of the Paraná basin (E.J. Milani, 1998)	130
Figure II-1-4-5	Geological and tectonic map around the Paraná basin (modified by Mantovani et al., 1991)	131
Figure II-1-4-6	Principal archs, faults in the Paraná basin (M.C.L. Quintas, 1995)	135
Figure II-1-4-7	Simplified Geological map of the Paraná basin, with tectonic elements and geographic references (E.J. Milani et al., 1995)	136
Figure II-1-4-8	Sequence-stratigraphic chart for the Paraná basin	138
Figure II-1-4-9	Isopach map of the Rio Ivai supersequence (E.J. Milani et al., 1998)	141
Figure II-1-4-10	Isopach map of the Paraná supersequence (E.J. Milani et al., 1998)	142
Figure II-1-4-11	Isopach map of the Gondwana I supersequence (E.J. Milani et al., 1998)	143
Figure II-1-4-12	Occurrence of the Gondwana II supersequence (E.J. Milani et al., 1998)	144
Figure II-1-4-13	Isopach map of the Gondwana III supersequence sediments + volcanics (E.J. Milani et al., 1998)	145
Figure II-1-4-14	Isopach map of the Bauru supersequence (E.J. Milani et al., 1998)	146
Figure II-1-4-15	Genetic models of the intracratonic basin (Bott, 1981)	148
Figure II-1-4-16	Thermomechanical model for formation of intracratonic basin	150
Figure II-1-4-17	Isostatic model of Airy (Karner, 1982)	150
Figure II-1-4-18	Locations of drilling holes used by M.C.L. Quintas (1995)	153
Figure II-1-4-19	Calculated tectonic subsidences (backstripping method) (M.C.L. Quintas, 1995)	155
Figure II-1-4-20	Iso-attenuation map of the first distensible event (440 Ma) (M.C.L. Quintas, 1995)	160
Figure II-1-4-21	Accumulated thickness of sills, modified from Zalan et al., (1986) (M.C.L. Quintas, 1995)	161
Figure II-1-4-22	Iso-attenuation map of the second distensible event after the simulation of erosion (296 Ma) (M.C.L. Quintas, 1995)	162
Figure II-1-4-23	Sense of rupture of Gondwana (Turner et al., 1994)	163
Figure II-1-4-24	Iso-attenuation map of the third distensible event after the simulation of erosion (144 Ma) (M.C.L. Quintas, 1995)	164
Figure II-1-4-25	Bouguer anomaly calculated from observed data (M.C.L. Quintas, 1995)	167
Figure II-1-4-26	Anomaly calculated due to the Paraná basin, considering anomalies generated by sediments, igneous rocks, sills and "root" (M.C.L. Quintas, 1995)	168

Figure II-1-4-27	Gravimetric trend anomaly generated by the second order polynomial (M.C.L. Quintas, 1995) .....	169
Figure II-1-4-28	Residual anomaly subtracted the second order trend anomaly from the Bouguer anomaly indicating zones of major attenuations related with two distensible events (M.C.L. Quintas, 1995) .....	170
Figure II-1-4-29	Hypothetical model for geotectonic evolution of segments adjacent to Paraguay belt, inferred by geological observations in south western Goiás region (extracted from Pimental and Fuck, 1987) .....	171
Figure II-1-4-30	Tectonic provinces of basement rocks and lineaments inferred from residual gravimetric anomalies (M.C.L. Quintas, 1995) .....	172
Figure II-1-5-1	Geological map of central Paraná basin .....	174
Figure II-1-5-2 (a), (b), (c)		
	Photos of igneous and sedimentary rocks in central Paraná basin .....	175
Figure II-1-5-3	Principal arch faults in the central Paraná basin (M.C.L. Quintas, 1995) .....	178
Figure II-1-5-4	Dyke swarm of the Ponta Grossa Arch .....	179
Figure II-1-5-5	Poles of joints of basalt dykes in the central area (plotted on lower hemisphere) ..	180
Figure II-1-5-6	Flight line locations of aeromagnetic data in central Paraná basin .....	183
Figure II-1-5-7	Total magnetic intensity of aeromagnetic data in central Paraná basin .....	184
Figure II-1-5-8	2nd vertical derivative of total magnetic intensity in central Paraná basin .....	185
Figure II-1-5-9	Total horizontal derivative of total magnetic intensity in central Paraná basin ...	186
Figure II-1-5-10	Total horizontal derivative of pseudogravity in central Paraná basin .....	187
Figure II-1-5-11	Analytic signal of total magnetic intensity in central Paraná basin .....	188
Figure II-1-5-12	Reduced to the pole magnetic anomaly in central Paraná basin .....	189
Figure II-1-5-13	Pseudogravity in central Paraná basin .....	190
Figure II-1-5-14	Magnetic map in the Paraná basin (total intensity) .....	191
Figure II-1-5-15	Magnetic map in the Paraná basin (declination) .....	192
Figure II-1-5-16	Magnetic map in the Paraná basin (inclination) .....	193
Figure II-1-5-17	Magnetic anomaly occurred by uniformly magnetized bodies in the southern hemisphere (Geodesy and Geophysics, 1969) .....	194
Figure II-1-5-18	Susceptibilities classified by rock types .....	198
Figure II-1-5-19	Examples of stereo-projection of NRM after 20mT demagnetization by alternating current .....	199
Figure II-1-5-20	Analyzed map of pseudogravity .....	202
Figure II-1-5-21	TM image (RGB=234) of the central Paraná basin .....	204
Figure II-1-6-1	Generalized map of the Midcontinent rift of North America, after P.W. Weiblen (1980) .....	206
Figure II-1-6-2	Generalized map of the Lake Superior region .....	206
Figure II-1-6-3	Generalized map view of the Kawishiwi area of the Duluth Complex .....	207
Figure II-1-6-4	Formation of aulacogene (b) associated with the rupture of the continent (a) (S. Ueda, 1989) .....	209

Figure II-1-6-5	Possible analogies between the geometry of the igneous rocks associated with the Tertiary opening of the North Atlantic and those in the Midcontinent Rift System	209
Figure II-1-6-6	Shear mechanisms for producing extensional features in rocks	210
Figure II-1-6-7	Hypothetical transition in tectonic regimes proposed for the Midcontinent Rift System	210
Figure II-1-6-8	Rifting models for the Midcontinent Rift System (from Norman, 1978)	211
Figure II-1-6-9	Regional patterns of geophysical anomalies in the Midcontinent Rift System	211
Figure II-1-6-10	Interior structure of crush zone of the shear fracture formed by rock failure test (a) and those of vein (b~d) (K. Otsuki et al., 1991)	212
Figure II-1-6-11	Formation model of Duluth mineralized intrusive complex	212
Figure II-1-6-12	Reconstruction of the position of the American, European, Siberian, Kazakhstan, north China, and several smaller plates	214
Figure II-1-6-13	Diagram of geological geotectonic zoning and the Siberian continental drift	215
Figure II-1-6-14	Isopach map of thickness of crust, limited by the surface of Mohorovicic and that of the Paleozoic (and is some places Mesozoic) foundation	215
Figure II-1-6-15	Map of the Norilsk region showing the outcrop of the lavas (areas surrounded by lines with attached hatching), main tectonic elements and principal ore junctions (from Naldrett et al, 1992)	216
Figure II-1-6-16	Thickness of the Nadezhinsky formation (lower+middle+upper) suite which illustrates the basin into which lavas were accumulating at the time of eruption (after Naldrett et al, 1992)	216
Figure II-1-6-17	Plan showing the outline of the Northwest Talnakh intrusions, showing the distribution of lenses of massive sulfide	217
Figure II-1-6-18	Formation model of Norilsk ore deposit	217
Figure II-1-6-19	Post - Paleozoic geotectonics of South America (modified from W.M. de Rezende, 1972; et al.)	220
Figure II-1-6-20	Comprehensive analysis map among the basement structure, basin sediment, gravity anomaly, regional stress field, pseudogravity map and TM image in the Paraná basin	222
Figure II-2-2-1	Location map of JERS-1/SAR image analysis	225
Figure II-2-2-2	Flow chart of producing JERS-1/SAR mosaic image	227
Figure II-2-2-3	JERS-1/SAR mosaic image	229
Figure II-2-3-1	Interpretation map based on JERS-1/SAR mosaic image	231
Figure II-2-3-2	Landsat TM mosaic image	234
Figure II-2-3-3	Interpretation map based on Landsat TM mosaic image	235
Figure II-3-1-1	Presence configuration around the Paraná flood basalt (after White and McKenzie, 1989)	238
Figure II-3-1-2	Generalized geological sketch map of the Paraná basin (Melfi et al, 1988)	239
Figure II-3-1-3	Sequence-stratigraphic chart for the Paraná basin (simplified from Milani et al., 1974)	241

Figure II-3-1-4	Overview of the Paraná flood basalts	243
Figure II-3-1-5	Duration time of activity and eruption rate for the Paraná flood basalts	244
Figure II-3-1-6	Characteristics of the acidic rocks concerned with the Paraná flood basalts	246
Figure II-3-1-7	Isopachs of combined sill thicknesses with the Paraná basin sediments (Bellieni et al, 1984)	248
Figure II-3-1-8	Activity of alkalic magmatism contemporaneous with the Paraná flood basalts (Peate, 1997)	250
Figure II-3-2-1	Distribution of collected samples in the survey area	257
Figure II-3-2-2	Drill location of collected core and cuttings samples in the survey area	259
Figure II-3-2-3	Occurrences of lavas in the central part of Paraná flood basalts	262
Figure II-3-2-4	Occurrences of sills around the southeastern part of Paraná basin	263
Figure II-3-3-1	Geochemical characteristics of the Paraná flood basalts (from Peate, 1997)	268
Figure II-3-3-2	Geochemical classification for the Paraná flood basalts (after Peate et al., 1992)	276
Figure II-3-3-3	Distribution of geochemical classified lava and intrusion in the Paraná flood basalts	278
Figure II-3-3-4	AFM diagram and SiO <sub>2</sub> vs. alkali diagrams for lava samples	280
Figure II-3-3-5	Mg number vs. SiO <sub>2</sub> , TiO <sub>2</sub> and P <sub>2</sub> O <sub>5</sub> diagrams for lava samples	281
Figure II-3-3-6	Mg number vs. Al <sub>2</sub> O <sub>3</sub> , Fe <sub>2</sub> O <sub>3</sub> and MgO diagrams for lava samples	282
Figure II-3-3-7	Mg number vs. CaO, Na <sub>2</sub> O and K <sub>2</sub> O diagrams for lava samples	283
Figure II-3-3-8	Mg number vs. Nb, Zr and Y diagrams for lava samples	285
Figure II-3-3-9	Mg number vs. Rb, Sr and Ba diagrams for lava samples	286
Figure II-3-3-10	Mg number vs. Th, U and La diagrams for lava samples	288
Figure II-3-3-11	Mg number vs. Cu, Ni and Au diagrams for lava samples	287
Figure II-3-3-12	Mg number vs. Pt, Pd and Pt+Pd diagrams for lava samples	289
Figure II-3-3-13	Histograms of Cu, Au, Pt and Pd contents for lava and intrusion of the Paraná flood basalts	291
Figure II-3-3-14	Decision of thresholds by accumulation frequency curve of transition and noble elements for lava and intrusion	292
Figure II-3-3-15	Distribution map of Cu content of lava and intrusion samples in the Paraná flood basalts	293
Figure II-3-3-16	Distribution map of Au content of lava and intrusion samples in the Paraná flood basalts	294
Figure II-3-3-17	Distribution map of Pt content of lava and intrusion samples in the Paraná flood basalts	295
Figure II-3-3-18	Distribution map of Pd content of lava and intrusion samples in the Paraná flood basalts	296
Figure II-3-3-19	Spider diagrams of trace elements for lava samples	298
Figure II-3-3-20	Plots of <sup>87</sup> Sr/ <sup>86</sup> Sr isotopic ratio and <sup>143</sup> Nd/ <sup>144</sup> Nd isotopic ratio for lava samples	300
Figure II-3-3-21	Vertical variations of major elements in lava samples (drill hole: RP-3)	301
Figure II-3-3-22	Vertical variations of trace elements in lava samples (drill hole: RP-3)	302

Figure II-3-3-23	Vertical variations of transition and noble elements in lava samples (drill hole: RP-3) .....	303
Figure II-3-3-24	Vertical variations of the ratios of selected trace elements in lava samples (drill hole: RP-3) .....	304
Figure II-3-3-25	Vertical variations of major elements in lava samples (drill hole: PP-2) .....	306
Figure II-3-3-26	Vertical variations of trace elements in lava samples (drill hole: PP-2) .....	307
Figure II-3-3-27	Vertical variations of transition and noble elements in lava samples (drill hole: PP-2) .....	308
Figure II-3-3-28	Vertical variations of the ratios of selected trace elements in lava samples (drill hole: PP-2) .....	309
Figure II-3-3-29	Vertical variations of major elements in lava samples (drill hole: AR-1) .....	311
Figure II-3-3-30	Vertical variations of trace elements in lava samples (drill hole: AR-1) .....	312
Figure II-3-3-31	Vertical variations of transition and noble elements in lava samples (drill hole: AR-1) .....	313
Figure II-3-3-32	Vertical variations of the ratios of selected trace elements in lava samples (drill hole: AR-1) .....	314
Figure II-3-3-33	(a) Ta/Yb vs. Th/Yb diagram for lava samples; (b) Zr/Nb vs. Y/Nb diagram for lava samples .....	316
Figure II-3-3-34	Ba/Ca vs. Sr/Ca diagram for lava samples .....	317
Figure II-3-3-35	(a) $Ce_N$ vs. $(Ce/Yb)_N$ and $(Ce/Sm)_N$ diagrams for lava samples; (b) Mg number vs. Gd/Yb and Nb/Zr diagrams for lava samples .....	318
Figure II-3-3-36	Zr vs. $TiO_2$ , Ni and Yb diagrams for lava samples .....	320
Figure II-3-3-37	Variation of selected elements and ratios by crustal contamination for lava samples .....	322
Figure II-3-3-38	Mg number vs. La/Sm and Th/Yb diagrams for lava samples .....	324
Figure II-3-3-39	Variation of Ni with forsterite in olivine from basaltic lava and intrusion .....	325
Figure II-3-3-40	Location of collected samples for Ar-Ar dating in the Paraná flood basalts .....	327
Figure II-3-3-41 (a), (b), (c)	Laser step-heating results and plateau age for the Paraná flood basalts .....	328
Figure II-3-3-42	Magma types and Ar-Ar data in the Paraná flood basalts (after Turner et al., 1994 ; Stewart et al., 1996) .....	333
Figure II-3-3-43	Chemical stratigraphy and Ar-Ar dating data by drill samples along north-south direction in the Paraná basin .....	334
Figure II-3-3-44	Schematic transitional model of magmatism for the Paraná flood basalts .....	337
Figure II-3-4-1	Intrusions studied by the Canada-Brazil cooperative project .....	340
Figure II-3-4-2	Borehole locations for the coal prospecting in the eastern margin of the Paraná basin .....	342
Figure II-3-4-3	Isopach map of the total thickness of sills in the eastern margin of the Paraná basin .....	343
Figure II-3-4-4	Isopach map of the total thickness of sills in the Lomba Grande Block .....	344
Figure II-3-4-5	Isopach map of the total thickness of sills in the Santa Catarina Block .....	345



Figure II-3-4-6	Isopach map of the total thickness of sills in the Ponta Grossa Arch Block	346
Figure II-3-4-7	Lomba Grande Block A-A' section (scale; 1:250,000, H/V; 1:10)	347
Figure II-3-4-8	Lomba Grande Block B-B' section (scale; 1:250,000, H/V; 1:10)	349
Figure II-3-4-9	Lomba Grande Block C-C' section (scale; 1:250,000, H/V; 1:10)	350
Figure II-3-4-10	Santa Catarina Block A-A' section (scale; 1:250,000, H/V; 1:10)	351
Figure II-3-4-11	Santa Catarina Block B-B' section (scale; 1:250,000, H/V; 1:10)	351
Figure II-3-4-12	Santa Catarina Block C-C' section (scale; 1:250,000, H/V; 1:10)	353
Figure II-3-4-13	Santa Catarina Block D-D' section (scale; 1:250,000, H/V; 1:10)	353
Figure II-3-4-14	Ponta Grossa Arch Block A-A' section (scale; 1:150,000, H/V; 1:6)	355
Figure II-3-4-15	Ponta Grossa Arch Block B-B' section (scale; 1:150,000, H/V; 1:6)	356
Figure II-3-4-16	Ponta Grossa Arch Block C-C' section (scale; 1:150,000, H/V; 1:6)	357
Figure II-3-4-17	Ponta Grossa Arch Block D-D' section (scale; 1:150,000, H/V; 1:6)	358
Figure II-3-4-18	Location map of the coal drills for sampling	359
Figure II-3-4-19	Mg# - major element diagrams (SiO <sub>2</sub> , TiO <sub>2</sub> , P <sub>2</sub> O <sub>5</sub> ) for intrusive rocks	361
Figure II-3-4-20	Mg# - major element diagrams (Al <sub>2</sub> O <sub>3</sub> , Fe <sub>2</sub> O <sub>3</sub> , MgO) for intrusive rocks	362
Figure II-3-4-21	Mg# - major element diagrams (CaO, Na <sub>2</sub> O, K <sub>2</sub> O) for intrusive rocks	363
Figure II-3-4-22	Mg# - trace element diagrams (Rb, Sr, Ba) for intrusive rocks	364
Figure II-3-4-23	Mg# - trace element diagrams (Th, U, La) for intrusive rocks	365
Figure II-3-4-24	Mg# - trace element diagrams (Nb, Zr, Y) for intrusive rocks	366
Figure II-3-4-25	Mg# - chalcophile element diagrams (Cu, Ni, Au) for intrusive rocks	367
Figure II-3-4-26	Mg# - chalcophile element diagrams (Pt, Pd, Pt+Pd) for intrusive rocks	368
Figure II-3-4-27	(A) Th/Nb - Gd/Yb diagram for intrusive rocks; (B) Th/Ta - Gd/Yb diagram for intrusive rocks	371
Figure II-3-4-28	(A) Mg# - <sup>87</sup> Sr/ <sup>86</sup> Sr initial ratio diagram for intrusive rocks; (B) Mg# - <sup>143</sup> Nd/ <sup>144</sup> Nd initial ratio diagram for intrusive rocks; (C) <sup>87</sup> Sr/ <sup>86</sup> Sr initial ratio - <sup>143</sup> Nd/ <sup>144</sup> Nd initial ratio diagram for intrusive rocks	372
Figure II-3-4-29	Vertical variations in major and trace-element in sill intersected by drill (AT03)	374
Figure II-3-4-30	Vertical variations in major and trace-element in sill intersected by drill (AT08)	375
Figure II-3-4-31	Vertical variations in major and trace-element in sill intersected by drill (TG95)	376
Figure II-3-4-32	Vertical variations in major and trace-element in sill intersected by drill (TG97)	377
Figure II-3-4-33	Vertical variations in major and trace-element in sill intersected by drill (TG228)	378
Figure II-3-4-34	Vertical variations in major and trace-element in sill intersected by drill (TG62)	379
Figure II-3-4-35	Vertical variations in major and trace-element in sill intersected by drill (TG114)	380

Figure II-3-5-1	Frequency diagram of assay data of Pt (A), Pd(B), and Pt + Pd(C) for lava samples .....	384
Figure II-3-5-2	Frequency diagram of assay data of Pt(A), Pd(B), and Pt + Pd(C) for intrusion samples .....	385
Figure II-3-5-3	Pt - Pd correlation diagram for lava samples .....	387
Figure II-3-5-4	Pt - Pd correlation diagram for intrusion samples .....	388
Figure II-3-5-5	(A, B, C, D, and E) Mantle -normalized metal element patterns for selected lava samples .....	390
Figure II-3-5-6	(A, B, and C) Mantle -normalized metal element patterns for selected intrusion samples .....	391
Figure II-3-5-7	(A) Gd/Yb - Pt+ Pd diagram for lava samples; (B) Gd/Yb - Pt+ Pd diagram for intrusion samples .....	393
Figure II-3-5-8	Cu - Pd discriminant diagram between the field of rocks formed by sulfur - saturated magmas and the field of rocks formed by sulfur- undersaturated magmas(Brooks et al.,1999) for lava samples .....	395
Figure II-3-5-9	Cu - Pd discriminant diagram between the field of rocks formed by sulfur - saturated magmas and the field of rocks formed by sulfur- undersaturated magmas(Brooks et al.,1999) for intrusion samples .....	396
Figure II-3-5-10	La/Sm - Pd/Cu diagram for lava samples .....	397
Figure II-3-5-11	Mg# - Pd/Cu diagram for lava samples .....	399
Figure II-3-6-1	Stream sediment geochemical maps of Ni, Cu, Pt, and Pd by MINEROPAR (Licht, 2000) .....	402
Figure II-3-6-2	NE - SW trending horst and graben structure by Milani (1997) (Licht, 2000) ...	402
Figure II-3-7-1	Distribution of the native copper in the Paraná flood basalts .....	405
Figure II-3-7-2	Microscopic image .....	407
Figure II-3-8-1	Geological section (Uruguaiana – São Miguel d'Oeste) .....	411
Figure II-3-8-2	Map of Cu, Ni, Zn, Ba, Co, S for stream sediments in Paraná (Ponta Grossa arch) .....	413
Figure II-3-8-3	Contour map of Cu, Ni, Zn, Ba, Co, S for stream sediments in Paraná (Jaguariaíva) .....	414
Figure II-3-8-4	Contour map of Cu, Ni, Zn, Ba, Co, S for stream sediments in Paraná (Rio Alohzo) .....	416
Figure II-3-8-5	Contour map of Cu, Ni, Zn, Ba, Co, S for stream sediments in Paraná (Reserva) .....	417
Figure II-3-8-6	Contour map of Cu, Ni, Zn for stream sediments in Rio Grande do Sul (São Gabriel arch) .....	418
Figure II-3-8-7	Contour map of Fe, Cr, Mn for stream sediments in Rio Grande do Sul (São Gabriel arch) .....	419
Figure II-3-8-8	Contour map of Ba, Co, S for stream sediments in Rio Grande do Sul (São Gabriel arch) .....	420

## Tables

Table I-1-2-1	Laboratory test	4
Table I-3-1-1	Production of main minerals of Brazil	9
Table I-3-1-2	Mineral production of main companies of Brazil	10
Table I-3-2-1	Major geological events in the South America	16
Table I-3-3-1	Type of PGE deposits in the world and their reserve and production	39
Table I-3-3-2	Samples already collected and analyzed by CPRM PGE project	42
Table II-1-2-1	Mafic and ultramafic bodies and related sulfide ores	66
Table II-1-2-2	Major flood basalts and continental breakup (White and McKenzie, 1989)	68
Table II-1-2-3	Composition of starting materials of melting experience (Takahashi et al., 1998)	85
Table II-1-2-4	Variety of the magma expected from the heterogeneous mantle plume model	90
Table II-1-2-5	Abundance of some transitional metals in earth and planetary materials (Naldrett, 1989)	90
Table II-1-3-1	Classification of mafic and ultramafic bodies (Naldrett, 1989)	93
Table II-1-3-2	Comparison of PGE reserves in the major Ni-Cu-PGE deposits	94
Table II-1-3-3	Volume percentages of the magmatic rock types in the Noril'sk region (Fedorenko, 1994)	99
Table II-1-4-1	Intracratonic basin in the world	149
Table II-1-4-2	Locations of drilling holes (M.C.L. Quintas, 1995)	154
Table II-1-4-3	Basic Parameters used in thermomechanic model (M.C.L. Quintas, 1995)	156
Table II-1-4-4	Ratios of tectonic subsidence and total subsidence with the time	156
Table II-1-5-1	Natural remanent magnetizations (NRM) and susceptibility of basalt lavas and gabbro sills in the central area of the Paraná basin	198
Table II-2-2-1	List of JERS-1/SAR data	226
Table II-3-2-1	Microscopic observation results of the lava samples in the Paraná flood basalts	265
Table II-3-3-1	Analytical results of major, trace and metal elements for the Paraná flood basalts in this survey	277
Table II-3-3-2	Samples for EPMA	323
Table II-3-3-3	Samples for Ar-Ar dating	331
Table II-3-3-4	Nomenclature scheme for the Paraná magma types, and their relationship to previous groups from the Paraná and Etendeka literature (Peate et al., 1992)	335
Table II-3-3-5	Comparison of magmatisms of each magma type for the Paraná flood basalts	336
Table II-3-4-1	Sulfur isotopic ratios of intrusive rocks and sediments	382
Table II-3-5-1	Platinum and Palladium concentrations of lava and intrusion samples	383
Table II-3-5-2	Metal elements concentrations of lava and intrusion samples	389
Table II-3-7-1	Microscopic observation of polished section	406
Table II-3-7-2	Metal mineral analysis	408
Table II-3-8-1	General interpretation	412

# **Part I General Discussion**

## **Chapter 1: Introduction**

### **1-1 Circumstances for Starting the Survey**

Platinum-group metals (hereinafter referred to as “PGM”) are very important from economic and strategic viewpoints. In addition to their use as jewelry, their use in various industrial fields especially in the field of electronics and the products to control environmental pollution (automobile catalyst) is now becoming increasingly important. The world PGM resources are unevenly distributed in the largest quantity in South Africa and in the second largest quantity in Russia. The total of PGM distributed in these two countries accounts for 98.5% of the world PGM resources. Among the quantities of PGM consumed in Brazil (approximately 4.85 tons in ‘2000), its use as automobile catalyst (80.6 % of the total consumption) has been rapidly extended. Currently, Brazil imports the entire quantity of PGM required for automobile catalyst.

In spite of its importance as resources, few PGM data had been collected by Brazil before 1990. With this situation as a background, Geological Survey of Brazil (hereinafter referred to as “CPRM”) implemented its project “National PGM Project” covering the entire land of Brazil from 1990 to 1995.

Subsequent to the “PGM National Project,” MMAJ and CPRM decided in June, 2001 to enforce a regional geological survey of Ni-Cu-PGM ore deposits in the Paraná basin located in the south part of Brazil based on the technical cooperation between the above organizations. The side of Brazil intend to promote prospecting of Ni-Cu-PGM ore deposits by both domestic and overseas companies in accordance with the results of the survey.

Most of the PGM ore deposits are accompanied by three types of basic to ultrabasic intrusive complex. For example: layered intrusive rocks (Bushveld in South Africa), intrusive rocks related to flood basalt (Noril’sk in Russia) and intrusive rocks related to greenstone (Kambalda in Australia). The objective of the survey is to investigate the possibility of the Noril’sk-type Ni-Cu-PGM ore deposit related to the flood basalt in Paraná basin situated in the south part of Brazil.

In Brazil, The five projects based on the technical cooperation between Brazil and Japan have been conducted since 1980 in the districts below.

Anta Gorda District	(survey of resources development)	FYs 1980-1983
Ribeira District	(survey of local development plan)	FY 1984
Palmeiropolis District	(survey of resources development)	FYs 1986-1988
Currais Novos District	(survey of resources development)	FYs 1989-1991
Currais Novos District	(follow-up survey)	FY 1992
Alta Floresta District	(survey of resources development)	FYs 1998-2000

## 1-2 Summary of the Survey

### 1-2-1 Purpose of the Survey

The purposes of this survey are to extract promising district as Ni-Cu-PGM ore deposits from Paraná district in the south of Brazil, to enforce the existing data analysis, satellite image analysis and ground truth survey, to conduct the general analysis of the results obtained, and to efficiently extract promising existence of deposits from regional area.

### 1-2-2 Survey Area

The survey area is situated in the south of Brazil ranging from the latitude 15° - 34° south in the north- south direction to the longitude 46° - 60° west in the east- west direction with the total area of 1,400,000 km<sup>2</sup> (Fig. I-2-1-1). With regard to the topography of the survey area, most of the survey consists of plateaus of around an elevation of 500 m and grassy plains. However, the central to eastern part of the survey area consists of mountains in an elevation of 1,000 - 1,800 m.

### 1-2-3 Survey Method

The survey method consists of the existing data analysis, satellite image analysis and the ground truth survey. Table I-1-1 shows the volume of the individual surveys as well as the items and quantities of laboratory tests.

#### (1) Existing Data Analysis

A lot of the existing data were involved concerning Paraná basin, such as geological and geochemical theses, reports and drawings, aeromagnetic and gravimetric data, PGM prospecting reports by Canada and Brazil and drilling data for oil prospecting. These materials were collected, analyzed and compiled from CRPM, the local geological survey organizations,

colleges and universities, mining and oil companies. The results of the satellite image analysis were also used in these tasks.

## (2) Satellite Image Analysis

The satellite image analyses were conducted at the whole area and the central part of the survey area within a range of approximately 250,000 km<sup>2</sup>. Mosaic images of JERS-1/SAR data in the central part and Landsat TM data in the whole area were of the survey area prepared, read from geological viewpoints and interpreted together with the existing data. The geological structures related to the generation of ore deposits such as lineaments and circular structures were confirmed on the SAR images to extract the promising area for deposit.

## (3) Ground Truth Survey

The ground truth survey was conducted based on the results of the existing data and satellite image analyses. Rock specimens collected from lava, intrusive rocks, etc. were subject to laboratory tests. All the results thus obtained were comprehensively examined, possibility of deposit was studied and prospecting techniques were proposed for the future.

### 1-2-4 Configuration of the Survey Mission

Japan side :

Kenji Nakamura:	JMEC
(Japan Mining Engineering Center for International Cooperation)	
Akitsura Shibuya: (First fiscal year)	JMEC
Taizou Matsumoto: (Second fiscal year)	JMEC
Kenzo Masuta:	JMEC
Takayoshi Murakami:	JMEC

Brazil side :

Wilson WILDNER:	CPRM
(Geological Survey of Brazil)	
Adalberto DIAS: (First fiscal year)	CPRM
Carlos ALBERTO:	CPRM
Norberto LESSA: (First fiscal year)	CPRM
Luis Antonio Chierigati: (Second fiscal year)	CPRM
Paulo Rogerio Ribeiro da Silva: (Second fiscal year)	CPRM
Sergio J. Romanini: (Second fiscal year)	CPRM

1-2-5 Period and Quantity of the Survey

(1) Satellite Image Analysis:

(First fiscal year) July 17 - August 8, 2001

(Second fiscal year) December 11 - December 16, 2002

(2) Existing Data Analysis and Ground Truth Survey:

(First fiscal year) August 9 - November 2, 2001

(Second fiscal year) July 3 - September 28, 2002

(3) Laboratory Tests and Comprehensive Analysis:

(First fiscal year) November 3, 2001 - March 15, 2002

(Second fiscal year) September 30, 2002 - March 15, 2003

**Table I-2-1 Laboratory test**

Item	Amount	
	2001 Fy	2002 Fy
Thin section	189	26
Polished thin section	3	52
Polish chip	5	
X - ray diffractometer	4	
Whole rock analysis and minor element analysis (61 elements)	198	426
Stream sediment analysis (30 elements)	316	282
Water analysis (69 elements)	182	
Panning sample analysis (11 elements)	5	
Radiometric age determination (Ar – Ar method)	16	
Isotopic measurement (Sulfur)	4	8
Isotopic measurement (Strontium, Neodymium)	34	36
EPMA	10	
Ir, Rh, Re analysis		34

## Chapter 2: Geography of the Survey Area

### 2-1 Location

Fig. I-2-1-1 shows the location of the survey area. The area covered by this survey is located from the central to southern part of Brazil, ranging from longitude 45° to 57° west and from latitude 15° to 35° north. The eastern side of the survey area faces to the Atlantic Ocean, while its western side is close to the borders of Paraguay and Argentine, and its southern side is close to the border of Uruguay.

### 2-2 Topography

The topography of the survey area is rather steep from the coastal mountains to its central part as the edge of Paraná basin shifting from a smooth plateau to a plain. This plain leads to a large grassy plain in the central part of South America Continent called a pampas. The maximum height of the survey area is around 1500 m above the sea. In particular, the hilly area with few rises and falls extends from the central to the southern part of the survey area where pasturing and wheat growing are mainly conducted.

While no dune is developed on the eastern coast of the survey area, tidelands and lagoons are developed on the southern coast.

### 2-3 Drainage Systems

The main drainage system in the survey area is divided as Paraguai River system, Paraná River system and Uruguai River system. The Paraguai River system with Mato Grosso plateau as its source flows down to the south and joins the Paraná River.

The Paraná River with plateaus surrounding Brasilia as its sources runs through São Paulo Province and Paraná Province and flows down in parallel with the inland side of the coastal mountains. Then it joins the Paraguai River, flows into the La Plata River which runs along the border between Argentine and Uruguay, and flows into the Atlantic Ocean. The Iguazu River which is famous for Iguazu Waterfall is a branch of the Paraná River.

Besides, a river runs in the southern part of the survey area and flows into the Lake Patos, a lagoon on the Atlantic coast. Its main stream is the Jacuí River which runs from the west to east through Porto Alegre City.





Fig. I-2-1-1 Location of the Paraná basin area, Brazil

## 2-4 Climate

The climate in most of Brazil is either tropical or subtropical. Although the northern part of the survey area belongs to the subtropical zone, the three provinces located from the central to southern part of the area, i.e. Paraná Province, Santa Catarina Province and Rio Grande do Sul Province, belong to the temperate zone. Temperatures there differ much depending on the geographical locations and rises or falls. The seashore of Santa Catarina Province and the periphery of the Paraná River are the places with the highest temperatures of approximately 20 to 25°C, while the temperatures of the central and the southernmost parts are around 17°C. Rain falls regularly there throughout a year. In August and September, however, there is a rainy season just like the rainy season in Japan. In winter, snow falls in the places with high elevation.

## 2-5 Plantation

In the north-western part of the survey area, especially in the western part of Mat Grosso Province, shrubbs, bushes and grassy plains which grow in swamp are complicatedly mixed up.

Along the eastern coast of the survey area, the plants suitable for muddy land grow as a characteristic of the place, while mangrove grows along the northern to the central coast of the survey area. On the wet coastal mountains developed a little nearer to the inland, jungles of evergreen trees are distributed.

On the flat land from the central to the southern part of the survey area, the thick-growing gramineous plants constitute a treeless grassy plain.

In the Paraná Province, Santa Catarina Province and Rio Grande do Sul Province, Paraná Pine Trees (*Araucaria*) grow thick. They are utilized for lumber and food (seeds only) and their economic efficiency is high. In addition, nuts and yerba mate are produced there.

## **Chapter 3: Geology, Mineral Deposits, and Mining of the Survey Area**

### **3-1 Recent Mining Situation**

#### **3-1-1 Mining Production**

The Federal Republic of Brazil is abundant in many mineral resources. Its niobium and rutile reserves rank first; tin, second place; bauxite, third place. Iron ore production ranks second place (reserve ranks sixth place) in the world. In addition, magnesium, manganese, tantalum, gold, and many other mineral resources are produced in Brazil. Meanwhile, the productions of bauxite, tin ore, bullion, and manganese ore rank fourth place. Besides these, Brazil is a major producer of rare earth and other non-ferrous metals. The quantity of the aluminum bullion imported to Japan from Brazil accounts for some 17 % of the total import of aluminum bullion. Brazil also supplies Japan with nickel bullion, manganese ore, and other ores.

Brazil reformed the Constitution in 1995. Since then, the restriction of investment by foreign firms has been abolished. As a result, the exploration and development of mineral resources have been opened to foreign firms, and privatization of the government-owned corporations has been on the increase. For example, Companhia Vale do Rio Doce(CVRD), formally owned by the government, was privatized in 1997.

Table I-3-1-1 and Table I-3-1-2 respectively show the production of major mineral resources and production quantities by company.

**Table I-3-1-1 Production of main minerals of Brazil**

Commodity	Unit	1997	1998	1999	99/98(%)	2000	00/99(%)
Copper	Metal ( t )	39,952	34,446	31,371	-8.9	31,786	1.3
Zinc	Metal ( t )	152,634	87,485	98,590	12.7	100,254	1.7
Tin	Metal ( t )	18,291	14,238	13,202	-7.3	14,200	7.6
Nickel	Metal ( t )	31,936	36,764	41,522	12.9	45,317	9.1
Niobium	Nb <sub>2</sub> O <sub>5</sub> ( t )	25,688	33,795	31,352	-7.2	31,190	-0.5
Tantalum	Ta <sub>2</sub> O <sub>5</sub> ( t )	153	377	390	3.4	419	7.4
Chromium	Cr <sub>2</sub> O <sub>3</sub> ( t )	112,274	209,596	207,123	-1.2	276,105	33.3
Gold	total ( k g )	52,335	46,031	51,422	11.7	52,420	1.9
	company ( k g )	41,062	37,787	42,367	12.1	42,025	-0.8
	garinpeiro(kg)	11,273	8,244	9,055	9.8	10,395	14.8
Iron	ore(1,000 t )	184,970	197,500	194,000	-1.8	210,000	8.2
Fluorite	1,000 t	78	72	45	-37.5	43	-4.4
Manganese	conc. (1,000 t )	2,124	1,940	1,656	-14.6	2,192	32.4
Aluminum	Bauxite (1,000 t )	11,671	11,961	13,839	15.7	13,846	0.1
Kaolin	1,000	1,165	1,374	1,517	10.4	1,735	14.4

Data from SUMARIO MINERAL 1999 and 2000(DNPM)

**Table I-3-1-2 Mineral production of main companies of Brazil**

Commodity/Company	Unit	1996	1997	1998	1999	98/99(%)
<b>Aluminum</b>	1,000 t	1,197.40	1,189.00	1,208.00	1,249.60	3.4
Albras		339	338	344.7	361.2	4.8
Alcan		93.4	93.3	102.5	102.4	-0.1
Alcoa		283.4	279.7	281.4	289	2.7
Aluvale		50.2	50.6	51.5	50.2	-2.5
Billiton		210.7	206.5	206.9	212.9	2.9
CBA		220	221	221	233.9	5.8
<b>Copper</b>	t	172,075	177,060	167,205	193,014	15.4
Caraiba		172,075	177,060	167,205	193,014	15.4
<b>Tin</b>	t	18,361	17,525	14,342	11,989	-16.4
Parapanema		15,242	14,763	11,429	10,112	-11.5
Cesbra		1,611	1,739	1,347	1,396	3.6
Best		1,085	1,023	853	481	-43.6
<b>Nickel</b>	t	16,432	18,200	25,748	32,268	25.3
Codemin		6,223	6,751	6,891	6,503	-5.6
Niquel Tocantis		7,849	8,849	13,008	16,430	26.3
Morro do Niquel		2,360	2,600	1,184	0	-100
Fortaleza		-	-	4,665	9,335	100.1
<b>Zinc</b>	t	186,339	185,701	176,806	187,010	5.8
CMM		100,016	95,556	104,714	109,398	4.5
Inga		22,914	19,445	1,224	0	-100
Paraibuna		63,409	67,690	70,868	77,612	9.5

Data from Brazil Mineral, May 2000

### 3-1-2 Mining Policy

The Government of Brazil formulated a "Comprehensive 10-Year Plan" in 1964 as part of mineral resource evaluation. The evaluation was conducted by the Departamento Nacional da Producao Mineral (DNPM). The major projects implemented by the competent department are as follows:

- (1) 1:1,000,000 geological mapping project
- (2) Basic regional geological survey project
- (3) Specific project for resource development

In addition, the following special projects were carried out.

- (1) RADM project : 1:250,000 mapping was conducted by using radar image that covers the entire land including the Amazon.
- (2) The air-borne geophysical exploration project by using gamma spectrum
- (3) Continental shelf survey project

In addition, Projecto Geofísico Brasil-Canada (PGBC: 1975-79), the air-borne geophysical exploration was conducted (magnetic and  $\gamma$ -ray) in broader areas over Para Province and Goiás Province. The result of the project led to finding diverse ore deposits in surroundings of Carajas district to the central area of Goiás Province.

In 1970, CPRM (Companhia de Pesquisa de Recursos Minerais) was set up. Since then, all of the projects under DNPM were carried out by CPRM, which is a government-owned corporation under the Minister of Mine and Energy. The "Comprehensive 10-Year Plan" was also conducted by CPRM and completed in 1979, four to five years behind from the original schedule.

Since 1980, the "Second Comprehensive 10-Year Plan" was conducted. The plan included the planning of a basic geological study (1980-1989). As a result of this plan and implementation, geological mapping (on the scale of 1:50,000 to 1:250,000), geophysical and geochemical prospecting project, and hydraulic mapping project, etc. were conducted. However, along with the stagnant economy, many of the project implementations were behind the schedule.

The Government of Brazil has been promoting organizational reformation. For example, DNPM has been transformed into an independent administrative agency. As a result, the main business of DNPM has transformed itself into a agency of mining claim management, mine safety, mine pollution prevention measures, etc. Meanwhile, CPRM discontinued its own exploration since 2000, and trying to focus on the role of geological survey office.

In the past, every province had a resource exploration and development corporation to explore mineral resources within the province. For example, METAMIG Corporation for Minas Gerais Provinces, METAGO for Goiás Provicne, and CBRM for Baia Province used to engaged in mineral resource explorations. At present, these companies have been liquidated, and mine claims were controlled by the provincial government.

### 3-1-3 Exploration and Development

INCO, Utah/BHP group, Billiton, a subsidiary of SHELL, RTZ, and other foreign-capital controlled private companies are engaging active explorations. Meanwhile, CVRD, Paranapanema, and other domestic-capital controlled companies are engaging in mineral resource prospecting, especially centering on the finding of gold ore deposit.

RTZ developed Morro do Ouro gold deposit in Paracatu City in 1987. In addition, the company engaged in the exploration of many mining concessions succeeded to BP, and also expressed the participation in the development of Salobo copper deposit of CVRD (J/V Project).

Aoki Corporation from Japan once acquired 49% of Nova Astro's share and began to develop Saramangore gold mine, owned by Nova Astro, in the Lorengo district in Amapa Province since 1986. Although the gold mine produced about 350 to 800 kg of gold a year, Aoki Corporation withdrew from the operation.

Sumisho Mineral Resources Development Co., Ltd. planned and carried out a number of projects, including the exploration of beach placer deposit in southern Salvador and rare metals and rare earth explorations in Tocantins Province. Mitsui Mining Co., Ltd. conducted rare earth explorations in Goias Province in 1991.

### 3-1-4 Recent Mining Situation

Mining productions in Brazil except those of iron ore and niobium have stagnated in recent years. Since neighboring countries one after another succeeded in developing mines by inviting foreign firms and began to increase mining productions and exports, the Government of Brazil also began to invite foreign firms to boost mining production. Although the mining production in Brazil is stagnant, domestic demand for copper continued to increase. To meet such demand, Caraiba Copper Smelter, the only copper smelter in Brazil, is planning to double copper production.

Caraiba Mine is located deep inside Bahia Province, northeast of Brazil. The mine produced 102,416 tons of copper concentrate (34,446 tons of copper) in 1998. However, since copper ore reserve for open-cut mining was almost exhausted in Caraiba Mine, its copper production for 1999 was expected to go below 30,000 tons.

According to a document of DNPM, as for copper supply in 1998, Caraiba Smelter produced 167,205 tons of copper, 54,150 tons of copper scraps were collected, and 128,781 tons of copper cathode were imported mostly from Chile. In total some 350,000 tons of copper were supplied for domestic demand in 1998.

The copper production in Caraiba Mine and collection of copper scraps amounted to some 90,000 tons while domestic demand for copper recorded more than 310,000 tons. Thus, some

220,000 tons of copper is in short supply a year in Brazil.

Brazil has to import 200,000 tons of copper a year to meet domestic demand. A vast amount of copper reserve waits for explorations in Carajas district in Para Province. The copper ore deposits in the district are owned by CVRD, the largest iron ore producer in the world, which was privatized in 1997. The development project of the copper mine in Carajas area is smoothly progressing with CVRD. The copper production plan is 700 thousand tons per year from operating the five mines until 2007. As for the first step, development preparation began in May, 2002, aiming at the commencement of operating Sossego Mine in the middle of 2004. The operation of Solobo Mine, the biggest mine in the Carajas area, is planned to commence from 2007. The agreement to strategically study the possibility of a copper development joint-project with CVRD and the world's largest copper producer, Chile's state-owned CODELCO, was concluded in November, 2001, but the concrete plans have not yet been made. CODELCO has already established a branch in Brazil and is already carrying out prospecting.

Development of these copper deposits depend on the company. CODELCO, a government-owned corporation in Chili and the largest copper producer in the world, is negotiating with CVRD for explorations of copper in Brazil.

Brazil can produce a little over 50% of zinc ore for domestic demand, and imports zinc concentrate from Peru to meet the domestic demand shortage.

Rio Tinto Brazil Co., Ltd. began to produce nickel in Fortaleza Mine in 1998. The mine has continued to boost production. The company also produces and exports some 20,000 tons of copper, cobalt, and platinum mattes a year to Outokumpu Co., Ltd. Brazil also occupies over 90% of niobium production of world (source: Mineral Summary 2000, DNPM). Some 80% of the niobium is produced by CBMM, which has completed a plant construction to enhance production processes.

Regarding Platinum Group Elements, the target minerals of this survey, prospecting was carried out with an investment of 5.2 million US dollars by CPRM as the national platinum project till the end of July, 1995. The field survey of the project was finished by 1998, and the preparation of the analysis charts and reports is progressing at present. In addition to the above work, Altoro Mineracao Corporation seems to be undertaking regional geochemical prospecting and drilling survey in Ceara Province.

Brazil moved to civilian control from military rule and proclaimed the Constitution in 1988. This constitution which has been rather favorable to domestic companies, allows a foreign firm to own at most 49% of share in a company. Today, however, the Government of Brazil is formulating a series of reform package bills, called "Reformation of Brazilian Mineral Sector(Reforma do Sector Mineral Brasileiro)," to pass the parliament by around July 2001 and push forward the reforms. The reform bills include the modernization of mine concession



management to prevent speculative ownership of mines, a tax reform to introduce incentives for mine exploration and development, formation of mine safety and mine closure regulations, and restructuring of the government agencies.

### 3-1-5 Mining Related Regulations

The 1988 Constitution of Brazil defines that spot side partner contributes the majority, and the rest for a foreign mining company to own less than half of shares of a joint venture in Brazil, respectively. Since then, the mining industry in Brazil has changed substantially. It seems that the Government of Brazil still thinks that investments from foreign countries are necessary and therefore does not take extreme measures that will discourage foreign investments.

The new Constitution also encourages individual diggers (garinpeiro). Under the new Constitution, individual diggers are allowed to apply for mining right in a primitive manner, which was banned in the past.

## 3-2 Summary of Geology and Ore Deposits in Brazil

### 3-2-1 Summary of Geology

#### (1) Precambrian in Brazil

Geological distribution of Archean and Proterozoic in Brazil is compiled in detail in the report of project finding survey FY 1992 (MMAJ, 1993). Therefore, here we give our brief summary by referring to the document prepared by Jenks, W.F. ("World Geology" translated by Yoshio Katsui, Vol. 16, Chapter 4: Geology of South America).

The wording of "South American Platform" as advocated by Almeida (1971) means a stable continental district of Precambrian age in South America. In the margin of this stable continent, structural movements and igneous activities arising one after another in Phanerozoic eon caused continental growth. Table I-3-2-1 shows the major geological events in the South American Continent, while Fig. I-3-2-1 shows the ages of the major structural movements and igneous activities there.

From the data of geological structures and radiation age measurement, Almeida (1971) divided Precambrian age of South America into the following three groups:

Late Precambrian age:	570 ~ 1800 Ma
Middle Precambrian age:	1800 ~ 2600 Ma
Early Precambrian age:	>2600 Ma

As shown in Fig. I-3-2-2, five major platforms (Guiana, Guaporé, São Luis, San Francisco, La Plata River and Imataca composite rocks are included in the South American platform.

The largest stable mass of them is Guiana shield where the northern part of Amazon basin in Brazil and the southeastern district of the Orinoco River in Venezuela are included. Guaporé Craton is distributed to the south of Amazon basin constituting the basement of the basin. Probably it belongs to the same structural unit as that of Guiana Shield. Other shields are distributed in São Luis district extending over Minas Gerais and Bahia Province, Uruguay and La Plata River area in the northern part of Argentine.

**Table I-3-2-1 Major geological events in the South America**

Western Marginal Belt	Platform District:
(No record remains)	3400-3000 Primitive platform (North Guiana Shield)
(No record remains)	3000-2700 Imataca Orogenic Cycle
(No record remains)	2000-1800 Trans-Amazon Orogenic Cycle gave impact to the entire platform
(No record remains)	1800-1700 Roraima formation became a plain. (continental sediment, marine sediment in part)
~1300 Metamorphism in fragments of the platform (the northeastern part of Colombia)	1400-1100 Uruacuan orogenic cycle (the eastern part of Brazil)
750~600 Brazilian Orogenic Cycle (Gneiss on the southwestern coast of Peru, etc.)	750-500 Brazilian orogenic cycle -- destruction and re-welding of the old platform
550~350: Thick continental shelf and slope sediments of the lower Palaeozoic	550-350 Marine sediment (Amazon, Parunaiba and Parana basin)
~280 Glaciogenic deposits (the southern part of Bolivia, the western part of Argentine and Chile)	~280 Gondwana continental glacier (the southern part of Brazil and Argentine)
~200 Volcanic activities of andesite in the Triassic period (Chile and coasts in Peru)	~200 Mafic volcanic movement (Guiana Shield)
~180 Development of volcanic island arcs and intrusion of western Marginal belt batholith (convergent plate boundary)	~180 Large-scaled extrusion of Parana basalt, etc. (with its peak in 130 ~ 120 Ma)
↓	↓
~40	~110
~118-88 Long and large marginal basin arose in the southern part of Chile and	~140-80 Contrary to the state in Africa, rapid clockwise revolution in South America
~150-80 Subduction of Caribbean plate. (Colombia, Venezuela)	Basin formation on the continental edge through trench forming
	Continuation of thick sediment activities
~60-10 Caribbean plate and South American plate were lateral fault to the right and transformed — migration fault. Probably lateral fault to the left in the southern end of South America	~80-0 Continuation of sediment activities on the continental shelf
~20-0 Upheaval of Andes Mountains, continuation of subduction, neutral/felsitic volcanic activities	

(Figures represent ages. Unit: Ma)

The oldest age that has ever been measured is 3000 Ma or older mainly derived from Guiana shield especially from Imataca composite rock. Reports on such oldest age scarcely exist in relation to the Guiana shield in Brazil. The radiation ages obtained through the whole-rock analysis of the above rocks and other metamorphic rocks in South America are 3000 - 2700 Ma.

The core or primitive platform of the above craton has been either cut up or covered by the

Figura 4.1

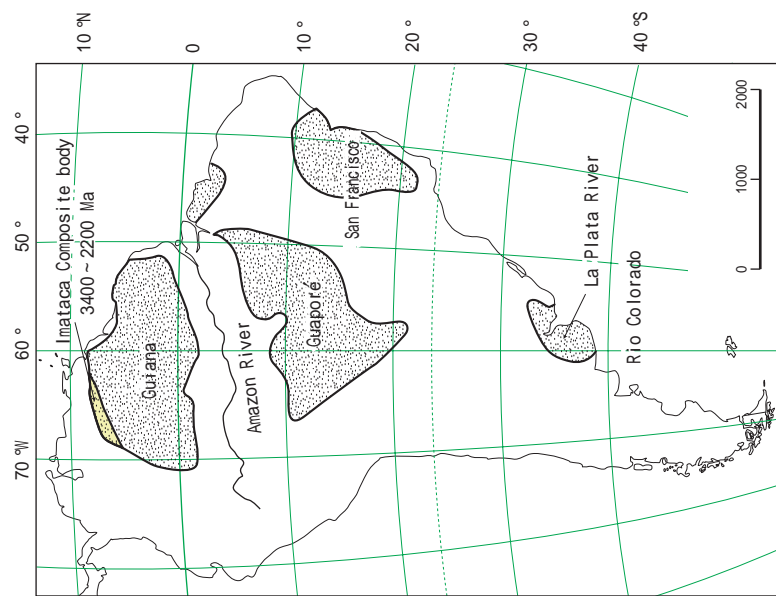
**Cronologia dos principais eventos tectônicos e magmáticos**

Idade (Ma)	Unidades geocronológicas	Principais eventos			
		Extensional (anorogênico)	Compressional (orogênico)	Ciclos tectonogeológicos	
65	FANEROZÓICO	CENOZÓICO			
		MESOZÓICO	Sul-atlantiano		
		PALÉOZÓICO			
235					
460					
460		Pós-brasiliano			
570			Brasiliano 600 ± 100Ma	Ciclo Brasiliano	
1.000	PROTEROZÓICO	NEO	Rondoniano ± 1.000Ma		
		MESO	Parguazense ± 1.500Ma	Uruaçuano/K'Mudku 1.200 ± 100Ma	Ciclo Uruaçuano
		PALÉO	Uatumã ± 1.800Ma	Transamazônico 1.900 ± 100Ma	Ciclo Transamazônico
1.800					
2.600	ARQUEANO		Jequié/Aroense 2.700 ± 100Ma		

*Obs.:* Os principais eventos geotectônicos pré-cambrianos do Brasil são aproximadamente sincrônicos através do País, mas nem sempre se correlacionam perfeitamente com os eventos pré-cambrianos em outras partes do mundo.  
As subdivisões do Proterozóico (Paleo, Meso e Neo), como aqui usadas, não correspondem necessariamente às subdivisões internacionais (propostas por Cowie et al., 1989).

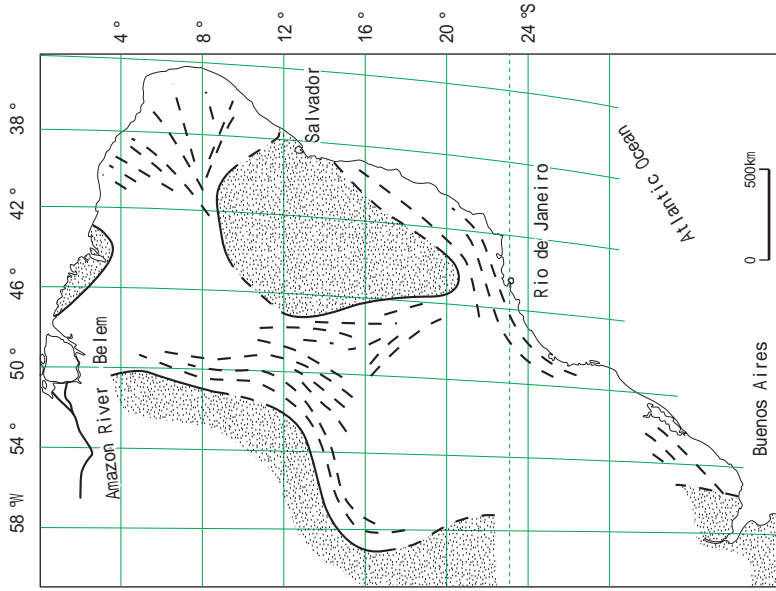
Fontes: US Geological Survey; CPRM, 1995.

**Fig. I-3-2-1** - Ages of major tectonic movements and igneous activities in Brazil



Distribution of Precambrian major stable craton in the South America. After Cordani et al.(1972), Hurley & Rand(1973)

**Fig.I-3-2-2 Distribution of Precambrian major stable craton in the South America**



Direction of folding or metamorphic belts (broken line) at east of South America. Dotted area shows old stable massif. After Cordani et al. (1972).

**Fig.I-3-2-3 Direction of folding belt at Brazilian orogenic cycle**

subsequent major orogenic movements. The first of such movements which is known as Transamazonian orogenic cycle took place before 2000 ~ 1800 Ma.

Most of the South America platforms currently exist to the east of Andes Mountains were caked at the end of Transamazonian orogenic cycle. It is presumed that the continental crust of South America had an area of at least 10 million km<sup>2</sup> at that time.

The values of subsequent radiation age measurements were focused on 1400 ~ 900 Ma (Uruacuan orogenic cycle). Another major orogenic movement may have occurred in Minas Gerais and Goias Province in Brazil and the mountainous district of Sierra Nevada de Santa Marta in Colombia.

Subsequently, a further larger Precambrian orogenic movement occurred before 750 ~ 450 Ma. This movement is called Brazilian orogenic cycle. The curly metamorphic/igneous rock zones were developed in the manner as to cut up and wrap the platforms under the impact of Transamazonian orogenic cycle (Fig. I-3-2-3). It is considered in general that the orogenic cycle continued during the late Precambrian age. However, the cycle extended to Ordovician.

We consider that it was in the age of Brazilian orogenic cycle that the core of Precambrian platform was cut to pieces and largely extended.

As stated above, the development of the South American Platform of Precambrian Age ended with Brazilian orogenic cycle. The ages of many plutonic rocks of synkinematic granite were around 650 Ma. Afterwards, the final/latter changes continued till 650 ~ 500 Ma, and an especially large-scaled change occurred 540 Ma. Because of this change, the sedimentary rocks in/among the margins of the platform were intensely folded, cut at faults and influenced by advanced metamorphism and intrusion of many neutral/acidic plutonic rocks depending on places.

Fig. I-3-2-4 shows the major divisions of Brazilian geological structure in Precambrian by DNPM (1995a), while Fig. I-3-2-5 shows distribution of sedimentary basins of Phanerozoic eon.

## (2) Palaeozoic

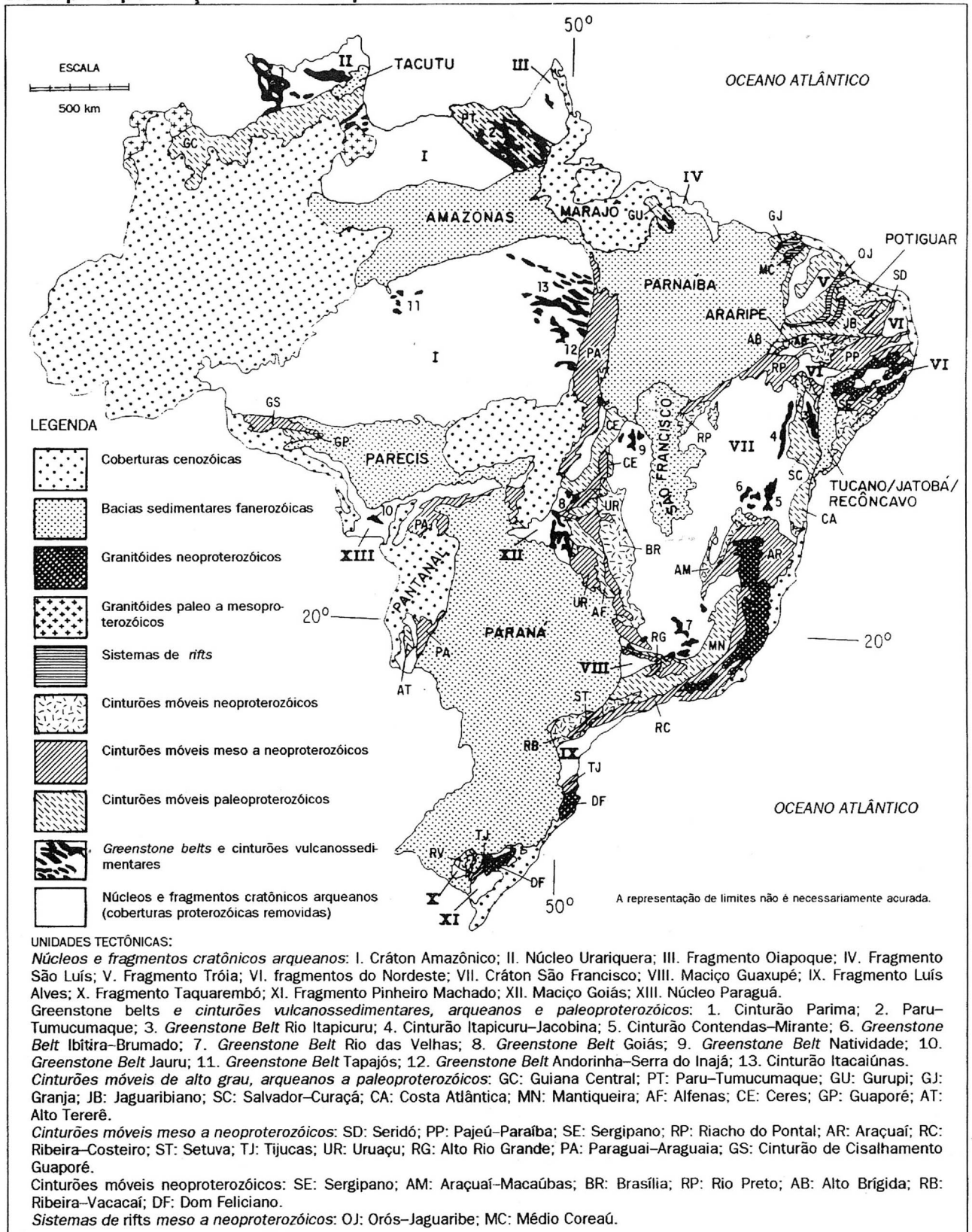
In South America, three major sedimentary basins among platforms, ie. Amazon, Parnaiba and Paraná basins arose in Palaeozoic. These sedimentary activities were activated in early Palaeozoic. Sediments and volcanic rocks were continuously provided up to Mesozoic age.

### a) Amazon Basin

It is not yet known well about the basement of lower Palaeozoic sedimentary rocks. The first layer containing fossils in Amazon basin is of Silurian system.

Mapa 4.1

**Brasil: principais feições tectônicas pré-cambrianas**

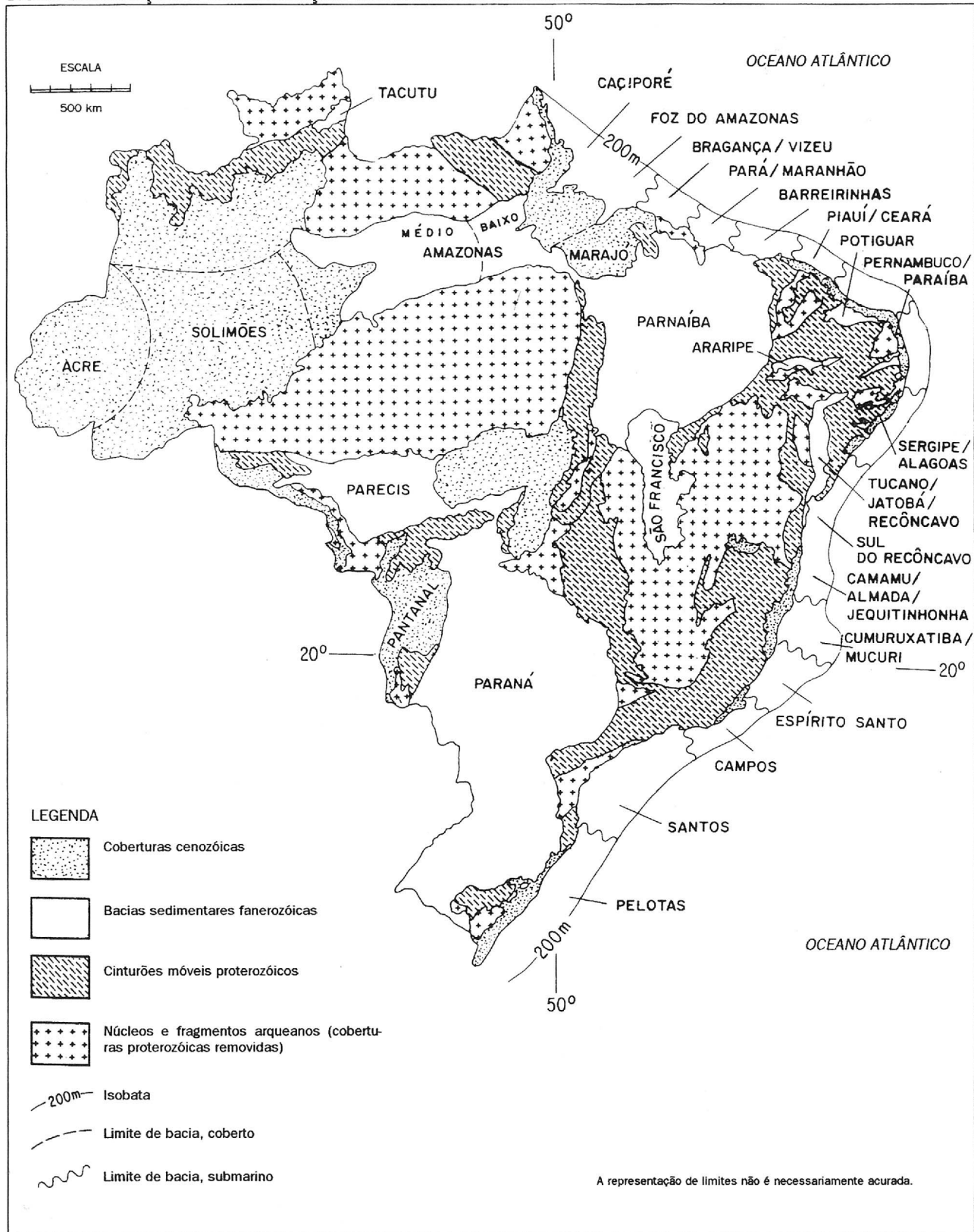


Fontes: USBM e DNPM, 1995.

**Fig. I-3-2-4 Major geological structure sections in Precambrian age in Brazil**

Mapa 4.2

**Brasil: distribuição e denominação das bacias sedimentares fanerozóicas**



Fontes: USBM e DNPM, 1995.

**Fig. I-3-2-5 3-2-5 Distribution of sedimentary basins in the Phanerozoic eons in Brazil**



A part of thick Devonian system developed in Amazon basin is abyssal facies containing abundant fossils in part. Maeuru formation unconformably covers Silurian system in outcrop area. However, it is known as a result of drilling conducted in the central part of the basin that marine sedimentary activities were continuously made from Silurian to Devonian. In the eastern part of the basin, subsidence was larger and sediments were thick as it went toward the supply source. In the southern and northern ends, on the other hand, the sediment thinned out accompanying local unconformity in the southern and northern edges of the basin.

In late Carboniferous, relatively thin and wide distribution of sandstone layer (Monte Alegro formation) was observed after the periods of erosion and no sediment. Most of Nova Olinda formations of the final Carboniferous were distributed only in the central part of Amazon basin. In the eastern part of Manaus, a thick stratum of evaporite consisting of halite and anhydrite exists under the land surface, and its maximum thickness is reported as approximately 500 m (Bigarella, 1973). Also in the eastern part of Manaus, sandstone exists under the land surface which may have evaporates of Permian system on its upper layer and its maximum thickness reached 645 m (Bigarella, 1973). The total thickness of the above-mentioned layers of Palaeozoic is estimated as 7000 m and 3000 m in the central part and western part of Amazon basin respectively. No proof of glacier activity of late Carboniferous has been discovered.

#### **b) Parnaíba Basin**

Parnaíba Basin was developed between Guaporé and San Francisco platforms and having Palaeozoic geo-history similar to that of Amazon basin. Unlike long-extending Amazon basin, Parnaíba basin was almost in a circular shape, and the utmost subsidence and sediment were made in its center.

Here, marine deposits of Silurian and Ordovician systems cover Precambrian basement rock with clear unconformity. These strata are further conformably covered by the sandstone containing abundant fossils of Devonian system, siltstone and shale.

Small-scaled unconformity exists on the upper layer of lower Carboniferous system where upper Carboniferous and Permian systems are accumulated with its thickness having reached 700 m at maximum in the center of sedimentary basin.

#### **c) Paraná Basin**

Although Paraná basin was only an extremely shallow depression during Palaeozoic, it was developed to become a large structural basin in Mesozoic. The basin covers wide areas of the central/southern parts of Brazil, the eastern part of Paraguay and the northeastern part of Argentina.

On the basin edge in the eastern part of Paraguay, the marine sandstone, which may be of

Ordovician system, is distributed covering Precambrian metamorphic rocks, and the marine sandstone is slowly inclined westward to the side of Paraná basin.

The oldest Palaeozoic in Uruguay is the marine sediment of lower Devonian system, but it lacks Devonian system in Paraguay.

In the margin of Paraná basin, the continental sediment strata of upper Carboniferous system are observed in many places unconformably covering the above-referred lower Palaeozoic stratum. Palaeozoic sedimentary activities in Paraná basin ends with sedimentation of continental clastics of lower Permian system.

### (3) Mesozoic - Dismantling of Gondwana Continent -

Till the end of Palaeozoic, South American platform was unified as the main part of huge Gondwana continent. In this way, dismantling of Gondwana continent started in an essentially stable condition. South America and Africa constituted a continental mass before dismantling of Gondwana continent through opening of a graben and a large-scaled plate motion that took place in Mesozoic.

On the eastern side of Andes Mountains, no sedimentary rocks of early/middle Triassic is observed even in the three large Palaeozoic sedimentary basins (Amazon, Parnaiba and Paraná basins). In the late Triassic, however, Paraná Basin became one of the largest old deserts in the world, and animal fossils of the reptiles and amphibia similar to those produced in South America are saved at the bottom of the lake or riverbed sediments under large-scaled sandstone layer.

In latter Triassic period, large-scaled igneous activities began on the eastern side of Andes Mountains (see Fig.I-3-2-6). Dolerite dikes of the late Triassic period are widely distributed in Guiana shield with strikes of NNE-NE on the western side and NNW on the eastern side and K-Ar age of approximately 220 Ma. There are mafic intrusive rocks of the similar age also in Amazon Basin. The average age of the oldest Mesozoic mafic rocks existing in the basin is 181 Ma.

In latter Jurassic period, a large-scaled basaltic lava eruption began to occur on the South American platform. These lava flows known as Paraná basalt (or Serra Geral basalt) flow reached its largest scale in the early Cretaceous period (about 130~120 Ma). This age also conforms to the time when sea-floor spreading started in the South Atlantic Ocean.

At present these lava flows are exposed mainly in Paraná Basin that extends over the southern part of Brazil, Paraguay and the northern part of Argentine. Same kinds of lava flows are also discovered under young sediments in Chaco basin extending over the northern part of Argentine and the western part of Paraguay. Basalt of the same age is observed also in Mato

# SOUTH AMERICA

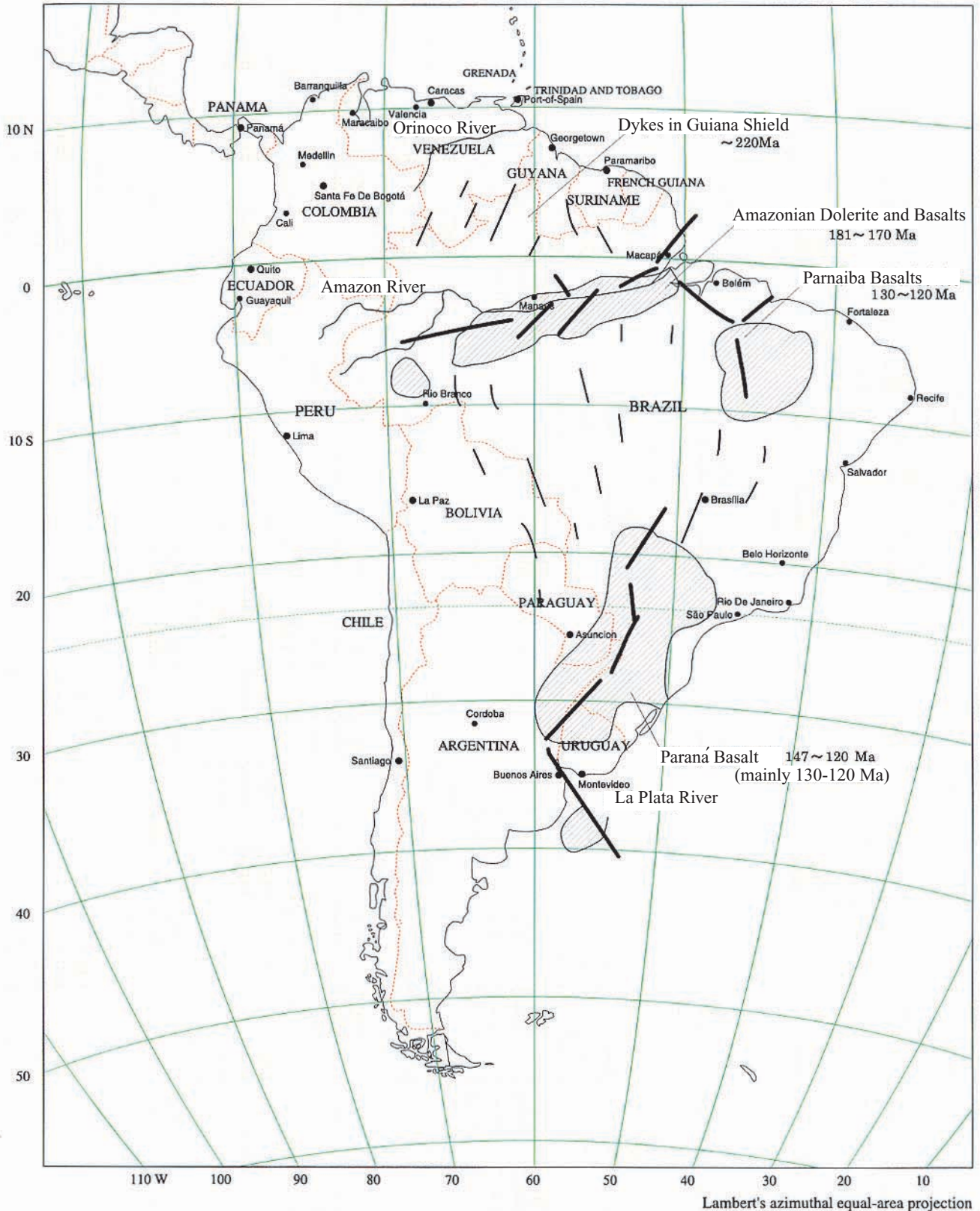
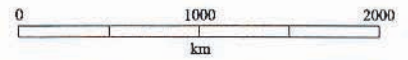


**Fig.I-3-2-6 Mesozoic mafic igneous activity at the east South America**  
 (Compiled from Rezende, 1972; Bigarella, 1973; McConnell, 1975; Zamborano & Urien, 1974 and Cordani et al., 1967)

Grosso State in the southwestern part of Brazil. Further, it is known that there exist lava flows almost comparative to those of Paraná basalt, ranging from the mouth of La Prata River to the offshore.

Most of these lava flows consist of tholeiitic basalts, obviously derived from upper mantle that is scarcely mixed with earth crust. A number of diabase (meaning the same as dolerite) sills and dikes are developed in the distribution area and margin of lava flows, and their age is the same as that of basaltic rocks.

Such large-scaled effusion of mafic rocks is an important evidence of Gondwana continent division. A lot of deep cracks may have been developed not only beneath and around Paraná Basin but also toward Guiana shield to the north.

Dolerite sills and dikes are widely developed in Amazon basin. These sills reached to the depth of 600 m under the ground in the center of the basin. Their youngest age as measured is 170 Ma (early Jurassic period), and this age is older than most of the basalts in Paraná Basin. The sills and dikes in Paraná Basin were measured by Cordani as 127 Ma. The basalt lava of almost the same age occupies an area of 100,000 km<sup>2</sup> in the center of Paraná Basin.

Judging from the patterns of the faults and cracks in the South American Continent and its eastern edge, the continent was destroyed into mosaic-like shield blocks one after another. One of the cracks was made in the southern part from which a lot of tholeiitic basalt of Paraná basin effused. Dolerite and basalt intrusion and effusion occurred in the cracks in the northern and northeastern parts of Amazon/Parnaiba basins and platforms in their periphery.

Throughout the early Cretaceous, intensive trench forming took place in the northeastern parts of Brazil as well as on the eastern coast. In some of submerged zones, non-marine clastic sandstone and shale of late Jurassic were observed. These strata are covered with continental sediments of lower Cretaceous system. However, these sediments are distributed only in graben with its local thickness of 5 km.

The first abrasion, which took place in, Aptian period flooded from a narrow and extended bay to Brazilian coasts. At first, blocked by its convex structure, it was possible for this primitive bay to be enlarged and connected only in the southern part. Therefore, dry climate continued in the inland and thick strata of evaporate was sediment (Ponte et al., 1977). Afterwards, a stratum of carbonate rocks was piled from Albian stage, and then it was inclined to the seaside and thick sediment was accumulated on the continental edge.

### 3-2-2 Outline of Ore Deposits

The location of ore deposits in Brazil is described on the 1:2,500,000 scale “Mapa Geologico do Brasil” (DNPM, 1995b). In addition to this map, the location and outline of major ore deposits are summarized on the 1:7,000,000 scale attached to the CPRM (1995).

#### (1) Ore deposits of Archean Era

Gold, copper, manganese, and iron ore deposits that accompany Greenstone belt volcano-sediments, and nickel, copper, chromium and asbestos deposits that accompany basic to ultra-basic composite rocks are known as ore deposits of this era.

The primary gold ore deposits related to the Greenstone belt include the Morro Velho ore deposit in Minas Province, the Mara Rosa, Crixas, Pilar de Goias ore deposits in Goias, and others. Some of them have copper mineralization.

Tapajos, Madeira, and the southeastern part of Pará Province are typical placer gold ore deposit distribution areas in Amazonia. It has been known that the provenance of the gold is the auriferous quartz vein in metabasites and amphibolites in Complexo Xingu. Today, some of these basic rocks are considered to belong to the Greenstone belt.

These belts are distributed as volcano-sediments in the Salobo area and as Jacareaçanga metamorphic rocks in the Tapajos area. Grupo Vila Nova and others are distributed as an ore deposit host rock from Amapá Province to the northeastern part of Pará Province.

Auriferous quartz veins generated by the remigration of gold and gold deposits generated by the intrusion of granites of the Proterozoic often occur in the crush zone in the NW-SE and NE-SW directions.

#### (2) Ore deposits in the lower Proterozoic

In addition to the primary gold ore deposits that are occurred in the Greenstone belt, conglomerate-type gold ore deposits, sedimentary gold, copper, and manganese ore deposits, iron ore deposits, deposits that accompany basic to ultra-basic rocks, and volcanic polymetallic ore deposits are known as ore deposits of this era shifting from the Archean to the Proterozoic.

There are auriferous and uranium ore deposits, which is held in a conglomerate layer, called the Witwatersrand type and the Blind River type as a conglomerate-type ore deposit. Mineralization in the metaconglomerate layer of Grupo Jacobina in Bahia Province, Supergrupo Minas in Minas Province, and Cidade de Goias in Goias Province are good examples of the auriferous and uranium ore deposits.

The Serra Pelada gold ore deposit in the transgressive sedimentary facies of a Rio Fresco

layer type distributed near the Serra dos Carajás (the Carajás mountain range), the Bahia copper ore deposit, and the Azul manganese ore deposit are sedimentary-type ore deposits.

An iron ore deposit is classified as Algoma-type and Superior-type BIF (Banded Iron Formation). The deposits in Supergrupo Minas at the iron square zone in Minas state, and an iron ore deposit that are located in Grupo Grao Para in the Carajás area, Pará are good examples.

The Americano do Brasil in Goiás Province, the Mangabal ore deposit, and the Ti-Fe-V ore deposit in the Campo Alegre de Lurdes gabbro – anorthite composite mass in Bahia Province are Ni-Cu-Co ore deposits that accompany basic to ultra-basic intrusive rocks.

Boquira Pb (-Zn-Ag) ore deposit in Bahia Province, Barra do Perau Pb (-Ag-Zn) ore deposit in Paraná Province, and Palmeiropolis Zn (-Pb-Cu) ore deposit in Tocantins Province are typical volcanic polymetallic deposits.

### (3) Ore deposits in the middle Proterozoic

A tin ore deposit is a major ore deposit of this era. In addition, nickel, chromium, and asbestos ore deposits have been known. Some diamond ore deposits have also been found.

With the development of the platform-type sedimentary basin, the tectogenesis occurred in this era. A thick layer of sediment that accompanies acid - neutral volcanic rocks and pyroclastic rocks is widely distributed. Granites that penetrate through this layer develop and a tin deposit is formed. Almost all the tin mineralization in Brazil belongs to this era; in particular, it is distributed much from Amazonia to the Goiás area.

Alpine type ultra-basic rocks intrude near a fold belt, and have mineralization of nickel, chromium, asbestos (the Morro Feio, Dois Irmao, Quatipuru deposits, and others).

The kimberlite intrusion accompanied by the first diamond mineralization in Brazil, which is the source of the palaeo-placer deposits of each subsequent period, belongs to this.

### (4) Ore deposits in the upper Proterozoic

Pegmatite ore deposits that accompany granite intruding the tectonic zone of the Brasiliano orogenic movement and pegmatite, non-ferrous metal ore deposits that occur in sedimentary rocks of the fold belt, copper deposits that are mineralized in volcanic and sedimentary rocks, iron – manganese ore deposits near the Amazon craton, etc. are ore deposits of this era.

The pegmatite ore deposits are distributed in Minas Province, Bahia Province, the northeastern part of Brazil, and other areas and contain beryllium, tin, niobium, tantalum,

lithium, etc.

The non-ferrous deposits in sedimentary rocks include the Panelas Pb (Au and Ag) deposit, the Sete Barra fluorite deposit, and Perau Pb-Zn deposit in Paraná Province, the Itapeva Cu deposit in São Paulo, etc. In addition, the Vazante Zn deposit and Morro Agudo Pb-Zn deposit in Minas Province are good examples of the Mississippi Valley type deposit.

Also, the copper ore deposits that in volcanic and sedimentary rocks include the Pedra Verde ore deposit in Seara Province and the Canidade de São Francisco ore deposit in Sergipe.

A deposit in the Corumba area in Mato Grosso do Sul is a typical iron – manganese sedimentary ore deposit.

#### (5) Ore deposits in the Phanerozoic eons

A molasse-type sediment develops in the rift zone of the southern part of Brazil from the late Proterozoic Era to the early Palaeozoic, and the Camaqua copper mine and the Caninde de São Francisco Pb-Zn ore deposit in Rio Grande do Sul occur as a disseminated or vein-like ore deposit.

Various types of sedimentary deposit occur in the sedimentary basin generated with the blocking of craton. In the Paraná basin, uranium mineralization is found in the Devonian stratum in Goiás Province, and coal seam and peat beds are found in the sedimentary stratum of the Carboniferous in Rio Grande do Sul Province. In the Amazon basin, halite and potassium - gibbsite ore deposits are known in the Carboniferous - Permian strata, and a gas field is discovered in the sandstone bed of the Carboniferous.

Halite, potassium, sulfur, petroleum, and gas deposits occur near the Parnaíba basin from Sergipe to Goiás Province.

Various kinds of mineral such as phosphor, niobium, titanium, nickel, uranium, zirconium, and diamond are generated as mineralization that is accompanied in alkaline rock, carbonatite, and kimberlite rock masses, which are considered to have resulted from igneous activities concurrent with the period of the division of the Gondwana land.

On the other hand, some of the residual and alluvial deposits occurred from the Cenozoic to the Recent, are of much commercial value. The bauxite, kaolin, placer gold, and placer tin deposits in the Amazon are representative examples. In the Amazonia province where these types of deposit are found, a primary ore-bearing, which supplies the minerals above as an ore source, is very likely to exist. The Brazilian government is putting a great deal of effort into the exploration and development of this area.

### 3-2-3 Mines, Ore Deposits, and Ore Showings

The location of major mines and ore deposits in Brazil is summarized by ore type in the DNPM (1995) and the outline is set out in the table. The maps by ore type are shown in the present report (Figs. I-3-2-7, I-3-2-8, I-3-2-9, and I-3-2-10).

Major ore deposits are described in the DNPM and CVRD (1986, 1988, and 1991). For reference purposes, the summary of these ore deposits included in the fiscal 1992 Report of project finding survey (MMAJ, 1993) is available in Japanese.

### 3-2-4 Principal mineral provinces

The Principal mineral provinces (Fig. I-3-2-11) of Brazil are as follows.

- (1) Quadrilátero Ferrífero (Iron Quadrangle)-southern Espinhaço
- (2) Serrinha
- (3) Crixás
- (4) Rio Maria
- (5) Carajás
- (6) Jacobina
- (7) Serra do Navio
- (8) Tapajós-Rondônia
- (9) Pitinga
- (10) Roraima
- (11) rombeteas-Jari
- (12) Paragominas
- (13) the southern alkaline belt

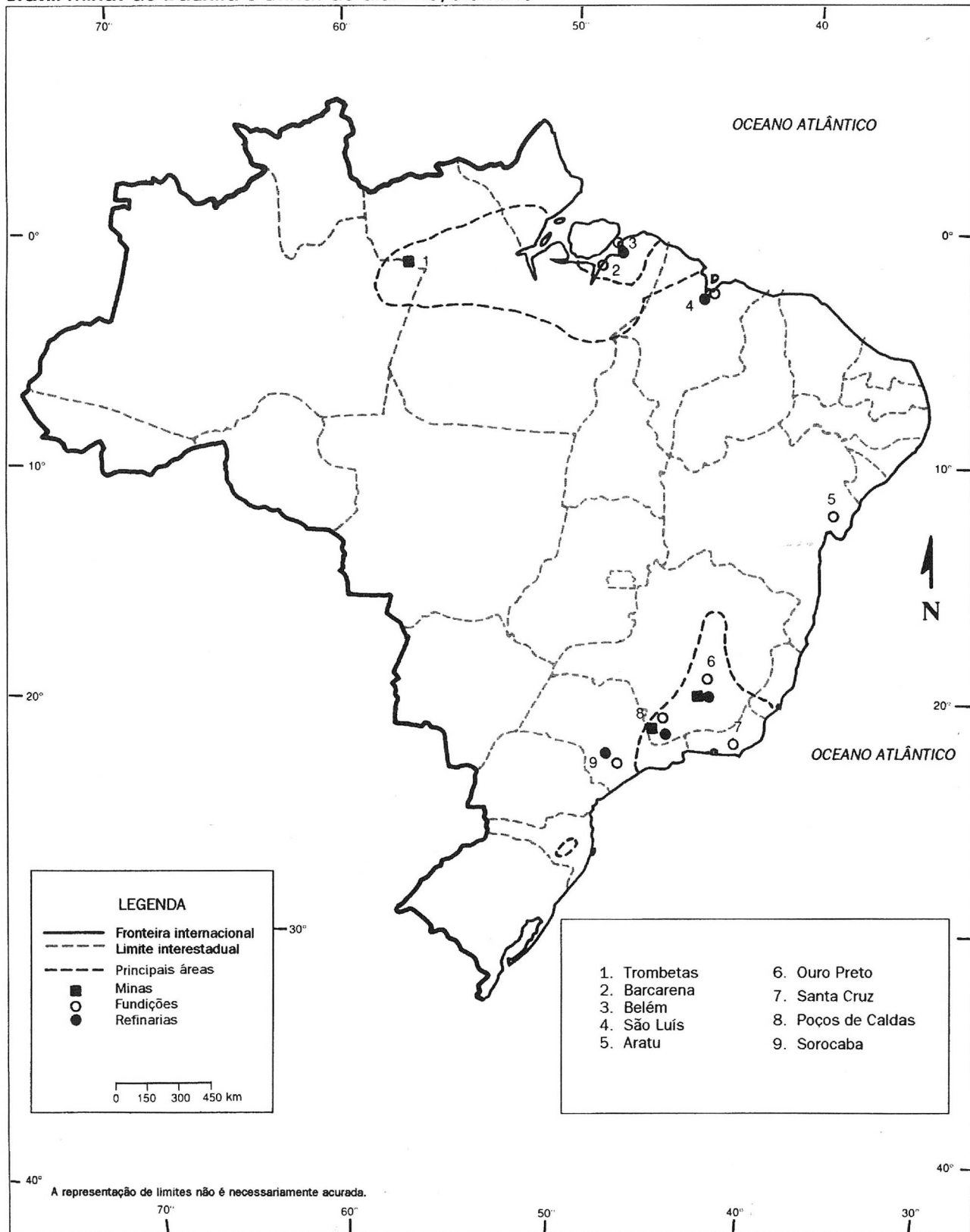
The Quadrilátero Ferrífero-southern Espinhaço mineral province comprises high-grade basement and supracrustal rocks of Archean, lower Proterozoic, and middle Proterozoic ages. The Archean supracrustal rocks are volcanic-sedimentary sequences of the greenstone belt type and host gold deposits. Gold is either associated with conglomerates, genetically similar to those of Witwatersrand. Lower Proterozoic sedimentary sequences in the Quadrilátero Ferrífero host huge high-grade iron deposits of the Superior type.

The Archean granite-greenstone belt terrane dominates the mineral provinces of Serrinha, Crixás and Rio Maria. They host gold deposits. And chromite is also produced in the Serrinha province.



Mapa 6.1

**Brasil: minas de bauxita e usinas de alumina/alumínio**

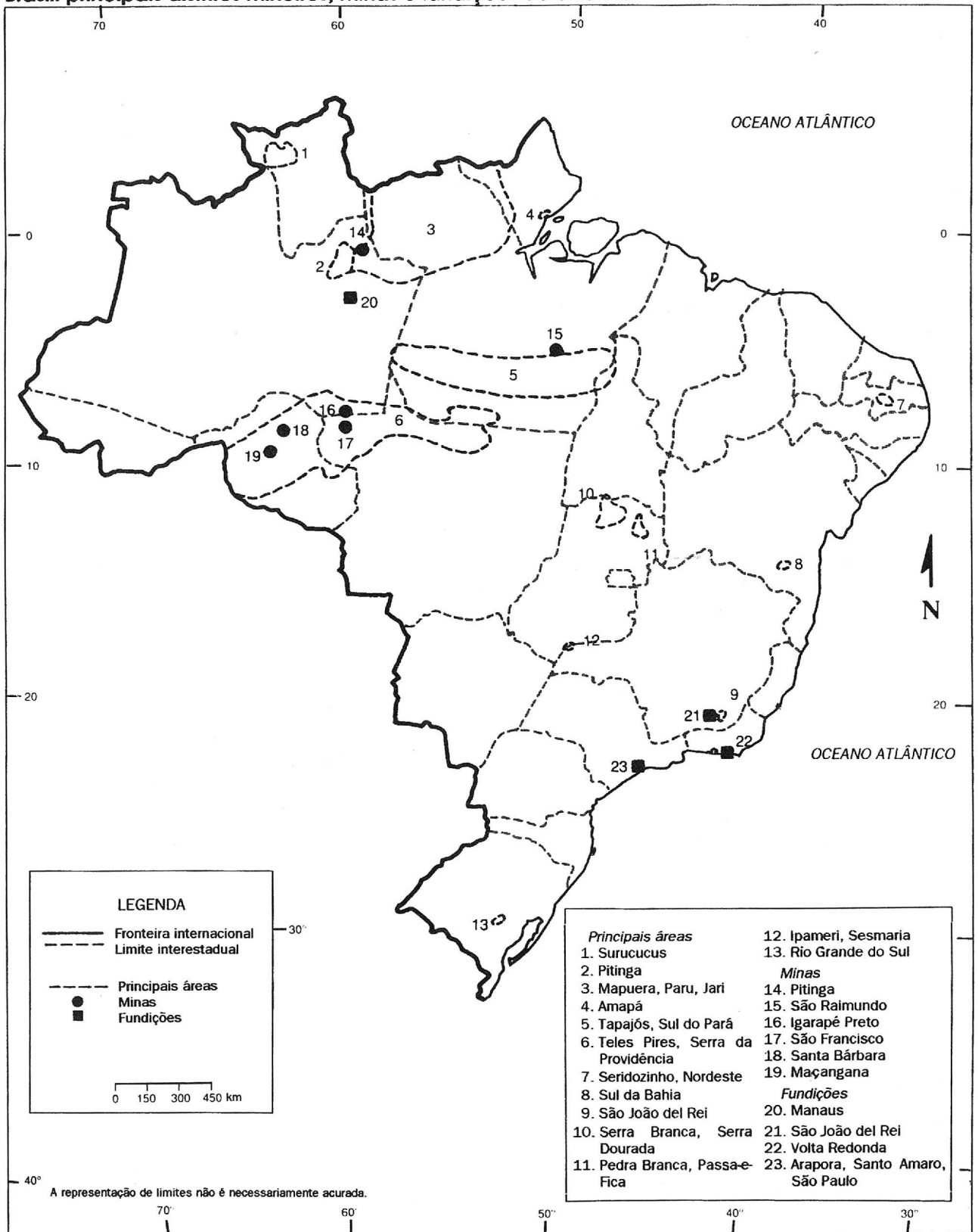


Fontes: USBM e DNPM, 1995.

**Fig. I-3-2-7** Distribution of aluminum ore deposits and smelting factories

Mapa 6.2

**Brasil: principais distritos mineiros, minas e fundições de estanho**

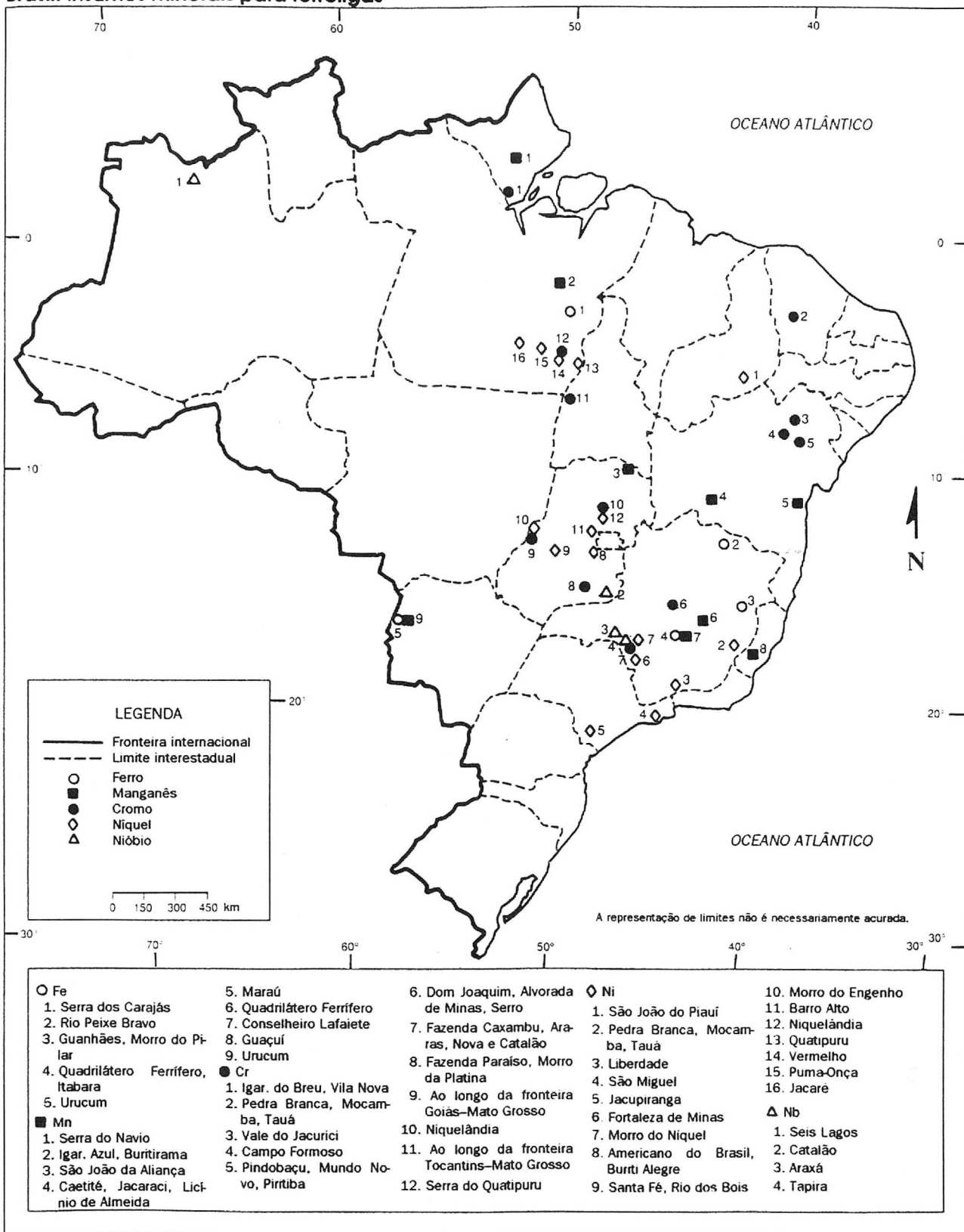


Fontes: USBM e DNPM, 1995.

**Fig. I-3-2-8** Distribution of tin ore deposits

Mapa 6.3

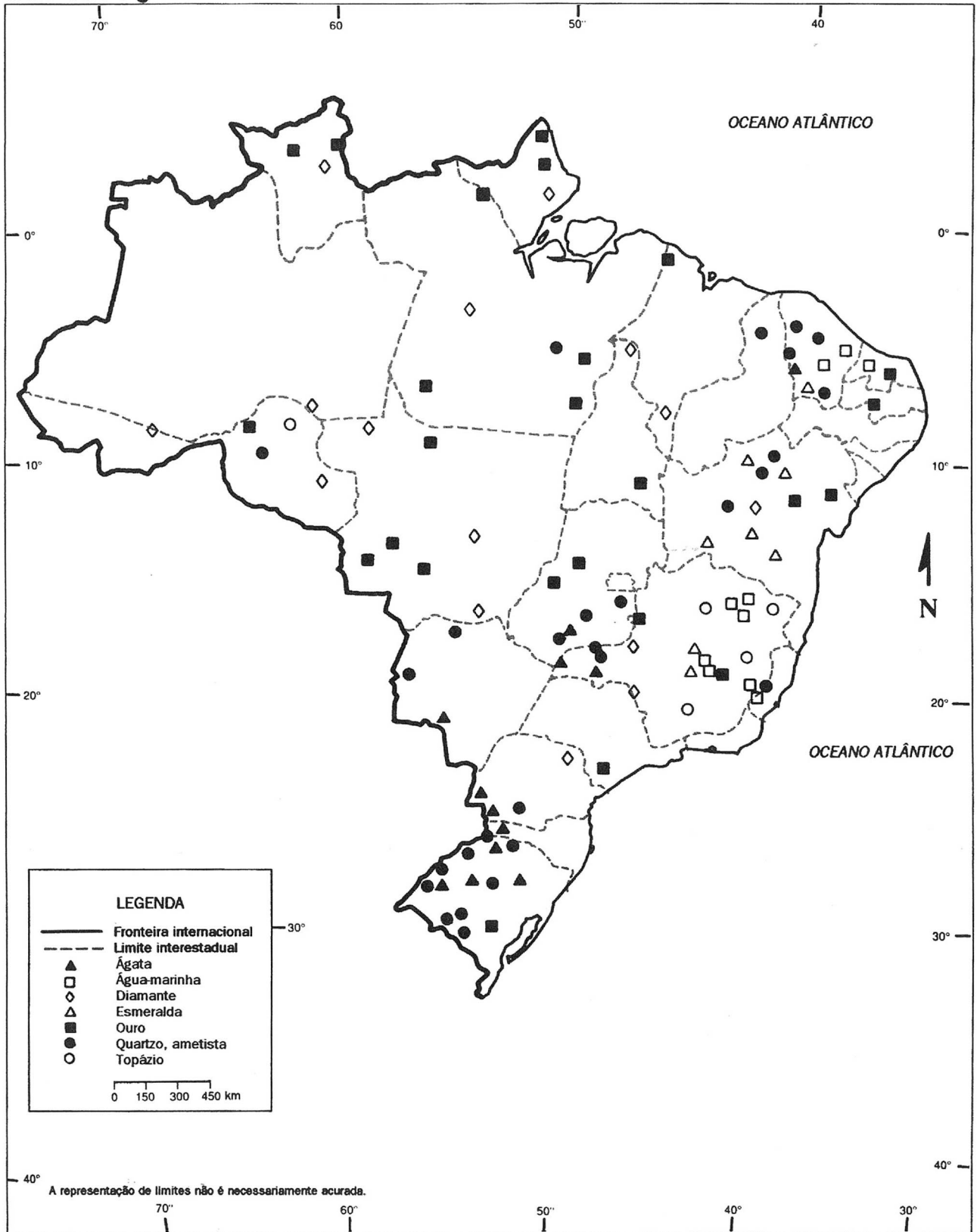
**Brasil: insumos minerais para ferroligas**



Fontes: USBM e DNPM, 1995.

**Fig. I-3-2-9** **D** Distribution of Fe/Mn/Cr/Ni/Nb ore deposits

Mapa 6.4  
**Brasil: ouro e gemas**



Fontes: USBM e DNPM, 1995.

Fig. I-3-2-100 Distribution of gold and gem stone deposits

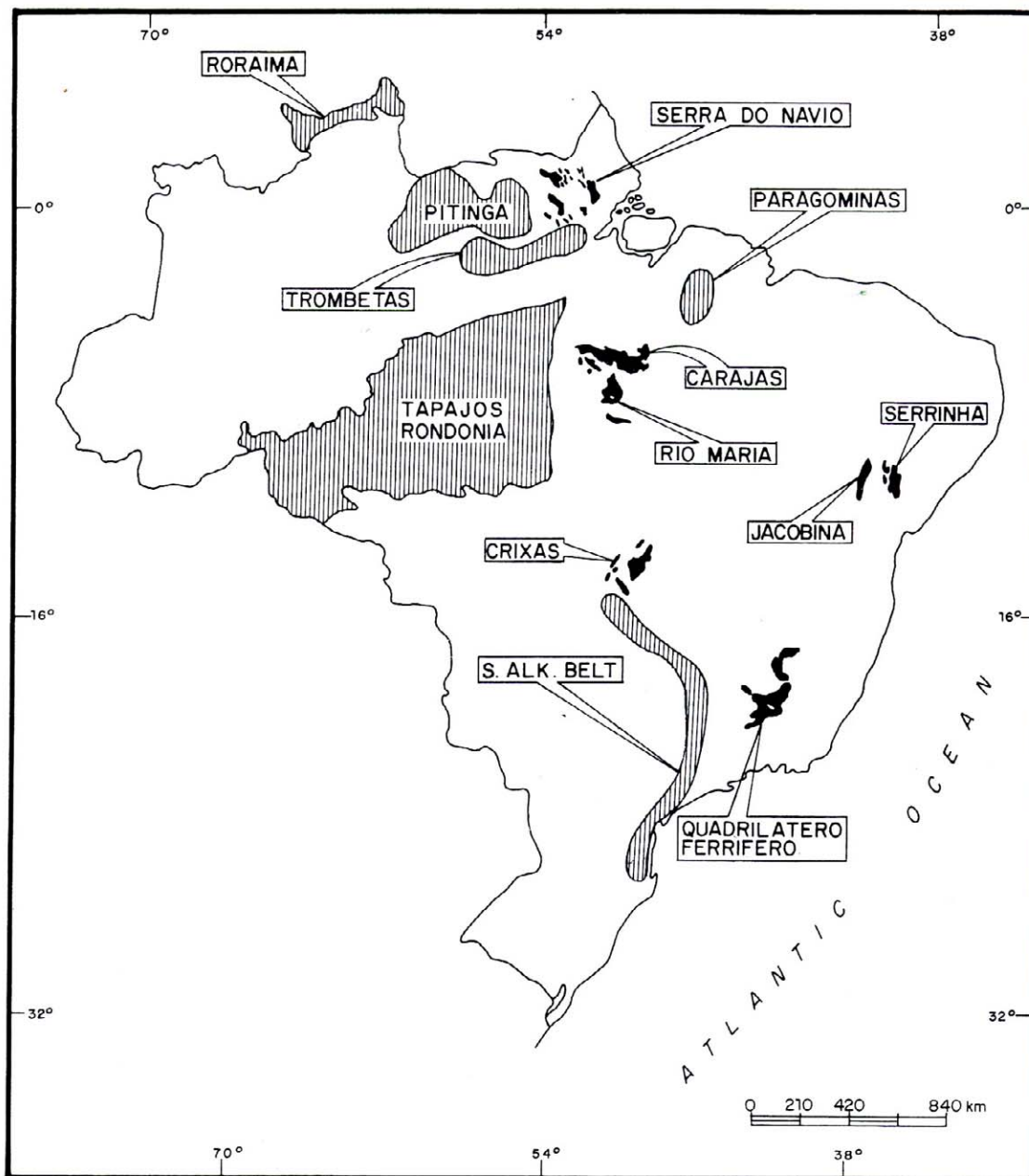


Fig.I-3-2-11 Principal mineral provinces of Brazil

The Carajás mineral province is an Archean rift basin with bimodal volcanic rocks associated with iron-formation and clastic sedimentary rocks. It includes iron, manganese, gold, copper, bauxite, tin, and nickel. Iron deposit is classified Algoma type and gold deposits are formed of placer deposit and lateritic deposit. Beside, copper deposit is Cu-Zn-Pb volcano—sedimentary deposit, and nickel deposit is laterite type.

The Jacobina mineral province is dominated by a lower Proterozoic sedimentary sequence. Gold deposit is associated with conglomerates. Chromite is also produced in layered ultramafic intrusions in the basement. Granitic intrusions in ultramafic rocks generated emerald deposit.

The Serra do Navio mineral province is underlain by basement rocks and lower Proterozoic metasedimentary rocks. Manganese deposit hosts these metasedimentary rocks. Gold and chromite are also produced.

The Tapajós-Rondônia, Pitinga and Roraima mineral provinces, located in the Amazon region, are geologically almost unknown. They produce the largest amount of tin, gold. These provinces are characterized by an extensive continental felsic volcanic sequence and associated anorogenic granites. Besides cassiterite and gold there are many deposits of colombite, wolframite, rare earth element, and fluorite.

The Trombetas-Jari and Paragominas mineral provinces comprise Tertiary lateritic terrane of shales of Cretaceous age. They host huge deposits of bauxite and kaolin.

In the so-called southern alkaline belt, several carbonatite intrusions occur. They host the largest niobium deposit in lateritic caps of the carbonatite. Carbonatite-laterite-related deposits also include titanium, apatite rich in rare earth elements, and vermiculite.

### 3-3 PGE National Program of the CPRM

#### 3-3-1 Histories

The platinum group metal (PGM) or the platinum group element (PGE) consists of six elements: platinum (Pt), palladium (Pd), rhodium (Rh), ruthenium (Ru), osmium (Os), and iridium (Ir). These elements are similar in physical and chemical properties and are produced naturally in combination. They are known as precious metals like silver. They are difficult to melt in high temperatures, chemically inactive to many elements, and excellent in catalytic capability. The elements are extremely high in specific gravity; iridium has a specific gravity of 22.65, the highest in nature. Also, the melting point of osmium is as high as 3,045 °C and that of platinum is as high as 1,769 °C. These platinum group elements are always contained in basic to ultra-basic rock as a compound or a natural alloy.

The PGM combines with anions such as oxygen, sulfur, arsenic, antimony, bismuth, tellurium, tin, and lead to serve as cations. Also, the PGM is mixed with titanium, iron, gold, and mercury into a natural alloy. Some of the popular minerals are sperrylite (PtAs<sub>2</sub>), braggite ((Pt, Ni)S), cooperite (Pt, Pd)S, natural platinum, natural palladium, and natural osmium.

The importance of the PGM lies in its physical and chemical properties (The application of the PGM depends on its physical and chemical properties). The PGM is important not only as jewelry and investment property but also to electronic components and pollution-control substances (e.g. automobile catalyst) in various industrial fields. Also, it is used for the fuel cell as a new technology and applied to a new electronic industry and medical treatment.

The PGM reserves in the world concentrate in South Africa. Russia is the second place in the PGM reserves. These two countries account for 98.5% of the world's reserves. The same applies to the amount of production. Some people are anxious about the future, stable supply of the PGM because of this uneven distribution.

With this in view, the Brazilian government started to carry out a basic study about the potential of its country's PGM resources in 1990s. The government paid particular attention to the Mesozoic flood basalt that widely covers the southwestern part of Brazil (Geological Map of Paraná Basalt area in Fig. I-3-3-1).

Against this background, Paraná Mine Public Company (Mineropar) showed a positive attitude in liaison with the Brazilian government's effort and carried out a wide-range stream



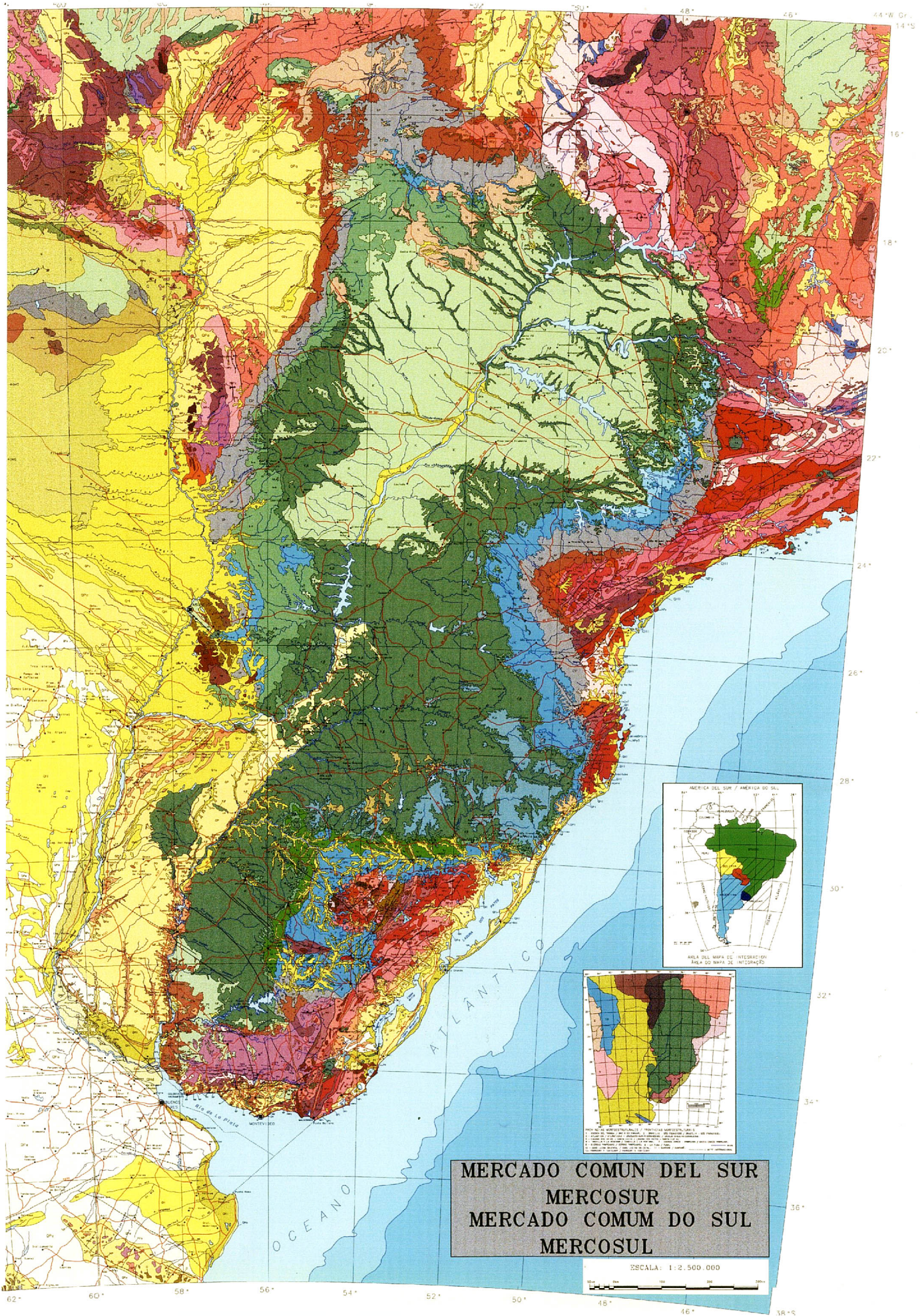


**Fig. I-3-3-1** Geological map of Paraná basalt region



sediment geochemical survey (area: approximately 160,000 km<sup>2</sup>, number of samples: approximately 700) in Paraná state cooperation with a governmental organization in 1994. Although the sampling density of this reconnaissance survey (one sample at approximately every 230 km<sup>2</sup>) was extremely low, this survey allowed Mineropar to determine the geochemical anomalies of nickel, chromium, and copper as well as platinum and palladium in the southwestern part. Subsequently, Mineropar conducted its own survey in the anomaly area, and analyzed sill-like doleritic rocks discovered at some points and obtained high geochemical anomalies of palladium from some of the doleritic rocks.

### 3-3-2 Overview of CPRM's Platinum Project

It seems that CPRM-led PGE (PGM) (PGE: Platinum group element; PGM: Platinum group mineral) project was promoted actively at the first phase until 1995. However, information on the following progress has been hardly available. Therefore, this section describes CRPM's operation during 1990 to 1995, based on the report by Farina (1996).

#### (1) Geological Conditions

PGM ore deposits can be formed under many geological environments. In reality, however, they are limited to basic to ultra-basic basement rock bodies. Farina (1988) classified such geological environments into 15 categories. According to Farina, the following three types of ore deposits account for 99% of the world's reserves and 98% of the production in the world.

##### a) Layered Intrusion (LI)

Layered intrusion is distributed in the plate and anorogenic belts, disregarding flood basalts and basic to ultra-basic intrusive rock bodies in continental environment.

##### b) Sill and other intrusive rock bodies (FB: Flood Basalt)

Layered intrusion (mainly sill), consisting of dolerite to gabbro composites. This was related to rifting and flood basalts in the continent. The rock body is found in the plate or in anorogenic belts.

##### c) Lava of Komatiite constituents and layered intrusive rock in Greenstone Belt (GB)

##### d) Anorogenic basic-ultra-basic intrusive rock bodies (AI)

Those classified into this type can be reclassified by later examination when they are considered as important.

##### e) Unclassified basic to ultra-basic intrusive rock body (MU: complex or Mafic and / or ultramafic unclassified bodies)

This covers those that the definition of an ore deposit type does not fit the objects.

Table II-3-3-1 lists PGM reserves in the world and PGM production volumes in the world.

(2) National program of platinum group deposit exploration

CPRM started this program under the following four conditions:

- Highly economical and political significances that platinum group has
- Brazilian land has high potential for geological development, especially the land is rich in basic to ultra-basic rock bodies.
- No exploration has been done.
- Brazil does not produce platinum group.

This program began in 1990, defining the scientific basis on the goals and the exploration method. This program is permanent, and set the first stage end to 1995.

**Table I-3-3-1 Type of PGE deposits in the world and their reserve and production**

Type	Examples	World Reserve Base(1988) %	World Production Base(1988) %
<b>LI</b>	<ul style="list-style-type: none"> <li>▪ Bushveld (South Africa)</li> <li>▪ Sudbury (Ontario, Canada)</li> <li>▪ Stilwater (Montana, USA)</li> <li>▪ Great Dike (Rodesia)</li> </ul>	90.2	50
<b>FB</b>	<ul style="list-style-type: none"> <li>▪ Noril'sk, Talnakh, Mairk e Taymir (Siberia, Russia)</li> </ul>	8	37
<b>GB</b>	<ul style="list-style-type: none"> <li>▪ Thompson, Manitoba (Canada)</li> <li>▪ Kambalda (West Australia)</li> <li>▪ Fortaleza de Minas (Minas Gerais, Brazil)</li> </ul>	1.2	11
<b>Others</b>		0.6	2
<b>Total</b>		100	100

LI: Layered Intrusion, FB: Flood Basalt, GB: Greenstone Belt

Eleven standing geological engineers and three non-standing geological engineers have dealt ten projects, with support from CPRM regional offices in Brazil.

This program is under the Government of Brazil and aims to support and subsidize mining companies in the private sector who engage in wide area exploration. However, the program does not include those are at the detail survey stage to explore an ore deposit and who engaging in economical evaluation.

This program is applicable to any person or company who engages in exploration in areas where the production of platinum is promising. In other words, this program neither defines any specific mining sites nor guarantees any ores under the name of CPRM.

### (3) Exploration Method

The exploration method almost controls the result of the program--whether succeeding the program or not depends on the exploration method. The following items were selected, for which a training program will be provided, at the time of starting this project.

#### Training:

A workshop will be held on the following items to train individual teams.

- Geology and petrology on basic and ultra-basic rocks
- Mineralogy on platinum ore deposits
- Ultra-basic rock in Greenstone Belt
- Overview of laterite and gossan
- Practical training of geochemical prospecting
- PGE ore deposits and how to explore

#### Selecting target points:

The target points were selected by examining the following factors:

- To extract basic to ultra-basic rock bodies, especially large rock bodies, by using existing geological maps.
- Data on airborne magnetic prospecting.
- Geochemical anomaly of Ni, Cu, Co (Cr)
- Ore deposits of Ni, Cu (Co) sulfides
- Definition of ore deposit types (LI: layered Intrusion; FB: Flood Basalt; GB: Greenstone Belt;

AI Anorogenic Intrusion; MU; unclassified intrusion)

#### Selective Geological Mapping:

Focuses on platinum exploration by reediting and revising existing geological maps to make or edit a selective geological map.

#### Mineralogical Pan-Concentrate Prospecting:

Exploration of heavy minerals separated from alluvial sediments by panning is important since the density of platinum group elements is extremely large. The prospecting method should be routinized; the quantity of a raw sample is supposed to have 15 to 20 liters. In a special case, the soil sample must also be included in the target of test.

#### Geochemical prospecting:

As a routine, two types of a sample should be gathered. One is a sample of heavy minerals and the other is a sample of stream sediments at the same site. Soil samples should be gathered when necessary.

#### Ground physical exploration:

Magnetic exploration and IP exploration should be conducted in a special case.

Exploration by drilling: Should be conducted when necessary.

#### Laboratory testing:

Laboratory testing includes the following types of routine work:

- Rock: Petrography.
- Rock accompanying sulfides: To describe rocks and copper minerals and others; to analyze rocks for Pt, Pd, Au, Cu, Co, Ni, and Mg.
- Gossan: To analyze for Cu, Co, Zn, and Ni; to conduct chemical analysis for Pt, Pd, and Au.
- Heavy minerals (panning concentrate): To identify minerals by stereoscope and electron microscope; to analyze minerals for Pt, Pd, Au, Cr, and sometimes for Ir.
- Fluvial sediment and soil: To analyze for Cu, Ni, Co, Zn, Au, and Cr; to analyze rocks for major 13 oxides, REE, S, Ba, Sr, Rb, H<sub>2</sub>O<sup>+</sup>, and H<sub>2</sub>O<sup>-</sup> when necessary.

#### Data Processing:

Each of the samples must have a data file where coordinates, geology, and other data are entered.

#### Map and Report making:

To examine and analyze data collected at field survey and laboratory. The result shall be made in the form of an annual report including maps.

#### (4) Work so far completed

Table II-3-3-2 lists prospection records for 1992 to June 1995. Fig. I-3-3-2 shows locations of rock bodies by types.

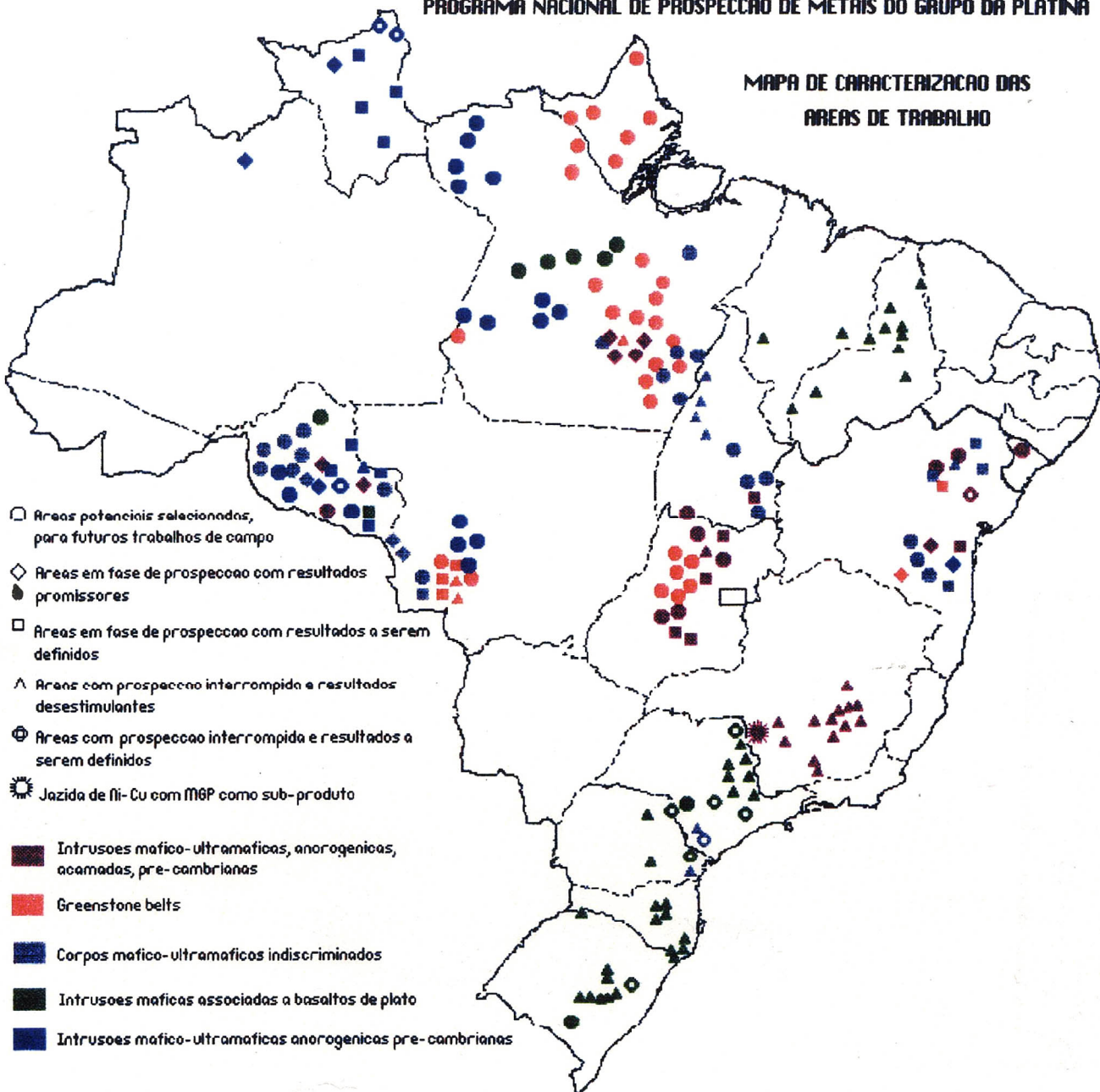
**Table I-3-3-2 Samples already collected and analysed by CPRM PGE project**

Project	Pan Concentrate		Stream Sediments		Soils		Rocks		Totals	
	Sampled	Analysed	Sampled	Analysed	Sampled	Analysed	Sampled	Analysed	Sampled	Analysed
Platina - RS/SC	41	41	0	0	0	0	359	162	400	203
Platina - SP/PR	419	210	440	440	48	48	278	207	1,185	905
Platina - MG	4,572	1,633	3,030	1,352	3,372	3,124	954	590	11,928	6,699
Platina - BA/SE	342	163	315	315	8	8	234	112	899	598
Platina - PA/AP	3,160	62	2,101	2,063	0	0	165	97	5,426	2,222
Platina - AM/RR	258	247	133	123	27	27	382	162	800	559
Platina - RO	895	167	621	454	433	375	599	497	2,548	1,493
Platina - GO/TO	1,469	1,029	408	388	1,128	826	710	710	3,715	2,953
Platina - MT	129	0	4	0	0	0	34	0	167	0
Platina - PI/MA	152	37	12	0	33	19	72	38	269	94
Total	11,437	3,589	7,064	5,135	5,049	4,427	3,787	2,575	27,337	15,726

Abbreviations of state names; AP: Amapa State, BA: Bahia State, GO: Goias State, MA: Maranhao State, MG: Minas Gerais State, MT: Mato Grosso State, PA: Para State, PI: Piau State, PR: Paraná State, RO: Rondonia State, RR: Roraima State, RS: Rio Grande do Sul State, SC: Santa Catarina State, SE: Sergipe State, SP: São Paulo State, TO: Tocantins State.

PROGRAMA NACIONAL DE PROSPECÇÃO DE METAIS DO GRUPO DA PLATINA

MAPA DE CARACTERIZAÇÃO DAS  
ÁREAS DE TRABALHO



■ PRECAMBRIAN LAYERED ANOROGENIC MAFIC-ULTRAMAFIC INTRUSIONS	□ - SELECTED POTENTIAL AREAS FOR FUTURE FIELD WORK
■ GREENSTONE BELT	◇ - AREAS WITH PROSPECTING WORK IN PROGRESS AND WITH GOOD RESULTS
■ UNCLASSIFIED MAFIC- ULTRAMAFIC BODIES	□ - AREAS WITH PROSPECTING WORKS IN PROGRESS AND RESULTS TO BE DEFINED
■ MAFIC INTRUSIONS ASSOCIATED WITH PLATEAU BASALTS	△ - AREAS WHERE PROSPECTING WORK HAS BEEN STOPPED DUE TO UNSTIMULATING RESULTS
■ PRECAMBRIAN ANOROGENIC MAFIC-ULTRAMAFIC INTRUSIONS	⊕ - AREAS WHERE PROSPECTING WORK HAS BEEN STOPPED BUT WITHOUT DEFINITIVE RESULTS
	☼ - NI-CU DEPOSITS WITH PGM AS BY-PRODUCT

Fig. I-3-3-2 Target areas and bodies for PGE Prospecting by CPRM

## (5) Results

### a) Layered Intrusion--LI type

- 1) Serra da Onca rock body (Para Province); 36 samples, Pt 04-800 ppb; 42 samples: Pd 10-400 ppb
- 2) Serra da Puma rock body and Igarape Carapana rock body (Para Province): similar to Serra da Onca rock body. However, no details were surveyed.
- 3) Cacoal rock body (Rondonia Province): Pt 10-20 ppb at pan sample; Pd 30 ppb, Au 10-1450 ppb; Cu 450-900 ppm at soil sample; Ni 1600-3000 ppm.
- 4) Serra do Colorado rock body (Rondonia Province): The rock is interesting but not surveyed.
- 5) Barro Alto rock body (Goiás Province): Pt 440 ppb. Almost no analysis.
- 6) Tapuruquara rock body (Amazon Province): Initial stage of survey.

### b) FB Type--Flood Basalt

The survey targeted sills and intrusive rock bodies in the dolerite of the Mesozoic era in the Paraná basin and Parnaíba basin. The sources of sulfur found include the Pedra do Fogo formation and Motuca formation in the Parnaíba basin, where a gypsum seam was observed; pyrites in the shale of the Devonian period; and coal seam in the Carboniferous. Meanwhile, a gypsum seam is extremely rare in the Paraná basin except the Irati formation. The Brazilian basins and the Russian basins including Noril'sk are similar in many points except the following:

- 1) Massive sulfide deposit and basic rock: Most of them are contaminated pyrite only; they hardly accompany chalcopyrite. There are few whose total S exceeds 1-2%.
- 2) Large-scale concentration of Nickel and copper: Chalcopyrite and malachite were observed in spots. Their quantity has no significance.
- 3) Magmatogenic layering
- 4) Existence of olivine and picrite rock:  
Olivine is missing in most of sills except rock bodies in Port Alegre Provincial capital and in José Fernandes of Paraná Province. This will be a target for future survey.
- 5) Assimilation of host rock and re-crystallization: identical-spot low-temperature(?) thermal metamorphism is known.
- 6) Existence of platinum minerals in Pan-concentration

Port Alegre Province capital----Picrite rock is located in a 6-km<sup>2</sup> rock body called "Lomba Grande."

The quantity of olivine accounts for 17-36% (maximum: 50%), which could be called

“dolerite/gabbro.” The quantity is interested from mineralogical viewpoint. However, porphyritic chalcopyrite, a small quantity of natural copper, and moshrite(?) (NiAs) were observed. No conditions of “a”, “b”, “c”, “e”, “f” are recognized.

Jose Fernandes gabbro rock body---Located in Adrianapolis Country of Paraná Province. It has an 5-km<sup>2</sup> area in irregular form. Olivine accounts for 15-20% of the rock body. The host is made of a variety of beds in the Precambrian age. Except for the Paraná basin, this rock body is the only dyke of the Mesozoic era.

A small quantity of pyrrhotite, chalcopyrite, pentlandite, cubanite, sphalerite, and mackinawite were observed in polished sections. Gold grains were observed in Pan-concentration. No conditions of “a”, “b”, “c”, “e”, and “f” were recognized.

#### c) GB type--Ultra-Basic Rock in Greenstone Belt

##### 1) Fortaleza de Minas (Minas Gerais Province)

This is a Ni/Cu ore deposit. According to a mine owner, the rock contains Ni=2.6%, Cu=0.4%, Co=0.06%, Pt=0.32 ppm, Pd=0.47 ppm, Rh=0.06 ppm, Ir=0.1 ppm, Os=0.09 ppm, Ru=0.2 ppm, Au=0.09 ppm, PGE + Au = 1.33 ppm.

The grade of the ore deposit in the oxidized zone fall into: Ni=0.74%, Cu=0.48%, Co=0.03%, PGE + Au=1.76 ppm.

Ore amounts include: 5.3 x 10<sup>5</sup> tons of sulphide minerals and 445 x 10<sup>3</sup> tons of oxide minerals. Gossan is important for prospection, which is distributed in wide areas. The average thickness of the mineralization belt stands 3 m only.

##### 2) Serro and Morro do Pilar (Minas Gerais Province)

It is widely known that platinum minerals are produced in Alluvium in Ribeirao Limeira in Pilar County and Corrego Bom Sucesso in Serro County in Minas Gerais Province. According to 89 samples of Pan-concentrations gathered, 13 samples had 6-3,550 ppb of Pt and 24 samples had 10-10,000 ppb of Pd, both of which were detected together with Au. A grain from Corrego Bom Sucesso had 92.2% of Pt, 5.9% of Pd, and 2% of Ti according to the ERMA analysis. Another grain from the same area showed 40-83% of Pt and 13-56% of Pd.

##### 3) Guajeru area (Bahia Province)

This area is located in Guajeru, Malhada das Pedras, and Janio Quadros Counties. A number of Pan-concentrations show 40-720 ppb of Pt + Pd, accompanying 10-1380 ppb of Au.

#### d) AI type--Anorogenic Intrusive Rock

Most of the anorogenic intrusive rocks are not surveyed or just under initial stage of survey.



What is interesting are found in Rondonia, Para, and Roraima Provinces.

1) Pedra Preta and Cotingo sills (Roraima Province)

Sills consist of dolerite of anorogenic intrusive rock in the Proterozoic period. The sills reach more than 100 km in length in the entire Brazil land. In Venezuela and Guiana, the sills are 2 km in thickness.

e) MU type--Unclassified Ultra-Basic Rock

1) Rio Branco/Alta Floresta area (Rondonia Province)

This area is located in Alta Floresta D'Oeste County and Sao Miguel do Guaporé Country in Rondonia Province.

The major lithofacies include gabbro, troctolite, metagabbro and amphibolite. Metamorphism and shear zone are observed. The metagabbro may indicate a combination of pentlandite, chalcopyrite, pyrite, pyrrhotite, arsenopyrite, bravoite, violaraite, sphalerite, and platinum groups.

Pan-concentrations by EMPA identified platinum minerals--64-95% of Pt, 1.8% of Pd, and 4.7% of Rh while 8 samples of Pan-concentrations in the metagabbro indicated 30-660 ppb of Pt and 10-220 ppb of Pd. In addition, Cu and Ni of fine-grained fluvial sediment samples indicated marked anomaly.

2) São Felipe / Santa Lizia area (Rondonia Province)

This area has gabbro, norite, olivine-gabbro, amphibolite, and metagabbro rock bodies. The composite is known as having combinations of chalcopyrite, pentlandite, violaraite, bravoite, pyrite, pyrrhotite, and platinum groups. Although fine-grained fluvial sediment samples indicates Cu and Ni anomaly, Pan-concentrations indicated no platinum minerals.

3) Nova Brasilândia Rock Body

This rock body consists of fine-grained to coarse-grained-basic rocks, metagabbro, and amphibolite. Some of them was altered while other shear zones went through hydrothermal alteration.

As for minerals of the metagabbro, pyrite, pyrrhotite, chalcopyrite, pentlandite, bravoite, violaraite, and arsenopyrite were recognized. 44 samples of pan-concentration indicate 60-21,890 ppb of Pt, 10-7,890 ppb of Pd. Pan-concentration indicated a small quantity of mineral grains--59.7 % of Pt. Fine-grained fluvial sediment samples indicated anomaly of 270 ppm of Ni, 120 ppm of Cu, and 175 ppm of Co, at maximum.

We conducted two test borings (94 m, 181 m) at IP anomaly points in a sulphide mineralization belt (sulphide mineral: 25 %). Although pyrite and pyrrhotite were recognized, no PGE mineralization was observed.

## **Chapter 4: Summary of Investigation Results, and Conclusion and Proposal**

### **4-1 Summary of Investigation Results**

This project started in anticipation of whether we can find Noril'sk style copper-nickel-PGE sulfide ore deposits in the Paraná flood basalts. Studies on LIPs (Large Igneous Provinces), including the flood basalt that formed ore deposit of this type, have just made rapid development since 1995. Because discussions are still on the progress on the characteristics and origin of LIP, researchers have naturally different opinions.

Given this situation, this survey began, based on existing literature, by reviewing the characteristics and genesis of flood basalts around the world, chemical stratigraphy and geological structure of the Noril'sk ore deposits and Siberian trap, and considering the exploration criteria of the Noril'sk style ore deposits. According to the exploration criteria studied, the approaches from analyzing both the geological structure and the geochemistry of the basalts were conducted in order to extract an area with similar geological environment to the Noril'sk region in the Paraná Basin. That is, the geological structure analysis of the entire basin was carried out using the existing documents, satellite images, and gravity/geomagnetic data. At the same time, the analysis of the major chemical compositions and trace elements, such as Pt, Pd, Au, and REE, and isotope analysis for rock samples collected during the survey were also carried out. This resulted in defining the geochemical characteristics of the Paraná flood basalts. Based on comprehension of these results, we carried out study for the area that has a potential for existence of ore deposits.

#### **4-1-1 Genesis of Flood Basalt and PGE Sulfide Ore Deposit**

A number of theories exist concerning the genesis of flood basalt, including a theory that supports active involvement of the mantle plume and a theory that emphasizes ascensions of the asthenosphere in continent breaking up. However, there has been no established theory yet concerning the genesis of flood basalt. Since 1995, a new theoretical model has been attracting researchers. According to this model, vast amounts of oceanic crust (slab) that subducted from continental margins deposited at the deep of the mantle, and ascended as heterogeneous mantle plume. The flood basalt magma characteristically erupted huge amounts of lava in a short period generally within 1 Ma or less. The heterogeneous plume that consists of basalt constituent having low melting temperature and peridotite constituent. In addition to such variety of the theory, magma activities of flood basalt vary depending on the location, so the theory of flood basalt formation does not necessarily lead to direct linkage to the existence

of PGE ore deposits.

Most PGE concentrate in the earth's core and are rarely included in the continental crust that is markedly differentiated. Therefore, it is reasonable to think that the original magma of PGE deposit was brought from the deep part of the earth. The source materials of flood basalt that yielded the PGE mineralization may have been brought from mantle plume that ascended from the core and mantle boundary zone. The magma is also expected to be generated with large scale melting of plume and surrounding mantle. During the formation of flood basalt, large magma quantities are generated compared to periods of ordinary igneous activity. At this stage, PGE that ordinarily concentrates in solid phases is considered to have a high possibility to be caught in the melt with relatively large quantity. Since PGE concentration is affected by factors of the supplies of SiO<sub>2</sub> and sulfur by crustal contamination, and the local tectonic setting, such factors that influence to PGE concentration are important for forming PGE ore deposits from the magmas generated by the above process.

#### 4-1-2 Exploration criteria of the Noril'sk style deposit

Assuming that the Noril'sk ore deposits in Russia belong to a type of orthomagmatic sulfide ore deposit, we considered the geological environment that satisfies the common requirements for the genesis of orthomagmatic sulfide has been formed connected to the flood basalt magmatism in the Noril'sk region. Based on such standpoint, a document survey regarding the world orthomagmatic sulfide deposits and the Noril'sk ore deposits was carried out.

The magmas related to the genesis of the Noril'sk ore deposits were initially sulfur undersaturated and rich in PGE, and were also picritic to basaltic compositions of high temperature. The Noril'sk ore deposits were formed in an area with large quantities of such magmas, that is the center of plume related magmatic activity. Considering the forming environment of the Noril'sk ore deposits from the view point of the condition of orthomagmatic sulfide ore deposit forming, the follows are presented as the exploration criteria for orthomagmatic ore deposit accompanied with flood basalt:

- (1) The existence of sulfur undersaturated PGE rich magmas as lavas or intrusions.
- (2) The existence of magmas showing the signatures of crustal contamination and sulfide segregation associated with above PGE rich magmas as lavas or intrusions.
- (3) It is desirable that the magmas are high temperature picritic to basaltic composition that easily contaminates the crust materials.
- (4) The center of the magmatic activity where the large volume of silicate magmas are supplied through crustal suture zone

#### 4-1-3 Geology and Geological Structure of the Paraná Basin

After Paleozoic in age, intracratonic basins such as Parana Basin, etc. were formed in the Gondwana continent. M. S. M. Mantovani et al. (2001) calculated the thickness of lithosphere of South-American plates using the tidal gravity anomalies. According to the results, the thickness of lithosphere of Parana Basin is 10 to 20 km or more thinner than that of surrounding basement rocks. At this kind of portion with thin lithosphere, intracratonic basins are formed by changes of regional stress field and mantle plume (Bott, 1971; Makenzie et al., 1978). The Noril'sk ore deposit was formed in Gydansk-Omsk rift (Zonnenshain et al., 1990) and Duluth ore deposit in Midcontinent Rift (MCR) of North America.

From Paleozoic to Mesozoic in age, the Parana Basin was repeatedly deposited and eroded due to dilation and constriction of mantle plume. The present total thickness of the sedimentary rocks attains a maximum of more than 4,000 meters. In Early Cretaceous in age, tholeiite basaltic magma was active in rift and subsequently Gondwana continent was ruptured (Rezende, 1972). The sedimentary rocks and volcanic rocks of Parana Basin can be divided into the following six Supersequences (SS) according to geologic ages (Milani et al., 1998; Fig. II-1-4-9). They are the Rio Ivai SS (Ordovician to Silurian), the Parana SS (Devonian), Gondwana I SS (Late Carboniferous to Early Triassic), the Gondwana II SS (Early to Middle Triassic), the Gondwana III SS (Early Cretaceous) which mostly comprises thoreiitic flood basalt (maximum thickness 1,723 m) and the Bauru SS (Late Cretaceous).

As the flood basalt lava is distributed thickly in the NE-SW direction along the Parana River, the area is estimated to have been a rift. Drillings for oil exploration revealed that a large amount of sills and dykes associated with flood basalt magmatism intruded into the rift. There are two zones which accumulated thickness of sills and dykes are larger. The one is an area where extends in the NW-SE direction from the east of Parana River to Ponta Grossa Arch and the other an area where are located in the boundaries between Matto Grosso do Sul Province and Sao Paulo province in the northern area of the Basin and extends in the N-S direction. In the TM false color image (RGB=234), they are expressed as geographyc features uplifted in the form of thin strings and sometimes continue over 100 kilometers.

Based on the residual gravity anomaly map (M. C. L. Quintas, 1995), A large and high anomaly is present along Parana River in the NE-SW direction of the central area of Basin. The high gravity anomaly of the rift may be due to the density difference between asthenosphere ( $3.33 \text{ g/cm}^3$ ) and lithosphere ( $2.80 \text{ g/cm}^3$ ). Other large high anomalies and large low anomalies are considered to indicate basement structures blocked by faults in the N-S direction, NE-SE direction, and NW-SE direction.

With respect to the basement structure of the cetral region of the Basin based on

aeromagnetic anomalies, large and high pseudogravity anomalies are recognized in the N-S direction in the eastern part and the western part, while a large and low pseudogravity anomaly is recognized in the N-S direction at the central part of the central region. The former are inferred to be regions with basement rocks in comparatively shallow depth and the latter a region where basement rocks collapsed due to flood basalt magmatism. The high pseudogravity anomaly in the western part may be possibly a part of Paraguay-Araguay belt and the high pseudogravity anomaly in the eastern part a part of Sao Francisco craton under the flood basalt lava pile. In the large low anomaly of the central part, high anomalies and low anomalies are recognized in the NE-SW direction, which run nearly in the same direction as Parana River. The low anomaly along the right side of Parana River coincides with high residual gravity anomaly and thick part of flood basalt lava.

Many magnetic lineaments which indicate faults are present on the pseudogravity anomaly map and so on. Principal directions of faults are NW-SE direction, NE-SW direction, and E-W direction. The magnetic lineaments in the NW-SE direction are continuous faults which have sharp boundaries. The magnetic lineaments in the E-W direction are poorly continuous. Most of faults in the E-W direction seem to be secondary shear faults derived from sinistral wrench faults in the NW-SE direction. The unclockwise rotations of them coincide with those mentioned by Turner et al. (1994) and W.M. de Rezende (1972). A large amount of sills and dykes are recognized in the areas where Rio Alonzo fault in the NW-SE direction and rift along Parana River in the NE-SW direction intersect.

#### 4-1-4 Promising Areas of Emplacements of Ni-Cu-PGE Ore Deposits Estimated from Geological structure

We will present a comprehensive explanation of Precambrian basement rocks, sedimentary rocks and flood basalts in Post- Early Paleozoic, and faults in the Parana Basin and consider the relation among the rift zone and the regional stress field, and promising areas of emplacement of Noril'sk-type Cu-Ni-PGE ore deposit (Fig.II-1-5-25).

A large low anomaly zone in the central part of the pseudogravity anomaly map overlaps with a zone where sedimentary sequence and flood basalt lava are thicker, with a zone where a large quantity of sills and dykes intruded, with a high residual gravity anomaly zone, and with a high attenuation factor zone. Based on these facts, it is concluded that the large low anomaly zone was rift zone associated with flood basalt magmatism.

The direction of the rift zone extends in the N-S directions in the northern Basin; in the NE-SW directions the central Basin, and branches into the NE-SW and NW-SE directions in the southern Rio Alonzo fault. The inside of the rift zone has repetitions of high anomaly zones and low anomaly zones in the NE-SW direction. These anomaly zones in the NE-SW

directions were formed by stair-step normal faults (vertical direction: maximum compressive principal stress axis  $\sigma_1$ ) in the extensional stress in the NW-SE directions field (minimum compressive principal stress axis  $\sigma_3$ ).

Many magnetic lineaments which represent faults in the NW-SE direction are recognized on the pseudogravity anomaly map. For example, Rio Alfonzo fault on the geological map are represented by several magnetic lineaments on the pseudogravity anomaly map. The faults in the NW-SE directions are estimated to be sinistral transcurrent faults because they have sharp boundaries and are accompanied with many secondary shear faults in E-W directions. In the Duluth ore deposit, many secondary shear fractures occurred in the form of Cymoid Loop-like tensional fractures in areas where the rift zone and transcurrent faults cross. The Duluth Complex intruded there and formed the ore deposit. The Noril'sk ore deposit was also formed in the volcano-center where magma extruded most intensely in the Gydansk-Omsk rift zone (Tamrazyan, 1962).

As the results mentioned above, we propose the following four promising areas, which rift zone and transcurrent faults cross, of emplacements of Ni-Cu-PGE ore deposits.

- (1) The area where the Tiete structural line in the NW-SE direction crosses through Paran River
- (2) The area where the Guapiara fault in the NW-SE direction crosses through Parana River.
- (3) The area where Rio Alfonzo fault in the NW-SE direction crosses through Parana River.
- (4) The western part of Torres - Posadas fault in the southern region of Parana Basin

All of these areas are estimated to have been the volcano-center of flood basalt magmas. The largest volcano-center is found in the area (3) where the Rio Alfonzo fault crosses through Parana River. Among four areas, it is concluded that areas where the Guapiara fault and the Rio Alfonzo fault in the NW-SE directions cross through Parana River are the most promising area of emplacements of Ni-Cu-PGE ore deposits.

#### 4-1-5 Geochemical Characteristics of Paraná Flood Basalts

##### (1) Classification of Magma Type

Six types of lava units of Paraná flood basalts are divided into Low-Ti type and High-Ti type by Peate et al. (1992). Since the Ti contents of Paranapanema and Ribeira are intermediate in this survey, the two above were geochemically judged not to be classified into Low-Ti type nor High-Ti type. Therefore, the two above were newly classified as the Intermediate-Ti type, and the magma types of Paraná flood basalts were classified as follows. The difference of Ti contents among the three types is obvious, and each type shows different

trends of fractionation in Mg#-TiO<sub>2</sub> diagram.

	Peate et al. (1992)	This survey
Low-Ti type	Gramado	Gramado
	Esmeralda	Esmeralda
	Ribeira	
Intermediate-Ti Type	—	Paranápanema-Ribeira
High-Ti Type	Paranápanema	Pitanga
	Pitanga	Urubici
	Urubici	

Geochemical examinations were carried out for both lava samples and intrusion samples in this survey. Both samples show entirely the same geochemical trend. Therefore, both lava and intrusion samples were classified into the above five magma types. As for distribution, Pitanga is distributed in the northern part of the Paraná Basin, Pitanga and Paranápanema-Ribeira are distributed in the central part, and Gramado, Esmeralda and Urubici are distributed in the southern part. Pitanga and Paranápanema-Ribeira are intermingled in the intrusions of the Ponta Grossa Arch in the central part. The results of the geochemical examinations are summarized in Table II-4-5-1.

## (2) Partial Melting and Crustal Contamination

Pitanga, High-Ti type, is distributed from the northern to the central part of the Paraná Basin. This magma type shows the smallest degree of partial melting. It is thought to have been generated in relatively deeper portion in the upper mantle. Paranápanema-Ribeira, the Intermediate type, is distributed in the central area of the Paraná Basin. The degree of partial melting of this type is shown larger than that of Pitanga. This means that it has been generated in a shallower portion than Pitanga was generated. The effect of the crustal contamination is considered limited in these two types of magma because of poor contents of U and Th that concentrate in the crust. Mantovani et al. (2000) described that the two types above were generated from a similar magma source with different degrees of partial melting. The large quantities of the two magma types above erupted and were piled with a thickness of approximately 1,800 meters along the Paraná River in the central part of the Paraná Basin, which is thought to be the center of the magmatic activity.

The Low-Ti type magmas (Gramado and Esmeralda) show relatively large degree of partial melting. They are thought to have been generated in relatively shallower portions compared to



the other magma types. The increases of LIL elements such as Th, U and the likes that concentrate in crust, and Sr isotopic ratio are observed in both magma types. It is thought to be the effect of crustal contamination. The effect is particularly marked in Gramado. Esmeralda is considered to be the most primitive magma among all the magma types because of its low contents of light rare earth elements and a relatively high Nd isotopic ratio.

As regards the Low-Ti types of magma, the following three points are thought to have a close relationship. The first is that the magma was generated in a shallow portion. The second is that the magma was highly affected by crustal contamination, and the third is the existence of acidic rocks, which are considered to be the products of lower crust melting, in the southern part of the Paraná Basin. More specifically, the following process is thought to have occurred. That is, the acidic magma was generated from the melt of the lower crust by the mantle plume heating. After generating the acidic magma, this magma and the magma generated by the melting of the mantle plume itself mixed and yielded Gramado type magma. Finally, just after the commencement of expanding the Atlantic, Esmeralda type magma is thought to have been generated that is less influenced by crustal contamination although the origin is the same as Gramado.

### (3) PGE Contents of the Paraná Flood Basalts

The original magmas of the Paraná flood basalts are thought to be PGE rich as a whole, particularly Pd rich (Refer to Table II-3-5-1) although there are some differences among the magma types. The most PGE enriched magma is Paranapanema-Ribeira. The average content of Pt and Pd summing is approximately the same as that of the Tuklonsky lava, the most PGE enriched lava in the Noril'sk region. Paranapanema-Ribeira is also rich in Cu. The magma of this type as lavas is distributed along the Paraná River in the central part of the Paraná Basin, and much native copper is observed in the cavities. The geochemical anomaly in PGE, Ni, Cu, and other elements that is observed in the western part of the state of Paraná (by the stream sediment geochemical survey carried out by MINEROPAR) possibly shows the distribution of Paranapanema-Ribeira that has high PGE contents. Paranapanema-Ribeira as intrusions is distributed in the Ponta Grossa Arch intermingled with Pitanga of High-Ti type. The magma type of the higher PGE content next to Pitanga is Esmeralda that has the most primitive chemical composition. The PGE depletion by sulfur saturation is rarely observed in Paranapanema-Ribeira and Esmeralda.

Regarding Gramado and Pitanga, there are two populations of samples, PGE enriched and depleted. These two types are thought to have been initially PGE enriched. The depletion of PGE, however, is thought to have occurred due to sulfur saturation in a part of the magma. As the cause of sulfur saturation, the crustal contamination in Gramado, and the crystallization differentiation in Pitanga are both thought to have occurred. Pd contents of 133.8 ppb were

obtained by analyses of the intrusion sample (KN104) of Pitanga type that was collected in the Ponta Grossa Arch. This value exceeds the Pd content of ordinary basaltic magma, and suggests the existence of sulfide that includes Pd.

According to the facts above, all magma types of Paraná basalts are considered to be initially sulfur undersaturated and rich in PGE. They have the potential to form the ore deposits if satisfy other requirements demonstrated above.

#### 4-1-6 Mineralization Potential of the Paraná Flood Basalts

In the Noril'sk region, the majority of the lava and intrusion is basaltic, however, the sills which embed ore deposits contain picritic parts and the assimilation of country rock on a large scale in the picritic sill is observed. Picritic magma, however, is rarely observed in the Paraná flood basalts, and the basalts are more differentiated than in the Noril'sk region. The magma temperature of the Paraná flood basalts is thought to be lower than that of the Noril'sk region. It is thought to be possible that this low temperature obstruct the assimilation of country rock and the large scale segregation of immiscible sulfides. As assumed in Pitanga, though, there is a possibility of segregating immiscible sulfides by the progress of the simple crystallization differentiation without the influence of contamination. The saturation mechanism on sulfur mentioned above is the same process considered in the Skaergaard intrusion in East Greenland (Anderson et. al., 1998) and the Sonju Lake intrusion in Minnesota, USA(Refer to Appendix 2).

All the samples of intrusion including the Ponta Grossa Arch sill that could be collected in this survey were distributed in the marginal area of the Basin, the edge area away from the center of magmaic activity. The sills are mostly poor in sulfide, and the maximum thickness is approximately 200 m, which is comparatively thin. The rock compositions show basaltic, and although show high PGE contents, the magma temperature is lower than that of the magma of Noril'sk. The contamination effect of country rock in such intrusions is weak. This is considered to be the reason why only a faint dissemination of sulfides is observed (pyrite/pyrrhotite/chalcopyrite/sphalerite). The segregation of sulfides in a large scale magma chamber like the Skaergaard intrusion under the high R factor is necessary to generate sulfide ore deposit from basaltic magma with high PGE contents.

The location with the highest possibility of generating sulfide ore deposit is thought to be the eruption center of Paranápanema-Ribeira and Pitanga types, which have the largest quantities of magmas among the Patana flood basalts. The eruption center is thought to be located in the central area of the Paraná Basin along the Paraná River where the lava piles are the thickest. Based on the existing data analysis, the strong shrinkage of lithosphere by the ascension of the asthenosphere is observed in this area, and magma intrusion is estimated to be the most active in this area.

## 4-2 Conclusion and Proposal

From analyses of existing geological papers, geological survey on the ground surface, geophysical anomaly maps, drilling data of coal exploration and so on resulted in identifying geotectonic characteristics of the Parana Basin and geochemical characteristics of flood basalt magmas and possibility of emplacements of Ni-Cu-PGE ore deposits such as the Noril'sk, Duluth and Skaergaard ore deposits.

According to the dykes and sills in the basement rocks, although the drilling cores of coal exploration and the outcrops were investigated, no Ni-Cu-PGE mineralization was almost identified.

Hereafter, diamond drillings are proposed for identifying mineralization of dykes and sills in the basement rocks in the promising area where have been located at volcano-centers of flood basalt magmas. But, as most of volcano-centers are located at more than 1,000 meters below the ground surface, it is difficult for ore deposits to be economic.

## **Part II Detailed Discussion**

### **Chapter 1: Analysis of the Existing Data**

#### 1-1 Summary of the Collected Data

##### 1-1-1 Scientific Documents and Research/Survey Materials

Collected papers, documents and materials are arranged as “References”.

The main scientific documents and research/survey materials collected to evaluate PGE mineralization of Paraná flood basalt are as follows:

- The documents and research materials discussing igneous activity of Paraná flood basalt from the viewpoint of petrologic study
- The documents and research materials examining geophysical data on magnetism, gravity and terrestrial heat flow related to the generation of Paraná basin and the activity of Paraná flood basalt
- The documents and research materials containing petrologic studies of flood basalt, its igneous activity and cause of its generation related to the flood basalt distributed worldwide such as Deccan, Columbia River and Noril'sk
- The documents and research materials concerning generation of Noril'sk ore deposit and its PGE mineralization
- The documents and research materials concerning nickel and PGE ore deposits and mineralization related to large-scale basaltic magma activity such as flood basalt
- Materials and data on the coal exploring enforced in the half of 1980s by DNPM and CPRM concerning the districts where sediments were distributed on the out of east edge of Paraná flood basalt (see Fig. II-1-1-2 for the scope of the survey)
- The report and data of the survey to evaluate PGE mineralization jointly conducted by Geological Survey of Canada and CPRM for lava and intrusive rocks in the eastern edge of Paraná flood basalt and jointly conducted by DNPN and CPRM on the drilling core for coal exploring
- Geochemical survey data on stream sediments conducted by MINEROPAR in Paraná Province

## 1-1-2 Collected Data and Materials

### (1) Topographic Map

Fig. II-1-1-1 shows the index map of the topographic maps on a scale of 1:500,000.

In Brazil, the army manages topographic maps. Since the topographic maps of the survey area are controlled by the army offices located in Porto Alegre, São Paulo and Brasilia, it is necessary to visit these army offices to obtain all the maps concerned.

### (2) Geological Map

Fig. II-1-1-2 shows the index map of geological map on a scale of 1:100,000 made during the coal prospecting by CPRM .

There are maps on a scale of 1:2,500,000 that were scheduled to be completed and published at the end of 2000 by MERCOSUR, maps of each province made by DNPM and MINEROPAR, the map on a scale of 1:100,000 that was made during the coal prospecting by CPRM, and a map on a scale of 1:250,000 that was made during prospecting for water resources by CPRM in the 1970s. These maps are the representative geological maps of the survey area. Photocopies of the maps that were used in the survey were brought back to Japan.

### (3) Satellite Images

131 scenes of JERS-1 SAR images covering from the Ponata Grossa Arch in the eastern part of the Paraná Basin to near the border of Brazil in the western part of this area were supplied by ERSDAC to analyze the geological structure (Refer to Chapter 2, Part II.). 74 scenes of LANDSAT TM image and their mosaic image that covers the whole survey area were purchased from GEOIMAGE of Australia to analyze the general trend of the geological structure (Refer to Chapter 2, Part II.).

### (4) Airborne Geomagnetic Data

The coverage of the airborne geomagnetic data supplied by CPRM for the 2001 survey and the airborne geomagnetic anomaly chart that was purchased in FY2002 are shown in Fig. II-1-1-3.

In the survey of FY2001, the analysis of CPRM airborne geomagnetic data was requested from the CPRM branch in Porto Alegre. The results of the analysis were recovered in hard copy format.

In the survey of FY2002, the airborne geomagnetic data, which contains the total magnetism and flight courses (Shape file of Arc View, Esri), compiled by CPRM was supplied by CPRM. The data covers almost the entire area of Brazil. The hard copies of the airborne



**Fig.II-1-1-1 Index map of topographic maps on a scale of 1/250,000 in the survey area**

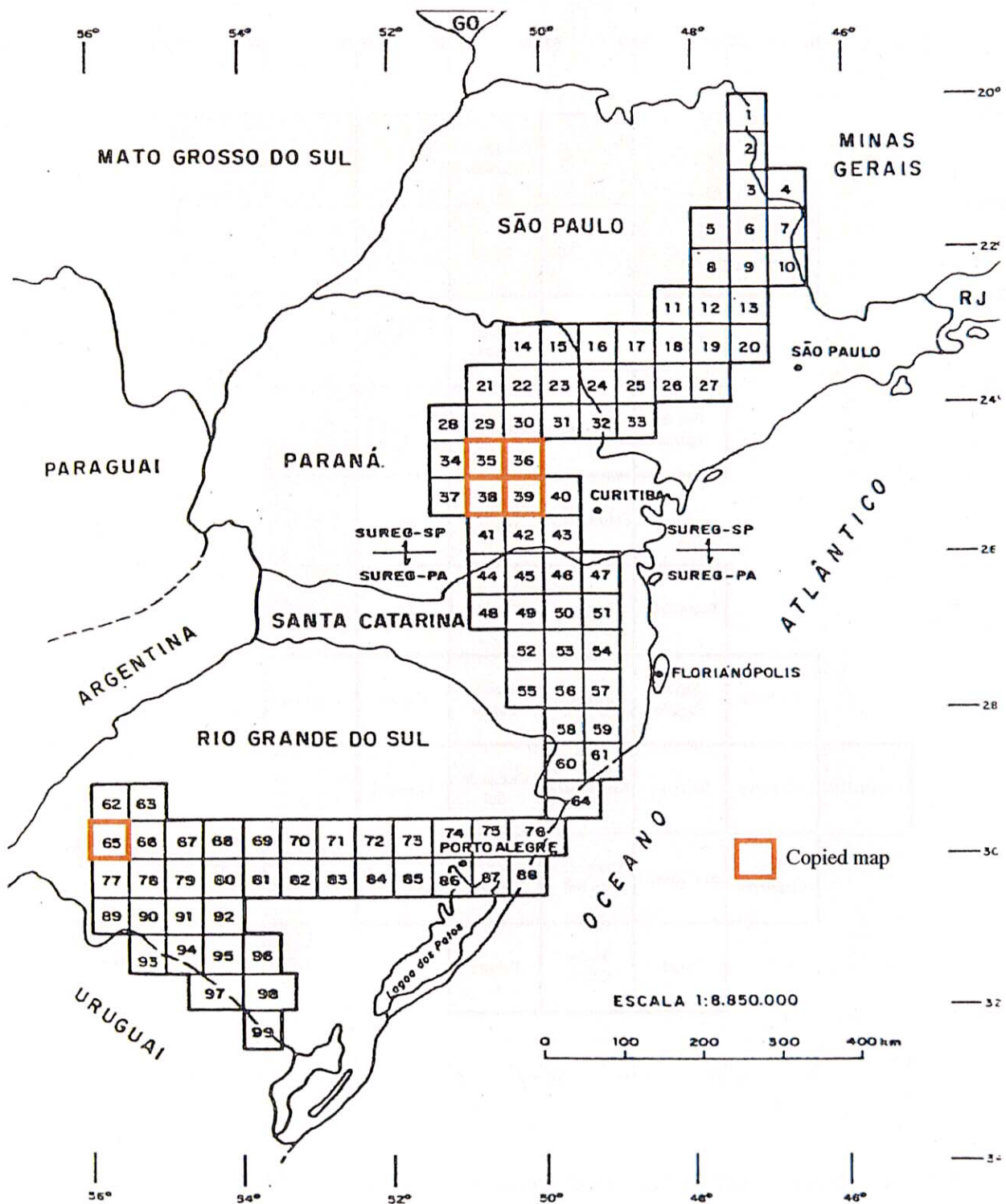


Fig. II-1-1-2 Index map of the geological maps on a scale of 1/100,000 made by DNPM - CPRM

PROJETOS AEROGEOFÍSICOS EXECUTADOS PARA A PETRÓLEO  
BRASILEIRO S.A. - PETROBRAS, INCLUSIVE CONTRATOS DE RISCO

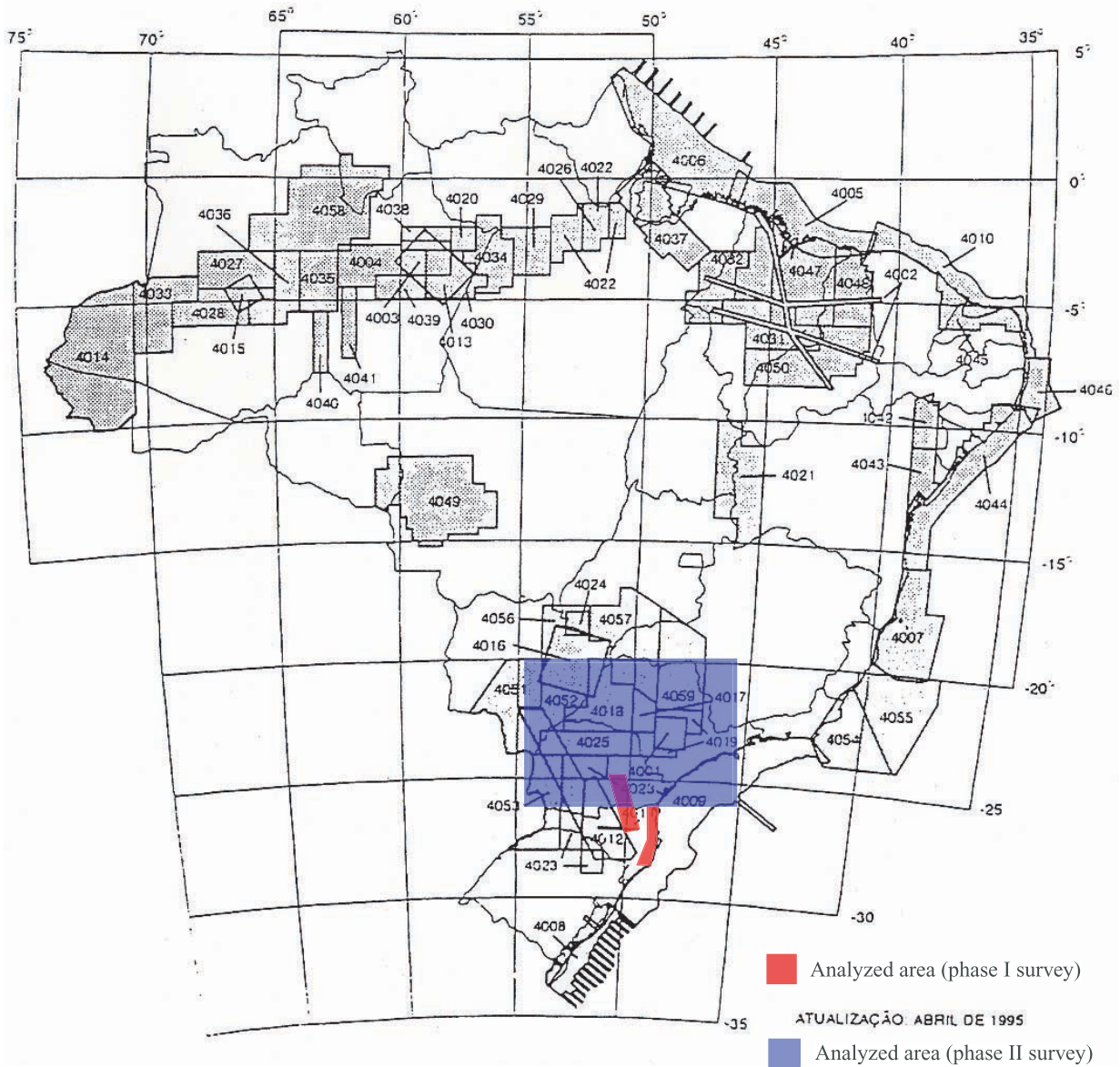


Fig. II-1-1-3 Index map of the airborne magnetic survey



geomagnetic anomaly chart of the Ponta Grossa Arch area were purchased from GETEC of Great Britain to analyze the geological structure. (Refer to Chapter 2, Part II.)

#### (5) GIS Data

The coverage of the GIS (Geographical Information System) data supplied by CPRM in FY2001 is shown in Fig. II-1-1-4. The data is compiled in the unit area of 4 degrees NS direction by 6 degrees EW direction and is composed of the topography (contours), water system, traffic (roads and air routes), and urban data. (The format is the Shape file of Arc View of Esri, the UTM coordinates with decimal longitude and latitude.)

The published GIS data in this area is as follows:

- The geology and ore deposit data of the member countries published by MERCOSUR in 2000.
- The geology, geological structure, ore deposits, topography, water system, traffic, and buildings that were published by CPRM in 2002.

#### (6) Drilling Data

The drilling data for the coal prospecting that was carried out by CPRM along the outer rim of the Parana flood basalt area was collected to analyze the underground sill distribution (Refer to Chapter 3, Section 3-4, Part II.). Besides the above data, columnar sections of 45 drilling cores as scanned image files (TIFF format) were collected. The locations of the drilling holes where the columnar sections are obtained are shown in Fig. II-1-1-5.

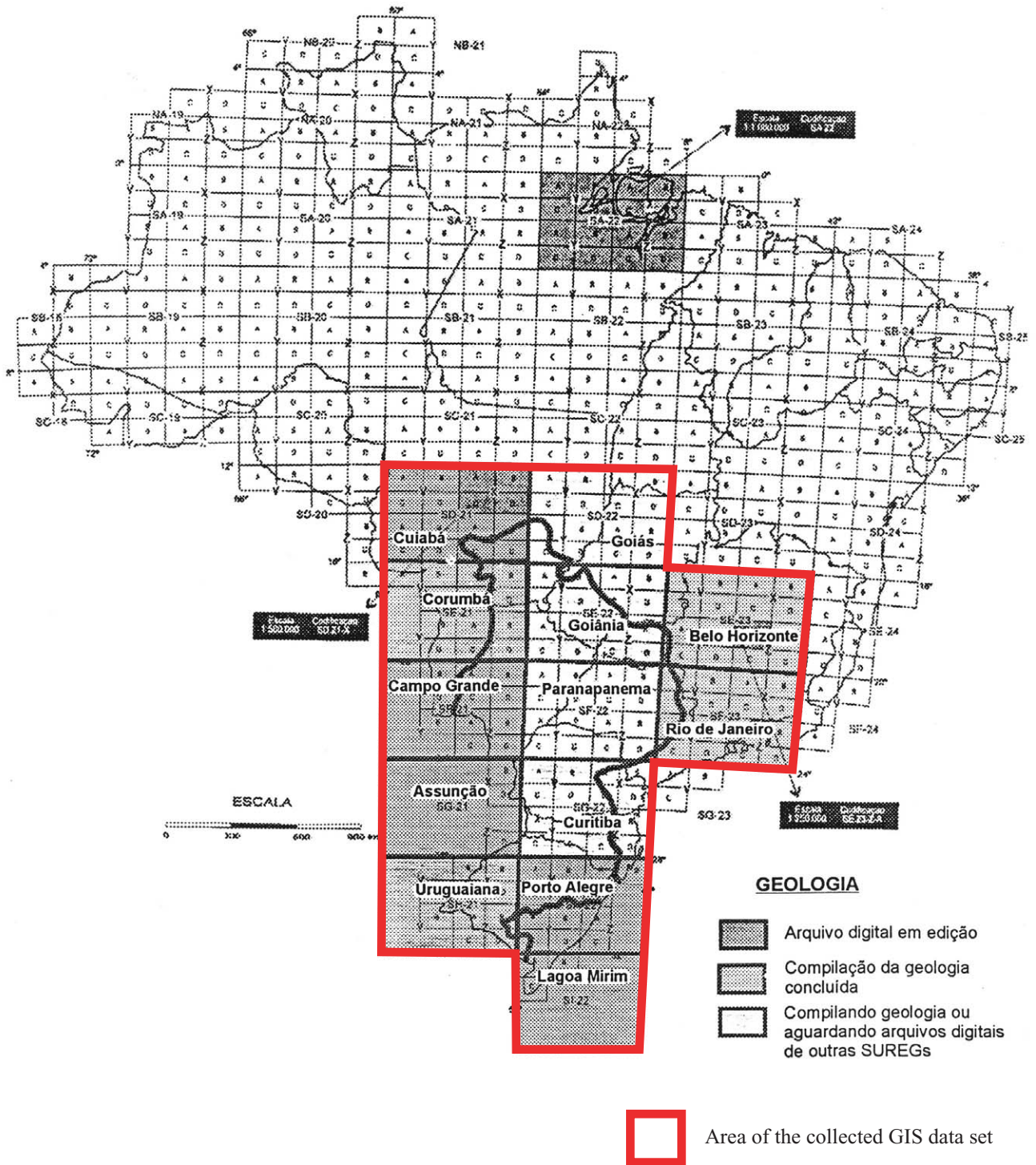


Fig.II-1-1-4 Index map of the GIS data set

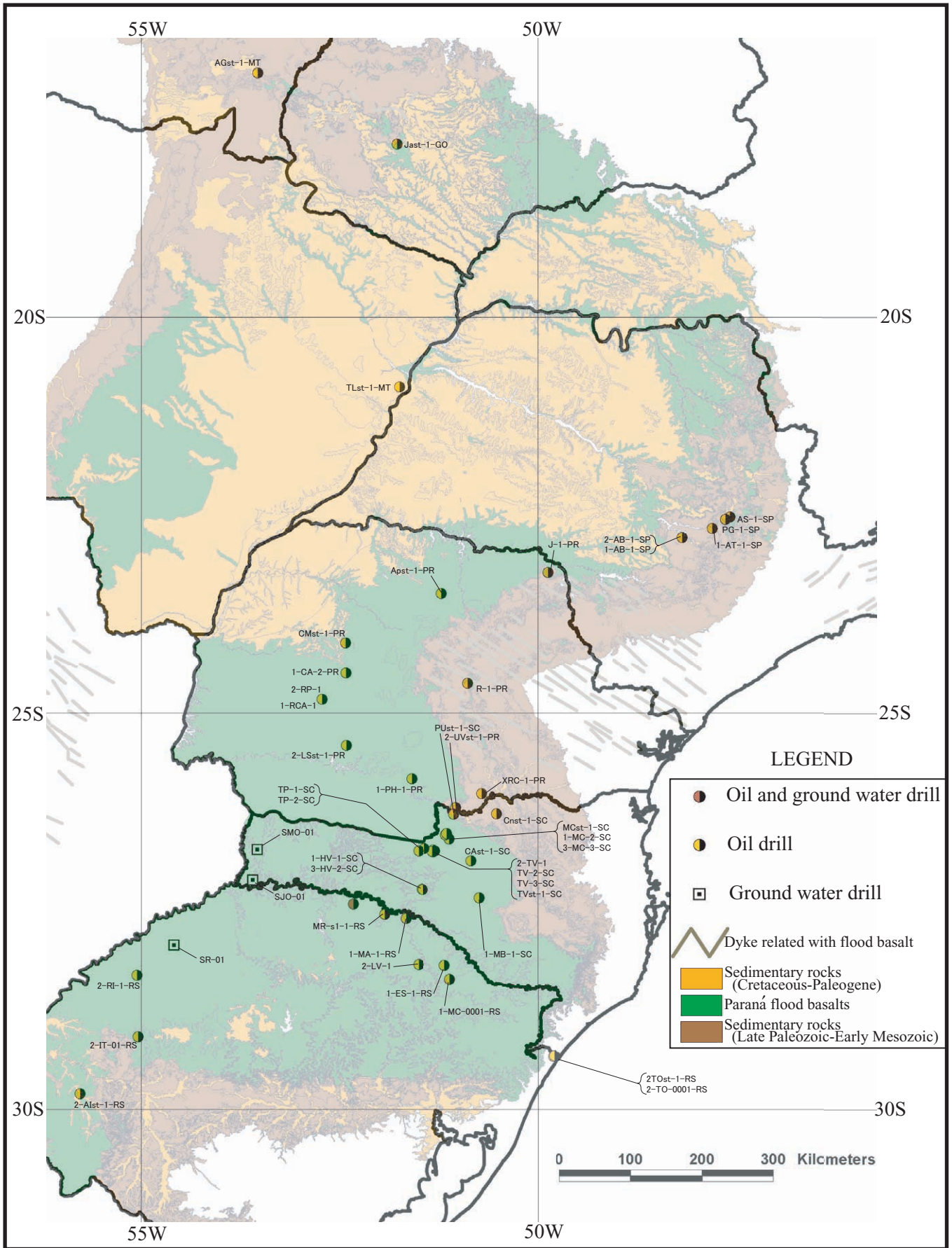


Fig. II-1-1-5 Index map of PETROBRAS's drill log

## 1-2 The Feature and Origin of the Flood Basalt around the World

### 1-2-1 Introduction

The classification of PGE ore deposits in the world is shown in Table II-1-2-1.

There are some PGE ore deposits that were generated by large scale basaltic igneous activity like flood basalt. For example, the Talnakh intrusive rocks (Noril'sk ore deposit) in the Siberian Trap, Insizawa-Ingeii intrusive rocks of the Karoo flood basalt in Africa, and Duluth composite rocks and the Crystal Lake gabbro of the Keweenawan basalt in North America are well-known flood basalt areas. This chapter will consider the characteristics and genesis of flood basalt, and the relationship between flood basalt and PGE ore deposits, for the estimation of PGE ore deposit mineralization within the Paraná flood basalt.

### 1-2-2 Characteristics of the Flood Basalt

#### (1) Distribution and Setting

Large-scale volcanic rocks such as flood basalt are called Large Igneous Province (LIP). The distribution of LIP in the world is shown in Fig. II-1-2-1. The age of forming, the starting period of activity, period of activity and distribution area of major flood basalt are reviewed in Table II-1-2-2.

Flood basalt is distributed in the Paraná basin of South America, the Ontong Lava plateau of the Pacific Ocean, the Deccan plateau of India, the North Siberian basin of Russia and the Columbia River in North America. The widest distribution area is the Paraná flood basalt and the erupted volume the Ontong Java is the largest.

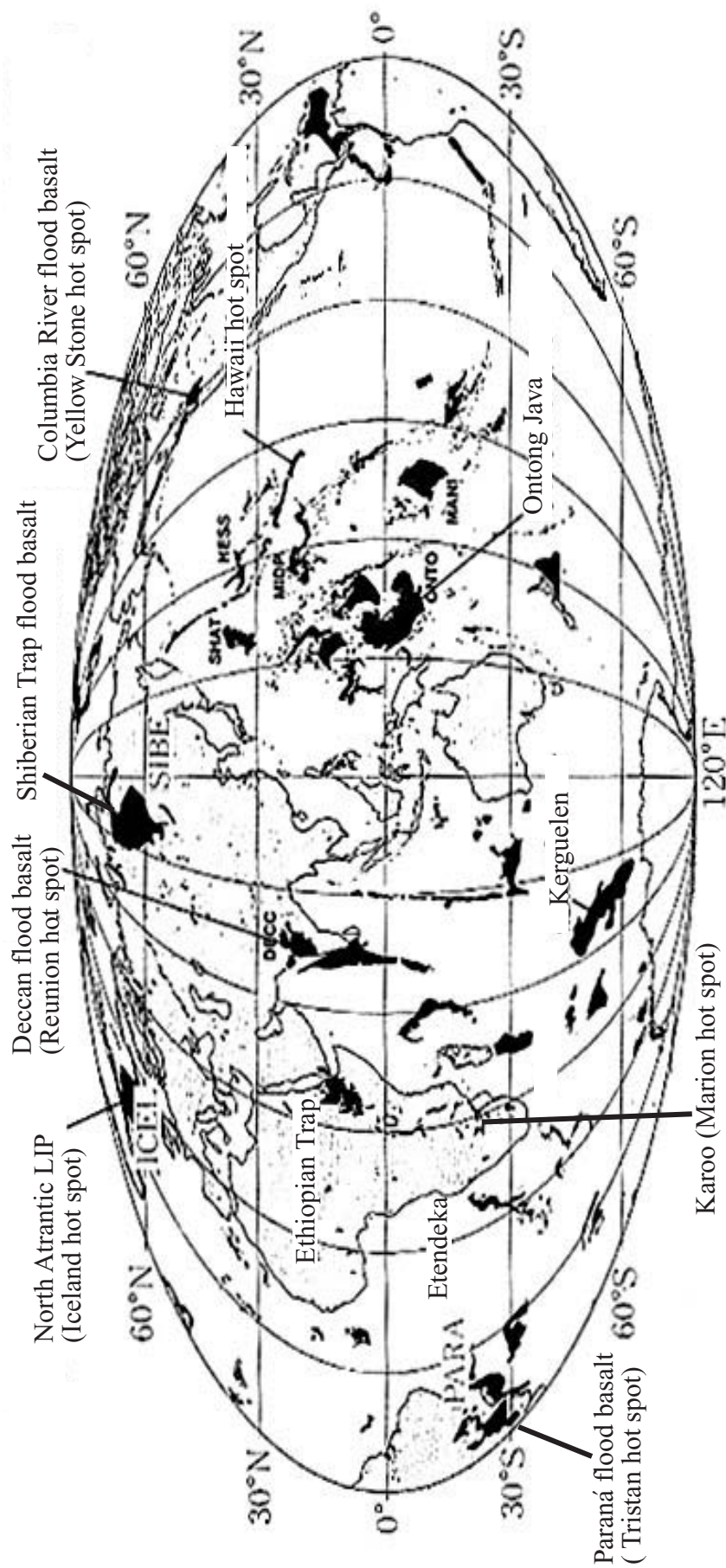
The huge volume of basalt magma (several hundred km<sup>3</sup> at a time) is erupted from the fissure that concentrated in a narrow area in a short time. Those are the characteristics of the eruption style of flood basalt. The period of eruption is about 1 Ma in major flood basalt. The period of the activity of flood basalt was comparatively short. For example, the period of main activity of the Paraná flood basalt was approximately less than 1 Ma, and that of the Etendeka flood basalt was approximately 2 Ma, making it a pair with the former.

Some flood basalt accompanied the continental breakup. In particular, there are many activities that erupted at the early stage of the drift of the super-continent. Therefore, each flood basalt has a counterpart, for example, the Deccan Trap and the Seychelle, the Paraná and the Etendeka, and the Ethiopia and the Yemen (the Red Sea), and so on (White and McKenzie, 1989, etc). When a fault of huge scale was formed, as a similar event in deep sea, plateau or basin was formed. Almost all the plateaus or basins are considered to have accompanied the sea-floor spreading activity on the triple junction of the mid-oceanic ridge.



**Table II-1-2-1 Mafic and ultramafic bodies and related sulfide ores**

<b>Petrological and tectonic setting</b>	<b>Ni-Cu ores</b>	<b>PGE ores</b>
<b>I. Synvolcanic (largely Archean)</b>		
<b>Komatiites</b>	E. Goldfields, Australia; Zimbabwe; Abitibi, Ontario	
<b>Tholeiites</b> <i>Picritic</i> <i>Anorthositic</i>	Pechenga, USSR Montcalm, Ontario	
<b>II. Rifted Plate Margins &amp; Ocean Basins</b> Associated with Continental Crust	<b>Circum-Ungava Belt</b> Thompson Ni Camp; Ungava Ni Ores	<b>Kemi-Koiligmaa Belt</b> Pemkat Intrusion
<b>Ophiolites</b> (No continental crust)		<b>Unst Ophiolite</b> Cliffs deposit
<b>III. Cratonic Areas</b> Flood Basalt-related	<b>Siberian Traps</b> Noril'sk-TaInakh <b>Karoo</b> Insizwa-Ingeii Intrusion <b>Keweenawan</b> Duluth Complex Crystal Lake Gabbro	←(by-product)
<b>Large Stratiform Complexes</b>	<b>Sheet-like</b> Sudbury	<b>Sheet-like</b> Bushveld: Merensky Reef UG- 2 Chromitite Stillwater: J-M Reef <b>Dyke-like</b> Great Dyke: Main sulfide zone
<b>IV. Emplaced During Orogenesis</b>		
<b>Synorogenic</b>	<b>Appalachia</b> Moxie & Katahdin intrusions, Maine	
<b>Late Orogenic</b>		<b>Alaskan Type</b> Tulameen Complex



Location of large igneous province (LIP).  
 (From White, R. and McKenzie, D. (1989); Takahashi, E. and Nakajima, K. (1997);  
 Courtillot, V., Jaupart, C., Manighetti, P. and Besse, T.J. (1999))

Fig.II-1-2-1 Global distribution of the major Large Igneous Province (LIP)

Table II-1-2-2 Major flood basalts and continental breakup (White and McKenzie, 1989)

Ocean Basin	Onset of Seafloor Igneous Province Spreading, Ma (Magnetic Chron)	Igneous Province	Flood Basalts			
			Age Span, (Ma)	(Main Age) Ma	Duration, my.	Area (x1000km <sup>2</sup> )
North Atlantic	58-56 <sup>a</sup> (24r)	British Tert. Ig. Prov. East Greenland West Greenland	63-52	(59)	2-3	500
South Atlantic	130-117 (M9-M4) <sup>j</sup>	Parana Etendeka	130-120	(~120)	'1 to a few'	1200
Indian Ocean-Seychelles	64 (27r) <sup>a</sup>	Deccan	128-113	(~120)	2	15
Red Sea-Gulf of Aden		Ethiopian Flood basalts Aden and Yemen traps	67-60	(66)	~0.53	>1000
Gondwana Breakup		Karoo Antarctic	30-15	(~25)	"most intense at earlier time"	750
---		Columbia River	29-20	(~27)	a few m.y.!	> 150
			200-175	(193)		
			179-162			
			17-6	(17-13.5)	<3.5 m.y.	200

Almost all the flood basalt has a hotspot that is concerned with its formation. For example, the Tristan hotspot relates to the Paraná flood basalt, the Yellowstone hotspot relates to the Columbia River flood basalt and so on. The eruption of flood basalt is considered to be the igneous activity of the early stage that accompanied a specific hotspot.

The example of the Paraná flood basalt is shown in Fig. II-1-2-2. The activity of the Paraná flood basalt began at the period of the expansion of the South Atlantic Ocean that forced the separation of South America and Africa (approximate 130 Ma, Fig. II-1-2-2(a)). At present, the Tristan hotspot (Mid-Atlantic ridge) is located in the Atlantic, midway in the Paraná flood basalt and the Etendeka flood basalt associated with forming the flood basalt (Fig. II-1-2-2(b)).

In Large Igneous Province, there are igneous rock bodies of the marginal part of continents besides flood basalt plateau, plateau, ridge and the line of seamounts. The igneous rock bodies of the marginal part of continents are markedly distributed in the marginal part of the continent in the North Atlantic Ocean. They are the large volume of igneous rock bodies that erupted just after the separation of continents. The igneous rock body was formed by the large volume of the eruption when the lithosphere became markedly thin. Compared to Deccan type mantle plume, the large volume of melt was generated by the ascending of the high temperature mantle to shallower part. For example, in the case of the igneous rock body offshore of Greenland, it was formed at 60 Ma of the separation of the continent, the activity still continues to make Iceland hotspot. In the case of the basalt plateau of the marginal part of the continent, almost all the part finally subducts into the mantle as the plateau.

## (2) Occurrence and Petrological Characteristics

The panoramic view photo of the Deccan flood basalt is shown in Fig. II-1-2-3. Since the Deccan flood basalt has not been affected by marked structural movement and is rarely covered by vegetation, the occurrence is well observed. As shown in the distant view photo, the piling of the lava flows looks like sedimentary rock. The characteristic occurrence is described below.

- Low viscosity: In the case of the Deccan flood basalt, one lava flow reached 200 kilometers.
- No clinker
- Less phenocryst

Since the density of basalt magma is higher than that of granitic rocks, that is the main rock component of the crust. It cannot pass through the crust easily and spreads horizontally forming dykes or sills. Therefore, dykes and sills of large scale develop in the distribution area of flood basalt.

Flood basalt is mainly composed of tholeiitic basalt that is accompanied by a small volume



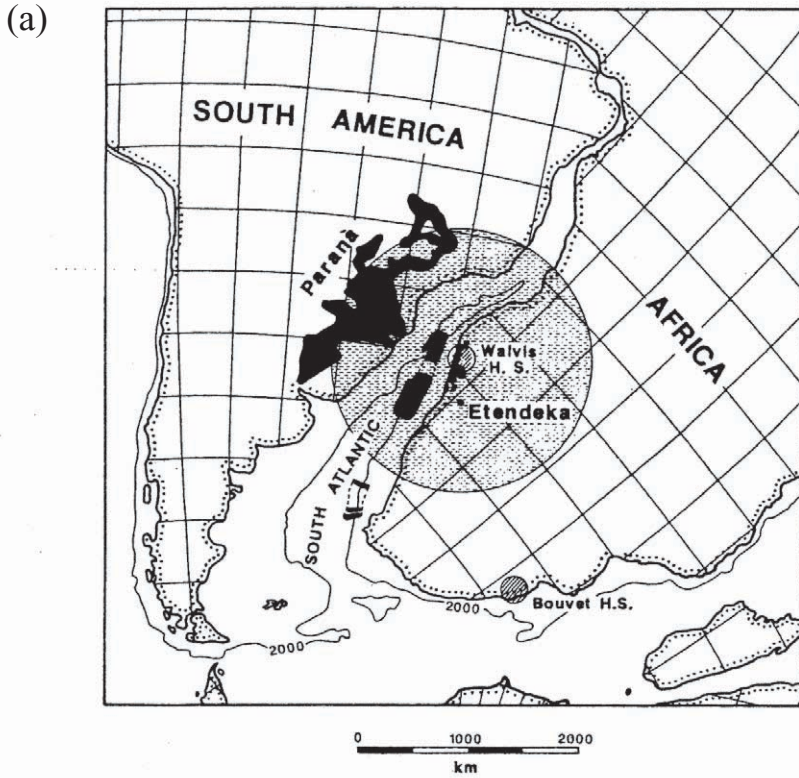


Fig. 15. Reconstruction of South Atlantic at anomaly M4 time (approximately 120 Ma) shortly after the onset of seafloor spreading. Solid shading shows areas of extrusive basalts. Extent of Paraná basalts from *Hawkesworth et al.* [1986], Etendeka basalts from *Eales et al.* [1984], offshore areas from seaward dipping reflectors reported by *Hinz* [1981], *Gerrard and Smith*, [1982] and *Austin and Uchupi* [1982]. Shaded area around Walvis hot spot shows extent of mushroom head of abnormally hot mantle. Equal area projection is centered on the hot-spot location.

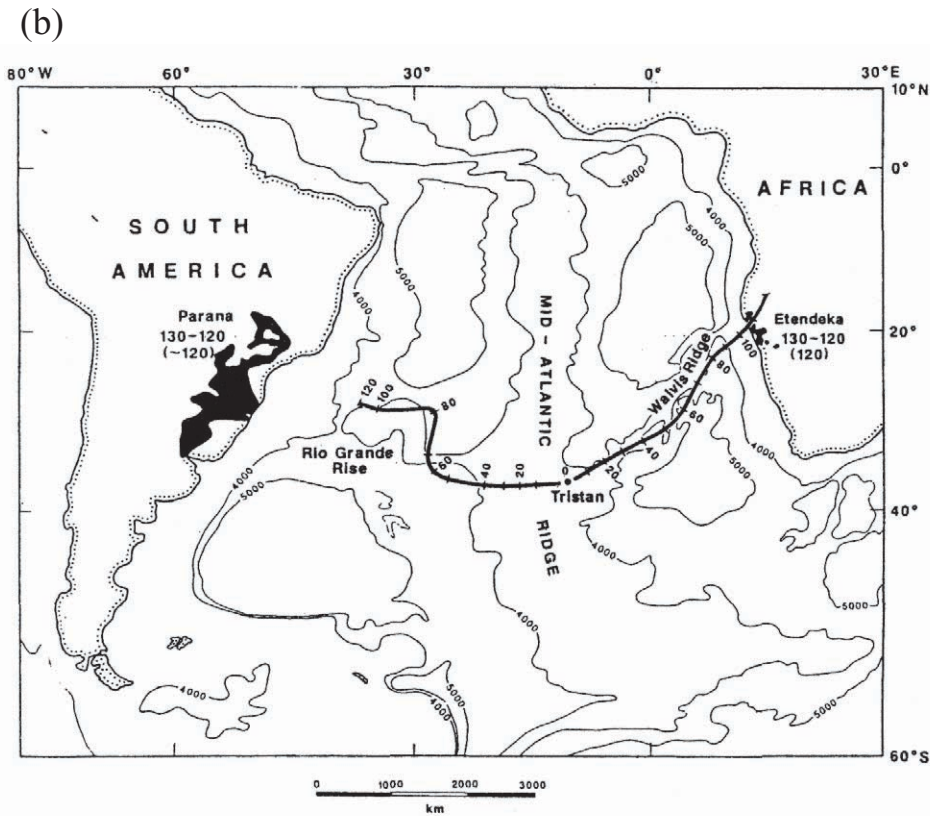


Fig. 16. Present configuration of the South Atlantic showing the thick volcanic ridges of the Rio Grande Rise and the Walvis Ridge produced above the mantle plume as the ocean opened. Hot-spot track is from *Duncan* [1984].

**Fig.II-1-2-2 Relationship of the continental breakup and the flood basalts**

The flood basalt occasionally accompanies the continental breakup. As the example, Paraná and Etendeka (*White and McKenzie*, 1989).



**Fig.II-1-2-3** Panoramic view of the lava flow in the Deccan Trap (Takahashi and Nakajima, 1997: The photographer is T. Fujii).  
The lava flow of the Deccan trap is horizontally piled, and it is seen the sedimentary rock in the distant view.

of alkaline basalt and picritic basalt. The chemical component of SiO<sub>2</sub> is generally 53 wt%. That is the transitional component to andesite, and poor in MgO, rich in FeO and TiO<sub>2</sub>. It means that flood basalt is differentiated more than MORB.

### 1-2-3 Genesis of the Flood Basalt

#### (1) Genesis of Flood Basalt Magma and Mantle Plume

Generally, flood basalt magma was considered to be formed from the high temperature mantle plume that upwelled to the shallow part of the upper mantle and partial melted the homogeneous mantle material on a large scale (McKenzie and Bickle, 1988, etc). For example, Richards et al. (1989) concluded that flood basalt was formed when the mantle plume head reached to lithosphere, and the mantle plume tail corresponded to the following activity of a hotspot.

With regard to the above genesis and activity of high temperature plume, there are two hypotheses. One is based on the traditional plate tectonics and the other is on the plume tectonics that have been suggested recently (Maruyama, 1994). In particular, the hypothesis based on the plume tectonics considers the generation of the plume and its nature from the viewpoint of material circulation of the interior of earth, and considers the activity of a hotspot and LIP.

#### a) Hypothesis about the Generation Mechanism of Mantle Plume

Based on the traditional plate tectonics hypothesis, the generation and activity of a high temperature mantle plume is considered to be the event on the surface of the earth. By this hypothesis, the mantle plume is a secondary event, the continental breakup and mantle convection occurred because of the conditions of lithosphere and upper mantle, and plate movement (Davies, 1988; Griffiths and Campbell, 1990; Hill, et al., 1992; Anderson, 1994a, b). Some researchers consider that the mantle does not move relatively from the viewpoint of the whole earth (Griffiths and Campbell, 1990).

On the contrary, the hypothesis that the mantle convection and plume from the deep part of mantle caused the continental breakup and the activity of large volumes of basaltic magma from a hotspot and LIP has been proposed. For example, White and McKenzie (1989) considered that the huge mantle plume that upwelled to the lower continental crust participated in the continental breakup, and the main part of the plume expanded the continental crust, and form from the rift zone to the crust of the marginal part of the continent.

#### b) Igneous Activity by Mantle Plume (On Hotspot)

Hotspot is known as the igneous activity that is related to mantle plume. Hotspot

participates to the forming of almost all flood basalt. The genesis and origin of hotspot are described follows:

### 1) Forming of Hotspot

A hotspot is considered to form by the upwelling (mantle plume) of a high temperature mantle material from the depth of the mantle. However, there are considerations about the forming of a hotspot that is formed by the ascending current by the small-scale convection within the upper mantle (White and McKenzie, 1995) and is formed by a local hot region within the upper mantle (Miyashiro, 1986; Anderson, 1989). These models are based on two layered mantle convection, and the origin of a hotspot is the boundary of the transitional zone between the upper mantle and lower mantle. The researchers who consider the whole mantle convection suggest that the plume of hotspot is generated from the layer of temperature boundary between the core and mantle. However, verification result of the whole mantle convection and the layered convection has not yet been obtained.

Almost all the active hot spots are considered to erupt basalt lava in the early stage of their activity (White and McKenzie, 1989; Coffin and Eldholm, 1994). Mantle plume is composed of plume head (several hundred to thousand kilometers in diameter) and plume tail (a circle of approximate 100 kilometers in diameter), and the plume head rises up several to several ten centimeters per year by the huge buoyancy. When the plume head reaches lithosphere, basaltic volcanic activity occurs with eruption of a huge volume of lava in a short period of about 1 My. The volcanic activity of the hot spot continues about 100 My by the plume tail to form a ridge and/or line of seamounts. Several low density masses (soliton) with different sizes are assumed within the plume. With regard to the upwelling velocity of soliton, the bigger it is the faster it is. When the plume reaches the shallow part of the upper mantle, since the magma temperature of the first activity is highest, the basalt igneous activity on a huge scale may be considered to occur in the early stage of the hotspot activity.

The style of hotspot activity is considered to markedly depend on the temperature, volume and components of the ascending mantle plume. The size of the temperature anomaly zone (plume head) below the hotspot is almost the same from the study by seismic wave tomography in Iceland and in the Azores, however, each volume of lava at surface differs.

### 2) Characteristics of the Hawaii Hotspot

The Hawaii hotspot maintains the same petrological characteristics during 70 Ma (K-Ar age of Suiko seamount of Emperor seamounts is 65 Ma). The mantle plume head 100 kilometers in diameter is observed in the shallow part of the upper mantle directly under the Hawaiian Islands. The sea bottom is shallower, being plume located, than that of the surrounding area. This swell is accompanied with plus gravity anomaly (plus Bouguer

anomaly) that is supported by the mantle plume. The low velocity layer of seismic wave is existed in the lower mantle under the Hawaii hotspot that is considered to be the mantle plume tail.

As the characteristics of volcanic activity, the chemical component and the effusive rate regularly change according to the development of the volcanic activity. Alkali olivine basalt erupts in the early stage of volcanic activity of the deep sea, and mainly olivine tholeiitic magma erupts on the surface in the same stage. In this stage, picritic magma with many olivine phenocrysts sometimes erupts. The differentiation series is alkali basalt => olivine tholeiite (picrite) => alkali basalt => hyper alkaline rock.

The Nd, Sr isotope component of the Koolau volcano of Oahu Island is closest to that of the primitive mantle. This volcano is tholeiitic basalt with  $\text{SiO}_2 \geq 53$  wt% and abundant in  $\text{SiO}_2$  (Fig. II-1-2-4).

Hauri (1996) proposed the idea that the melt by partial melting of peridotite that is the main component of the plume and basaltic component generates various magma that of the volcanoes of the Hawaiian Islands according to the mixing rates of volcanoes (Fig. II-1-2-5). It is difficult to explain by the traditional theory of homogeneous mantle plume melt that each magma component varies in spite of the close location of the volcano.

### c) The Generational Place of Mantle Plume

There are many opinions about the birthplace of mantle plume.

$\epsilon\text{Nd}$  value of much of the oceanic basalt and flood basalt is lower than that of MORB. Some of the primitive mantle shows  $\epsilon\text{Nd}=0$ . This value means that the source of the oceanic basalt and flood basalt is undifferentiated from that of MORB. The above also means the possibility that the source of the oceanic basalt and flood basalt is primitive materials of the lower mantle. That is, it is possible for the above source to be derived from the plume by upwelling from the upper mantle.

$^3\text{He}/^4\text{He}$  ratio of the volcanic glass and olivine phenocryst were measured. As the result, the high  $^3\text{He}/^4\text{He}$  ratio of the samples that were derived from the lower mantle is recognized by Kaneoka (1983).

The result of the high pressure experiment concerning the outer core and the lower mantle is shown in Fig. II-1-2-6.

According to Davis, 1990, the partial melted mantle materials in D'' layer near the boundary of the lower mantle and the outer core rise as the plume.

According to the high-pressure experiment of Boehler (1996), it was confirmed that the upper mantle does not melt while the outer core melts with the temperature of the boundary of the lower mantle and the outer core (Fig. II-1-2-6(b)).

In the case that a large quantity of hydrogen is contained, it is possible the temperature of



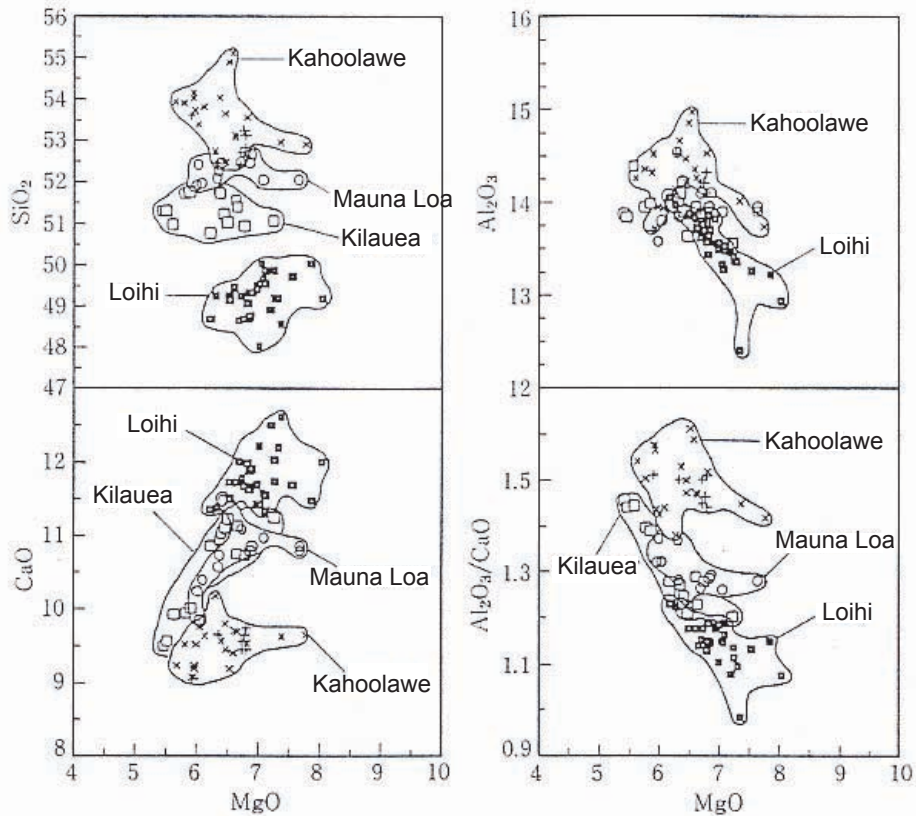


**Fig.II-1-2-4** Plots of SiO<sub>2</sub> vs.MgO, Al<sub>2</sub>O<sub>3</sub> vs.MgO, CaO vs.MgO Al<sub>2</sub>O<sub>3</sub>/CaO ratio vs.MgO for Hawaiian lavas (Frey et al., 1994)

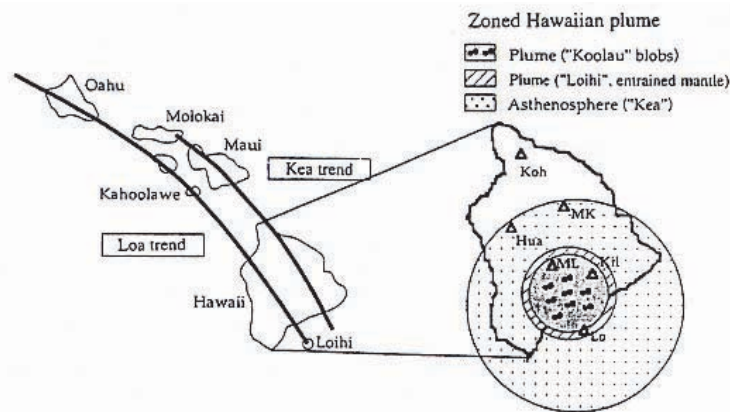


**FIG. 4** Schematic model of a zoned mantle plume beneath Hawaii; Loa trend and Kea trend are structural lineaments of volcanic shields identified previously<sup>51</sup>. The plume is zoned owing to the effects of thermal entrainment<sup>79</sup>. The centre of the zoned plume contains quartz eclogite blobs (Koolau component) in a peridotite matrix, while the outer zones consist of heated and entrained lower mantle (Loihi component), surrounded by passively upwelling (not heated) upper-mantle asthenosphere (Kea component). The passage of Loa Trend volcanoes over the plume centre causes them to have larger amounts of the Koolau component, whereas passage of Kea trend volcanoes over the periphery of the plume results in a larger proportion of the upper-mantle Kea component in these volcanoes<sup>53</sup>. Abbreviations for volcano names: Hua, Hualalai; others as in Fig. 3.

**Fig.II-1-2-5** Schematic model of a zoned mantle plume beneath Hawaii (Hauri, 1996)

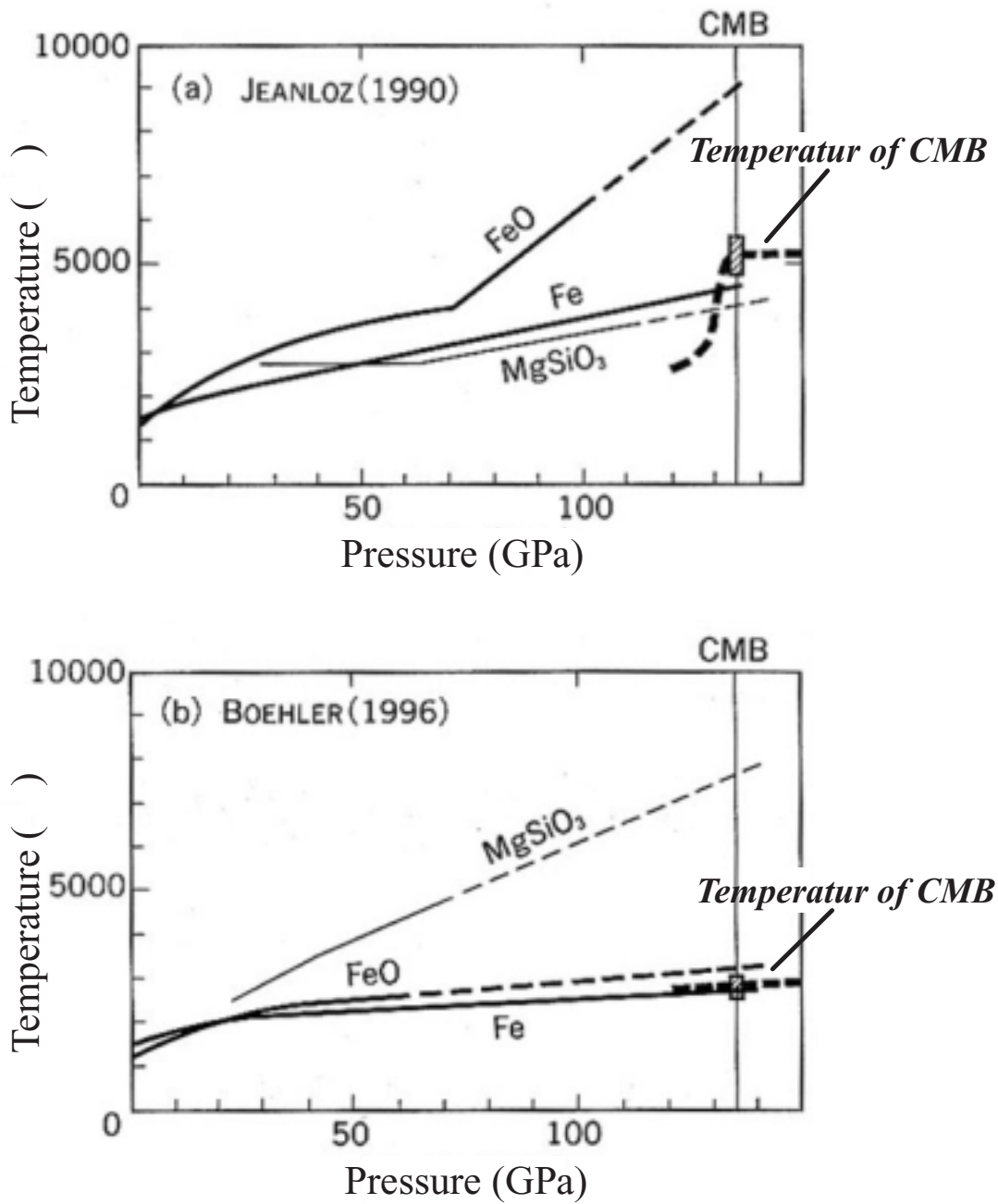


**Fig.II-1-2-6 Experimentally determined melting characteristics of core (Fe, FeO) and lower mantle material (MgSiO<sub>3</sub>; perovskite)**  
 CMB means "border of core and mantle". Broken and slash lines show temperature of the boundary of core and mantle ((a): Jeanloz (1990), (b): Boehler (1995)).

the outer core could be considerably lower than the traditional model (Takahashi et al., 1998). 3,000 to 4,000 degree Celsius appears proper according to a recent experiment.

Therefore, there is no necessity that the mantle plume rises from the border of the outer core and the lower mantle (Takahashi and Nakajima, 1997).

There is a theory that the super-plume upwells from the border of the outer core and the lower mantle and form the flood basalt or ocean plateau. this theory is suggested by the chemical component of HIMU basalt and the characteristics of it's isotope (Tatsumi, 1998).

#### d) Recycling of Materials in the Inner Earth

On the contrary to mantle plume, mantle convection is the work to the interior of earth. The oceanic plate is generated in the mid-oceanic ridge and subducts in the margin of the continent (Fig. II-1-2-7(a)).

Fukao et al., (1992) confirmed by using a seismic wave that the oceanic plate subducts to the depth of approximately 670 kilometers of Izu/Ogasawara and lies there. At the same time, he also confirmed that a part of the slab subducts into the lower mantle. The mantle convection is temporarily forced to stop by the phase change of peridotite at the discontinuity layer of a seismic wave of 670 kilometers. However, the stayed slab rapidly begins to fall to the boundary of the core and the mantle (Tackley et al., 1993; Honda et al., 1993).

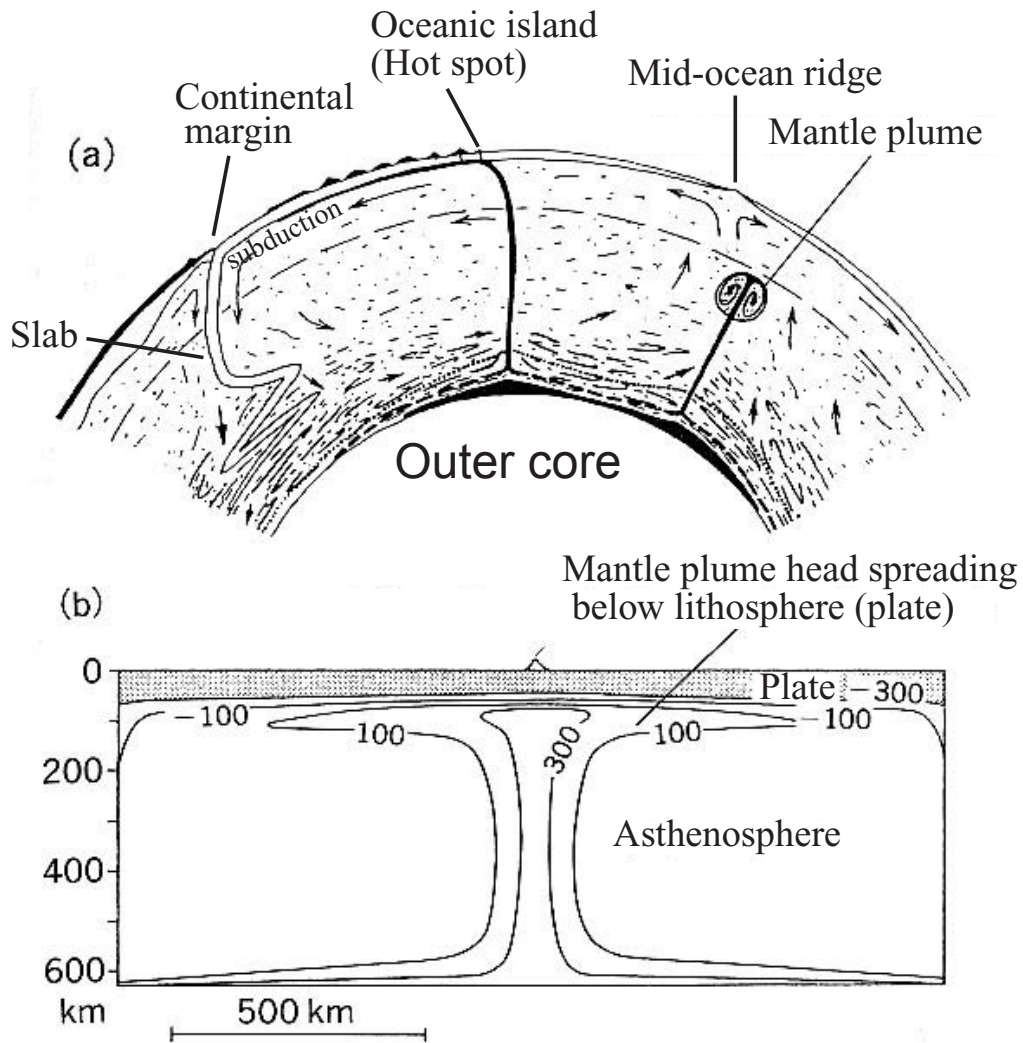
#### (2) Generation Model of the Flood Basalt by Homogeneous Mantle Plume

The study of the generation process of basalt magma is based on the melting model that is assumed for homogeneous mantle materials (McKenzie and Bickle, 1998 etc). Besides the above model, the generation model from picritic magma by crystallization differentiation is considered to apply to the whole flood basalt (Cox, 1980).

White and McKenzie (1989) considered the generation model of flood basalt magma by using the model of a homogeneous and high temperature mantle plume whose component is like pyrolite. The above model is shown in Fig. II-1-2-8. The explanation of the model is as follows.

- The mantle plume that is generated at the bottom of the upper mantle rises up. The difference of temperature between the plume and surrounding mantle is approximate 300 degrees Celsius at the bottom of the lithosphere. According to the simulation and laboratory experience, the head of the ascending flow appears like a huge mushroom-shaped cloud (Fig. II-1-2-7(b)).
- Picrite magma is generated from peridotite with a high temperature more than 1,500 degrees Celsius within the plume.





(a) Model of convection and plume in the mantle.  
(Davies, G.F. (1990))

(b) Temperature variations seen in cross-section through the Cape Verde Swell from the best fitting axisymmetric convection model of Courtney and White (1986). Temperature anomalies are labeled in degrees Celsius with respect to the mean asthenosphere temperature. Note the narrow central rising plume and the broad mushroom-shaped head of hot material deflected laterally by the overlying plate. (White, R. and McKenzie, D. (1989))

**Fig.II-1-2-7 A schematic model of the convection in the mantle**

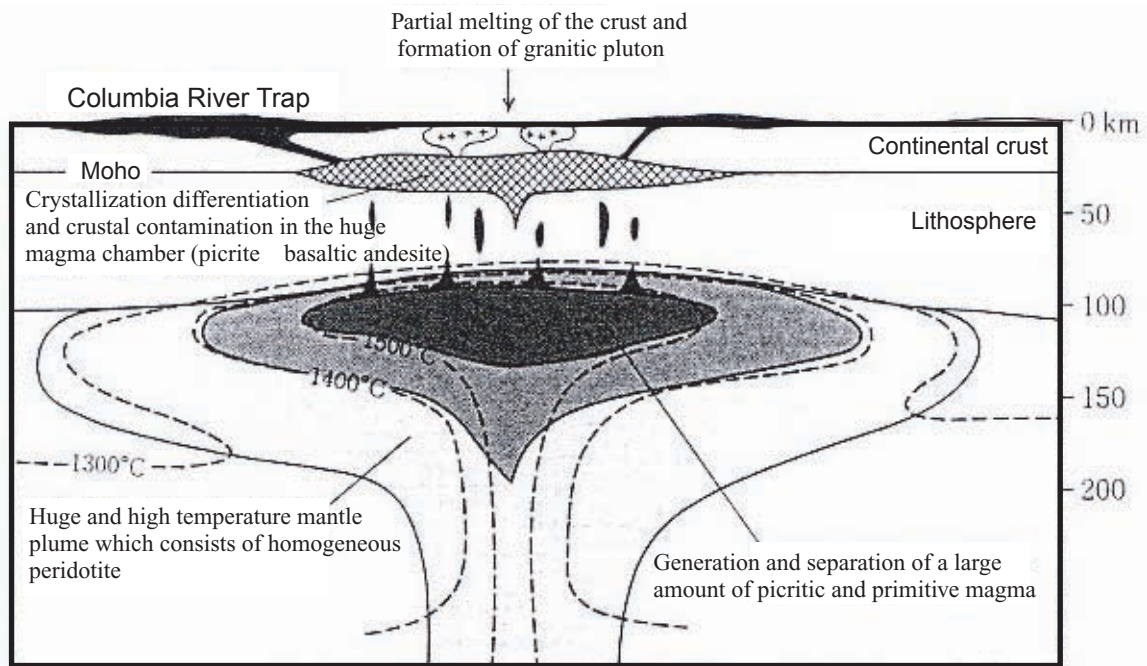


**Fig.II-1-2-8** A schematic model of homogeneous plume head for magma generation through study of the Columbia River flood basalts

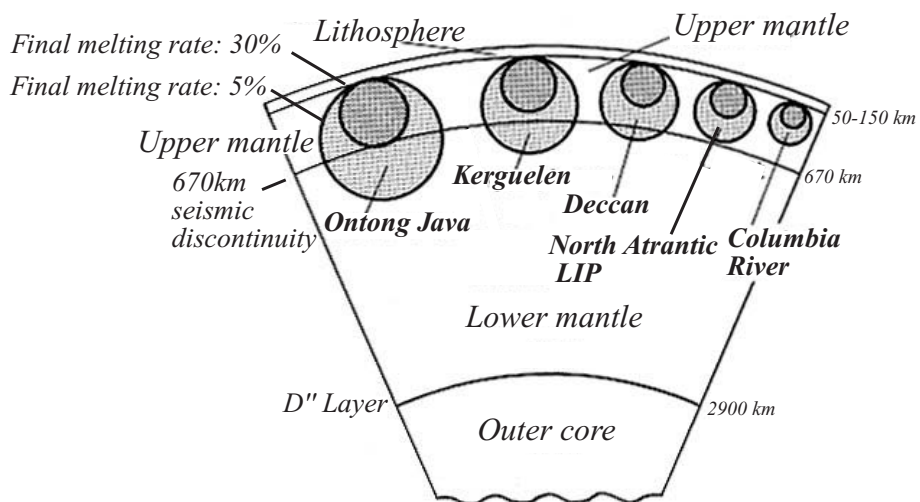


**Fig.II-1-2-9** Volume of plume heads calculated on the basis of McKenzie's model (McKenzie and Bickle, 1988)

The volume of them is shown as the section of the sphere before spreading at the bottom of lithosphere (From Coffin and Eldholm, 1994).

- Picrite magma separates and rises up from peridotite to form a huge magma reservoir in the under part of the continental crust (assuming at the depth of Moho discontinuity of the North American continent).
- Fractional crystallization progress within the magma Chamber. And, flood basalt magma is generated by the contamination with a huge volume of the crust materials

### (3) Problem of Generation Model of the Flood Basalt by Homogeneous Mantle Plume

Many problems are pointed out in the generation model of flood basalt by homogeneous mantle plume.

The chemical component of a mantle material like pyrolite is assumed in McKenzie and Bickle (1988). In this model, the volume of generated magma and its chemical component is decided by according to obtain initial temperature of the mantle upwelling. However, with application of peridotite melting model to the mantle plume that generate flood basalt on a large scale, it is pointed out that an illogically high temperature plume or unrealistic volume of plume becomes necessary.

For example, the calculated volume of mantle plume head (estimated size of mantle plume that was supplied LIP), that is based on the melting model of a homogeneous mantle with the volume of the existing basalt plateau and oceanic plateau, becomes 1,000 kilometers in diameter. The plume with a 1,000 kilometers diameter within the mantle with thickness of 2,900 kilometers is unnatural (Coffin and Eldholm, 1994: Fig. II-1-2-9).

In the case of the application of the same model to the volcanic activity of the Hawaii hotspot, the potential temperature of the plume is estimated to be approximately 1,560 degrees Celsius (Watson and McKenzie, 1994). The potential temperature of the upper mantle that locates below the mid-oceanic ridge, considering the generation temperature of MORB, is globally approximately 1,280 degree Celsius (McKenzie and Bickle, 1989). The above estimated temperature is higher by approximately 300 degrees Celsius than the potential temperature of the upper mantle. The magma that is generated by partial melting of a very high temperature plume and the partial melting of mantle becomes komatiite (Takahashi, 1996; Fig. II-1-2-10). Picrite magma is generated by the melting of mantle peridotite in the high temperature hotspot, however, almost all the flood basalt is tholeiitic.

It is necessary to remove MgO by crystallization differentiation of olivine and pyroxene for generating from peridotite and erupting MgO poor lava to the surface from the primitive and MgO rich basalt magma. But, a remarkable cumulate layer has not been recognized below the flood basalt by seismic prospecting.

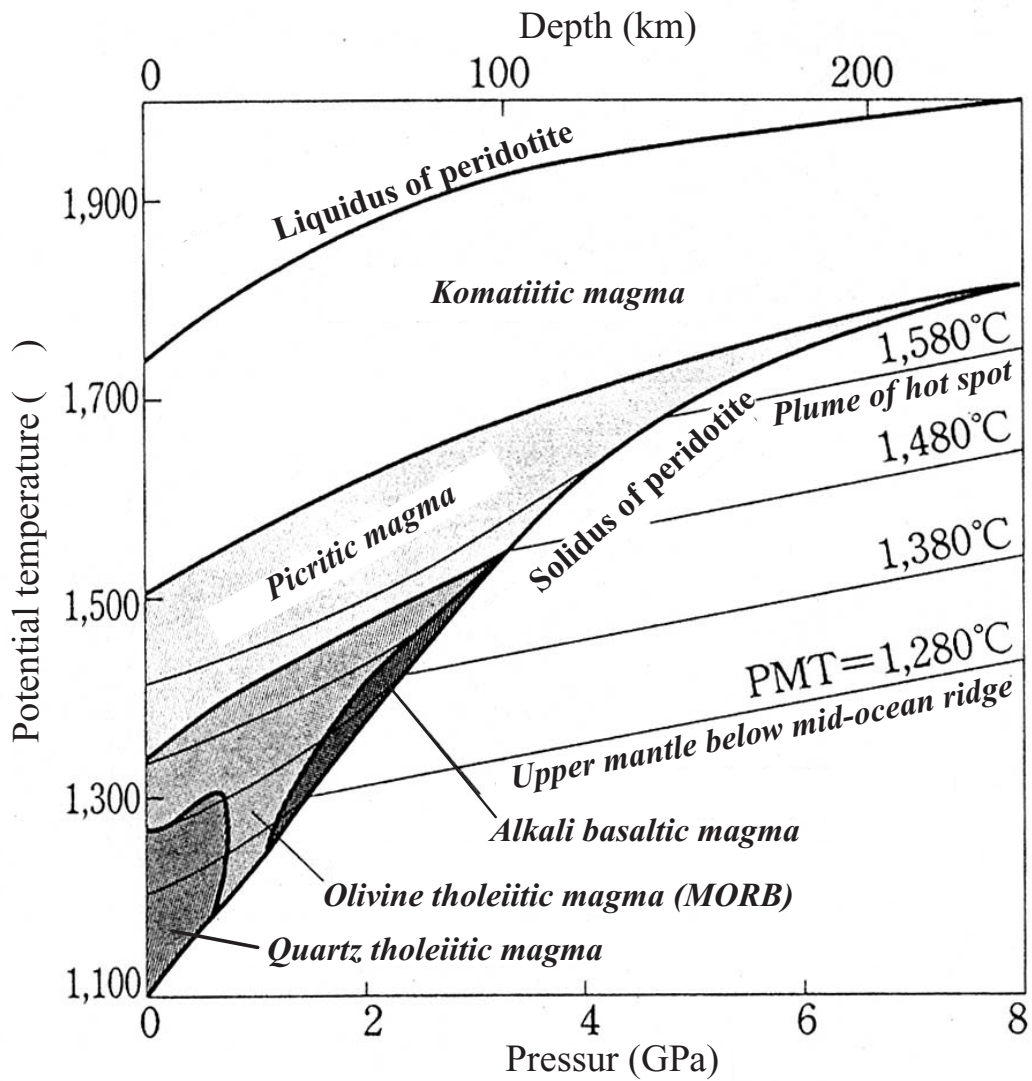


**Fig.II-1-2-10 Magma types generated by adiabatic decompressional melting of peridotite (Takahashi, 1996).**

PMT means the mantle potential temperature.

#### (4) Generation Model of the Flood Basalt by Assuming Heterogeneous Mantle Plume

The traditional model of mantle melting by homogeneous mantle plume cannot explain all the characteristics of flood basalt. Takahashi et al. (1998) proposed the generation model of flood basalt by heterogeneous mantle plume through his study of flood basalt.

##### a) Characteristics of the Columbia River Flood Basalt

The huge Yellowstone hotspot is considered to have participated in the initial activity to form the Columbia River flood basalt (Pierce and Morgan, 1993). The facies of the initial activity that is the Grande Ronde series basalt occupy 80 vol% of the total amount of eruption (Fig. II-1-2-11). The generated age of the Grande Ronde series basalt is 16-15 Ma and the SiO<sub>2</sub> content is 54-56 wt% that is basaltic andesite. The erupted amount is 2 x 10<sup>5</sup> km<sup>3</sup> and all the rocks are completely aphyric lava.

The facies of the latter half activity is basalt to dacite of the Saddle Mountain series. The period of the formation of the Saddle Mountain series is after 9 Ma.

The chemical component of the Columbia River flood basalt was described by Wright et al. (1988). The characteristics are as follows (Fig. II-1-2-12):

- More than 80 percent of the volume of the Columbia River flood basalt is basaltic andesite with 54 to 56 wt% of SiO<sub>2</sub> content. Compared to the components of primitive MORB, the average SiO<sub>2</sub> content is 4 wt% higher, the content of MgO is lower and rich in FeO. The chemical component of the Grande Ronde series basalt concentrates in narrow range considering its erupted volume.
- For MgO content, the component alternation trend of major and minor elements shows straight feature. This trend indicates that the chemical component of pre-eruption magma was controlled by crystallization of Al rich clinopyroxene that was stable only under the high pressure (Fig. II-1-2-12).

For the purpose of explanation of the high SiO<sub>2</sub> content in the Grande Ronde series basalt, not only the crystallization differentiation of olivine and pyroxene but also the contamination of the crust must be considered. Therefore, assuming the huge magma reservoir between the mantle plume head and the surface, in the magma reservoir the contamination of crust, including melting of the ceiling of the chamber, must be considered to progress at the same time as the constant crystallization.

Assuming the magma chamber on a large scale, although the magma must contain a large quantity of phenocrysts at the stage of crystallization differentiation, all the lavas are aphyric.



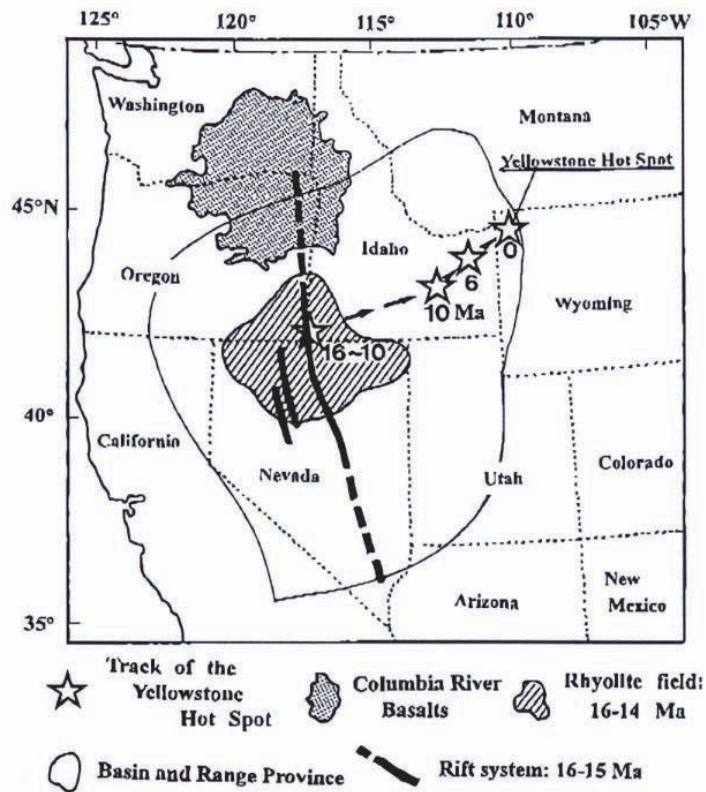


Fig. 1. Map showing the distribution of the Columbia River basalts (CRBs) and track of the Yellowstone hot spot. According to Pierce and Morgan [14], activity of the CRBs started due to the arrival of gigantic plume head of the Yellowstone hot spot ca. 16 Ma ago. The plume hit the boundary between Oregon, Idaho and Nevada where rhyolite volcanism occurred due to crustal anatexis. Much of the basalt magmas, however, traveled to the north through 1000 km long NS rift system and drained at the boundary between Washington and Oregon States. Simplified after fig. 1 of Pierce and Morgan [14].

Fig.II-1-2-11 Distribution of the Columbia River basalts and track of the Yellowstone hot spot

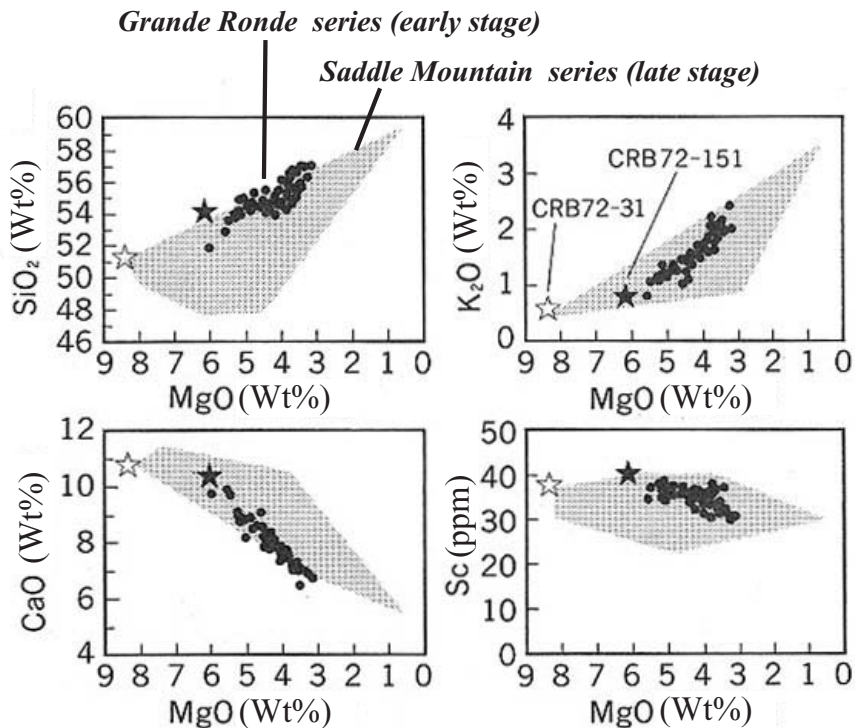


Fig.II-1-2-12 Feature of geochemical composition of the Columbia River flood basalts

CRB72-151 is the MgO-rich Grande Ronde series. CRB72-31 is the Saddle Mountain series which show similar geochemical composition of primitive MORB (Wright et al., 1988).

## b) Melting Experiment of the Columbia River Flood Basalt

The following knowledge has been obtained by the melting experiment of the Columbia River flood basalt. The result of the experiment by Takahashi et al. (1998) is shown in Fig. II-1-2-13.

The melting experiment under high temperature and high pressure for several kinds of Columbia River flood basalt that were initial materials was carried out. As the result of the experiment, the components of the melts that generated by the partial melting of the initial basaltic materials entered the region of andesite to basaltic andesite components ( $\text{SiO}_2$ : 54-60 wt%).

In the case that the initial material was almost similar to the primitive MORB (CRB72-151: the Grande Ronde series, CRB72-31: the Saddle Mountain series: Table II-1-2-3), it became obvious that the melt that corresponds to the chemical component and components of the main and trace elements was generated under the conditions of the pressure of approximate 2 GPa (corresponds to the depth of 60 km), the temperature range of 1300 to 1350 degrees Celsius and 30 to 50 vol% of partial melting (Fig. II-1-2-13).

Wright et al. (1988) considered that the chemical component of the magma of pre-eruption was on the control line of Al rich clinopyroxene from the characteristics of the chemical components of the Grande Ronde series basalt, however, almost all the residual materials of the experiment were Al rich clinopyroxene under the condition (2GPa, 1300-1350 degrees Celsius) that generates a melt similar to the Grande Ronde series basalt. The result of the experiment corresponded to the hypothesis of Wright et al. (1988)

The Grande Ronde series basalt must be generated from remarkably differentiated magma by the traditional model of homogeneous mantle plume. Assuming the initial magma with  $\text{MgO}=20$  wt%, the Grande Ronde basalt magma ( $\text{MgO} \leq 6$  wt%) must be considered the residual liquid after crystallization of 50 vol% of initial magma. Furthermore, the partial melting of mantle on a large scale and generation of a large volume of magma is necessary to generate Grande Ronde series basalt, however, the magma volume is decided by the potential temperature of upwelling mantle materials. The potential temperature must rise approximately 1200 degrees Celsius to 1500 degrees Celsius to increase the final volume of melting of mantle peridotite 10 vol% to 30 vol% (Iwamori et al., 1995). The picrite magma with  $\text{MgO}=20$  wt% or more, or the MgO rich komatiite magma must be generated within the mantle plume of adiabatic upwelling by approximately 1500 degrees Celsius (Takahashi et al., 1993: Fig. II-1-2-14).

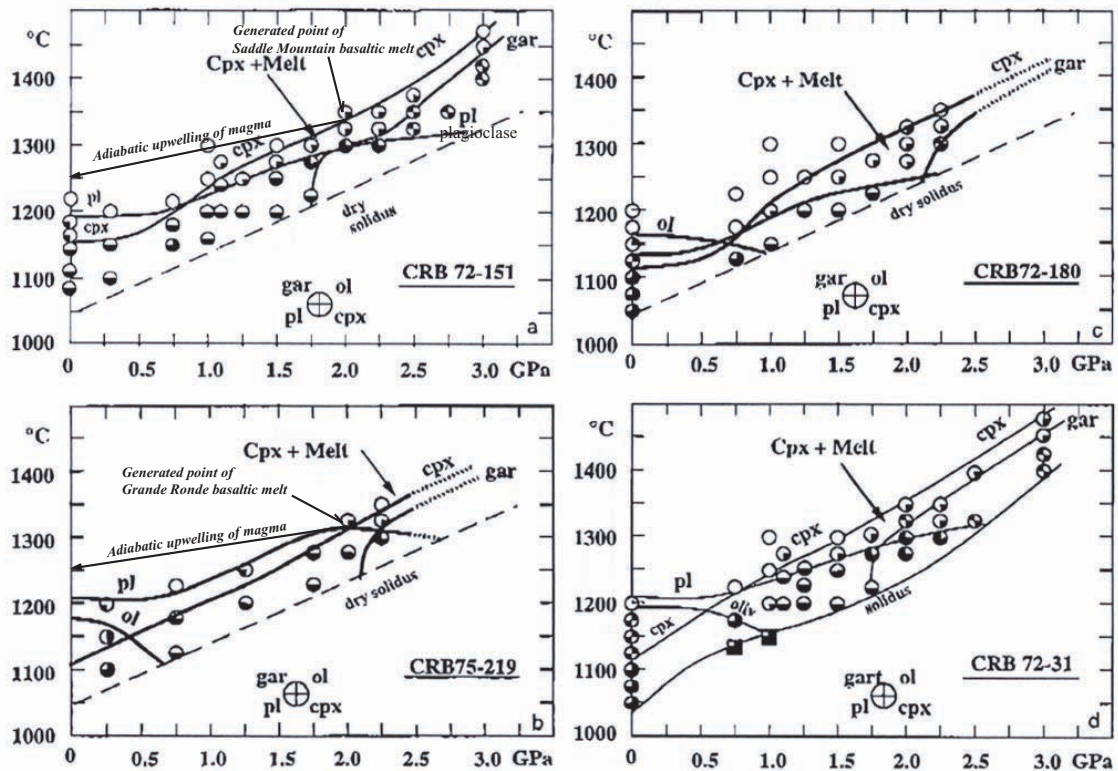


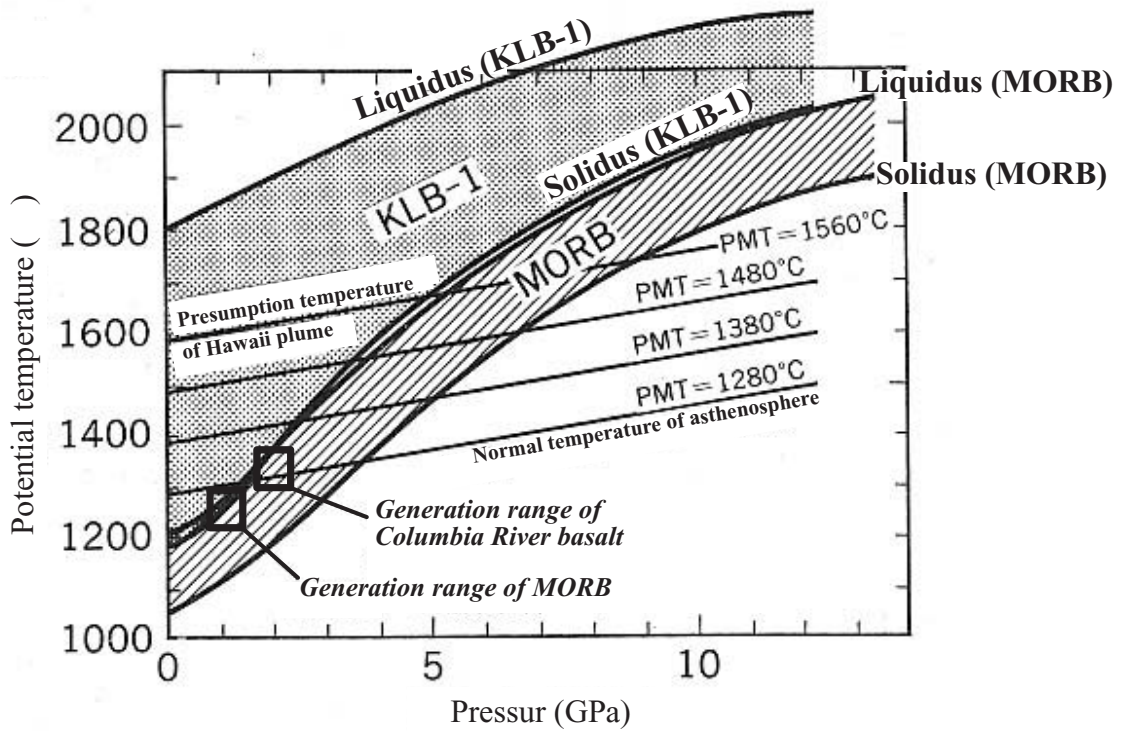
Fig. 3. (a)–(d) Melting phase relations on four representative Columbia River basalts listed in Table 1. Except for CRB75-219, clinopyroxene is the liquidus phase at pressures between 1 and 3 GPa (shaded area). The second liquidus phase changes from plagioclase to garnet at pressures around 2 GPa. Because of the steep  $dT/dP$  slope of the clinopyroxene liquidus, magmas formed at high pressures should be considerably superheated if they ascend and erupt rapidly [arrow in (d)]. This is consistent with voluminous eruption of totally aphyric lavas in the Grande Ronde stage of CRBs [42].

Fig. II-1-2-13 Melting phase relations on the Columbia River basalts listed Table II-1-2-3 (Takahashi et al., 1998)

Table II-1-2-3 Composition of starting materials of melting experience (Takahashi et al., 1998)

	CRB72-151 (a) Grande Ronde	CRB75-219 (b) Grande Ronde	CRB72-180 (c) Wanapum	CRB72-31 (d) Saddle Mt.	Av. N-MORB Mid Atlantic 49–52°N	Av. P-MORB Iceland
SiO <sub>2</sub>	53.80	51.52	49.17	50.76	50.54	48.83
Al <sub>2</sub> O <sub>3</sub>	15.19	14.98	14.45	16.02	16.38	14.48
FeO*	9.40	11.83	13.91	9.52	8.90	12.63
MgO	6.12	5.96	5.70	8.23	7.80	7.57
CaO	10.09	9.71	8.94	10.77	11.62	11.69
Na <sub>2</sub> O	2.88	2.76	2.54	2.29	2.79	2.16
K <sub>2</sub> O	0.69	0.60	1.01	0.39	0.09	0.17
TiO <sub>2</sub>	1.13	1.70	3.15	1.48	1.31	1.71
P <sub>2</sub> O <sub>5</sub>	0.26	0.32	0.65	0.19	0.13	0.18
MnO	0.16	0.18	0.19	0.14	0.16	0.2
Total	99.72	99.56	99.71	99.79	99.72	99.62





**Fig. II-1-2-14** Liquidus and solidus for a fertile peridotite (data: Takahashi, 1986) and primitive MORB (data: Yasuda, et al., 1994; Takahashi et al., 1998) under dry condition. Estimated site for the GR magma genesis (2GPa, 1350 °C) is located almost on the average asthenospheric mantle adiabat (PMT=1280 °C). Even considering the necessary latent heat the plume temperature for the Columbia River basalt may be PMT=1350 °C which is surprisingly lower than current temperature estimate for mantle plume. (Takahashi, 1997)

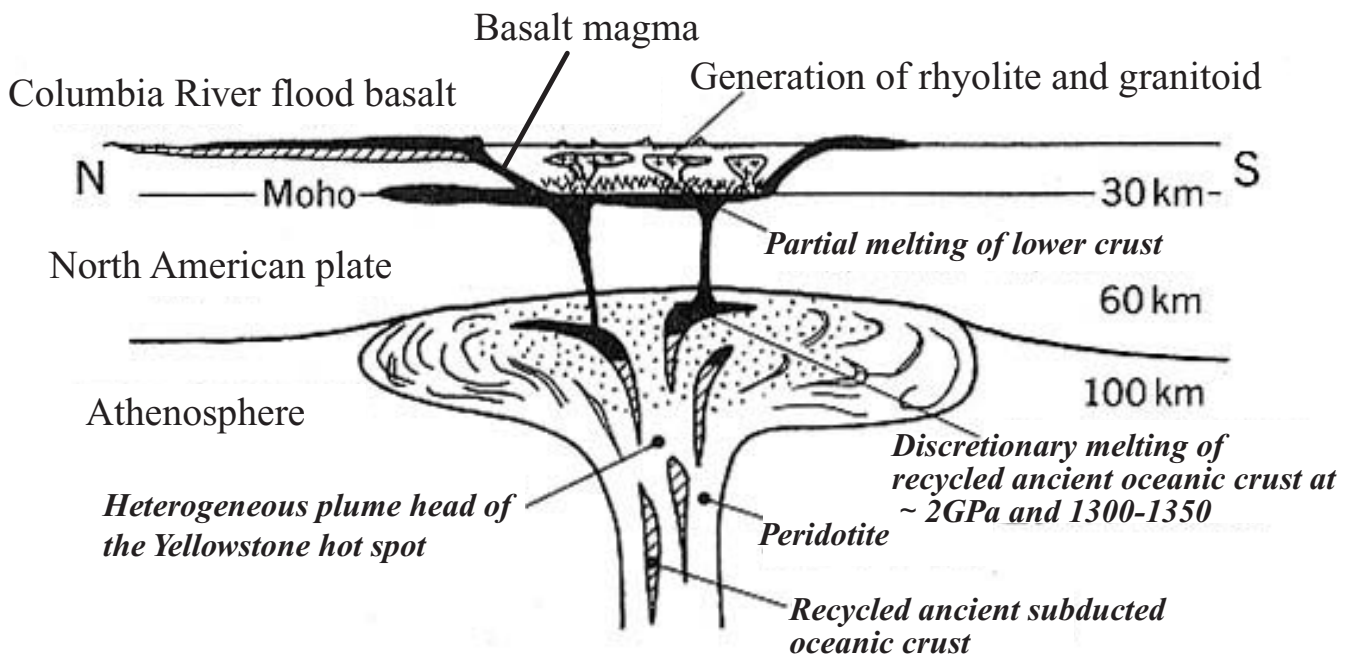


**Fig. II-1-2-15** A model for heterogeneous mantle plume head for the initial stage of the yellowstone hot spot (Takahashi et al., 1998)

## (5) Generation Model of the Flood Basalt by Heterogeneous Mantle Plume

### a) Application of Heterogeneous Mantle Plume Model to Columbia River Flood Basalt

The picrite magma that is generated by partial melting of mantle peridotite under the conditions of high pressure and high temperature is the original magma of flood basalt by the traditional model of flood basalt generation (Cox, 1980 and so on). However, it is difficult to explain the following two points: why basaltic andesite magma of large volume only erupted and why all of them are aphyric.

A new model for the generation of flood basalt has been proposed (Yasuda et al., 1994: Fig. II-1-2-14). The model is based on the high pressure melting experiment of MORB. Because the melting temperature of MORB (liquidus) is lower than the starting temperature (solidus) of melting of mantle peridotite under any pressure conditions, flood basalt is generated by the selective melting of the basalt component which is included in the mantle plume

Assuming that flood basalt is generated by the melting of the MORB component, the genesis of the Grande Ronde series basalt, that is markedly rich in SiO<sub>2</sub>, can be explained, because the melt that is generated by the basalt component contains much more SiO<sub>2</sub> than the melt that is generated by peridotite. Moreover, assuming the adiabatic ascending of the magma that is generated by partial melting of MORB under high pressure that is more than 2 GPa, the magma becomes the superheating condition (more than 1250 degrees Celsius) when the magma reaches the surface, because the viscosity is low and aphyric lava is formed at the time of eruption (Fig. II-1-2-14). This is a reasonable explanation.

As mentioned above, the proposed new model is that the mantle plume of Columbia River flood basalt generation is not the traditional model of the ascending of very high temperature and homogeneous peridotite, but the ascending of peridotite of a comparatively low temperature including a large volume of MORB that is subducted oceanic crust. The model of Columbia River flood basalt generation by heterogeneous mantle plume is shown in Fig. II-1-2-15.

Based on this model, the estimated temperature of the mantle plume is lower than that of the traditional model and approximately 50 degrees Celsius higher than the potential temperature of asthenosphere that is estimated by the conditions of MORB generation. The condition of 1325 degrees Celsius and 2.0 GPa for the generation of Grande Ronde series basalt was obtained. This condition corresponds to the final condition of the place that the magma separated after the adiabatic upwelling of mantle plume forming magma. Therefore, in conclusion, the heterogeneous mantle plume that generated the Columbia River flood basalt stopped upwelling at a depth of approximately 60 kilometers, and selectively melted mainly MORB component to generate tholeiitic basalt magma.

The important factor for the decision of the generation volume is the volume of the oceanic crust component. Therefore, the generation of flood basalt from the low potential temperature mantle plume is considered to be possible.

The original material that is similar to MORB shows an age older than 1 Ga by the isotopic ratios of Sr, Nd and Pb of Grande Ronde series basalt (Hooper and Hawkesworth, 1993). It is considered that the old oceanic crust which had subducted to the interior of earth upwelled by the plume activity accompanied with the beginning of the Yellowstone hotspot activity. In the hypothesis of Ringwood (1994), the subducted oceanic crust is stored in the seismic discontinuity layer at a depth of 670 kilometers, and the oceanic crust is locally heated by the upwelling from the lower mantle, and ascends to the shallow part of the mantle as plume.

If the hotspot participates in the generation of flood basalt, the ascending of the component of the old oceanic crust that is stored within the earth plays an important role. If MORB component itself is conveyed by plume, it is highly possible that plume generates near the seismic wave discontinuity layer at the depth of 670 kilometers that is a lower temperature, not in the boundary between the outer core where the differentiation by melting processes and the lower mantle (Takahashi, 1996).

#### b) Application Heterogeneous Plume Model to Other LIP and Hotspots

There is a possibility that the activity of heterogeneous mantle plume or a plume with different components participate in the generation of flood basalt, hotspots, ocean ridges and ocean plateaus of the world.

That the basalt of the Hawaii hotspot is richer in FeO and SiO<sub>2</sub> than the partially melted liquid of non-differentiated mantle peridotite which is similar to phyrophanite is pointed out (Hirose and Kushiro, 1993; Kushiro, 1996). The model, in which the tholeiitic basalt magma, that formed the shield volcanoes of Hawaii, is generated by mixing between of SiO<sub>2</sub> rich melt which is formed by the melted oceanic crust included in mantle plume and melt of generated by partial melting of peridotite, is proposed as an example of the activity of heterogeneous mantle plume (Hauri, 1996). There is a report that the recycled slab is included within the Hawaii plume that was generated approximately 1.5 Ga by Pb isotope age (Silver et al., 1998).

Some believe that the reason for the high La/Sm ratio in the Azores hotspot where the degree of partial melting must be higher compared to N-MORB, is the effect of subducted continental crust and the components of sedimentary rocks (Schilling et al., 1985; Schilling, 1985). E-MORB that is contaminated by plume component differs from N-MORB in isotopic ratio. The E-MORB of Iceland and the Azores hotspot is higher in <sup>87</sup>Sr/<sup>86</sup>Sr ratio than N-MORB. On the contrary, the <sup>143</sup>Nd/<sup>144</sup>Nd ratio of it is generally low.

The isotopic characteristics as the example of the activity of mantle plume with the different component of the basalt of Polynesia, and of ocean islands around Africa, whose isotopic components of Pb, etc. has the characteristics of HIMU is explained by recycled slab components (Zindler and Hart, 1986). However, the characteristic of the major elements is that they are rich in Fe, and markedly poor in SiO<sub>2</sub> which is different from Hawaii (Kogiso et al.,

1997). These original materials of such HIMU basalt are possibly different from the Hawaii hotspot, and there is the hypotheses that the main composition of the mantle plume that generates HIMU basalt of the ocean islands is meta-peridotite (Super plume). The meta-peridotite was generated by the melting and differentiation of the subducted oceanic crust to the D'' layer that is the boundary of the core and mantle (Tatumi, 1995).

The example of the application of the heterogeneous mantle plume model to the LIP of the world by Takahashi et al., (1998) is shown in Table II-1-2-4. Takahashi et al. (1998) explains the LIP generation of the world by the difference of the potential temperature of heterogeneous mantle plume and the final position of stoppage of the plume.

In the case of the Hawaii hotspot, it is considered that the Hawaii basalt is generated by partial melting of not only MORB component but also both the mantle plume and mantle peridotite because of the high potential temperature of the mantle plume and mixing with each other.

Almost all the basalt of the ocean island is alkali basalt. The reason can be explained by the high potential temperature of the plume.

Iceland is an active hotspot volcano the same as Hawaii. Because it is located just above the Mid-Atlantic ridge, mantle plume can upwell adiabatically near the surface. In the case, where the lowest potential temperature (PMT=1280 degrees Celsius: the potential temperature of asthenosphere) is considered, not only the MORB component but also a considerable volume of peridotite melt, and the magma that has a higher content of FeO and elements to concentrate in liquid than the ordinary MORB and similar to E-MORB is generated.

Because of no lithosphere in the axis of the mid-ocean ridge, the whole mantle plume upwells to the surface. Because the mantle plume goes up to a shallower part, the mantle plume becomes a very high temperature by the decompression effect. As a result, the large volume of melt is generated, and a huge ocean plateau is formed. There are some oceanic plateaus that were formed during 20 to 30 Ma, but are not accompanied by a volcanic line that indicates the following volcanic activity, which is different from hotspots (i.e. Manihiki plateau, etc.). This is probably because such oceanic plateaus were formed by the interaction of the high temperature anomaly part in the upper mantle and the mid-oceanic ridge.

#### 1-2-4 Activity of the Flood Basalt and PGE Mineralization

Almost all PGE concentrated within the core in the initial stage of the earth. Moreover, because it fundamentally concentrates in solid phase, it is rarely contained in the continental crust where the differentiation has been progressed (Table II-1-2-5). Therefore, it is reasonable that the PGE in flood basalt is of mantle origin. In the period of the forming of flood basalt, a

**Table II-1-2-4 Variety of the magma expected from the heterogeneous mantle plume model.**

<p style="text-align: center;">Lower ↑ 1300°C</p> <p style="text-align: center;"><b>Potential temperature of plume</b></p> <p style="text-align: center;">↓ Higher 1400°C</p>	<p>Shallower ← <b>Final depth of plume</b> → Deeper</p> <p>0 km ---                      --- 50 km ---                      --- 100 km</p>		
	<p><b>MORB</b></p> <p>olivine tholeiite</p>	<p><b>Columbia River flood basalt</b></p> <p>basaltic andesite</p>	<p><b>Oceanic island basalt</b></p> <p>alkali basalt</p>
	<p><b>Iceland</b></p> <p>Fe rich olivine tholeiite</p>	<p><b>Deccan flood basalt</b></p> <p>Fe rich olivine tholeiite</p>	<p><b>Hawaii shield volcano</b></p> <p>Fe, K and Ti rich olivine tholeiite</p>

**Table II-1-2-5 Abundance of some transitional metals in earth and planetary materials (Naldrett, 1989)**

(ppm)

	Fe	Ni	Pd	Ir	Pt
Carbonaceous chondrites (Planetary system)	270,000	16,000	0.545	0.540	1.02
Total earth (32.4% of core + 67.6% of mantle)	334,000	30,000	1.25	1.14	2.79
Earth's crust	50,000	75	0.001	0.001	0.005
Earth's mantle (Alpine peridotite)	60,000	2,500	0.013	0.006	0.073
Earth's core (Iron meteorites)	907,000	88,000	3.82	3.53	8.45

huge volume of magma was generated compared to the period of ordinary igneous activity. Consequently, melt on a large scale occurred and there is a possibility that PGE, which ordinarily concentrates in the solid phase, may be relatively highly concentrated within the melt.

Therefore, it seems to be most appropriate to consider that the origin of flood basalt with PGE mineralization is the magma that is of mantle plume origin and was generated by large scale partial melting of the plume itself and the surrounding mantle material.

However, the above condition can apply to the general LIP. Factors, such as the supply of silicate component and sulfur, and regional tectonic setting, seems to be more critical for the PGE concentration.

## 1-3 Noril'sk Cu-Ni-PGE Deposits and Key Factors in Their Exploration

### 1-3-1 Introduction

The Noril'sk region at the northwest margin of the Siberian Platform hosts several world-class orthomagmatic copper-nickel-PGE sulfide deposits. These deposits were discovered in the 1920's and are an important source of nickel and PGE supply for Russia and also for the world. It is well known that orthomagmatic sulfide deposits are accompanied by mafic to ultramafic magmatic activities and these exist in various geological environments (Table II-1-3-1). In these deposits, the Noril'sk deposits are classified into the type associated with flood basalts. In this type, the deposits are not only the biggest but also the only in operation in the world. Therefore, the deposits give the only model for the copper-nickel-PGE mineralization that is the survey target in the Parana basin area, which has the same geological environment as the Noril'sk region.

The Noril'sk deposits are hosted in the differentiated intrusions which belong to the Siberian flood basalts (Siberian trap), and the probable nickel ore reserves are equal to the deposits at Sudbury (Fig. II-1-3-1). Some 6,200 tons of PGE reserve is next to the Bushveld Complex and the Great Dike (Table II-1-3-2). The ore is characterized by high concentration of palladium, and the ratio of platinum and palladium is almost 1 : 3. The supply of palladium from the Noril'sk deposits reaches 60 % of the world demand, therefore the supply from the deposits is important for the world market.

In this survey, in order to clarify the key factors in the exploration of the "Noril'sk style deposits", documents regarding to the Noril'sk deposits were collected and analyzed, in a part of the existing data analysis.

### 1-3-2 Outline of Geology

The outline of geology and geological structure of the Noril'sk region are shown in Fig. II-1-3-2 and Fig. II-1-3-3, respectively. The Noril'sk region is located in the northwestern end of the Siberian platform. The geology is characterized by the volcanic sequence belongs to Siberian flood basalts whose thickness exceed 3,500 meters. The volcanic rocks of 2 to 3 x 10<sup>6</sup>km<sup>3</sup> erupted in the area of 3.4 x 10<sup>5</sup> km<sup>2</sup>. The region is one of the biggest basalt exposed area in the world. These basaltic rocks are overlying the Paleozoic sedimentary rocks whose thickness is approximately 5,000 meters and the Proterozoic basement rocks (granite, granitic gneiss, schist and amphibolite). The Noril'sk deposits are hosted in the sill-like intrusions within the Paleozoic sedimentary rocks. There are two ore junctions, the Noril'sk ore Junction and the Talnakh ore Junction, in the region. These are controlled by the Noril'sk - Kharaelakh

**Table II-1-3-1 Classification of mafic and ultramafic bodies(Naldrett, 1989)**

Class of Body	Examples
<b>I . Synvolcanic Environment</b>	
1. Komatiites <ul style="list-style-type: none"> <li>a. Lava Flows</li> <li>b. Dunite-Peridotite lenses</li> </ul> 2. Tholeiites <ul style="list-style-type: none"> <li>a. Picritic Bodies</li> <li>b. Gabbroic bodies</li> </ul>	Barberton(S. Africa) Kambalda area(W. Australia) Munro(Ontario, Canada) W. Australia Dumont Sill(Quebec, Canada) Kakagi Sill(Ontario, Canada) Dundonald Sill(Ontario, Canada) Centre Hill Complex(Ontario, Canada) Kaapmuiden Barberton(S. Africa) Kalgoorlie-Norseman(W. Australia) Dore Lake Complex(Quebec, Canada) Bell River Complex(Quebec, Canada) Big Trout Lake Complex(Ontario, Canada) Mulcahy Complex(Ontario, Canada) Bird River Sill(Manitoba, Canada) Windimurra Intrusion(W. Australia)
<b>II . Associated with Rifted Plate Margins and Ocean Basins</b>	
1. Floored by and Closely Associated with Continental Crust <ul style="list-style-type: none"> <li>a. Komatiitic</li> <li>b. Largely gabbroic</li> </ul> 2. Not floored by Continental Crust <ul style="list-style-type: none"> <li>a. Ophiolite complexes</li> </ul>	Cape Smith(Quebec, Canada) Thompson Belt(Manitoba, Canada) Fox River Sill(Manitoba, Canada) Labrador Trough(Quebec-Labrador, Canada) Kemi-Koillismaa Belt(Finland) Skaergaard(Thulean Province) New Caledonia Newfoundland Cyprus Turkey USA Greece
<b>III. Intrusion in Cratonic Areas</b>	
1. Intrusions Related to Flood Basalts 2. Large-layered Complexes with no Documented Relation to Flood Basalts <ul style="list-style-type: none"> <li>a. Sheet like               <ul style="list-style-type: none"> <li>i) With repetitive layering</li> <li>ii) Without repetitive layering</li> </ul> </li> <li>b. Dikelike</li> </ul>	Duluth Complex(Minnesota, U.S.) Noril'sk-Talnakh(U.S.S.R.) Defek Intrusion(Australia) Insizwa-Ingeli Complex(S. Africa) Ontario Nipissing Diabase(Ontario, Canada) Bushveld Complex(S. Africa) Stillwater Complex(Montana, U.S.) Muskox Complex(Canada) Sudbury(Canada) Great Dyke(Zimbabwe) Jemberlana(W. Australia)
<b>IV. Bodies Intruded in Orogenic Belts</b>	
1. Synorogenic Intrusions 2. Alaskan-type Complexes 3. Alkalic Bodies	Aberdeenshire Gabbros(Scotland) Rona(Norway) Seiland Province(Norway) Fongen-Hyllingen Complex(Norway) Duke Island(Alaska, U.S.A.) Union Bay(Alaska, U.S.A.) Tulameen(British Colombia, Canada) Northern California(U.S.A.) Urals Columbia Venezuela Gardar Province(Greenland) Kola Peninsula(U.S.S.R.) Numerous Kimberlites and Carbonatites



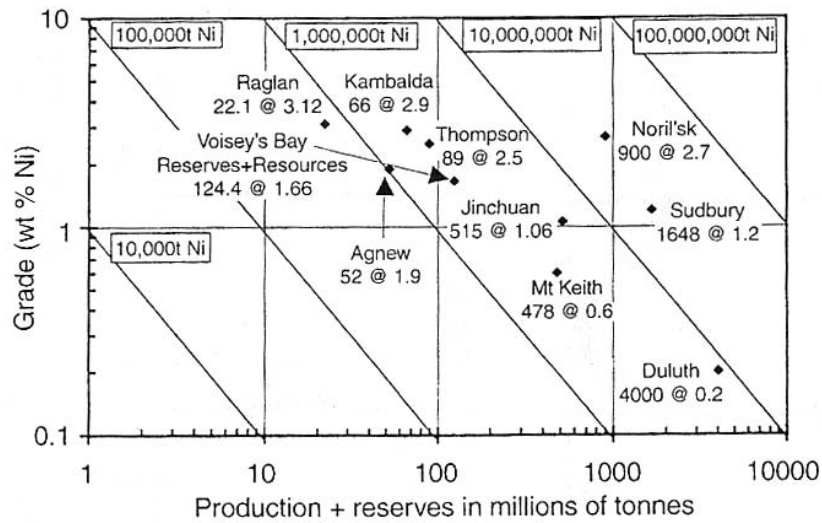


**Fig. 1** Plot of grade in wt.% Ni versus production + reserves in millions of tonnes for major Ni sulfide deposits of the world, modified after Naldrett (1994). Data for Sudbury are personal communications from INCO Ltd. and Falconbridge Ltd. (1990); those for Noril'sk are an estimate only; for Duluth are from Listerud and Meineke (1977); for Jinchuan are from Chai and Naldrett (1992a); for Kambalda, Agnew and Mt. Keith are from posters exhibited by Western Mining Corporation at the 13th Australian Geological Convention, Canberra, February (1996); for Thompson are personal communication from, O.R. Eckstrand (1990); for Voisey's Bay are reserves plus indicated and inferred resources announced by Mike Sopko, Chairman, INCO Ltd., in July 1998

**Fig.II-1-3-1** Grade versus production + reserves for major Ni sulfide deposits of the world (Naldrett, 1999)

**Table II-1-3-2** Comparison of PGE reserves in the major Ni-Cu-PGE deposits

Data from Buchanan(1979), Naldrett(1981), Robson(1985) and Naldrett(1987)

	Bushveld Complex			Great Dyke *	Sudbury	Noril'sk	Stillwater J-M Reef *
	Merensky Reef *	UG2 *	Platreef *				
Million Tonnes	2160	3700	1700	1679	310	1640	49
Grade (Total PGE+Au,g/t)	8.1	8.71	7.27	4.7	0.9	3.8	22.3
Contained PGE+Au (tonnes)	17496	32227	11900	7890	279	6232	1093
Percentage of total	26.8	49.4	18.2	12.1	0.4	9.6	1.7

\*: Primary Product

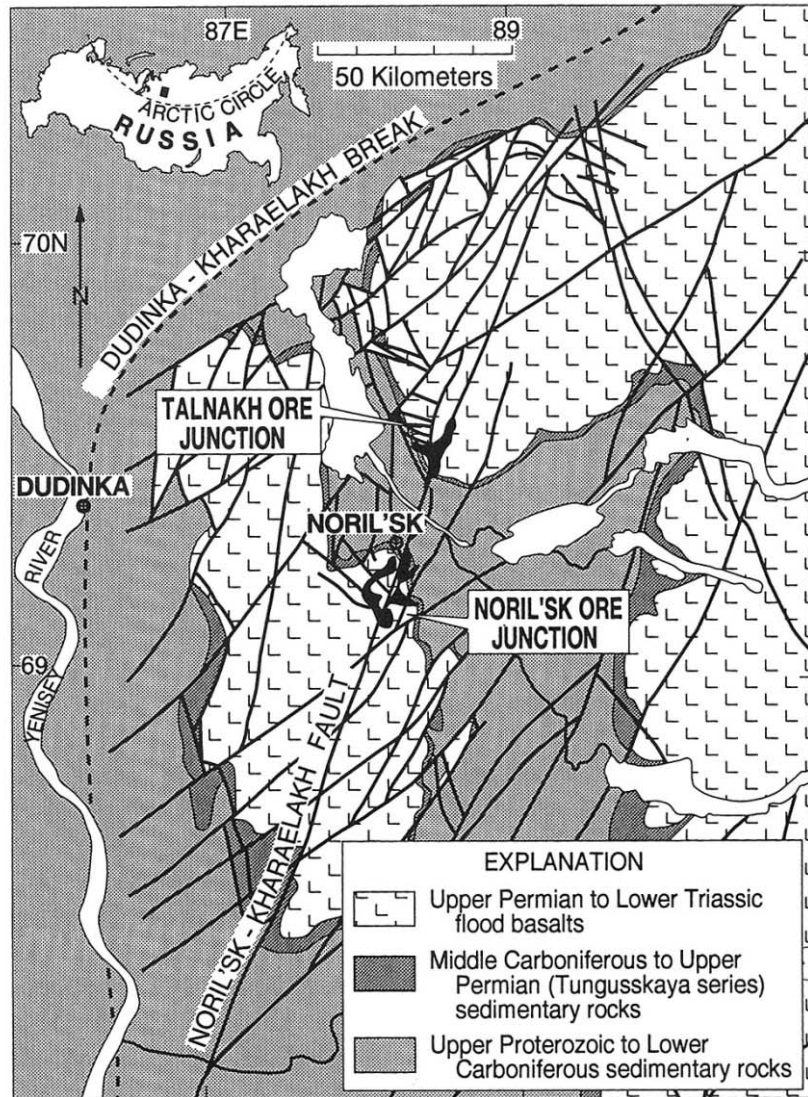


Fig. 1 Simplified geologic map of the Noril'sk-Talnakh district, showing major structural features and subsurface outlines of the Noril'sk-type, ore-bearing intrusions (black, true scale). The Kharaelakh and Noril'sk depressions are the ovoid areas, astride the Noril'sk-Kharaelakh fault and defined by the outcrop areas of basalt, which extend, respectively, north from the Talnakh ore junction and south from the Noril'sk ore junction.

Fig. II-1-3-2 Simplified geologic map of the Noril'sk-Talnakh district (Czamanske et al., 1995)

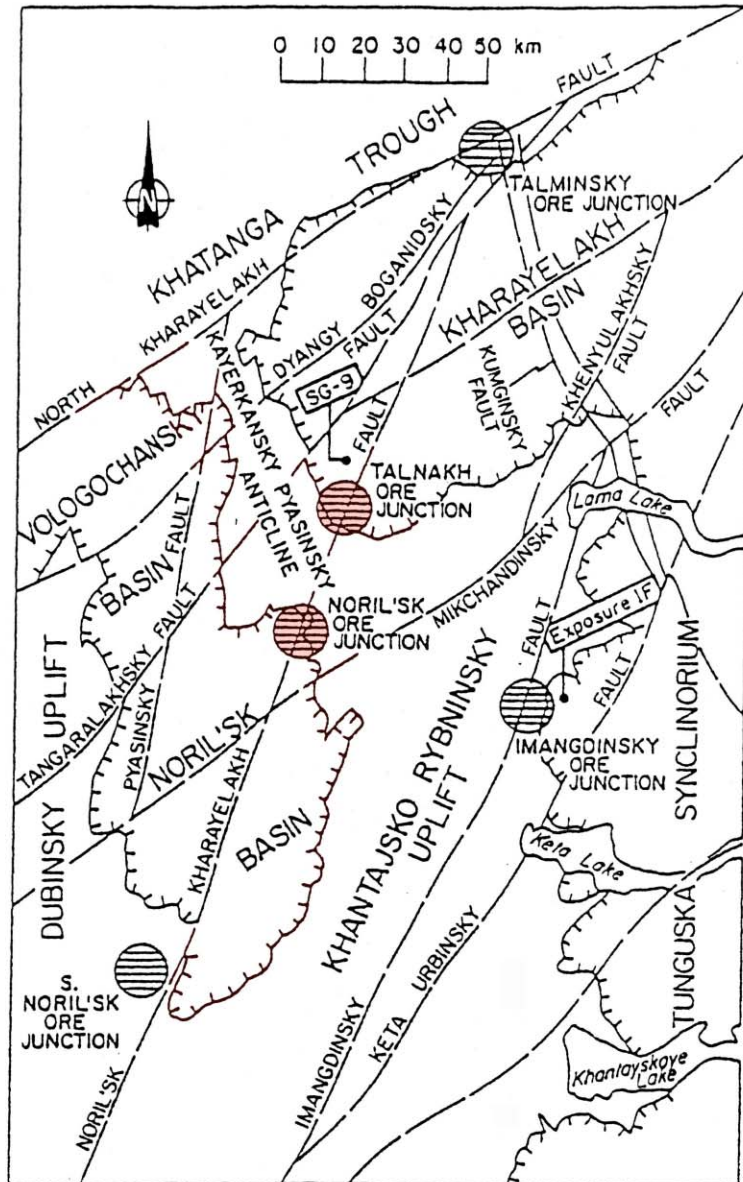


FIG. 3. Main structural elements of the northwest corner of the Siberian platform, together with the main ores zones and ore junctions. Locations of drill core SG-9 and exposure IF are also shown. After Naldrett et al., 1992. Map was compiled by V. A. Fedorenko on the basis of data collected by NKGRE (Noril'sk-Complex Geological Exploration Expedition) and TsNIGRI (Central Geological Institute for Exploration and Research, USSR Ministry of Geology).

Fig. II-1-3-3 Main structural elements of the northwest corner of the Siberian platform (Naldrett, 1992)

fault which is one of the biggest structures in the region.

The recent distribution of the flood basalt is controlled by the three major basin structures. These structures from north to south are the Kharayelakh basin, the Vologochansky basin, the Noril'sk basin, and the Tunguska synclinorium. These basin structures were formed by subsidence, which occurred after the sedimentation of the flood basalts. Therefore, at the time of the flood basalts eruption, basaltic rocks were presumed to cover entire Noril'sk region. The keel (backbone) like structure in the NW-SE direction was formed by Kayerkan - Pyasino Uplift. By this movement, the deposits accompanied by mineralized intrusions, which was originally hosted within the sedimentary rocks covered by flood basalts, is considered to have been partly exposed on the surface (Fig. II-1-3-4).

### 1-3-3 Siberian Flood Basalts

#### (1) Stratigraphy of Basaltic Rocks

The flood basalts sequence of 3,500 m is considered to have been formed in 1 Ma between the Permian and the Triassic. The sequence is composed of several lavas, tuffs, and intrusions, and their percentage is 83.8, 9.6, and 6.5, respectively (Table II-1-3-3). The eruption of the flood basalts running through sedimentary rocks of the Tungusskaya series, particularly evaporate layer which includes carbonate and sulphate, might have played an important role for concentrating large volume of sulfides in the ores. The characteristic of the Siberian flood basalts is including much more amygdaloidal materials than flood basalts of other areas. The percentage of the amygdaloidal materials reaches 36 % in the Noril'sk region.

The stratigraphy of the flood basalts is shown in Fig. II-1-3-5. The basaltic rocks are classified into three assemblages.

#### Early Assemblage

Early assemblage is composed of the lavas of Ivakinsky (Iv), Syverminsky (Sv), and Gudchikhinsky (Gd) (from lower to upper), and its total thickness is approximately 500 m. This assemblage is High-Ti type and evolved from trachybasalt through basalt to picrite.

#### Middle Assemblage

The lowest layer is Khakanchansky tuff that is covered by lavas.

This assemblage consists of the lavas of Tuklonsky (Tk), Lower Nadezhdinsky (Nd<sub>1</sub>), Middle Nadezhdinsky (Nd<sub>2</sub>), Upper Nadezhdinsky (Nd<sub>3</sub>), and Lower Morongovsky (Mr<sub>1</sub>). The total thickness of this assemblage is approximate 500 to 600 meters. The Tk lava, the lowermost of these, is a Low-Ti magma and is composed of basalt and picrite. The Nd<sub>1</sub> and Nd<sub>2</sub> lavas which cover the Tk lava were thought to have formed after crustal contamination and

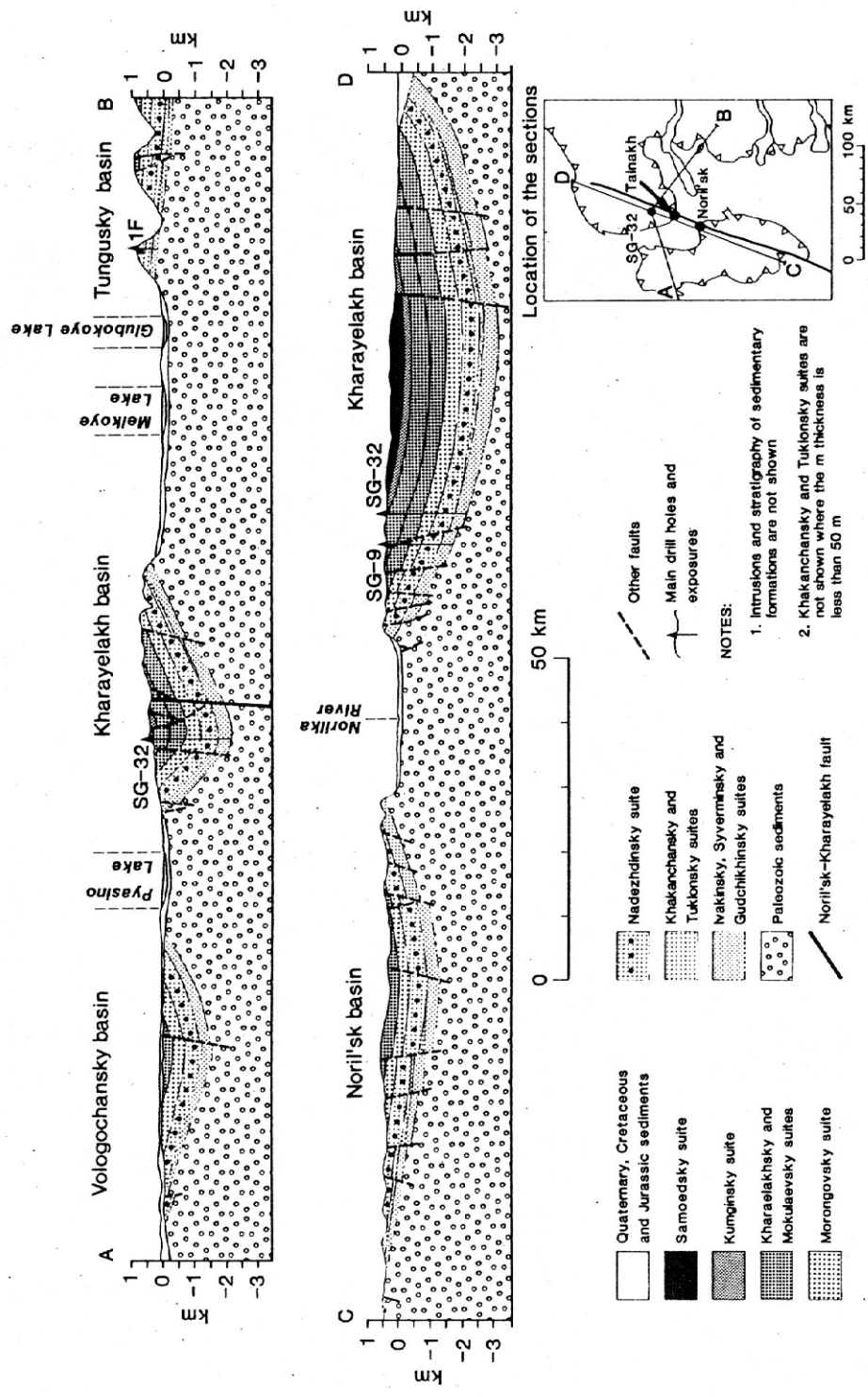


Figure 22.1c. North-south and east-west geological cross sections depicting the geology of the Noril'sk, Vologochansky, Kharayelakhsky and Tungusky synclinal sequences. Triangular boundary in inset map refers to margin of basaltic trap sediments under basalt sequence.

Fig.II-1-3-4 Geologic cross sections of the Noril'sk-Talnakh district platform(Lightfoot, 1992)

**Table II-1-3-3 Volume percentages of the magmatic rock types in the Noril'sk region (Fedorenko, 1994)**

**Table 15.1.** Volume percentages of the magmatic rock types in the Noril'sk region.

	Lavas	Tuffs	Intrusions	Total
Granodiorite	—	—	>0.01%	>0.01%
Alkalic and subalkalic mafic rocks	2.0%	0.9%	1.5%	4.4%
Normal mafic rocks	81.0%	8.7%	4.9%	94.6%
Picrites and picrite-like rocks	0.8%	—	0.1%	0.9%
Picritic-mafic ore-bearing intrusions	—	—	>0.01%	>0.01%
<b>Total</b>	<b>83.8%</b>	<b>9.6%</b>	<b>6.5%</b>	<b>99.9%</b>

Total volume (including eroded masses) 150 000 km<sup>3</sup>, within 45 300 km<sup>2</sup>.

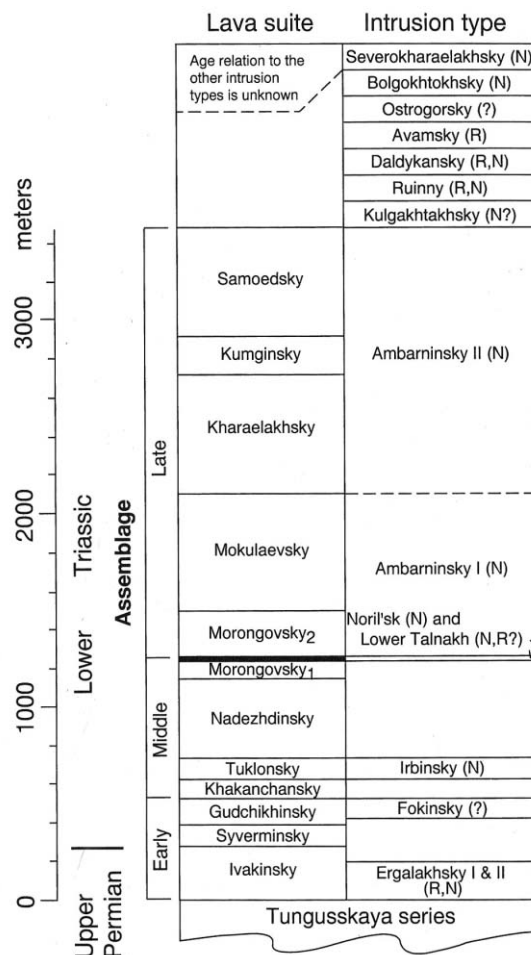


**Fig.II-1-3-5 Correlation chart relating flood basalt stratigraphy of the Noril'sk region (Czamanske et al., 1995)**

fractional crystallization of plagioclase, clinopyroxene and olivine of Tk basaltic magma. After eruption of these lavas, fresh mantle derived magma injected into the magma chamber, and parental magmas of the Nd<sub>3</sub> and Mr<sub>1</sub> lavas were formed.

The magmatic activity of this assemblage was important for the genesis of the Noril'sk deposits. As mentioned below, crustal contamination and sulfide segregation observed in Nd<sub>1</sub> and Nd<sub>2</sub> lavas are thought to have close relationship to the genesis of the deposits.

#### Late Assemblage

The assemblage consists of the lavas of Upper Morongovsky (Mr<sub>2</sub>), Mokulaevsky (Mk), Kharaelakhsy, Kumginsky, and Samoedsky from lower to upper. The total thickness of the assemblage is 2,000 to 2,300 m. The lavas are mainly composed of Low-Ti type magma.

#### (2) Crustal Contamination and Immiscible Sulfide Segregation

The crustal contamination, particularly the contamination of sulfur included in evaporates and other rocks, and following removal of immiscible sulfide melt from silicate magma are considered to be major requirements for the genesis of orthomagmatic sulfide deposits. Therefore, a silicate magma related to the genesis of ore may be depleted in sulfide and chalcophile elements. In the Noril'sk region these phenomena were clarified by the detailed geochemical studies of the related flood basalts. The crustal contamination and chalcophile elements depletion are markedly observed in the lavas of the middle assemblage.

Fig. II-1-3-6 shows La/Sm - Gd/Yb diagram for the lavas of the Noril'sk region. Tk lava shows low La/Sm and Gd/Yb. These rare earth elements ratios probably show the larger degree of partial melting of fertile magma. Comparing the Tk lava with the Nd<sub>1</sub> and Nd<sub>2</sub> lavas, which erupted after the Tk lava, the latter indicate increased La/Sm ratio, maintaining Gd/Yb constant. Since increasing of La/Sm with maintaining Gd/Yb constant means the crustal contamination, it is considered that contamination played a big role in the genesis of the magmas of the Nd<sub>1</sub> and Nd<sub>2</sub> lavas. Crustal contamination of these lavas is also indicated by initial ratio of <sup>87</sup>Sr/<sup>86</sup>Sr by Lightfoot et al. (1991a). The δ <sup>34</sup>S of the Noril'sk deposit indicates high values of +8 to +12‰. From this fact, sulfur is thought to have been supplied in the process of contamination from anhydrite that was included in the basement sedimentary rocks as one of the possibilities.

The reverse correlations between La/Sm and Ni, Cu, and Pt are obviously indicated in Fig. II-1-3-7. This fact suggests that Ni, Cu and Pt were depleted corresponding to the increasing of La/Sm in the Nd<sub>1</sub> and Nd<sub>2</sub> lavas, which contaminated crustal materials. This means that the crustal contamination and the depletion of chalcophile elements occurred at the same time in the same lava unit. Ni, Cu and Pt are the elements which are selectively distributed into sulfide melt when sulfide segregation occurs. They are selectively brought into the immiscible sulfide



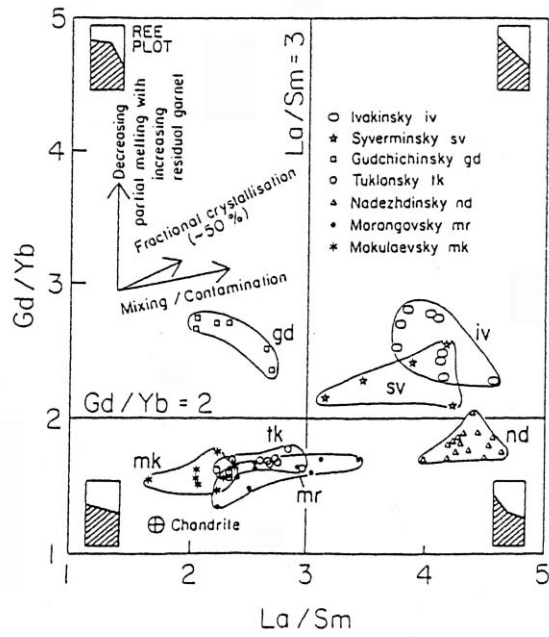
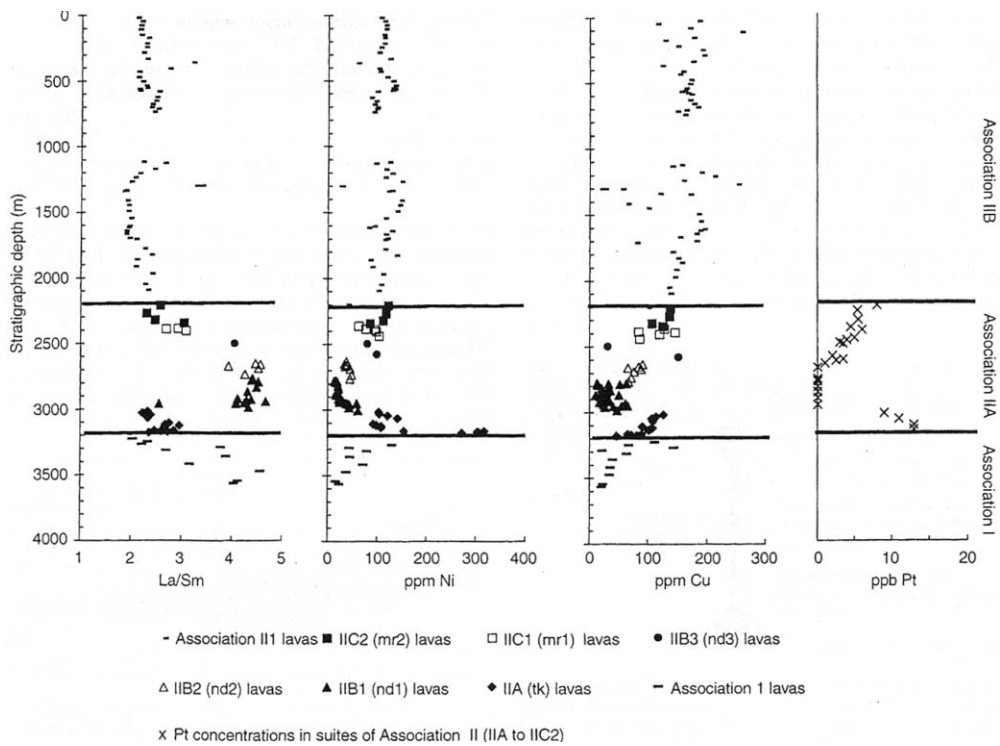


FIG. 6. Plot of Gd/Yb vs. La/Sm for basalts of the Noril'sk region. Adapted by Naldrett et al. (1992) after Lightfoot et al. (1990).

**Fig.II-1-3-6 Relation between La/Sm versus Gd/Yb for basalts of the Noril'sk region (Naldrett, 1992)**



**Fig.II-1-3-7 Vertical variation in La/Sm, Ni, Cu, Pt for basalts of the Noril'sk region(Naldrett, 1999)**



melt generated by crustal contamination, which decreases the solubility of sulfur in the silicate magma. Meanwhile, these elements are depleted in the silicate magma in which sulfide segregation occurs. Therefore sulfide melts segregated from silicate magma probably related to the genesis of the Noril'sk deposits.

The existence of the lavas which are depleted in chalcophile elements may be one of the indicators which suggest the existence of orthomagmatic sulfide deposit in the depth.

#### 1-3-4 Intrusions

##### (1) Intrusions

There are fifteen types of intrusive rocks in the Noril'sk region (Fig. II-1-3-5). Each type has its own geochemical and isotopic characteristics and some are considered to be comagmatic with lavas. Most of the intrusions intrude into the Tunguskaya series of Paleozoic, and exist within 2 km from the bottom of basaltic rocks (Fig. II-1-3-8). Although many drillings for petroleum prospecting were carried out in the Noril'sk region, the intrusions have not been discovered in the lower part of the Paleozoic formations. Almost all of the intrusions are sills that conformably intruded along the bedding of Paleozoic formations. However, some sills intruded along the tectonic structural lines. The thickness of many sills ranges between several meters to a hundred meters, but some sills reaches 150 to 200 meters in thickness.

Mineralization of sulfides is not observed in all sills. It is observed only in the "fully differentiated" sills which include picritic part. The amount of these mineralized sills occupy only 0.01 volume percent within the entire magmas of the Noril'sk region (Table II-1-3-3).

##### (2) Noril'sk Type Ore-Bearing Intrusion and Lower Talnakh Type Intrusion

The intrusions accompanied with economical mineralization are known as the Noril'sk type ore-bearing intrusion. This type is fully differentiated from picritic gabbrodolerite to leucogabbro (Fig. II-1-3-9). MgO varies from 29 to 4 wt%, from the lower to the upper in a intrusion, and economical disseminated ore and massive ore are included in the picritic unit of the lower part. There are only three Noril'sk type ore-bearing intrusions in the Noril'sk region. These are the Talnakh intrusion and the Kharaelakh intrusion in the Talnakh Ore Junction, and the Noril'sk-I intrusion in the Noril'sk Ore Junction. These intrusions are distributed closely relating to the Noril'sk-Kharaelakh fault.

The geologic section of the Talnakh intrusion is shown in Fig. II-1-3-10. As shown in the figure, the Lower Talnakh type intrusion is located with close relationship to the Noril'sk type ore-bearing intrusion (Talnakh intrusion). This intrusion is generally found a few tens to hundreds meters beneath the Noril'sk type ore-bearing intrusion. The Noril'sk type ore-bearing intrusion involves economical mineralization. The Lower Talnakh type intrusion also

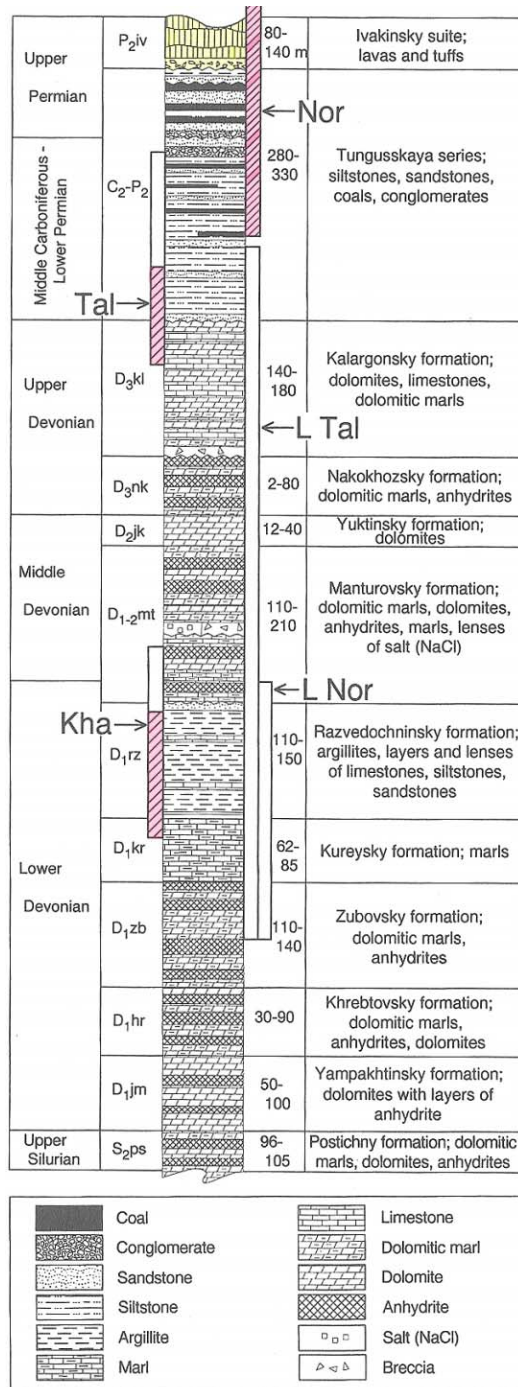


**Fig.II-1-3-8 Generalized stratigraphic column for Silurian to Permian formations based on typical stratigraphic thickness for the Talnakh ore junction. (Czamanske et al, 1995)**

Vertical bars show the approximate ranges in stratigraphic position of the base of each intrusion : Nor=Noril'sk; L Nor=Lower Noril'sk; Tal=Talnakh; L Tal=Lower Talnakh; Kha=Kharaelakh

Rock unit	Modal % olivine	MgO wt %	Notable phases	
Leucocratic gabbro	0-3	4-8	Pl <sub>1</sub>	
Quartz diorite (Russian: quartz gabbrodiorite)	0	1.2-1.7	Pl <sub>2</sub> + Aug + Qtz	
Magnetite gabbro	0-4	4.4-7	Pl <sub>2</sub> + Aug + Mt	
Prismatic gabbro (Russian: gabbrodiorite)	0-5	6-7	Pl <sub>2</sub> + Aug	
GABBRODOLERITE	Olivine-bearing	3-7	6-8	Pl <sub>2</sub> + Aug + Ol <sub>2</sub>
	Olivine	10-27	9-12	Pl <sub>2</sub> + Aug + Ol <sub>2</sub> + sparse Pl <sub>1</sub>
	Picritic	40-80	18-29	Ol <sub>1</sub> + Pl <sub>2</sub> + Aug + Sulfide + Pl <sub>1</sub> glom + sparse Pl <sub>1</sub>
	Taxitic	7-18	9-16	Pl <sub>2</sub> + Ol <sub>1,2</sub> + Aug + Sulfide + Pl <sub>1</sub> glom
	Contact	10-15	7-8	Pl <sub>2</sub> + Aug + Ol <sub>2</sub>

Fig.II-1-3-9 Generalized lithologic section for the "fully differentiated" main body of the ore-bearing intrusions. (Czamanske et al, 1995)

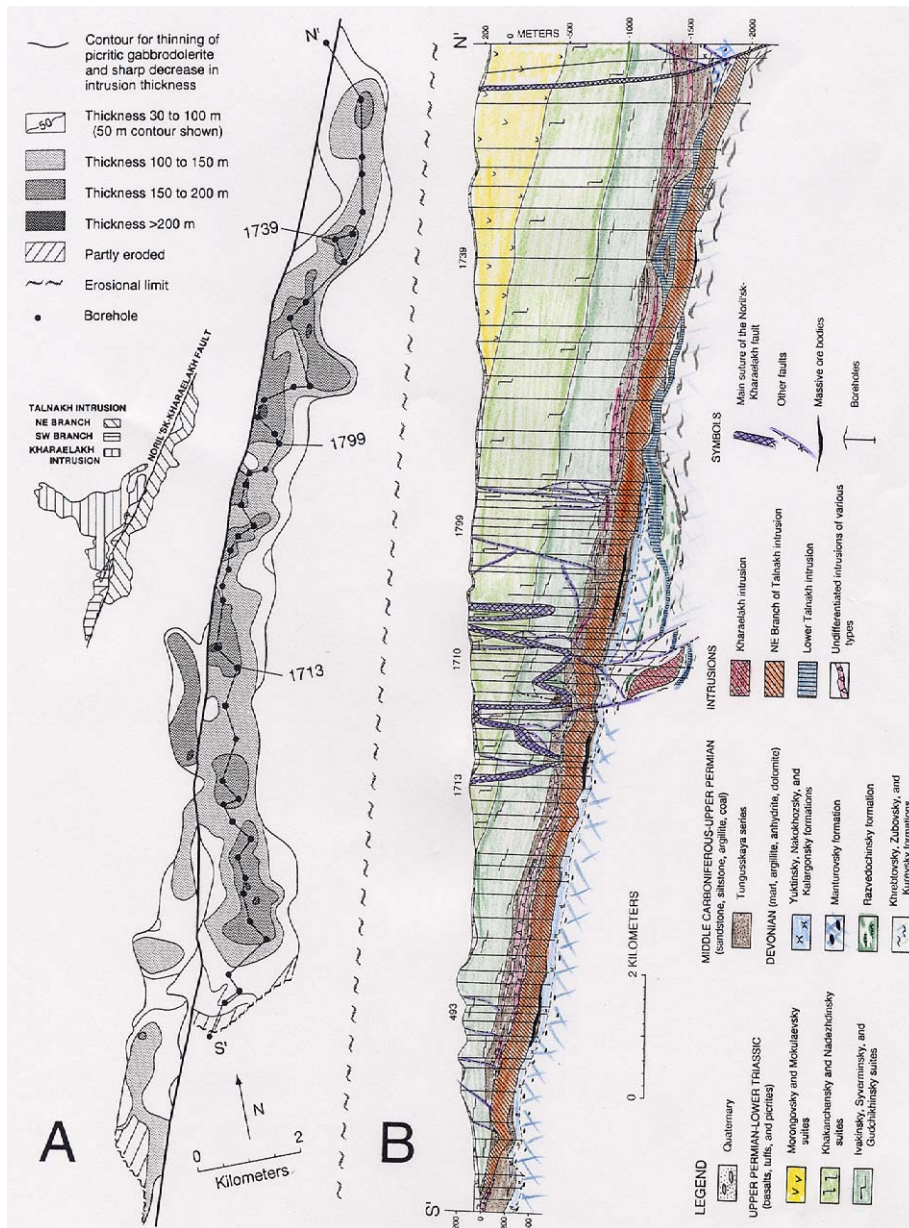


**Fig.II-1-3-10 A) Projection to the surface of the outlines of the main body of the NE and SW branches of the Talnakh intrusion (Czamanske et al, 1995);B) Cross section of the thickest part of the NE branch of the intrusion (Czamanske et al, 1995)**

involves copper-nickel-PGE mineralization, which is not economical.

The Noril'sk type ore-bearing intrusion and the Lower Talnakh type intrusion have different intrusive feature compared to other intrusions. Though most of intrusions intrude along the bedding plane, only the Noril'sk type ore-bearing intrusion and the Lower Talnakh type intrusion intrude with cutting bedding plane (Fig. II-1-3-11). These structures are called "insertion" by Russian geologists, and are considered to contaminate the country rocks on a large scale.

Fig. II-1-3-12 schematically shows the vertical variations of lithology and mineral assemblage of the Noril'sk type ore-bearing intrusion based on the drilling data. The most important boundary exists between picritic gabbrodolerite and olivine gabbrodolerite. This boundary corresponds to the upper part of the economical disseminated ore. Olivine and sulfide contents markedly increase in the lower part of the boundary. Forsterite component and Ni in olivine also discontinuously increase in the lower part of the boundary. These discontinuous changing is indicated by chemical composition of rocks (Fig. II-1-3-13). MgO, Cu, Ni and Pd markedly increase in the lower part of the boundary.

There are two types of ores, disseminated ore and massive ores. These are included in picritic gabbrodolerite and taxitic gabbrodolerite. The upper part of picritic gabbrodolerite corresponds to the upper part of the economic ore body. The word "taxitic" is used for igneous rocks which show various textures from fine-grained to pegmatitic by Russian geologists. The massive ore generally intrudes into the Paleozoic sedimentary rocks underlying intrusions and discontinuous with disseminated ore. Therefore, disseminated and massive ores are not considered to have been formed continuously by precipitation of immiscible sulfide melts. As mentioned below, the massive ore is considered to have been formed by the intrusion of mobile sulfide melt into the intrusive bodies in the last stage of intrusive activities. The intruded sulfide melt sometimes reached the upper part of the intrusive body and formed veins.

The Noril'sk type ore-bearing intrusion is characteristically accompanied by thick hornfels halos compared with other types of intrusions. The thickness of hornfels is 1.5 to 2.5 times of the intrusion itself. The hornfels is characterized by high-temperature hornfels containing clinopyroxene. However, the hornfels accompanied with the Lower Talnakh type intrusion is lower temperature hornfels containing hornblende and biotite, and its thickness is only 0.5 to 1.5 times of the intrusion itself. The thickness of hornfels of other types of intrusions becomes thinner and the thickness is thinner than that of intrusion itself. Therefore, the Noril'sk type ore-bearing intrusion might have been the highest temperature intrusion in all types of intrusions and have given thermal effect to its host rocks.

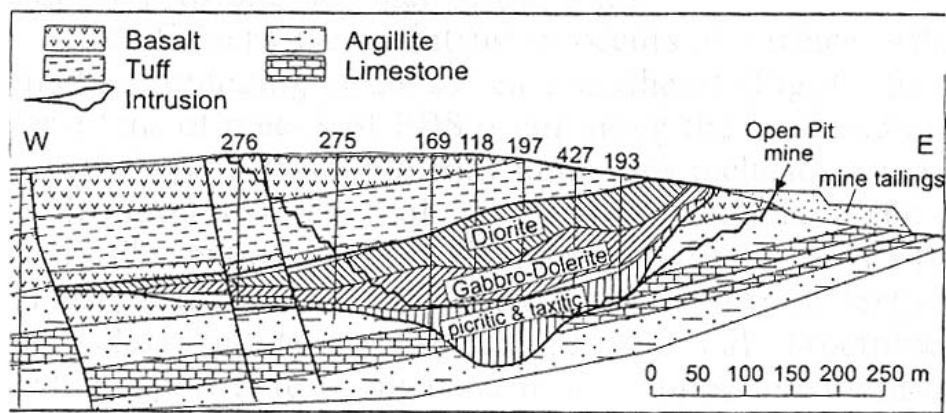


Fig. 3 Vertical section through the east branch of the Noril'sk I intrusion at the Bear's Brook open pit (from Distler and Kunilov 1994)

Fig.II-1-3-11 Cross section through the east branch of the Noril'sk I intrusion (Naldrett, 1999)



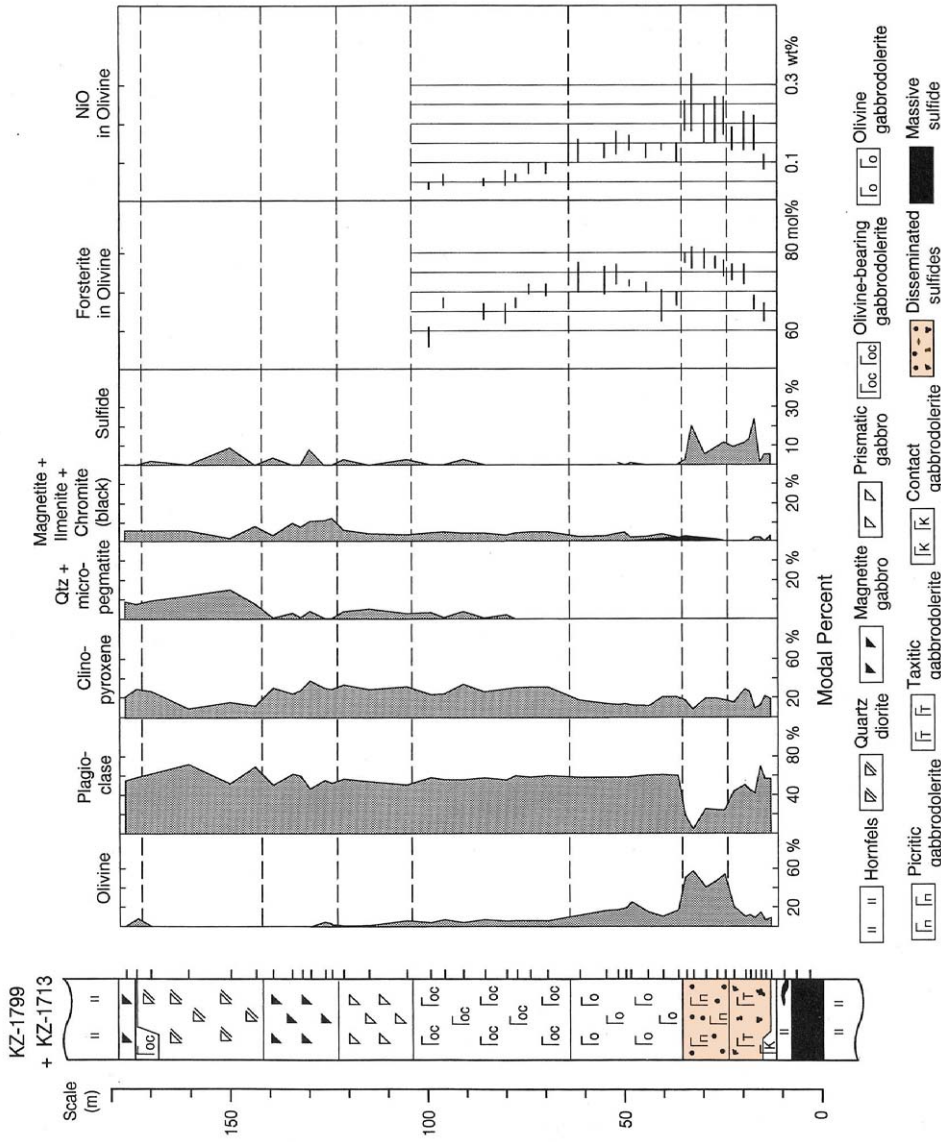


Fig. 16 Composite lithologic section, based on boreholes KZ-1713 and KZ-1799 (Appendixes 1 and 2; Fig. 17), with estimated modal proportions of significant mineral phases and ranges of forsterite and NiO contents in olivine, as determined by electron-microprobe analysis.

**Fig.II-1-3-12 Composite lithologic section of the Talnakh intrusion (Czamanske et al., 1995)**

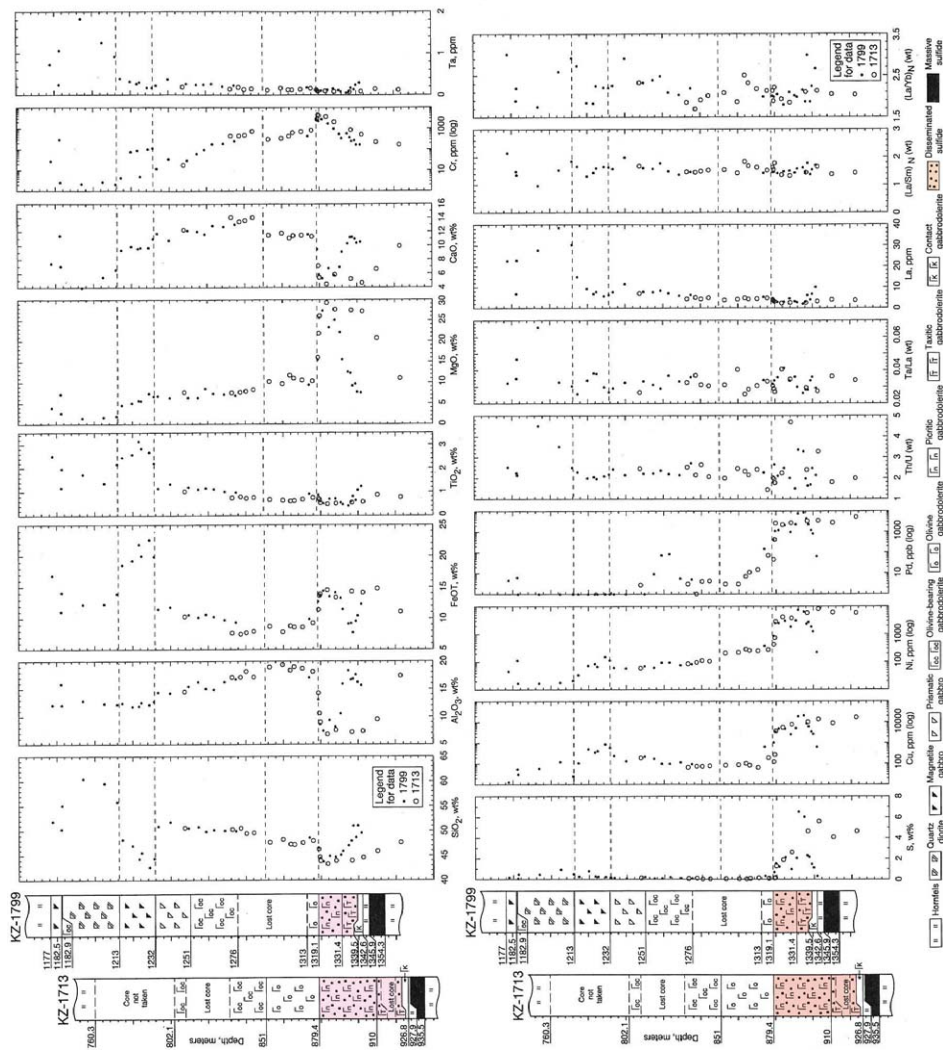


Fig. 17 Major- and trace-element variations with respect to stratigraphic position and rock type for a composite section for the NE branch of the Talnakh intrusion, based on complementary boreholes KZ-1713 and KZ-1799 (Fig. 5; Appendices 1 and 2). Aligment of the two lithologic sections is at the upper contact of the picritic-gabbroolerite unit.

**Fig.II-1-3-13 Vertical variations in major and trace element for the Talnakh intrusion(Czamanske et al., 1995)**



### 1-3-5 Genetic Model of the Noril'sk Deposits

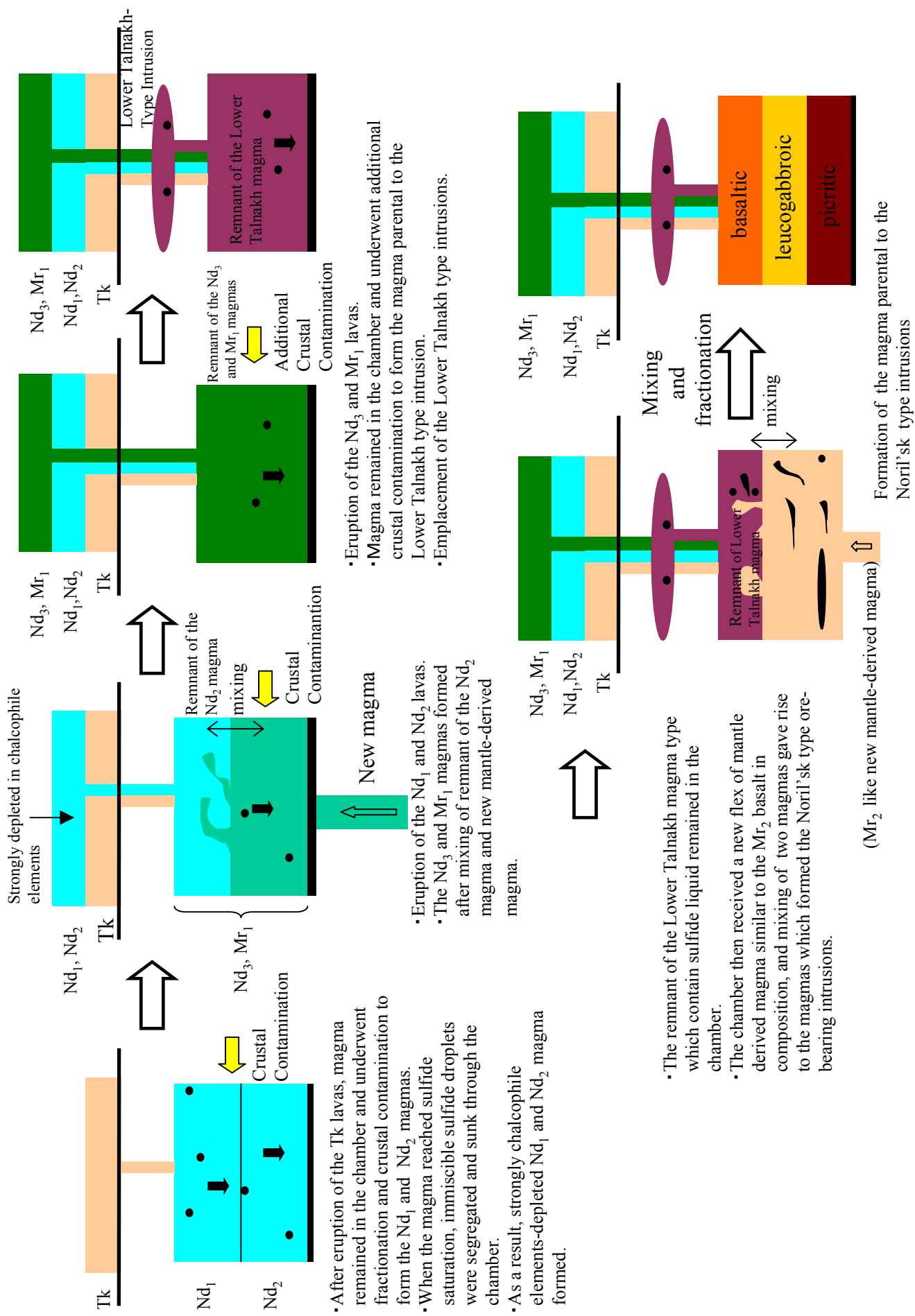
Many genetic models of the Noril'sk deposits are presented. There are several models such as the "single-magma-input model" in which ore genesis is considered as the process in a single magma chamber, the "multiple-magma-input model" in which multi-stage magma injections into magma chamber are assumed, and the "lava-conduit model" in which intrusion itself is considered as conduit through which magma ascends. In this report, we explain the "multiple-magma-input model" by Fedorenko (1994). In this model, immiscible sulfide melts accumulate in the process of multiple magma injections, and in this point this model has something in common with the "lava-conduit model" by Naldrett (1992). The Genetic model of Fedorenko (1994) is illustrated in Fig. II-1-3-14 and Fig. II-1-3-15.

#### (1) Evolution of the Parental Magmas to the Noril'sk Deposits

- a) After the eruption of the Tk lava, the magma remained in the magma chamber underwent fractional crystallization and crustal contamination to form the parental magma to the Nd<sub>1</sub> and Nd<sub>2</sub> lavas. When this magma reached sulfur saturation, immiscible sulfide melts were separated from the silicate magma and precipitated at the bottom of the magma chamber. As a result, chalcophile elements depleted parental magmas to the Nd<sub>1</sub> and Nd<sub>2</sub> lavas were formed.
- b) After the eruptions of the Nd<sub>1</sub> and Nd<sub>2</sub> lavas, the magma remained in the magma chamber mixed with mantle-derived fresh magma to form the parental magmas to the Nd<sub>3</sub> and Mr<sub>1</sub> lavas. During this magma reaction, crustal contamination and segregation of immiscible sulfide melts continued.
- c) After the eruptions of the Nd<sub>3</sub> and Mr<sub>1</sub> lavas, the magma remained in the magma chamber underwent additional crustal contamination and sulfide segregation to form the parental magma to the Lower Talnakh type intrusions. This magma intruded into the shallow level of crust, and weakly mineralized the Lower Talnakh type intrusions were formed.
- d) The remnant of the Lower Talnakh magma, containing sulfide disseminations, mixed with a new mantle-derived fresh magma similar to the Mr<sub>2</sub> lava in chemical composition in the magma chamber. As a result, the parental magmas to the Noril'sk type ore-bearing intrusions were formed.
- e) Above parental magmas underwent fractional crystallization and zoned magma chamber which differentiated from picritic to basaltic was formed.

#### (2) Formation of the Noril'sk Deposits

The Noril'sk type ore-bearing intrusions were formed by intrusive activities from the above

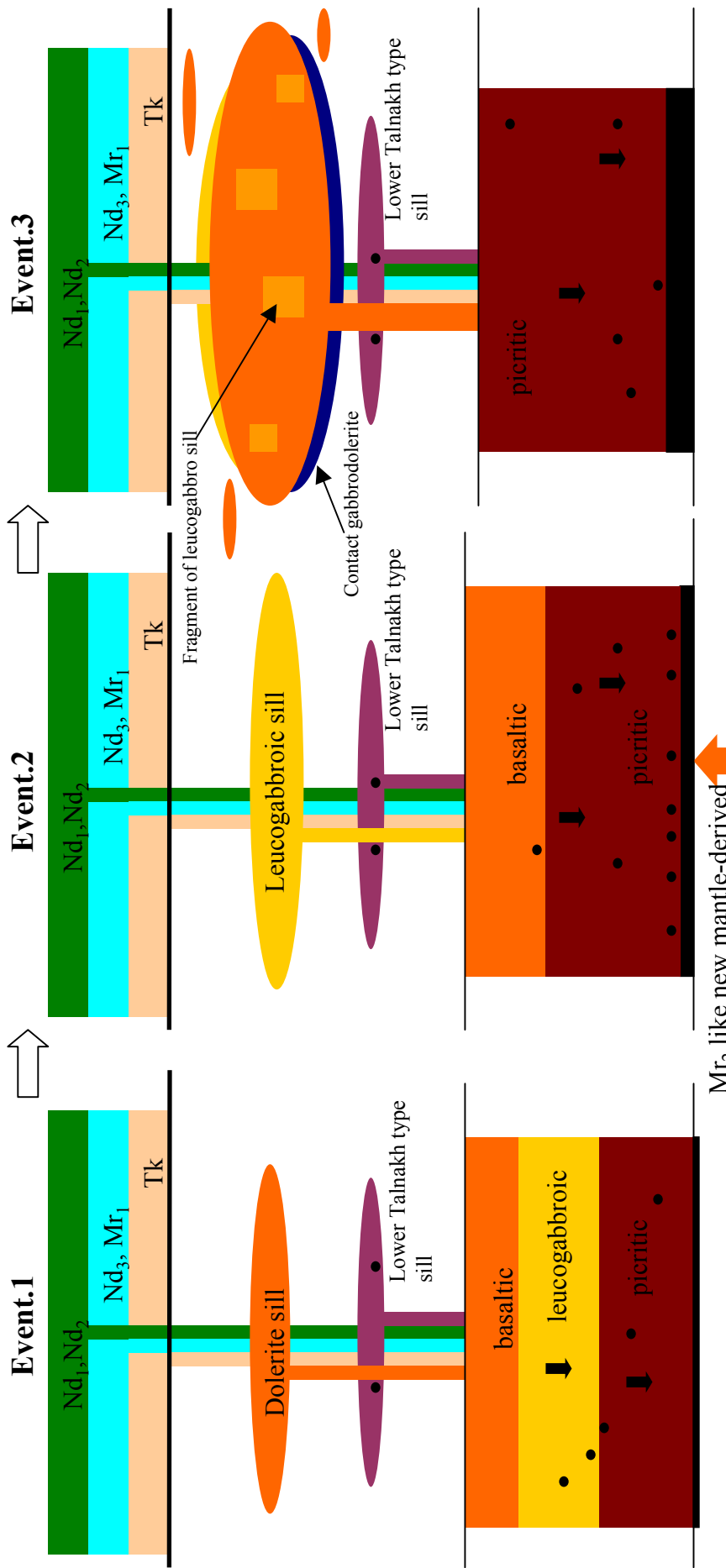


- After eruption of the Tk lavas, magma remained in the chamber and underwent fractionation and crustal contamination to form the Nd<sub>1</sub> and Nd<sub>2</sub> magmas.
- When the magma reached sulfide saturation, immiscible sulfide droplets were segregated and sunk through the chamber.
- As a result, strongly chalcophile elements-depleted Nd<sub>1</sub> and Nd<sub>2</sub> magma formed.
- Eruption of the Nd<sub>3</sub> and Mr<sub>1</sub> lavas.
- Magma remained in the chamber and underwent additional crustal contamination to form the magma parental to the Lower Talnakh type intrusion.
- Emplacement of the Lower Talnakh type intrusions.

- Eruption of the Nd<sub>1</sub> and Nd<sub>2</sub> lavas.
- The Nd<sub>3</sub> and Mr<sub>1</sub> magmas formed after mixing of remnant of the Nd<sub>2</sub> magma and new mantle-derived magma.

- The remnant of the Lower Talnakh magma type which contain sulfide liquid remained in the chamber.
- The chamber then received a new flex of mantle derived magma similar to the Mr<sub>2</sub> basalt in composition, and mixing of two magmas gave rise to the magmas which formed the Noril'sk type ore-bearing intrusions.

**Fig.II-1-3-14 Evolution of the magmas parental to the Lower Talnakh type and the Noril'sk type ore-bearing intrusions**



$Mr_2$  like new mantle-derived magma

**Event.1**

- Intrusion of basaltic magma from the upper part of the intermediate magma chamber to form the dolerite sill.
- In some intrusive systems, no further activity took place.

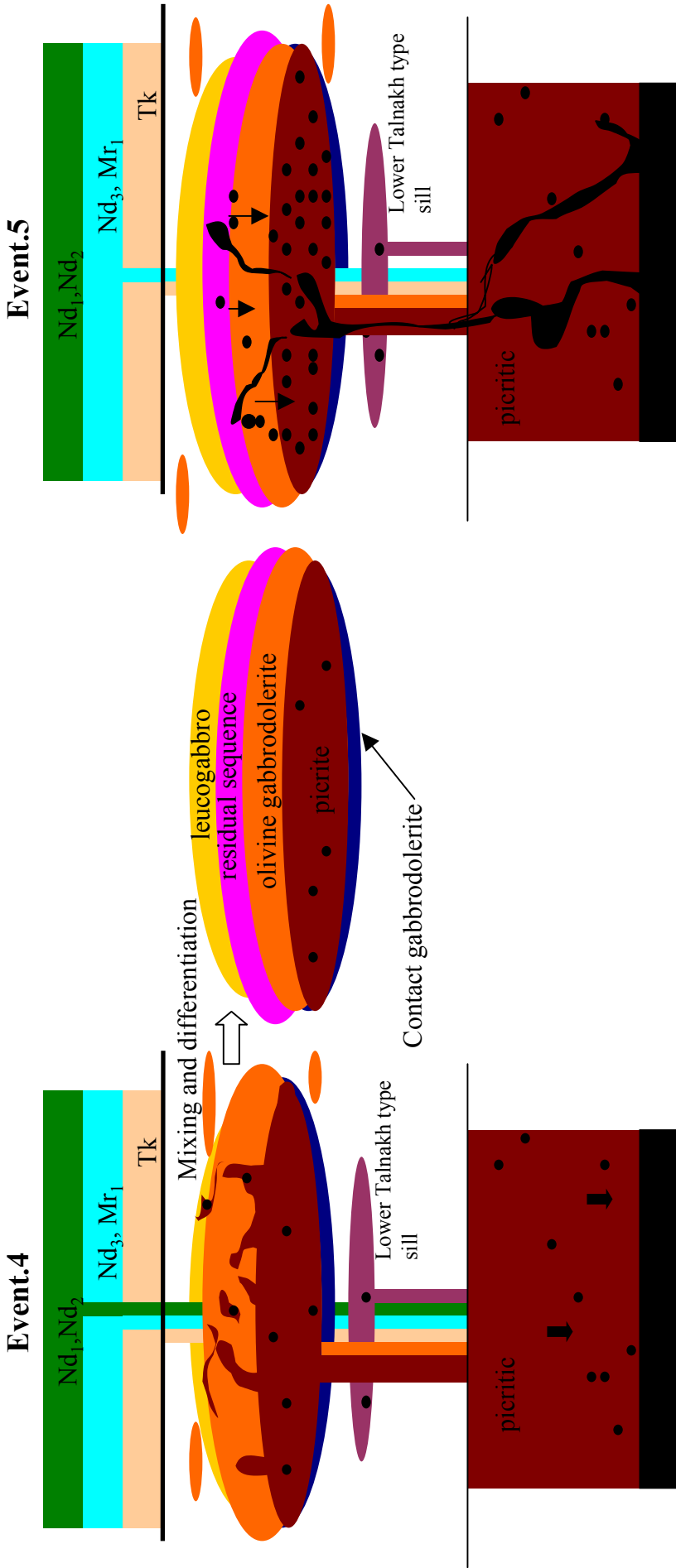
**Event.2**

- Leucogabbroic magma entered the still-liquid dolerite sill.
- The leucogabbro sill solidified before formation of the main body of the intrusion, meanwhile the chamber was being replenished by new mantle derived  $Mr_2$  like magma.
- New basaltic layer was developed at the top of the chamber.
- Sulfide liquid pooled lowermost in the chamber.

**Event.3**

- The third event was a second emplacement of the basaltic magma. The composition of the magma (7-8wt%MgO) was represented by the basal contact gabbrodolerite.
- This event caused inflation of the elongated area.
- Numerous lenses and short sills of dolerite were produced around the main body.

Fig.II-1-3-15(a) Formation of the Noril'sk type ore-bearing intrusion



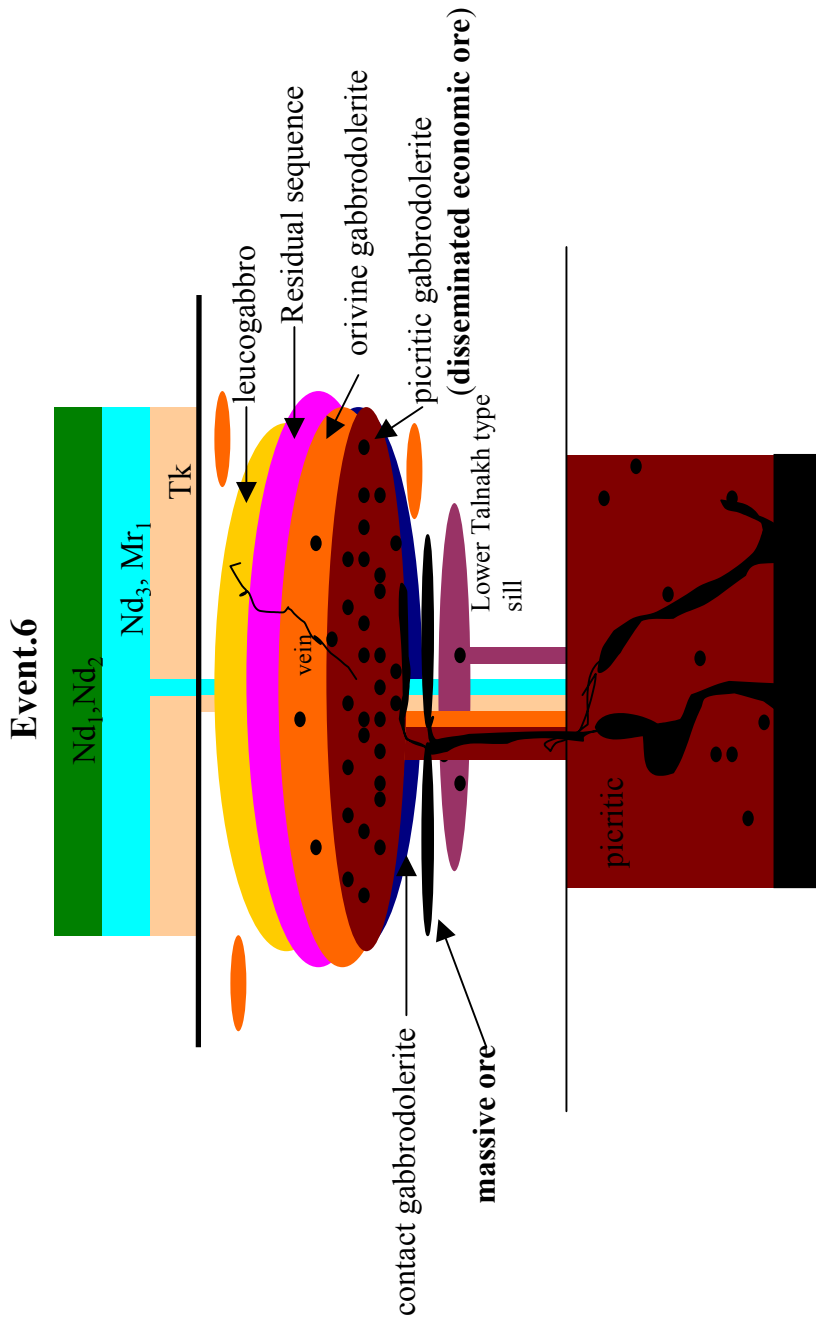
**Event.4**

- The fourth event was emplacement of picrite-like magma carrying small, disseminated sulfide droplets.
- The picritic magma mixed with basaltic magma, and this mixture differentiated and formed the regular sequence from picritic gabbrodolerite, through containing decreasing amounts of olivine, to the upper residual sequence.
- The fourth event terminated development of the majority of the Noril'sk type intrusions that were weakly mineralized.

**Event.5**

- Development of the intrusions carrying economic mineralization continued with the fifth and sixth events.
- Turbulent fountains of sulfide liquid were injected into the silicate magma and dispersed to form relatively large (up to 3cm) and small droplets.
- Being of great density, they fell quickly to the upper boundary of the dense picritic magma and then slowly descended into the picritic magma, giving rise to economic disseminated mineralization.

**Fig.II-1-3-15(b) Formation of the Noril'sk type ore-bearing intrusion**



**Event.6**

- The final, sixth event took place after solidification of the silicate intrusions with their disseminated ores.
- Massive ore bodies formed when sulfide magma pools were emplaced into the lowermost units of the ore-bearing intrusions and underlying metasedimentary rocks, and occasionally, as veins, reaching the roof of the intrusion.

**Fig.II-1-3-15(c) Formation of the Noril'sk type ore-bearing intrusion**

zoned magma chamber. These activities are divided into six events as shown below (Czamanske et al., 1995).

- a) From the upper part of the chamber, basaltic magma intruded into the shallower level and doleritic sills were formed. During this event, precipitation of the immiscible sulfide melts continued in the chamber. Some intrusive systems stopped their growths in this event.
- b) The leucogabbroic magma intruded into the doleritic sills which were still in a liquid phase, and gradually solidified. Fresh magma similar to the Mr2 lava in chemical composition was supplied into the chamber from mantle. This magma mixed with the remaining magma. The magma chamber with a layered structure from picritic to basaltic due to fractional crystallization grew again. During this stage, sulfide melts continued to pool at the bottom of the chamber.
- c) The third event was a second emplacement of the basaltic magma. The main body of the intrusions were formed by this event. This event caused inflation of the elongated area on the surface. MgO content of this basaltic magma is 7 to 8 wt%, and is thought to be represented by the contact gabbrodolerite that is the chilled margin of the Noril'sk type ore-bearing intrusions. Therefore, this contact gabbrodolerite is considered to have been formed during this event. This magma intruded just below the leucogabbroic sill that had already solidified. Finally doleritic sills including fragments of the leucogabbroic sill were formed. Small scale doleritic sills were formed around the main body. During this event, sulfide melts continued to pool at the bottom of the chamber.
- d) The fourth event was the intrusion of the picritic magma from the magma chamber into the main body of the intrusion. This event occurred when the contact gabbrodolerite grew 1 to 2 m in thickness. The picritic magma intruded like a turbulent flow, and reached the uppermost part of the intrusion where it mixed with basaltic magma. This magma conveyed drops of sulfide melt into the intrusion. The mixed magma fractionated to form weakly mineralized layered intrusions. During this stage, sulfide melts continued to pool at the bottom of the chamber.

Many of the intrusive systems stopped their activities at this event and unmineralized or weakly mineralized intrusions were formed. The formation of the economic Noril'sk type ore-bearing intrusion required additional fifth and sixth events. These events were intrusive activities from the sulfide pools developed at the bottom of the chamber.

- a) Turbulent fountains of sulfide melt were injected into the silicate magma from the sulfide melt pool formed at the bottom of the chamber. The injected sulfide melt dispersed to form relatively large (up to 3cm) and small droplets. Being of high density of the droplets, they

fell quickly to the upper boundary of the dense picritic magma and then slowly descended into the picritic magma, giving rise to economic disseminated mineralization. Through such process, economic disseminated ores were formed in the picritic magma. Irregular distribution of ore grades suggests that these injections occurred repeatedly.

- b) The final, sixth event, took place after solidification of the intrusions with disseminated ores. Massive ore bodies were formed when sulfide melt emplaced into the lowermost part of the intrusions and underlying metasedimentary rocks, and occasionally, as veins, reached the roof of the intrusions.

### 1-3-6 Genetic Model of the Orthomagmatic Sulfide Deposits and Key Factors in the Exploration of the Noril'sk Style Deposits

Leshner and Stone (1996), Keays (1995, 1997), and Brooks et al. (1999) reviewed the requirements for the genesis of the orthomagmatic sulfide ore deposits accompanied by mafic to ultramafic magmas. Based on these papers, the genesis of the orthomagmatic ore deposits and key factors in the exploration of the Noril'sk-style deposit which belongs to these deposits, are discussed.

Keays (1997) presented the following three requirements for the genesis of the economical orthomagmatic sulfide deposits.

- Generation of sulfur undersaturated magma and its transportation to shallow crustal level without reaching sulfur saturation
- Sulfur saturation of the magma and forming immiscible sulfide melt
- Reaction of the immiscible sulfide melt with voluminous silicate magma

#### (1) Generation of Sulfur Undersaturated Magma and its Intrusion to the Shallow Crustal Level

Since all of the large scale nickel-copper sulfide deposits are enriched in PGE in various degrees, the magma which forms the economic orthomagmatic sulfide ore deposits must be sulfur undersaturated when it generates and must be transported into shallow crustal level without reaching sulfur saturation, as the first requirement. If the magma is sulfur saturated during magma generation, or saturated when it rises, PGE, which is selectively partitioned into sulfide melt, should be removed from silicate magma with immiscible sulfide melt. Under such conditions, the genesis of ore deposits is impossible. Therefore, existence of sulfur undersaturated magma is the most important requirement for the genesis of the nickel copper sulfide ore deposits. Vogel and Keays (1997) reported that the sulfur undersaturated magmas and sulfur saturated magmas can be discriminated by their Pd-Cu diagram. The sulfur

undersaturated magmas are relatively enriched in palladium against copper compared with sulfur saturated magmas.

The magmas that satisfy the above requirement are the high- temperature magnesium-rich magmas generated by sufficient degrees of partial melting of the mantle (Brooks et al., 1999). The magmas that are rich in sulfur, nickel, and PGE are generated by sufficient partial melting of the mantle. On the other hand, the lower temperature magmas generated by lower degrees of partial melting, such as MORB (Mid-Oceanic ridge Basalt), would remain PGE and sulfur in the mantle (Keays, 1997). PGE rich magmas generated by sufficient degrees of partial melting may be geochemically represented by the Low-Ti type magma. The magmas must rise to upper crustal level without contaminated by crustal materials. The magmas that satisfy these requirements may not have signs of crustal contamination shown by some geochemical values such as increasing La/Sm and Th/Nb.

The above discussion is about the nature of magmas. In order to give rise to PGE rich fertile magmas, mantle itself may have to be fertile. As mentioned in chapter II: 1-2, mantle peridotite and recycled oceanic crust are thought to be the origin of flood basalt magmas. The former is rich in chalcophile elements, but the latter is thought to be poor in chalcophile elements. Therefore, if we consider mantle peridotite as a original material, qualitatively, generated magma would be rich in chalcophile elements. However, in case the oceanic crust, the hybrid magma that includes considerable amount of mantle peridotite must be considered.

## (2) Sulfur Saturation of the Silicate Magma and Forming Immiscible Sulfide Melt

The above mentioned sulfur undersaturated magmas need to contaminate crustal materials in the magma chamber when these are transported to subvolcanic level. The solubility of sulfur in silicate magma decreases due to this assimilation. When the magma is saturated in sulfur, immiscible sulfide melt begins to be segregated from the silicate magma. At this time, copper, nickel, PGE are distributed into the sulfide melt and segregated from the silicate magma. Therefore, the silicate magma becomes markedly poor in these elements. This mechanism may trigger to generate orthomagmatic sulfide ore deposits.

As for the mechanism for the sulfur saturation of the silicate magma, assimilation of crustal materials rich in sulfur (the Noril'sk deposit, the Kambalda deposit), and mixing with a second magma that is already saturated in sulfur (Merensky reef) are presented (Keays, 1997). Beside these ideas, Campbell et al. (1983) argued that magma that is already very close to sulfur saturation can be brought to sulfur saturation through mixing with a second magma that is also close to sulfur saturation. There is a discord of opinion regarding the necessity of the existence of sulfur in crustal materials which contaminate. In case of the Noril'sk ore deposit, many authors have attributed the significantly heavy sulfur isotope signature of the ores to assimilation of sedimentary sulfur. However, Lightfoot and Hawkesworth (1997) have argued



that sulfur saturation occurred due to an increase of approximately 5 wt% in the SiO<sub>2</sub> content of the sulfur undersaturated magma, brought about by assimilation of 20-25% crustal contamination. However, regarding the sulfur saturation process of the komatiitic magmas, Keays (1995) have argued that contaminate must contain appreciable quantities of sulfur in order the magmas to be saturated in sulfur. Although the discussion is not settled with respect to this point, in order to assimilate appreciable quantities of crustal materials, high temperature magma is desirable. Therefore, the existence of picritic magma may be important.

### (3) Reaction of the Immiscible Sulfide Melt with Voluminous Silicate Magma

The immiscible sulfide melt can be generated by above process. But this process is not enough to generate economic ore deposits. In order to generate economic ore deposits, the sulfide melt should react with voluminous silicate magma rich in chalcophile elements. If the sulfide melt contacts the silicate magma with equilibrium, chalcophile elements are overwhelmingly distributed into sulfide melt. With regard to mafic to ultramafic magmas, experimentally determined partition coefficients for chalcophile elements between sulfide melt and the silicate melt ( $D^{\text{sulfide/silicate}}$ ) are as follows; Co: 30, Ni: 100 to 200, Cu: 600 to 1,000, PGE:  $10^4$  to  $10^5$ . Therefore, concentration of these elements into sulfide melt occurs in order of  $\text{PGE} \gg \text{Cu} > \text{Ni} > \text{Co} \gg 1$ . Furthermore, the larger the mass of silicate melt reacts with sulfide melt (R-factor) is, the more sulfide melt accumulates.

Where does this reaction occur effectively? In order the immiscible sulfide melt to react with voluminous silicate magma, the geological settings where voluminous silicate magmas are supplied must be required. Such requirement may be satisfied in a center of magmatic activity where crustal suture exists. Therefore, in the center of magmatic activity, if the economic magmatic sulfide ore exists, voluminous silicate magmas which are depleted in chalcophile elements due to reaction with sulfide melt may be expected to exist. The existence of such depleted magma may be an indicator of sulfide mineralization in the underground.

The following is the discussion concerning whether the Noril'sk deposits satisfy above requirements or not.

According to the genetic model of the Noril'sk deposits, the magma which triggered genesis of the deposits is the magma of the Tk lava (Fig. II-1-3-14). Brüggmann et al. (1993) showed that the Tk lava had high concentrations of Pt and Pd which range 9-13ppb, increasing with decreasing MgO content. Since the lava is Low-Ti type, the lava might have originated with fertile magma derived by relatively higher degree of partial melting of mantle. The Nd<sub>1</sub> and Nd<sub>2</sub> lavas that erupted following the Tk lava are depleted in Pt and Pd. The lavas indicate the evidence of crustal contamination and sulfide segregation. But the Mr and Mk lavas erupted following the Nd<sub>1</sub> and Nd<sub>2</sub> lavas recover Pt and Pd concentrations, ranging 2-9 ppb. Therefore

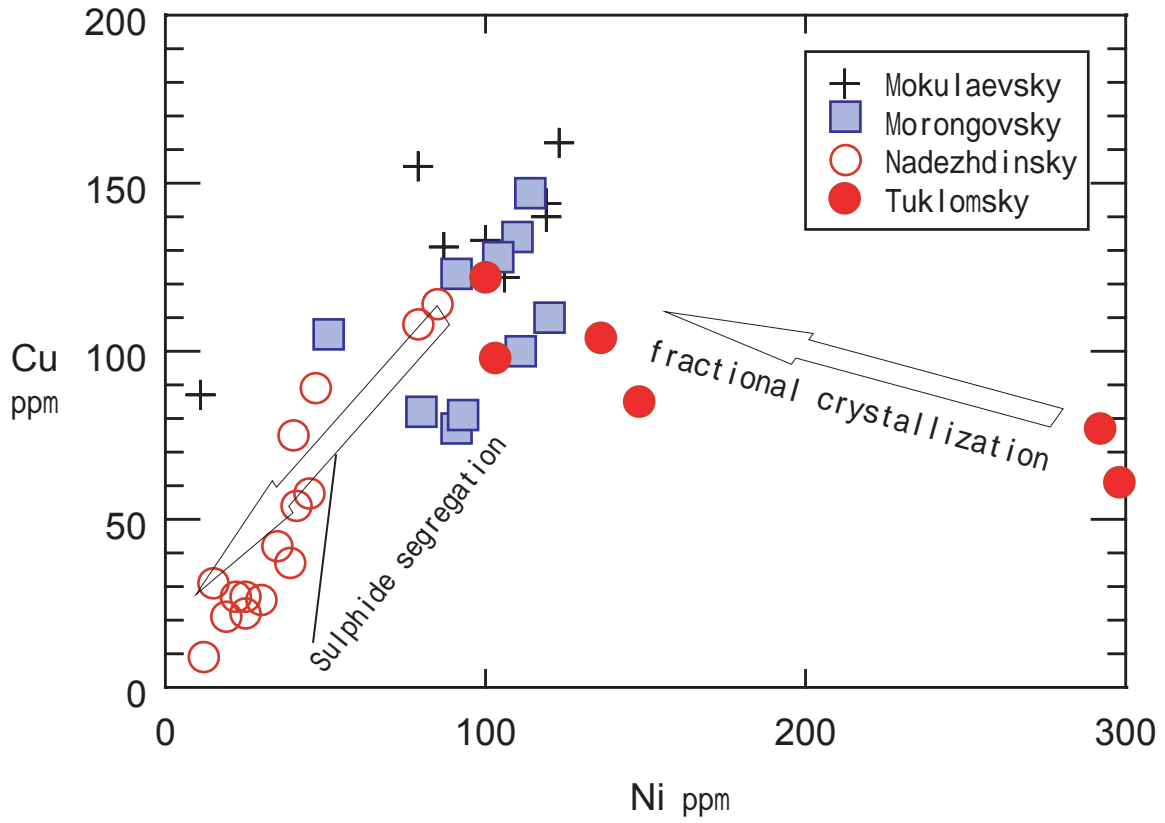


**Fig.II-1-3-16 Ni-Cu correlation in lavas from the Noril'sk region**  
Data from Brugmann et al.(1993)

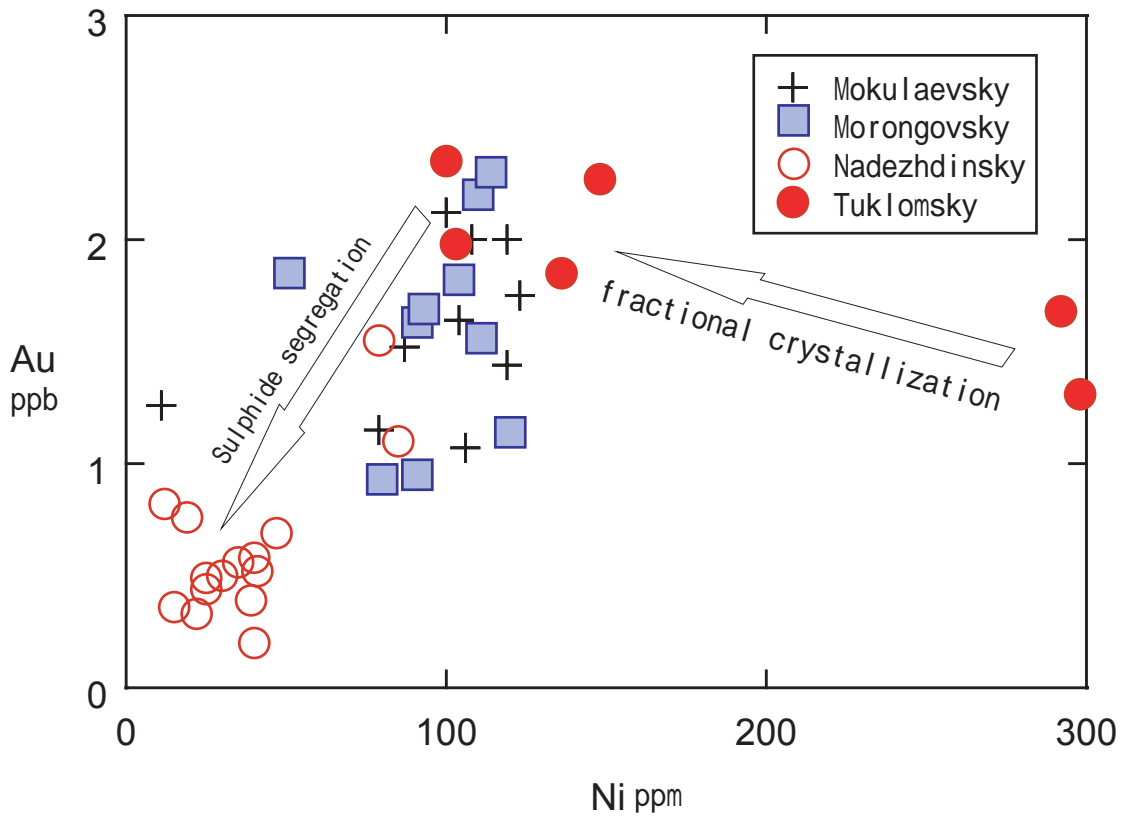


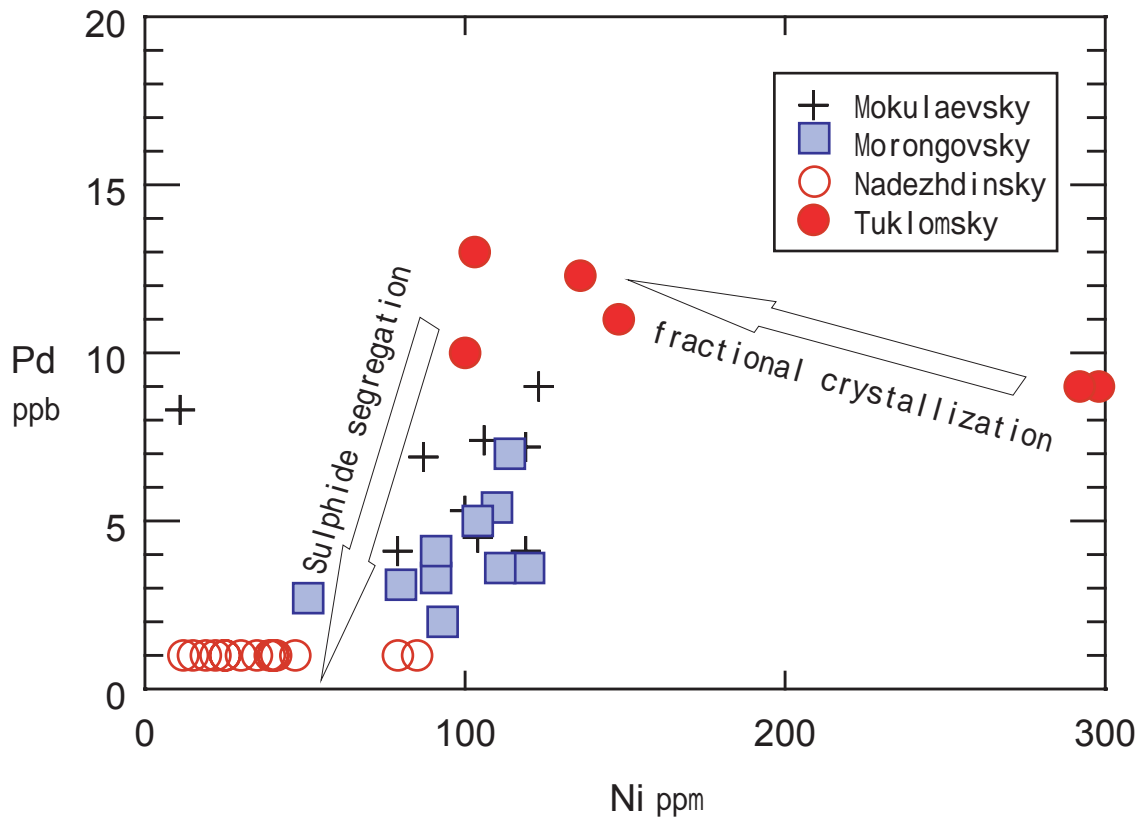
**Fig.II-1-3-17 Ni-Au correlation in lavas from the Noril'sk region**

the magmas generated the Noril'sk deposits are thought to be PGE rich fertile one derived from higher degree of partial melting.

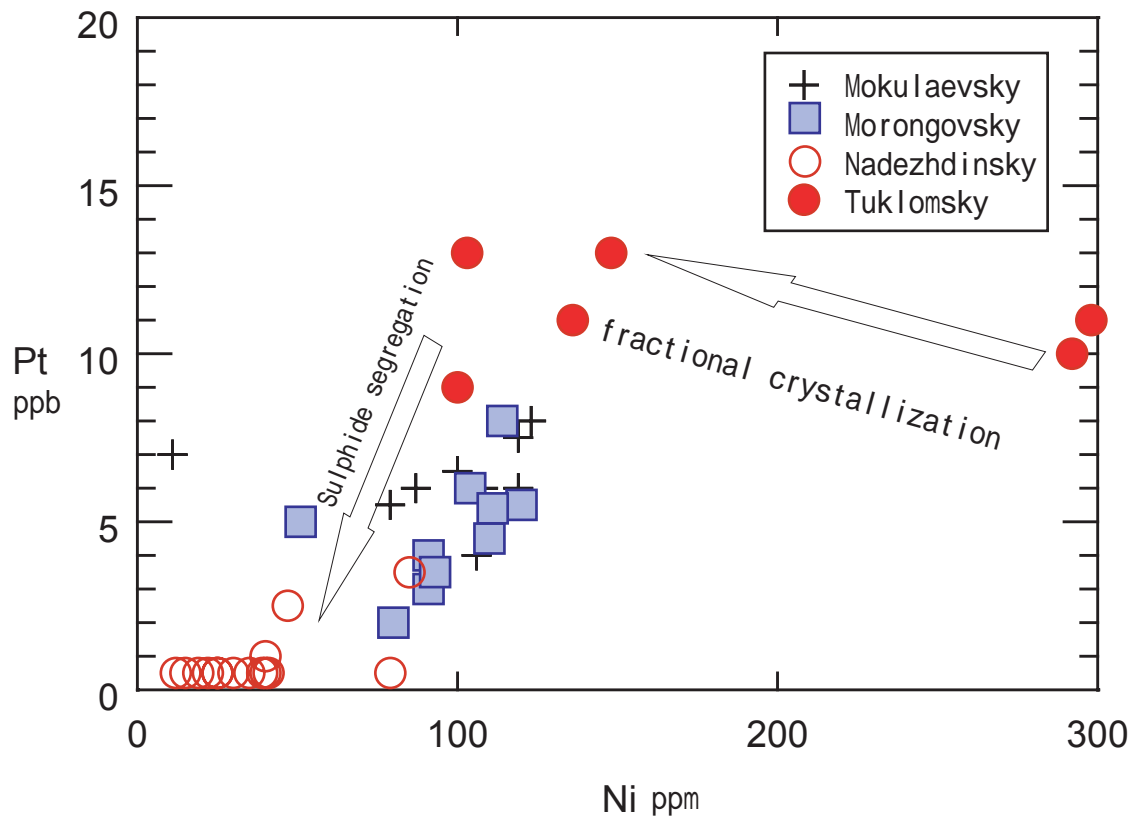
Fig. II-1-3-16 to Fig. II-1-3-19 illustrate the variation of Cu, Au, Pd, and Pt with Ni for the Tk, Nd, Mk, and Mr lavas. In these elements, only Ni is compatible to olivine, and strongly distributed into olivine during the fractional crystallization of mafic to ultramafic magmas. Therefore, the Ni content in the residual liquid decreases according to the progress of fractional crystallization. However Cu, Au, and PGE behave as incompatible elements and increase in residual liquid according to the progress of fractionation in the sulfur undersaturated magmas. Whereas in the sulfur saturated magmas, they are strongly distributed into immiscible sulfide melt and the magmas should be markedly depleted in these elements due to sulfide segregation. By these figures, we can recognize that, Cu, Au, Pd, and Pt gradually increase until Ni content reaches to 100 ppm by fractional crystallization. But when Ni content decreases less than 100 ppm, these elements begin to decrease rapidly. This may mean that the magma of the Tk lava reached sulfur saturation when Ni content reached to 100 ppm by fractionation of olivine, and removed immiscible sulfide melt. In the above four elements, the removal of Pd and Pt are remarkable. The reason is that Pd and Pt are distributed more strongly into sulfide melt than Cu and Au. Keays (1995) described that Pd content in a silicate magma decreases from 10 ppb to 2ppb if the magma separates only 0.01 % of immiscible sulfide under the assumption of the partition coefficient  $D^{\text{sulfide/silicate}}$  of 35,000 and R-factor of 10,000.

Fig. II-1-3-20 is the plot of above 4 lavas on Cu-Pd diagram by Vogel and Keays (1997). The Tk lavas which triggered the Noril'sk deposits are plotted in the field of sulfur undersaturated magmas. The Nd lavas generated by crustal contamination from the Tk lavas are plotted in the field of sulfur saturated magmas, indicating sulfide segregation. The Mr and Mk lavas erupted after the Nd lavas recover Pd content and are plotted again in the field of sulfur undersaturated magmas. Therefore, the Noril'sk deposits satisfy the first requirements (Generation of sulfur undersaturated magma and its transportation to shallow crustal level without reaching sulfur saturation) by the existence of the TK lava, and the second requirement (Sulfur saturation of the magma and forming immiscible sulfide melt) by the existence of the Nd lava.

The third requirement is also satisfied by the existence of the large volume of the Nd lava that is distributed around the center of the mineralization area of Noril'sk. The distribution of the Noril'sk deposits is controlled by the Noril'sk - Kharaelakh fault that is thought to be crustal suture which reaches mantle, and thick Nd lava distributes on and around this fault and the mineralized area of Noril'sk. This means that the Noril'sk deposits may exist in a eruption center of the Siberian flood basalts. Voluminous silicate magmas which originated the Nd lava might have ascended to upper crustal magma chamber through the suture zone such as the Noril'sk - Kharaelakh fault. In a magma chamber, these magmas might have reacted with



**Fig.II-1-3-18 Ni-Pd correlation in lavas from the Noril'sk region**  
Data from Brugmann et al.(1993)



**Fig.II-1-3-19 Ni-Pt correlation in lavas from the Noril'sk region**  
Data from Brugmann et al.(1993)

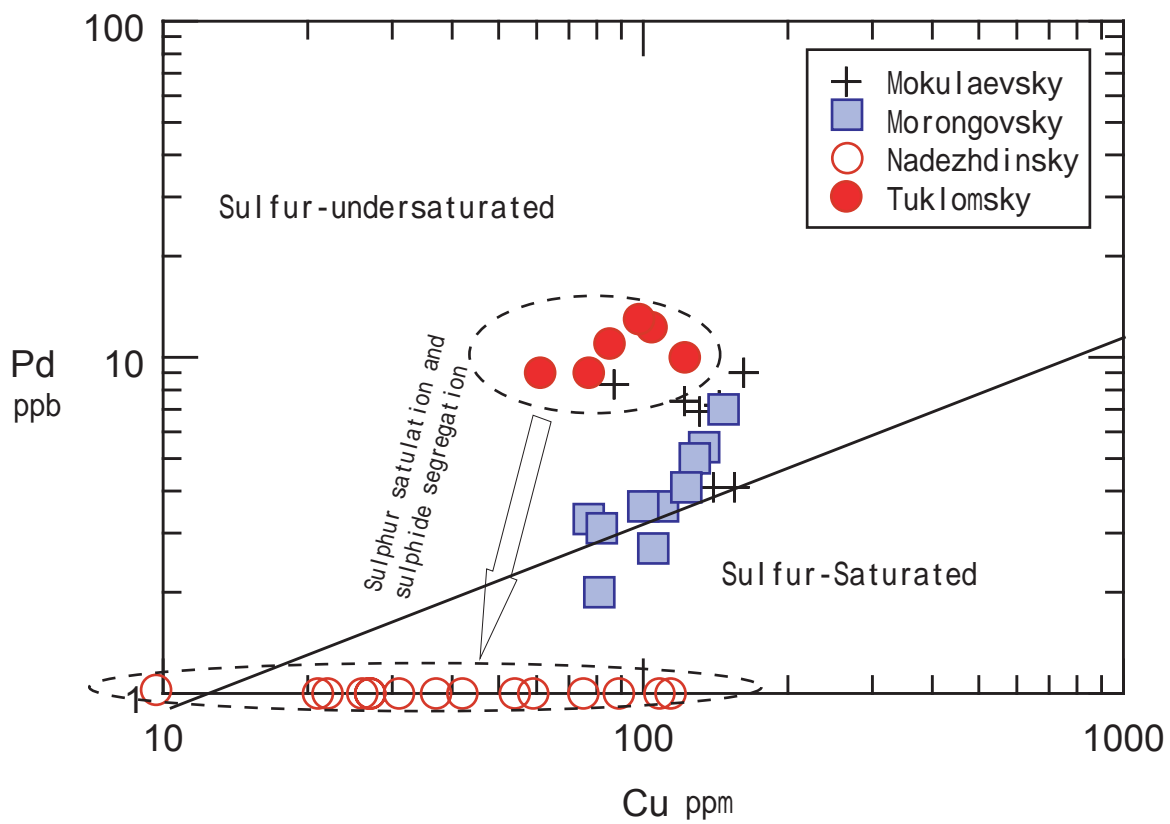


**Fig.II-1-3-20** Cu vs. Pd discriminant diagram for lavas from the Noril'sk region between the field of rocks formed by sulfur-saturated magmas and the field of rocks formed by sulfur-undersaturate magmas

sulfide melt which had been already formed from the Tk type magmas. As a result, chalcophile elements depleted Nd type magmas were formed. On the other hand, voluminous sulfide melt segregated from the magmas generated the Noril'sk deposits.

The ore generation in a center of magmatic activity in the Noril'sk region may be related to the types of intrusions. There are many types of intrusions in the Noril'sk region, but only the "fully differentiated" intrusions are accompanied by mineralization. The "fully differentiated" intrusions probably mean relatively larger scale ones than the other types, and magma injections into the intrusions must have occurred repeatedly in this type. These repeated magma replenishments into the intrusions may tend to occur in a center of magmatic activity.

As discussed above, the Noril'sk region has all of the theoretically considered requirements for generating the orthomagmatic sulfide deposits associated with mafic to ultramafic magma. Considering the genesis of the Noril'sk style deposits discussed here, it must be required to delineate the promising areas from the huge Parana basin area using the following geological settings as key factors in the exploration. If a area satisfied these geological environments, the immiscible sulfide precipitation and ore generation in the underground would be expected.

- a) The existence of Low-Ti and PGE rich magmas (lavas, intrusions)
- b) The existence of magmas showing the signatures of crustal contamination and sulfide segregation associated with above PGE rich magmas (lavas, intrusions)
- c) Being a center of the magmatic activity where crustal suture exists. Considering sills as conduits through which magmas of flood basalts ascend (Naldrett et al., 1992), the center of intrusive magmatism may be promising.
- d) The existence of picritic magmas (lavas, intrusions). The high temperature picritic magmas have higher potential to assimilate crustal materials to form immiscible sulfide melt. However, the amount of picritic magmas occupies only about 1 % of the total magmas of the Noril'sk region. It is desirable that the magmas are high temperature picritic composition to generate the Noril'sk style deposits, however, it is doubtful that picritic magmas were necessary or not.

The Skaergaard intrusion in East Greenland embeds a PGE reef type deposit. This is a representative PGE deposit, which is associated with differentiated tholeiitic basalt, and the sulfur saturation in this deposit is thought to have been caused by simple differentiation fractionation. In addition to the Noril'sk style deposit, this type of deposit also will be an important target in the Parana Basin area.

## 1-4 Geology and Geological Structure of Parana Basin

### 1-4-1 Tectonic Province of the South American Plate

#### (1) Effective Elastic Thickness of Lithosphere

M. S. M. Mantovani et al. (2001) calculated the effective elastic thickness ( $T_e$ ) of the South American plate using the tidal gravity anomaly, and discussed the relation to the tectonic province. The lithosphere is the outermost thin viscoelastic plate of the Earth. The underlying asthenosphere maintains the hydrostatic balance supporting the lithosphere mass by buoyancy. The elasticity of the lithosphere is shown by flexural rigidity ( $D$ ).  $D$  acts as the function of temperature gradient. Consequently, a cold lithosphere is expected to be strong and/or thick and a hot lithosphere is expected to be weak and/or thin. This  $D$  is commonly obtained by the coherence method, comparing the spectral distribution of gravity and topography. Ideally, for a maximum coherence value (=1) between the two distributions, a lithospheric load is totally supported by local isostasy ( $D \rightarrow 0$ ), while at its minimum (coherence = 0) the lithosphere block will support any load without deflection ( $D \rightarrow \infty$ ). The relation between flexural rigidity ( $D$ ) and the effective elastic thickness ( $T_e$ ) of the lithosphere is shown in the following equation.

$$T_e = [12D(1.0 - \nu^2)/E]^{1/3} \quad (1)$$

$E$  : Young's modulus;  $1.0 \times 10^{11} \text{ N m}^{-2}$

$\nu$  : Poisson's ratio; 0.25

There is a way to calculate the flexural rigidity  $D$  to know the response corresponding to the lithosphere's outer stress except the coherence method. The tidal power of the earth is used as the outer stress. The tidal power of the earth can be measured as the tidal gravity anomaly (TGA). M. S. M. Mantovani et al. (2001) newly devised the Regression method for the calculation of  $T_e$ , and calculated  $T_e$  in 50 earth tide observatories in the South America to present  $T_e$  geotectonic provinces. The former coherence method can't calculate  $T_e$  within a narrow tectonic unit, but the regression method made it possible.

#### (2) Earth Tide and Tidal Gravity Anomaly

The earth's tidal gravity is mostly caused by the attractions of the sun and the moon. The component of the earth's tidal gravity caused by the attraction of the moon (M2) can be observed more precisely than those caused by attractions of the other celestial bodies. The value of tidal gravity of the M2 component ( $M(\phi)$ ) can be derived by using the following

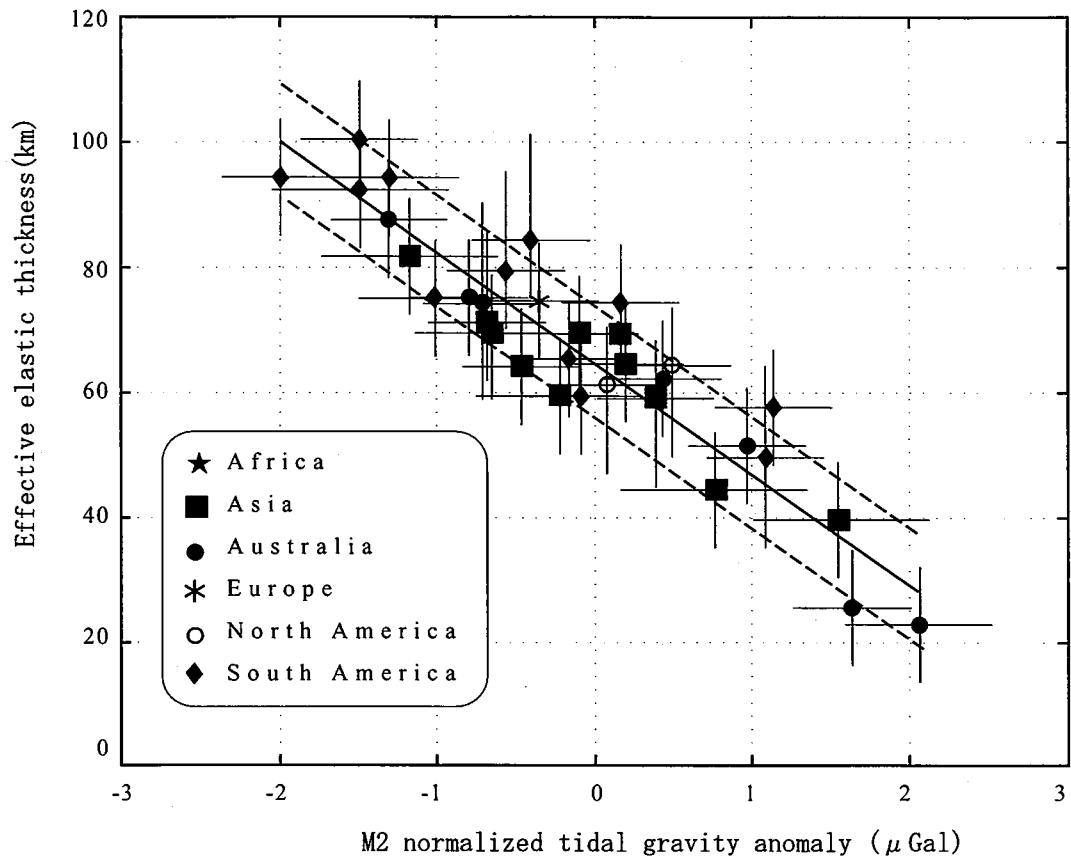


**Fig. II-1-4-1. World data set regression line (solid) and the standard deviation (dashed curves) of the calculated  $T_e$  for 36 stations. (M.S.M Mantovani et al., 2001)**



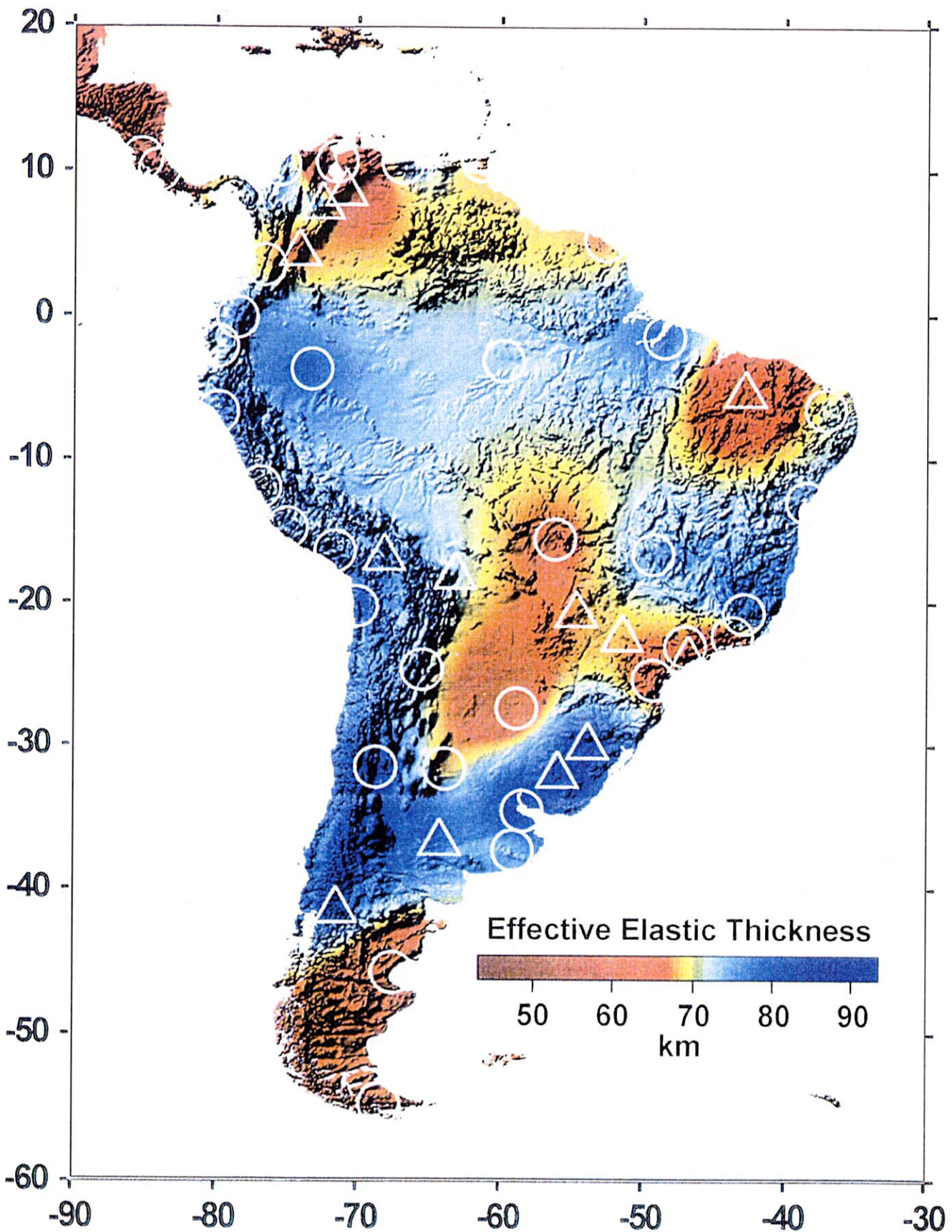


Fig. II -1-4-2. Effective elastic thickness ( $T_e$ ) pattern of the South American Plate .

Domains were defined within three intervals of  $T_e$  values:  $T_e < 68$  km (red: thin and/or hot);  $68\text{ km} < T_e < 72$  km (yellow/green) and  $T_e > 73$  km (blue: thick and/or rigid). White circles are locations of tidal gravity stations data and triangles are locations where exist published  $T_e$  estimates in correspondence with tidal gravity station. (M.S.M. Mantovani et al., 2001)

equation.  $\mathbf{A} = (A, \alpha)$  shows the observation data corresponding to M2 tidal gravity,  $\mathbf{M} = (M, \mu)$  the calculated value corresponding to M2 tidal gravity, and  $\mathbf{L} = (L, \lambda)$  the effect of the ocean load. The phase  $\mu$  of  $\mathbf{M}$  is assumed by 0. Under these conditions, TGA means the discrepancy between the observation data and calculation value of tidal gravity.

$$M(\phi) = 87.00 \frac{r(\phi)}{a_E} \cos^2 \phi \quad \mu \text{ Gal} \quad (2)$$

$$TGA = A \cos \alpha - L \cos \lambda - M \quad (3)$$

The Trans World Tidal Gravity Profile (TWTGP, 300 points,  $\mathbf{A}$ ) is maintained by the International Center for Earth Tides (ICET) in Brussels. The TGA values were calculated using TWTGP data of 50 observatories in South America. The  $T_e$  values at many observatories on each continent have been calculated using the Coherence method and Admittance method. For the 36 observatories in the world which have the  $T_e$  data, the correlation diagram between TGA and  $T_e$  was made and the equation (4) between TGA and  $T_e$  approximated by the least mean square method was calculated (Fig.II-1-4-1). Here,  $\cos^2 \phi$  is a term to adjust the latitude change of M2 tidal gravity. The correlation coefficient between TGA and  $T_e$  is 0.88. The calculated  $T_e$  values are shown in Fig.II-1-4-2.

$$T_e = 65.32 - 17.54 \frac{TGA}{\cos^2 \phi} \quad (4)$$

### (3) Effective Elastic Thickness of the South American Plate

The South American plate can be classified into a high  $T_e$  zone (low temperature and thick lithosphere;  $T_e > 72$  km, blue part) and a low  $T_e$  zone (high temperature and thin lithosphere;  $T_e < 68$  km, red part) (Fig.II-1-4-2). Compared with the geological structural map, the high  $T_e$  zone corresponds to the Rio de La Plata craton (1.9-2.2 Ga), the San Francisco craton (3.4-2.6 Ga) and the Amazon craton (3.1-2.5 Ga), the collision belts in Proterozoic and most of the Andes mountains (Fig.II-1-4-3). On the other hand, the low  $T_e$  zone corresponds to the Parana - Chaco basin, the Ponta Grossa arch, the Paranaiba basin, the Patagonia Peninsula, the coastal zone along the Calibian Sea and the Serra do Mal. The latter is the part where the magma has been active since the Triassic - Cretaceous. The transition  $T_e$  zone ( $68 \text{ km} < T_e < 72 \text{ km}$ , yellow part and green part) corresponds to the boundary zone of the geological tectonic provinces.

The flood basalt of Parana - Chaco basin had been most active from 133 to 130 Ma, and had floored among approximately 10 Ma. Most of the lava flows are considered to be originated from the mantle plume. The  $T_e$  value of the Ponta Grossa arch shows a low value of 58 km. The Ponta Grossa arch is inferred to be one of the feeders of Parana flood basalt on the basis of many dykes in the NE - SW direction. The Parana - Chaco basin shows the low  $T_e$  values from 47 to 68 km widely. The lithosphere in the Parana - Chaco basin is thinner under the extensional stress field and the Mantle Material below the basin is considered to exist at the



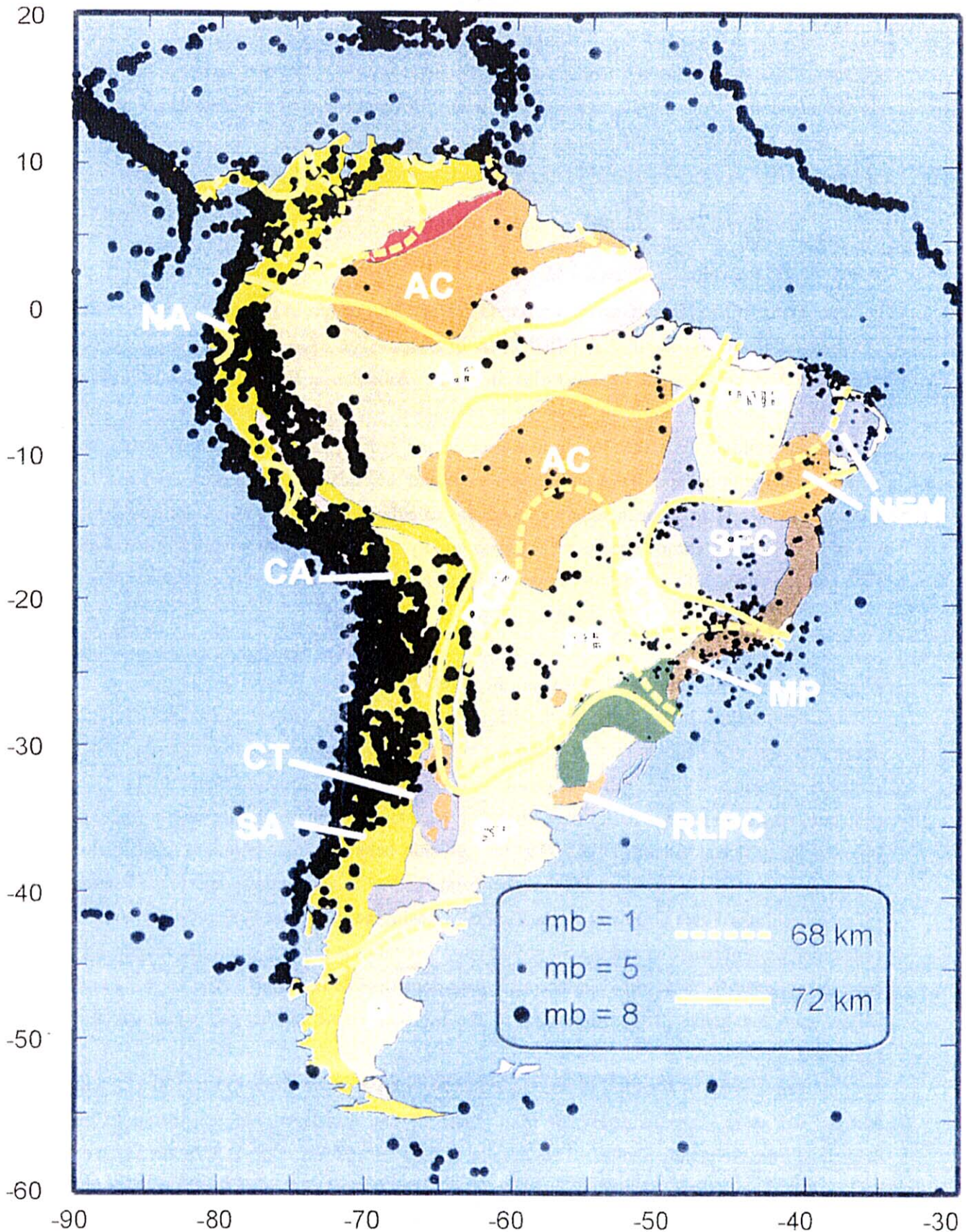


Fig. II-1-4-3. South America effective elastic thickness pattern in correspondence with tectonic provinces, seismic activity and the age provinces map of Condie (1982).

AB, Amazon Basin; AC, Amazon Craton; CA, Central Andes; CT, Chilena Terrane; MP, Mantiqueira Province; NA, Northern Andes; NEM, Northeastern Margin of South Atlantic Shield; P, Patagonia; PB, Parana-Chaco Basin; PCB, Phanerozoic collisional belts; PNB, Parnaiba Basin; RLPC, Rio de la Plata Craton; SA, Southern Andes; SFC, Sao Francisco Craton; SP, Southern Province. (M.S.M. Mantovavi et al., 2001)

shallower levels.

## 1-4-2 Geology and Geological Structure of Basement Rock

### (1) Geological Structure Province

The Gondwana continent is composed of Archean craton which was made blocks by faults and the surrounding folding zones in the Brazilian-Pan African orogenic movement (800-450 Ma) (Fig.II-1-4-4). A part of the basin in the early Proterozoic to Cambrian was formed in the last jointing stage of Gondwana continent which is composed of clastic rocks, carbonate rocks and igneous rocks. The structures of the basin and the folding zone in the Brazilian-Pan African orogenic movement changed remarkably in the Phanerozoic. The geology and geological structure of Parana basin is shown in Fig.II-1-4-5.

**Paraguay-Araguay Belt:** The belt deposited along the south-eastern margin of the Amazon craton in the early Proterozoic to Cambrian. The sedimentary rocks become more abyssal sedimentary facies toward the east. The belt is cut by the Transbrazilian fault in the NE-SW direction. The eastern part of the belt bounded by the fault continues below the sediments of the Parana basin. The belt runs in the N-S direction to Paraguay along the western margin of the Parana basin and runs in the ENE-WSW direction along the northern margin of the Parana basin.

**Western Goias Belt:** The belt is located in the northern side of Parana basin and is composed of orthogneiss, volcanic rocks and sedimentary rocks of the late Proterozoic (930-600 Ma). The volcanic rocks are originated from the oceanic origin geochemically. The crust of oceanic origin resulted in the rapture between the Amazon craton in the west and the San Francisco craton in the east. Many kind of granitic rocks (590-480 Ma) intrude into the belt.

**Brazilia Belt:** The belt is located in the north-eastern margin of the Parana basin as well as in the western margin of San Francisco craton. The belt is folded and thrust, and is composed of mica gneiss and diabase. The belt seems to have been once a subduction zone.

**Goias Massif:** The massif is composed of granitic rocks and green rocks of the Archean, and orthogneiss of the early Proterozoic (780-800 Ma). This Massif was affected by metamorphism of the Brazilian-Pan African orogenic movement. Mafic and ultramafic rocks intruded into granitic rocks and orthogneiss in the eastern margin of the Massif.

**Dom Feliciano Belt:** The belt is located in the direction of ENE-WSW in the eastern margin of the Parana basin. It is composed of granite, migmatite, orthogneiss and granulite. It is also distributed in the southeastern side of the Rio de La Plata craton and Ribeira Belt.

**Ribeira Belt:** It is located in the eastern margin of the Parana basin and is exposed in the direction of ENE-WSW. It is composed of volcanic rocks, sedimentary rocks, orthogneiss, amphibolites, mafic and ultramafic rocks, and granulites of the Proterozoic to the early



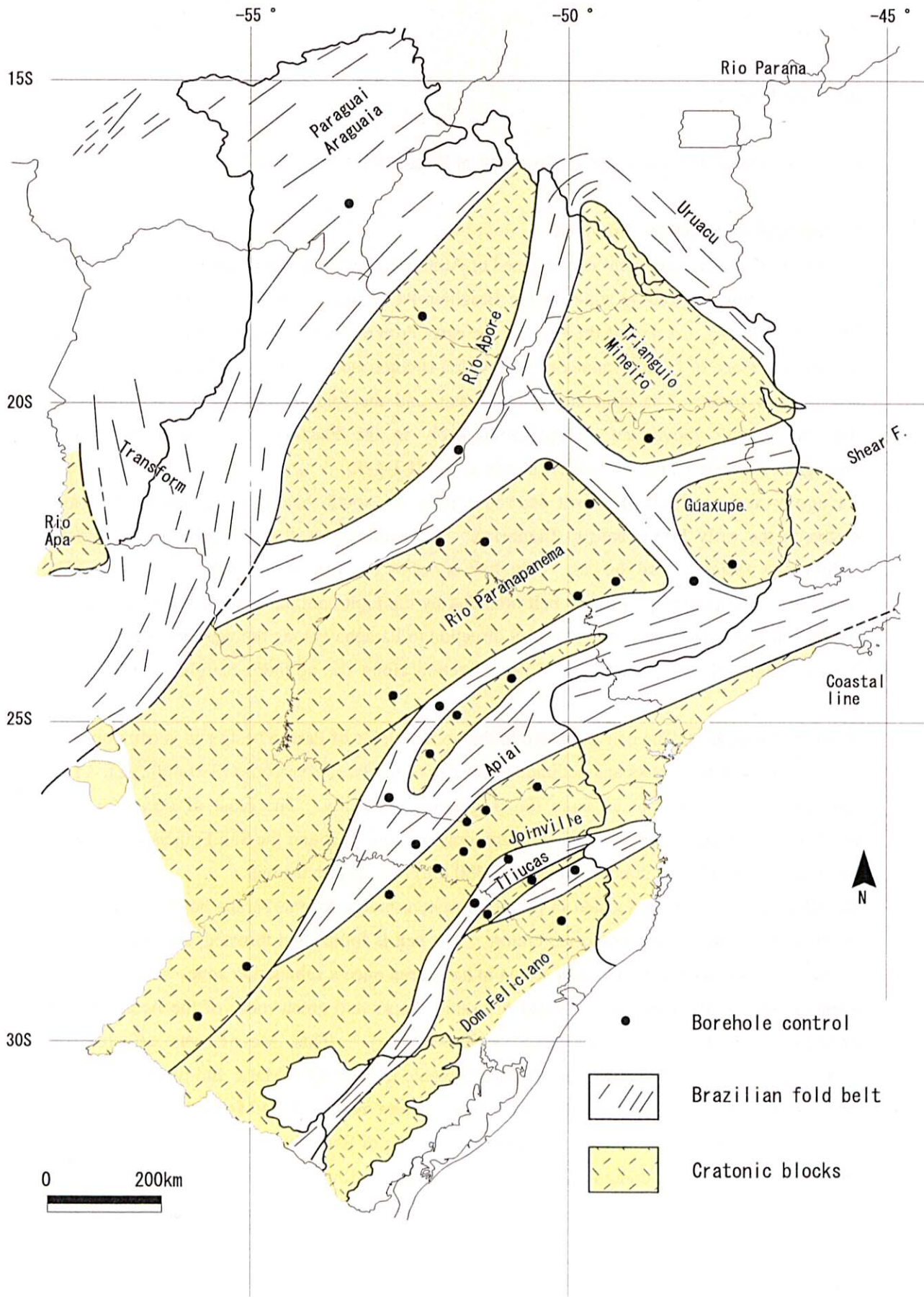


Fig. II-1-4-4. Schematic map of basement and tectonic framework of the Parana basin (E.J.Milani.,1998)



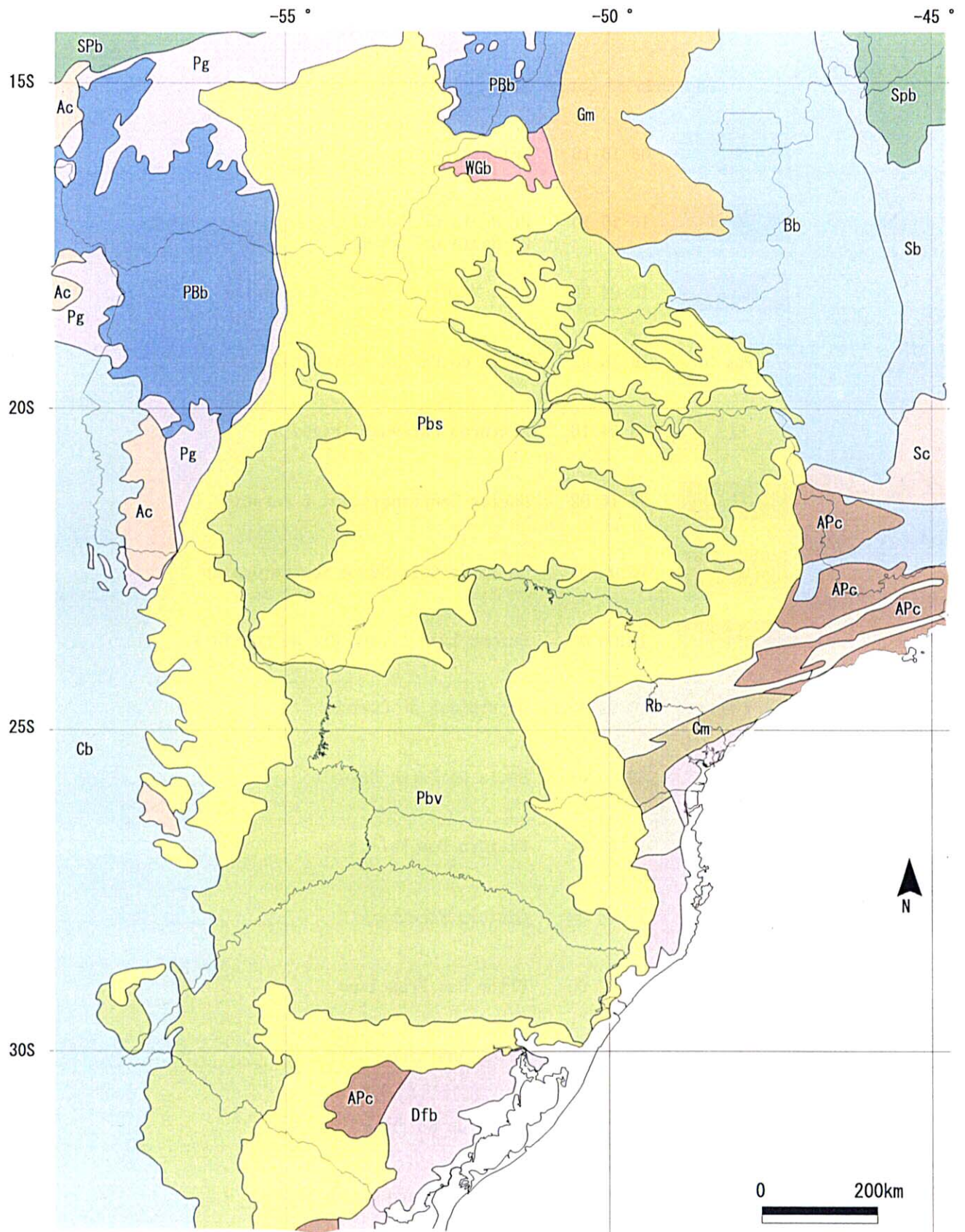


Fig. II-1-4-5. Geological and tectonic map around the Parana basin (modified by Mantobani et al., 1991)

Convendo de cores (RGB) Descrido

Bb	06 16 16	Faixa Brasilia
PBb	16 16 14	Pt-Bacia do Pantanal Ba-Bacia do Bananal
WGb	16 04 06	Arco Magmtico do Oeste de Goias
Pbs	16 16 02	Bacia do Parana-sedimentos
Pg	08 04 16	Cinturao Paraguai-Araguaia
SPb	06 16 02	Bacias Sanfranciscana e Parecis
Gm	16 06 02	Macio de Gois/Nappe Socorro-Guaxup
APc	16 06 00	Crtons:Luis Alves, Rio de La Plata
Cm	10 02 00	Microplaca de Curiuba
Pbv	08 16 04	Bacia do Paran-Basalto
Dfb	14 08 08	Cinturo Dom Feliciano
Rb	14 06 00	Cinturo Ribeira
Sc	12 02 00	Crton Sao Francisco
Ac	14 04 00	Crton Amaznico
Sb	06 14 14	Bacia do So Francisco
Cb	08 16 10	Bacia do Chaco

Paleozoic. The belt thrusts up the Curitiba microplate which is distributed in the SE direction.

**Rio de la Plata-Luis Alves Craton:** The Rio de La Plata craton is exposed in the NE-SW direction in the southern to eastern margin of the Parana basin. The Luis Alves craton, which is located in the southeast of Parana Province, is composed of granulites and the Campo Alegre Formation. The granulite metamorphosed in the Proterozoic. The Campo Alegre Formation includes molasse sediments and is composed of volcanic rocks and sedimentary rocks (580 – 500 Ma).

## (2) Arch and Lineament

The main tectonic directions in the basement of the Parana basin are the NE-SW and NW-SE directions. The tectonic directions of E-W and N-S partly also are observed (Fig.II-1-4-4, Fig.II-1-4-6). The tectonic direction of NE-SW is dominant in thrust and folding of the late Proterozoic in the basement. The tectonic direction of NE-SW corresponds to the direction of Brazilian-Pan African orogenic movement. The tectonic zone in the direction of NE-SW acted again in the Phanerozoic as the fractured zone within the crust in the compressive stress field.

In the late Ordovician, the first subsidence of the basin occurred, being accompanied with lateral fault in the direction of NE-SW. The re-movement of old lineament affected the depocenter and drainage of the basin and finally controlled the sedimentation of the basin. The dykes and sills along fractures in the direction of NE-SW are few on the ground surface.

Another dominant tectonic direction of the Parana basin was brought about due to the uplifting movement from the Devonian to the late Jurassic and the rifting of the South Atlantic Ocean in the Cretaceous. The lateral strike faults (shear fracture) within and in the margin of the basin were formed in the direction of NW-SE. Many tholeiitic dolerite dikes are filled up in the fractures of the NW-SE direction. The tectonic movement in the NW-SE direction also formed the Ponta Grossa arch, Campo Grande arch and Rio Grande arch, Guapiara fault, Rio Piquiri fault, Rio Uruguay fault, Sao Geronimo fault, Rio Alonzo fault and Ferreira fault, and Torres syncline. These cross the long axis of the basin. It is more than 600 km in length and regarded as one of the feeders of the flood basalt lavas. Many dolerite dykes and sills are observed in the direction of NW-SE.

The tectonic direction of E-W is presumed to begin at the same time as the rupture of the Gondwana continent which mean the opening of the Atlantic Ocean in the Cretaceous.

Asuncion Arch runs in the direction of N-S from the eastern part of Paraguay to Mato Grosso do Sul in the western part of the Parana basin. The arch shows the gentle flexure to the west. The earlier orogenic movement in the western margin of the Gondwana continent is presumed to have involved the Asuncion arch. The Goiania flexure zone in the NW-SE direction is located in the northeastern margin of the Parana basin. It show strong magnetic anomalies



and be accompanied with dykes of alkaline rocks and kimberlites.

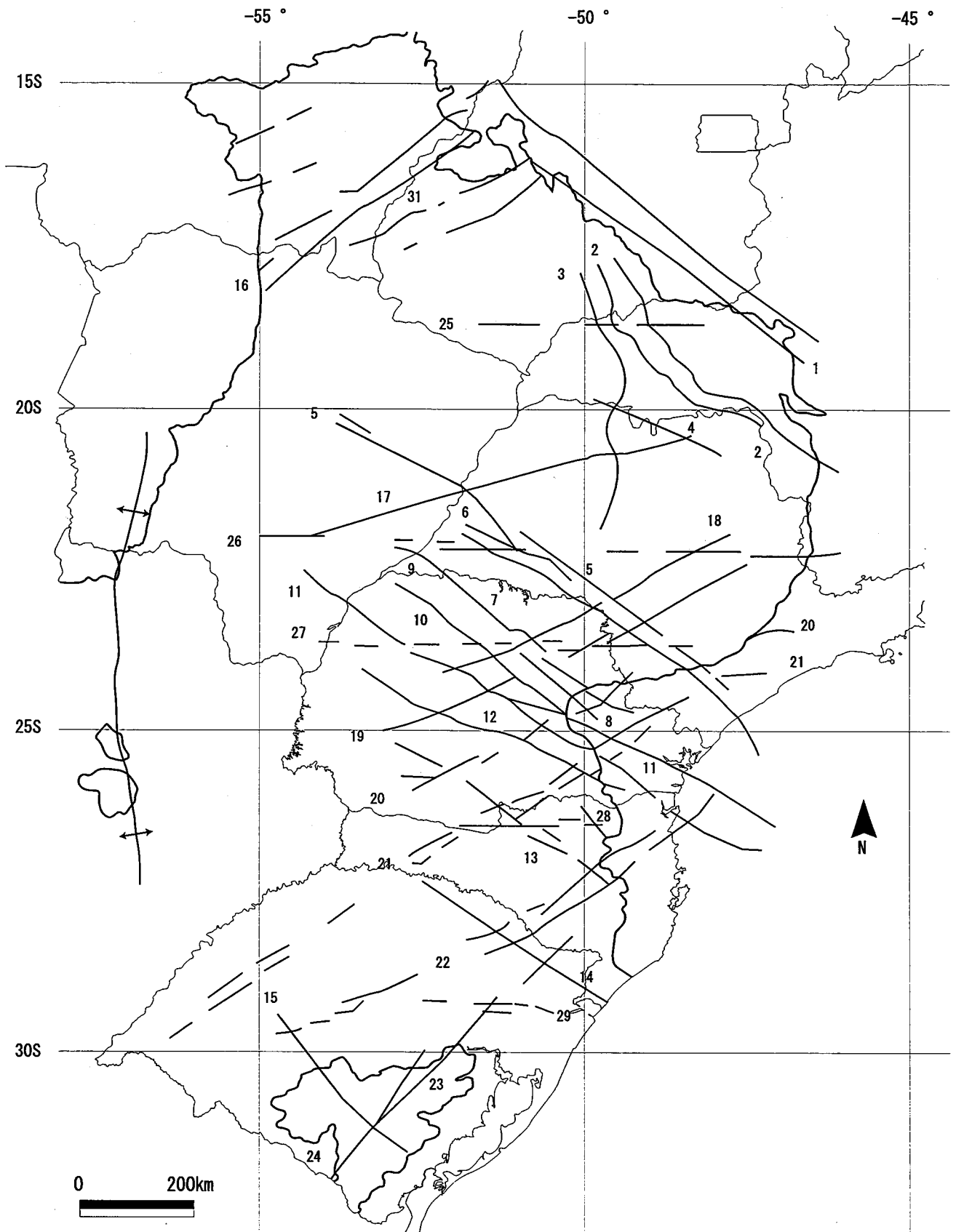
### 1-4-3 Geology and Geological Structure of Basin

The Gondwana continent was undergone successive collisions and tectonic collages during the Brazilian-Pan African orogenic movement and later become a stable continent from the late Pre-Cambrian to the early Paleozoic. The sedimentary rocks are deposited widely from the Paleozoic to Mesozoic in many basins of the Gondwana continent under the extensional stress field. These basins are called intracratonic basins. The Gondwana continent was ruptured in the Mesozoic. Each segment of continents (South America, Africa, Australia, India, Antarctica) exist several thousand kilometers apart. However, there are many resemblances between the geology of basins on each continent.

The Parana basin is one of the intracratonic basins which is located in the middle to the south-eastern part of the South American continent. The total area of the basin is 1,400,000 km<sup>2</sup> which consists of 1,100,000 km<sup>2</sup> on the Brazilian side and 300,000 km<sup>2</sup> on the Uruguay, Paraguay and Argentine sides. The Parana basin has an elliptic shape with the sedimentary axis in the NNE-SSW direction. The direction of the axis is in accordance with the direction of the Parana River. The extension of the basin is 1,750 km from the NNE-SSW direction and 900 km from ESE-WSW direction (Fig.II-1-4-5, Fig.II-1-4-7).

The sediments of the Parana basin are composed of glacier sediment, desert sandstone and marine sediments. The sediments were formed continuously changing the features as they influenced by several climatic and tectonic changes. The sediments of the basin partaccumulated to be more than 6,000 meters thick. Besides, the continental flood basalt which is called the Serra Geral Formation overlies the sediments of the basin. The Serra Geral Formation a large amount of volcanic sequences which is 1,723 meters in maximum thickness. All the sediments of the Parana basin, from the late Ordovician to the late Cretaceous, can be reviewed by six Supersequence (Fig.II-1-4-8, Milani et al (1997)).

The geology of the Parana basin can be compared with the world wide transgression and regression (period 390 Ma). The Rio Ivai Supersequence was deposited as the basal sediments of the basin in the Ordovician to the Silurian. In the Devonian, the Parana Supersequence was deposited by second transgressions. The Parana basin was located in the south-east marginal part of the Gondwana continent and was a big bay opening toward the paleo-Pacific Ocean. In the early Carboniferous, the Hercynian orogenic movement occurred and the sediments of the basin were eroded for a long time and became a peneplain. In the late Carboniferous to the Triassic, the Gondwana I and the Gondwana II Supersequences including glacial sediments were widely deposited for a long time. In the Triassic to the Jurassic, the Parana basin was completely isolated from the ocean, and became the big and dry Gondwana continent. In the



NW-SE direction: ① Arco de Alto Parnaíba; ② Flexura de Goiânia; ③ Baixo de Ipiacu/Campina Verde; ④ Alto de Cardoso; ⑤ Zona de Falha de Guapiara; ⑥ Falha de Santo Anastácio; ⑦ Falha de São Jerônimo-Curiúva; ⑧ Arco de Ponta Grossa; ⑨ Zona de falha Curitiba-Maringá; ⑩ Falha do Rio Alonzo; ⑪ Zona de Falha Cândido de Abreu-Campo Mourão; ⑫ Lineamento do Rio Piquiri; ⑬ Zona de Falha Cacador; ⑭ Sinclinal de Torres; ⑮ Arco do Rio Grande; ENE-WSW direction: ⑯ Zona de Falha Transbrasileira; ⑰ Lineamento de Aracatuda; ⑱ Falha de Guaxupe; ⑲ Falha de Jacutinga; ⑳ Zona de Falha de Taxaquara; ㉑ Zona de Falha de Lancinha-Cubatao; ㉒ Zona de Falha Blumenau-Soledade; ㉓ Falha do Leão; ㉔ Falha de Acotea; E-W direction; ㉕ Lineamento Cassilândia; ㉖ Lineamento Moji-Gua-Dourados; ㉗ Lineamento de São Sebastião; ㉘ Lineamento de Taquara Verde; ㉙ Lineamento de Bento Gonçalves. N-S direction; ㉚ Arco de Assunção; ㉛ Domo de Araguainha (Zalan et al., 1988, 1990).

Fig. II-1-4-6. Principal archs, faults in the Parana basin (M. C. L. Quintas, 1995).

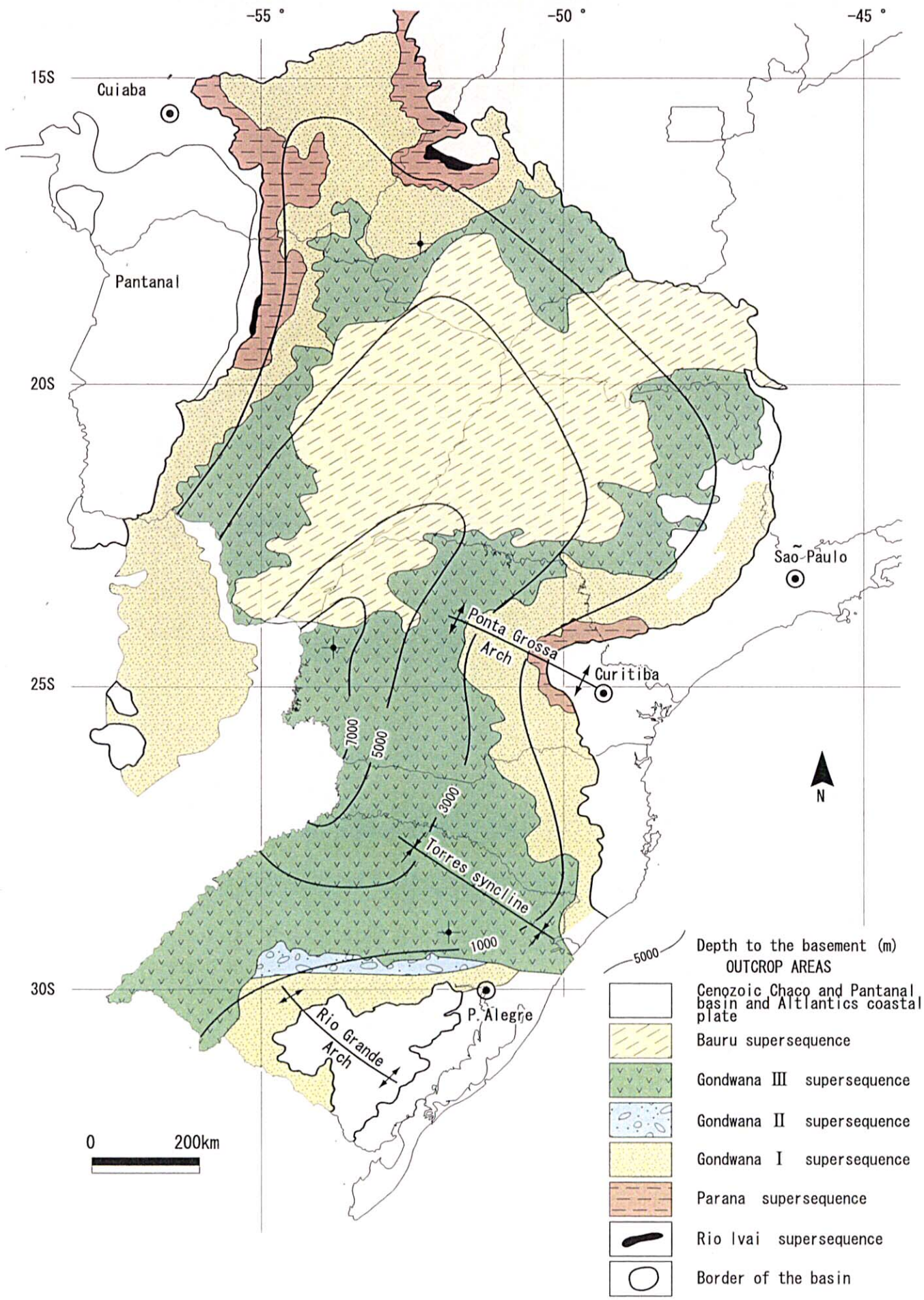


Fig. II-1-4-7. Simplified Geological map of the Parana basin, with tectonic elements and geographic references.(E.J.Milani et al, 1995 ).

early Cretaceous, a large volume of tholeiitic flood basalt magma which is the Gondwana III Supersequence flowed out and the rapture of the Gondwana continent began successively.

Rio Ivai : Ordovician – Silurian (450-428 Ma)

Parana : Devonian (410-365 Ma)

Godwana I (GI): late Carboniferous – early Triassic (310-245 Ma)

Gondwana II (GII): middle Triassic (237-218 Ma)

Gondwana III (GIII): late Jurassic – middle Cretaceous (150-128 Ma)

Bauru: late Cretaceous (115-65 Ma)

### (1) Rio Ivai Supersequence

The oldest sediment of the Parana basin is the Rio Ivai Supersequence deposited in the late Ordovician to the early Silurian (Fig.II-1-4-9). The Rio Ivai Supersequence overlies on the initial unconformity of the Phanerozoic, which is composed of basal conglomerate, arkose sandstone, quartzite (Alto Garcas Formation), diamictite (Lapo Formation) and marine shale including fossils (Vila Maria Formation). Vila Maria Formation was deposited in the maximum flooding surface (MFS). The Rio Ivai Supersequence was eroded later and became discontinuous and thinner.

The Rio Ivai Supersequence is several meters to 362 meters thick in Brazil. It becomes thicker toward the west to reach more than 1,100 meters in Paraguay. Still farther west, in Bolivia, the sedimentary rocks which correspond to the Rio Ivai Supersequence were deposited on the marine rift, have the thickness of several thousand meters. The Asuncion arch had never formed in this period. The Rio Ivai Supersequence is considered to have been deposited in the complete open bay of the south-western margin of the Gondwana continent. The subsidence velocity of the basin is considered to be faster due to a strong extensional stress field. This extensional stress field formed syncline and intracratonic basin in the marginal part of the Gondwana continent related to the late Ordovician Oclloyic orogenic movement.

### (2) Parana Supersequence

Parana Supersequence is composed of Furnas Formation and Ponta Grossa Formation in the Devonian. The last sedimentary rock of Parana Supersequence was mostly eroded during the Sub-Pennsylvanian period. The thickness of the Formation is 900 meters thick (Fig.II-1-4-10).

The Furnas Formation is composed of arkosic basal conglomerite and medium to coarse grained whitish kaolinitic sandstone. The Ponta Grossa Formation is composed of neritic black to grayish shale (including organic matter), siltstone and sandstone. The upper part of the Furnas Formation and to the shale of the Ponta Grossa Formation are transgressive sedimentary rocks. The boundary of the Furnas Formation and the Ponta Grossa Formation

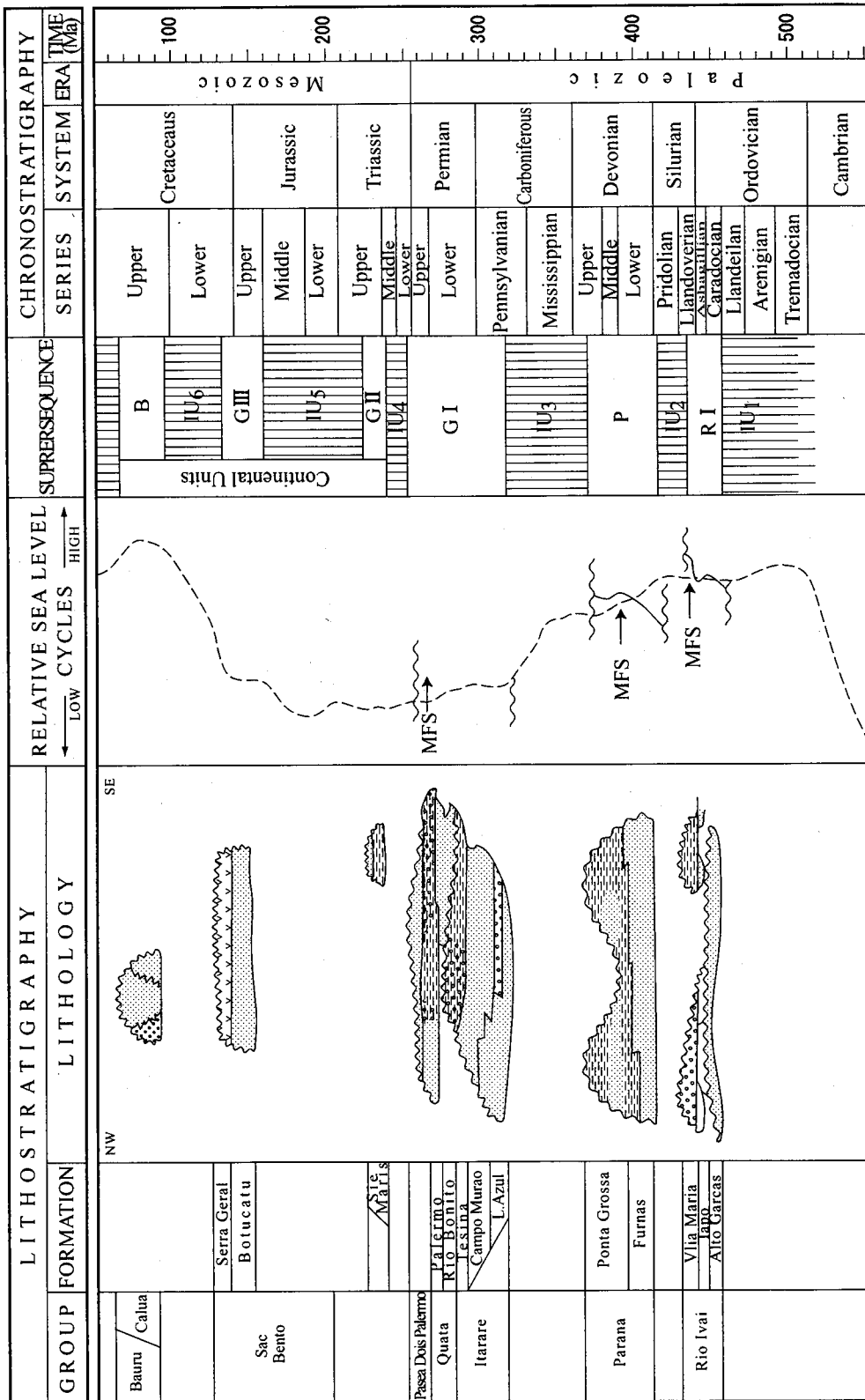


Figure II-1-4-8. Sequence-stratigraphic chart for the Parana Basin.

Relative sea level second order cycles derived from basin's stratigraphic record and referred to Vail's (1977) first order eustatic cycles (dotted line). The correlation of supersequences with absolute geologic time is approximate. Time table after Cowie & Bassett (1989). IU - interregional unconformity. Lithostratigraphic names for the Upper Permian/Lower Triassic interval: (E.J. Milani et al., 1998)

shows the second maximum flood surface (MFS). The sandstone of the Furnas Formation is 250 meters thick on average. Therefore, the thickness change in Parana Supersequence can be regarded as the thickness change of the Ponta Grossa Formation. The Ponta Grossa Formation thickens in the northern part and the middle part of the Parana basin. These subsidence zones are called the Alto Garças and the Apucarana. There is an upheaval zone between these subsidence zones and it is called as the Torres Lagos-Campo Grande arch. The Parana Supersequence is also present in the eastern part of Paraguay. The sedimentary rocks of 850 meters in thickness of the Parana Supersequence were confirmed by drilling around the Asuncion arch.

The subsidence velocity of the basin was slow due to inactive tectonic movement. This feature can be regarded by the fixed thickness of the Furnas Formation which is distributed all over the basin. Since the deposition of the Furnas Formation, the marginal part of the Gondwana continent became the compressive stress field and the lithosphere flexured. The subsiding velocity gradually sped up. The southern part of the basin was eroded from the Ordovician to the early Permian.

### (3) Gondwana I Supersequence

The Gondwana I Supersequence is the thickest of the other supersequence in the Parana basin (Fig.II-1-4-11). The thickest part of the Supersequence coincides with the axis of the present basin. In the early carboniferous, the topographic and climatic changes in the south-western marginal part of Gondwana continent involved lacuna (sedimentation stop) widely. In some parts, the lacuna had continued 45 Ma which was the longest lacuna in the Parana basin. The lacuna caused the wide unconformity of the Sub-Pennsylvanian and the lack of Mississippian.

A remarkable environmental change can be observed between the marine shale of the Ponta Grossa Formation in the Parana Supersequence and the glacier sediments of the Itarare Formation in the Gondwana I Supersequence. Two reasons for this environmental change can be considered. One is the Hercynian orogenic movement which had continued approximately 50 Ma and successively the peneplanation. Another is denudation of glacier and re-sedimentation after the glacier epoch. In the late Carboniferous to Permian, a transgression occurred due to the melting of the glaciers and the rise in the sea surface. In this period, the Itarare Formation, Rio Bonito Formation and Palermo Formation were deposited. The upper part of Palermo Formation was deposited during the maximum flood surface (MFS). The cycle of transgression-regression finished to form the red rock formation in the early Triassic. The Itarare Formation is mainly composed of diamictite and thick sandstone layers which are intercalated with diamictite. The Rio Bonito Formation is composed of coal (delta sediment), siltstone shale and sandstone. The Palermo Formation is composed of siltstone and sandstone.

The compressive stress field gradually increased in the south-western marginal part of Gondwana continent, and the Asuncion arch rose outside the western part of the basin. Finally, in the late Permian to the early Triassic, the basin was isolated from the ocean by the Asuncion arch. Since this period, the desertification and erosion continued for a long period within the continent. The Assitencia Formation overlies the Irati Formation and is composed of vitrinitic black shale, marl and limestone. These show rhythmical alterations with a thickness of approximately 10 centimeters. The Assitencia Formation includes evaporite layers of several tens centimeters in thickness in some limited shallow basins. The subsidence of the middle part of the basin lasted for a long period, however, the subsidence velocity gradually decreased in the late Permian to the early Triassic due to an extensional stress field.

#### (4) Gondwana II Supersequence

The Cape La Venrtana orogenic movement occurred in the southern margin of the Gondwana continent in the middle to late Triassic. The local upheaval and the lateral fault rock by the orogenic movement occurred along the lineaments of the basement. In the period, the extentional stress fields sometimes occurred in the south-western part of the Gondwana continent and they involved a graven. The Santa Maria Formation was deposited in a part of the Parana basin in the middle to the late Triassic (Fig.II-1-4-12). The Santa Maria Formation is composed of fine to medium grained white sandstone and conglomerate, and partly red shale, siltstone, calcrete and gypsum layers. These components are fluviatile-lacustrine deposits. The subsidence velocity was slow due to the Gondwana continent was stable.

#### (5) Gondwana III Supersequence

The lower part of the Gondwana III Supersequence is composed of fine to medium-grained quartzite and eolian sandstone which is called the Botocau Formation (Fig.II-1-4-13). Parana flood basalt lava is distributed in the whole Parana basin which covers or intercalate the Botocau Formation. The magma activity of the Parana flood basalt formed huge volumes of lava and dykes and has a maximum thickness of 2,000m under the maximum extentional stress field in the early Cretaceous. The subsidence velocity was the fastest due to the magma activity of Parana flood basalt.

#### (6) Bauru Supersequence

In the middle to the late Cretaceous, the flexure pilling up of flood basalt lava involved the subsidence of the basin and the Bauru Supersequence is deposited. The Bauru Supersequence is composed of sandy conglomerate including many kinds of gravel. The Bauru Supersequence is distributed in the central part to northern part of the Parana basin



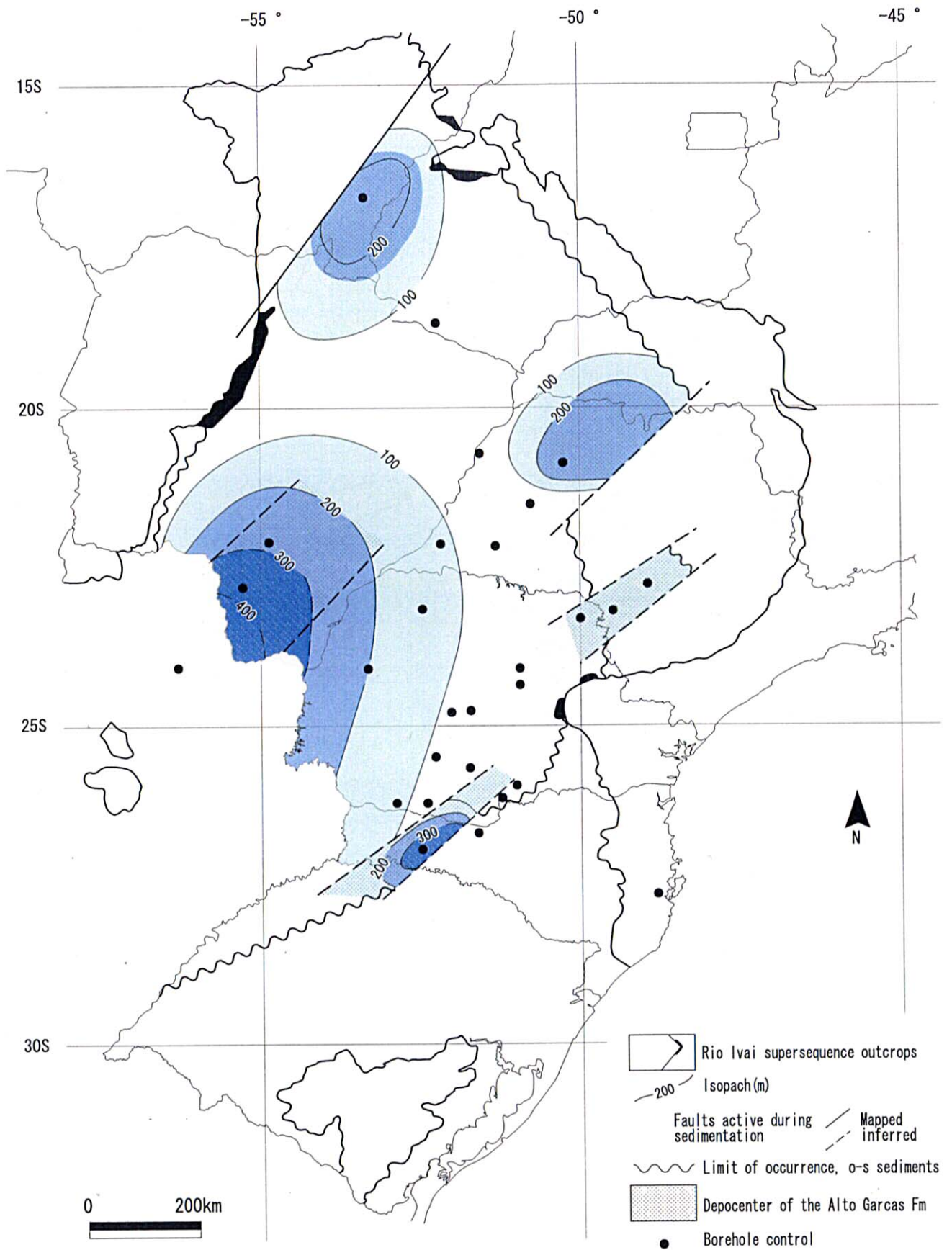


Fig. II-1-4-9. Isopach map of the Rio Ivai Sequence (E. J.M.Milani at al., 1998).



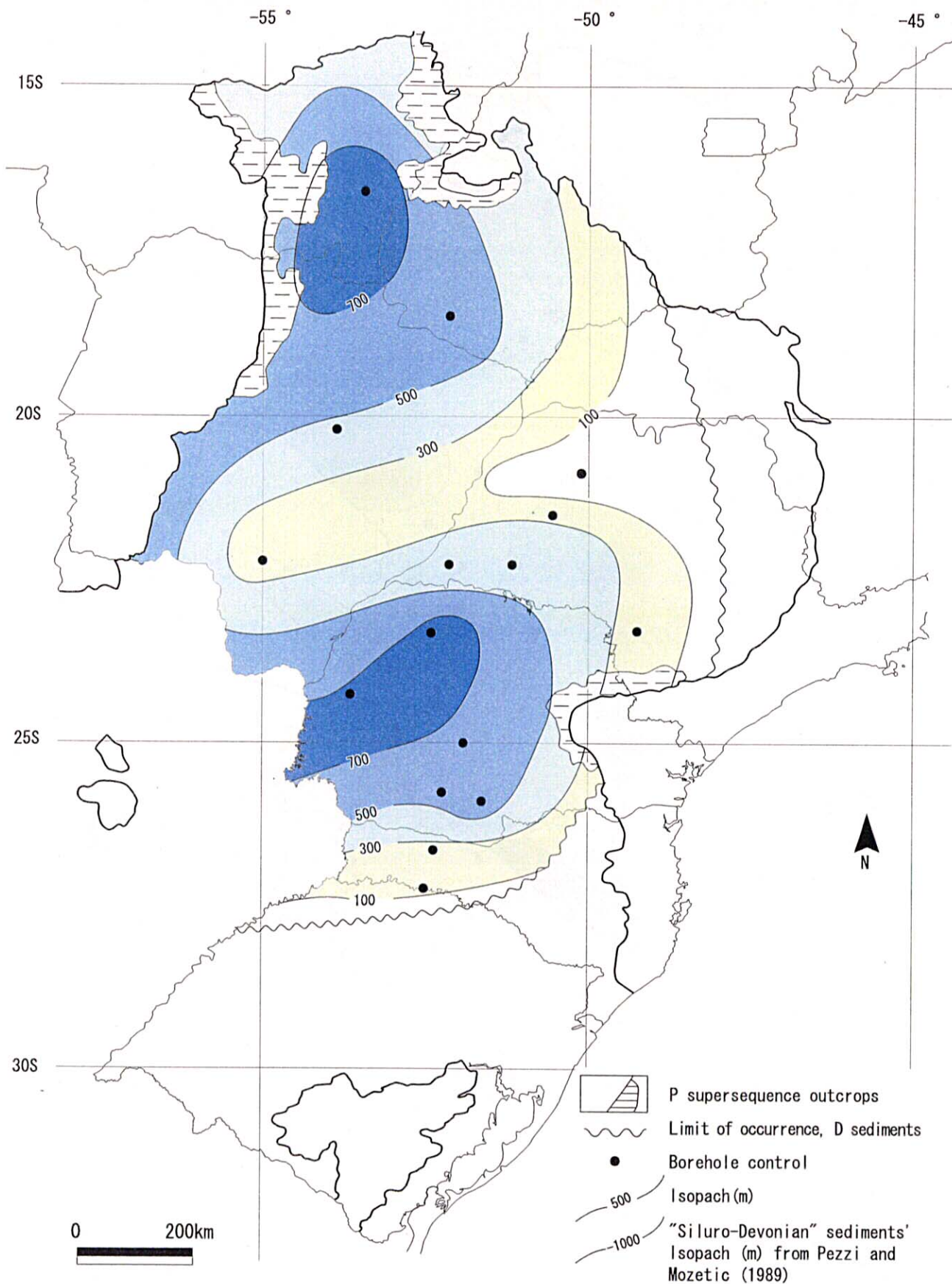


Fig. II-1-4-10. Isopach map of the Parana supersequence (E. J. M. Milani et al., 1998).

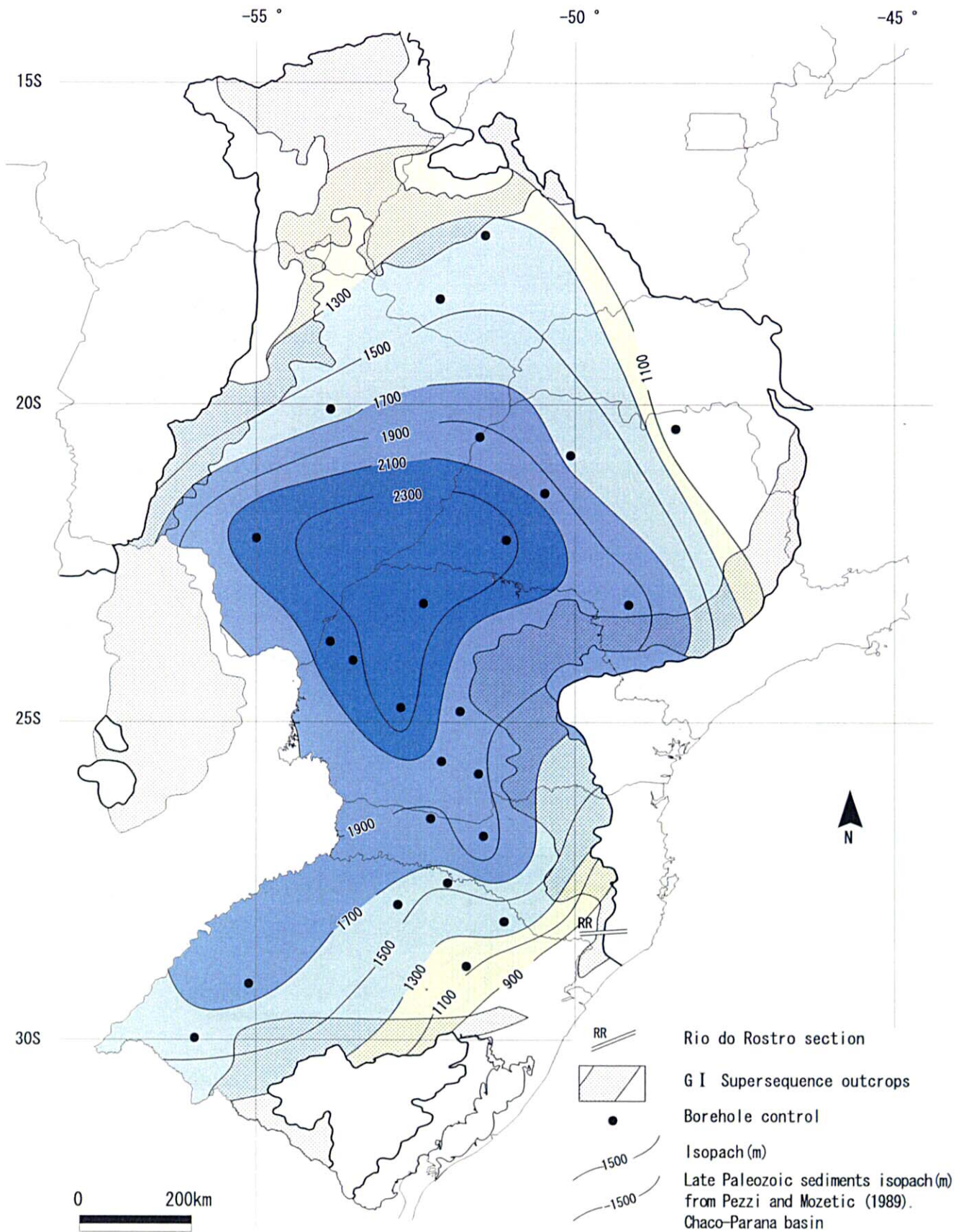


Fig. II -1-4-11. Isopach map of the Gondwana I supersequence (E. J. M. Milani et al., 1998).

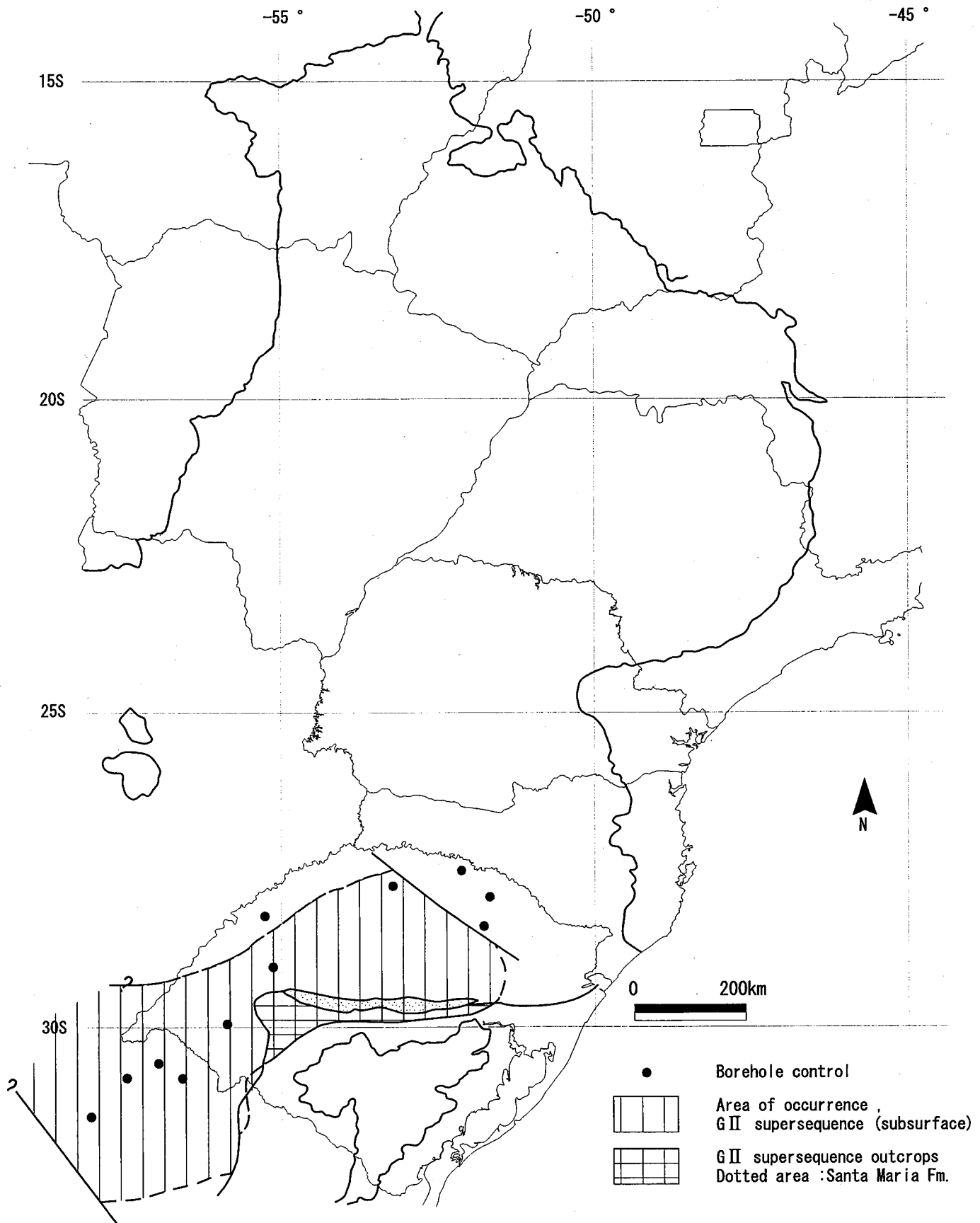


Fig. II-1-4-12. Occurrence of the Gondwana II supersequence (E. J. M. Milani et al., 1998).



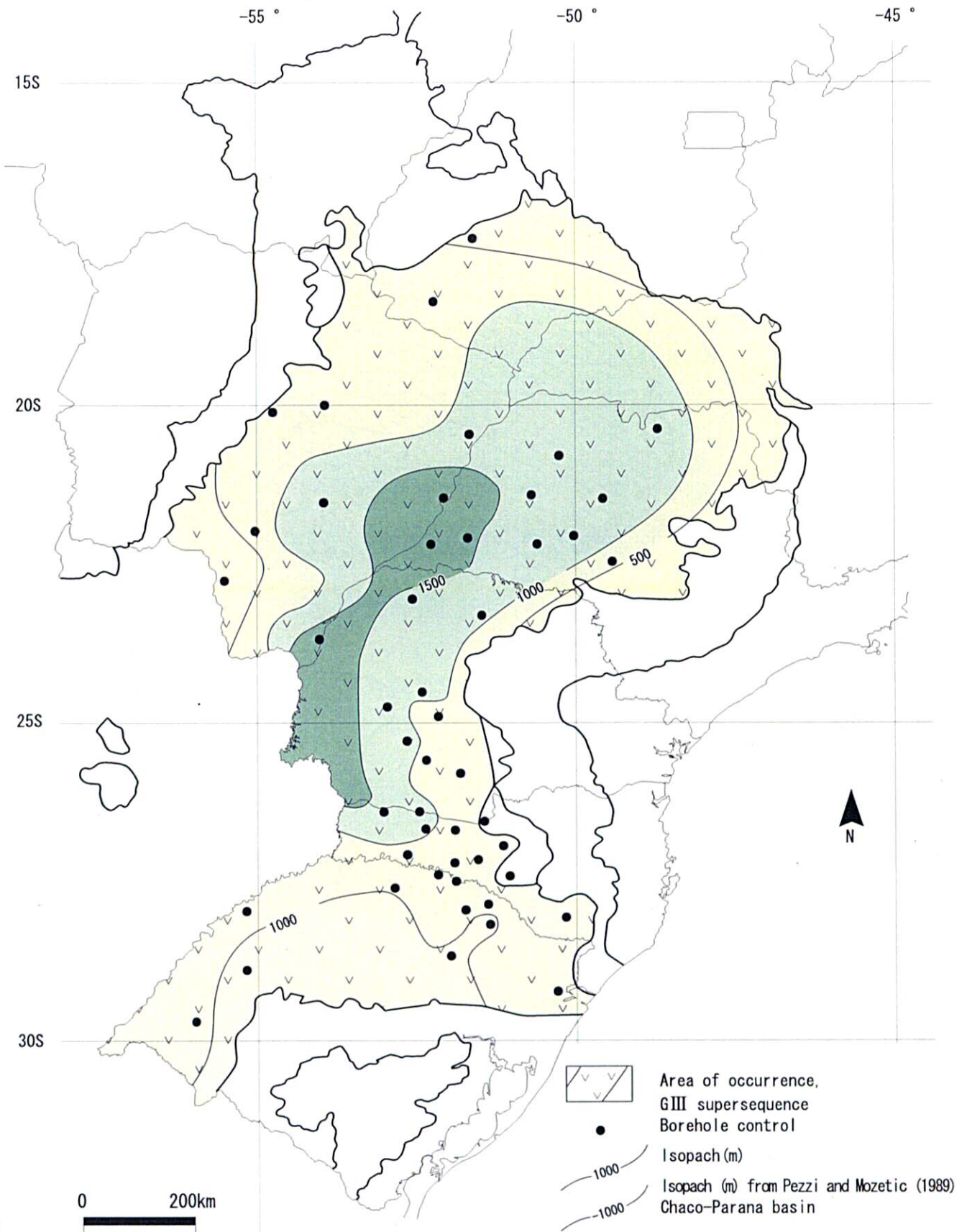


Fig. II-1-4-13. Isopach map of the Gondwana III supersequence sediments + volcanics (E. J. M. Milani et al., 1998).

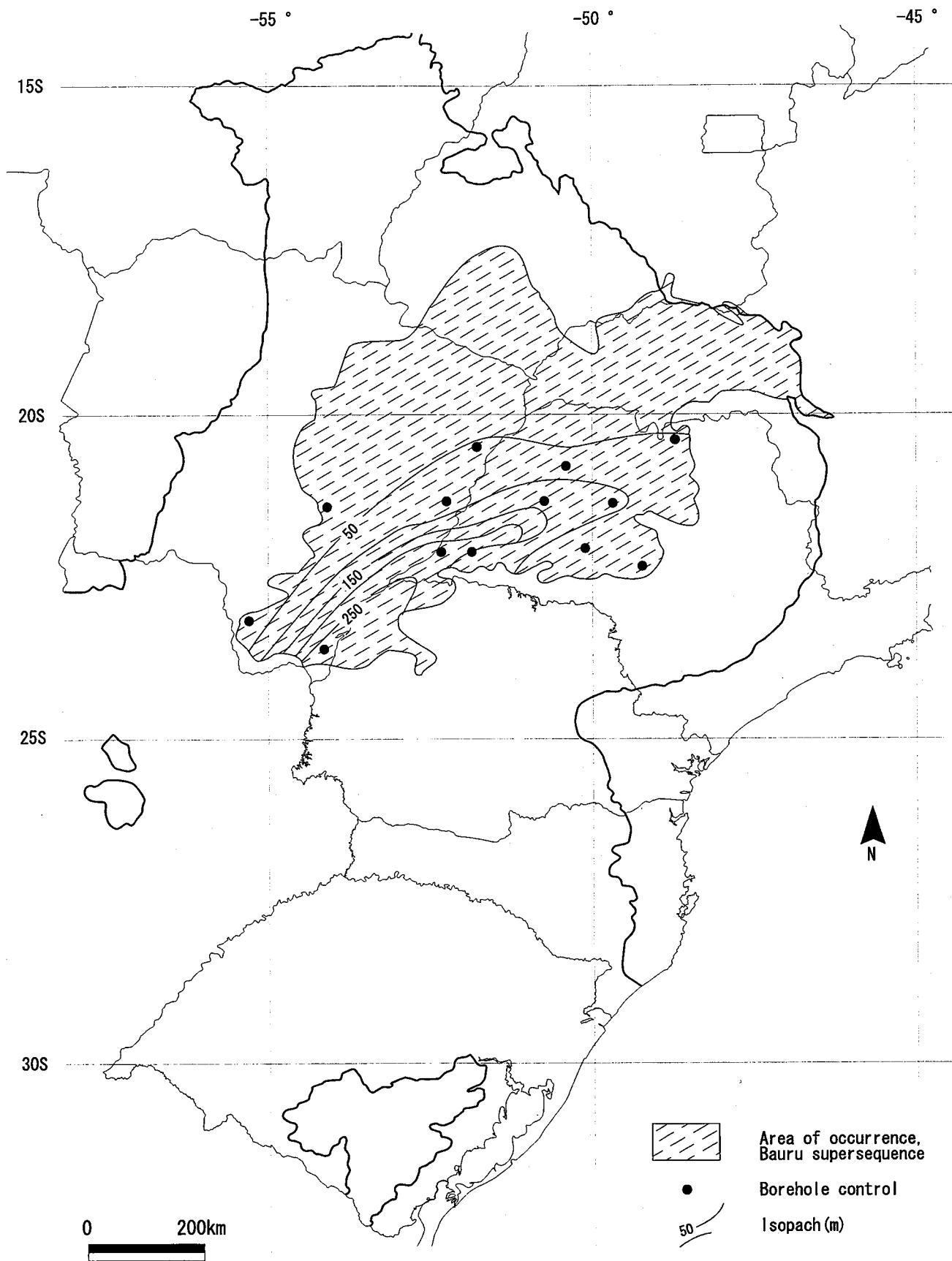


Fig. II-1-4-14. Isopach map of the Bauru supersequence (E. J. M. Milani et al., 1998).

(Fig.II-1-4-14). The history of the Parana basin had finished by the end of the Bauru Supersequence.

#### 1-4-4 Basement Structure analyzed by Geophysical Data

The study of the earth's interior with the gravity data has been based on isostasy theory. M.C.L. Quintas (1995) discussed the structure of basement rocks of the Parana basin using the isostasy model with gravity data and the thermodynamic model with oil-well drilling data.

##### (1) Origin of the Intracratonic Basin

The theory that the intracratonic basin was formed by the subsidence movement of the basin caused by thermodynamic activity of the earth's interior is most popular recently (Bott, 1971; Sleep (1971); McKenzie (1978) et al). Bott (1981) described that the active mechanism (plume rising) and passive mechanism (extensional stress) are two origins of the intracratonic basin (Fig.II-1-4-15).

In the case of the active mechanism, (1) The lithosphere is flexured by the rising and heating of the plume. The distensible stress field develops on the ground surface to form normal faults. (2) The axis of the distensible stress field is eroded and the thickness of the lithosphere decreases. (3) The thinning part of the lithosphere subsides by cooling and the intracratonic basin is formed

In the case of the passive mechanism, (1) The thickness of the lithosphere decreases due to the horizontal extensional stress field and asthenosphere rises. (2) Normal faults and grabens are formed by downward flexure of the lithosphere. (3) The Asthenosphere rises and the lithosphere subsides under the extensional stress field.

There are several intracratonic basins in the world (Table II-1-4-1). These basins have several common points such as the beginning of sedimentation before the rapture of Gondwana continent and the forming of rift before subsidence. These basins are presumed to be systematically formed by the origin of the earth's scale.

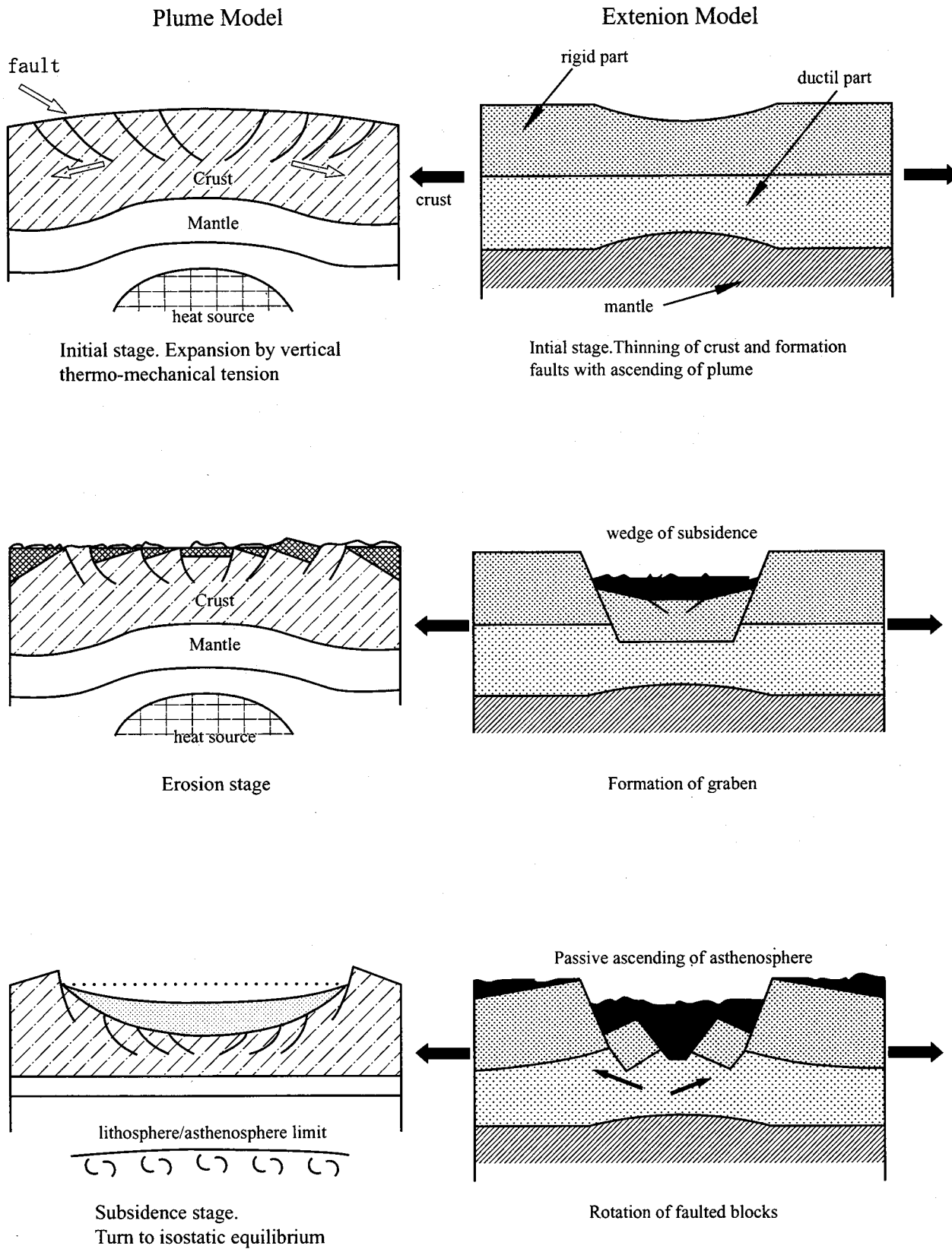


**Fig. II-1-4-15. Genetic models of the intracratonic basin (Bott,1981)**

**Table II-1-4-1 Intracratonic basin in the world**

Basin	Locality	Thickness (m)	Initiation (Ma)	Duration (Ma)
Parana	S.America	6,000 m	450 Ma	300 Ma
Illinois	N.America	6,000 m	510 Ma	300 Ma
Williston	N.America	3,700 m	500 Ma	310 Ma
Michigan	N.America	4,500 m	520 Ma	220 Ma
Parnaiba	S.America	4,000 m	500 Ma	300 Ma
Chad	Africa	develop	30 Ma	Develop

M.C.L. Quintas (1995)

## (2) Data Analysis Method

Two individual methods were used for the data analysis. (1) Stress analysis using a thermodynamic model ( $\beta$  or  $\varepsilon$ : extension / attenuation factor). Geological data from 81 oil exploration drillings were used in this analysis. The McKenzie (1978) model and Royden & Keen (1980) model, based on the theory of the extensional stress field, were used as the thermodynamic model. (2) Gravity data based on the isostasy model was analyzed. The data on the thickness of each layer of the Parana basin was used. Besides this data, gravity data, seismological data and drilling data were used in this analysis.

### a) Thermodynamic Model

When magma is generated within the asthenosphere, the continental lithosphere instantly ( $t = 0$ ) shrinks  $\beta$  (Fig.II-1-4-16). When the magma penetrates to the lithosphere, the density of the lithosphere increases and at the moment the lithosphere subsides by isostasy. As a result, rifting occurred at the upper part of the lithosphere (crust) and the graben is formed. The initial subsidence of the rift  $S_i$  becomes the sum of the subsidence by rigid movement ( $S_{\text{rigid}}$ ) and the subsidence by ductile movement of the lithosphere ( $S_{\text{ductil}}$ ). The initial subsidence  $S_i$  is indicated by the following equation.

$$S_i = \frac{[(\rho_m - \rho_c)t_c(1 - \frac{t_c \alpha T_m}{2a}) - \frac{a \alpha T_m \rho_m}{2}](1 - \frac{1}{\beta})}{[\rho_m(1 - \alpha T_m) - \rho_w]} \quad (5)$$

$T_c$  = initial thickness of continental lithosphere

$\alpha$  = coefficient of thermal expansion

$\rho_m$  = density of mantle



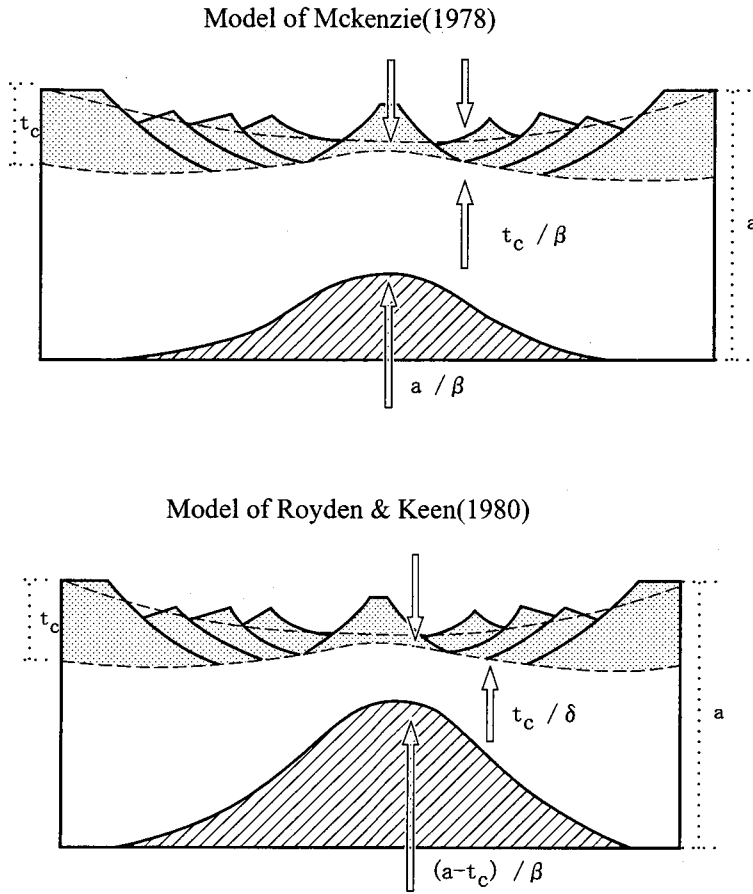


**Fig. II-1-4-16 Thermomechanical model for formation of intracratonic basin**

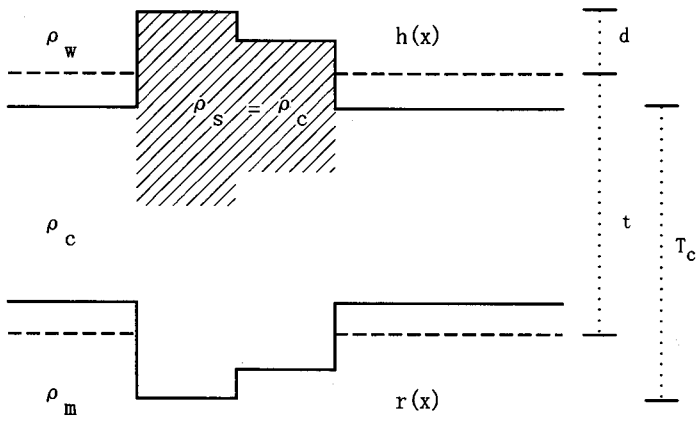


**Figure II-1-4-17. Isostatic model of Airy (Karner, 1982).**

$\rho_w$  = density of water  
 $a$  = thickness of lithosphere  
 $T_m$  = temperature of lithosphere basement  
 $\rho_c$  = density of lithosphere  
 $\beta$  = attenuation ratio

After initial subsidence of the basin, the lithosphere gradually refrigerates and attenuates and thermally subsides (flexural subsidence). This thermal subsidence  $S_t$  can be calculated by using the thermal conductivity equation. The total subsidence  $S_{total}$  becomes the sum of the initial subsidence  $S_i$  and thermal subsidence  $S_t$ .

$$S_t = e(0) - e(t) \quad (6)$$

$$e(t) = E_o \left( \frac{\beta}{\pi} \sin \frac{\pi}{\beta} \right) \exp^{-\frac{t}{\tau}} \quad E_o = \frac{(4at_m \rho_m \alpha)}{\pi^2 (\rho_m - \rho_w)} \quad (7)$$

$$S_{total} = S_i + S_t \quad (8)$$

The above is the McKenzie model (1978). This model is based on the premise of instant attenuation of the lithosphere ( $t$  is less than 20 Ma), however, refrigeration of magma is considered to continue more than 50 Ma. In this case, computational error of the subsidence is generated. Royden & Keen (1980) estimated that the thermal subsidence of magma by cooling became smaller than that of McKenzie model. They divided the lithosphere's attenuation into the upper part  $\delta$  and lower part  $\beta$  and calculated the attenuation ratio and the total subsidence (Fig.II-1-4-17).

$$\varepsilon = \frac{a}{\frac{t_c}{\delta} + (a - t_c) \beta} \quad (9)$$

#### b) Backstripping Method

The Backstripping method is the adequate method to calculate the thickness of the sediments through the history of the basin. The method is to release the target sedimentary layer from the consolidation pressure by stripping the layers younger than the target layer. The layer which is released from consolidation pressure rises to the initial horizon. The subsiding depth of the basement by the sediments can be obtained by calculating the thickness of the sedimentary layer in each period. The actual depth of basement  $Y$  can be calculated, compensating the effect of load of the sediments by the following equation which was proposed by Sclater and Christie (1980).

$$Y = S \left( \frac{\rho_m - \bar{\rho}_s}{\rho_m - \rho_w} \right) \quad (10)$$

$\rho_w$  = density of water,  
 $\bar{\rho}_s$  = average density of sediment  
 $S$  = measured total thickness of sediments,  
 $\rho_m$  = density of mantle

### c) Isostasy Correction

Although the ordinary Bouguer anomaly reduction is effective to reduce the influence of local topography, it is not enough to reduce the influence of large scale topography. For example, in case of a small mountain with 10 kilometers extension, the lithosphere can support the mountain without deformation. But, in the case of a mountain system with 1,000 kilometers extension, the lithosphere bends downward and isostasy correction becomes necessary.

The weight of the lithosphere keeps in equilibrium by flexure of the rigid lithosphere on the ductile asthenosphere according to Barrell (1914a). Because the rocks of the lithosphere are lighter than those of the asthenosphere, the Mass of the big mountain system is compensated by the depth of low density roots. Because the existence of roots are not reflected in the Bouguer anomaly correction, the Bouguer anomaly in the big mountain system indicates a large minus value. This minus anomaly is called the isostasy anomaly, which can be corrected by isostasy correction (Fig.II-1-4-17).

The Fourier transformation  $G_T(k)$  of the gravity anomaly which is caused by isostasy is shown in the following equation by Karner (1982) and Karner & Watt (1982).

$$G_T(k) = 2\pi\gamma \Delta \rho_1 H(k) \exp^{-kd} \left[ 1 - \frac{\Delta \rho_2 R(k) \exp^{-kt}}{\Delta \rho_1 H(k)} \right] \quad (11)$$

$H(k)$  = Fourier transform of gravity  $h(x)$  on the topographic surface

$R(k)$  = Fourier transform of gravity  $R(x)$  on the topographic root

$\Delta \rho_1$  = density difference of the topographic surface

$\Delta \rho_2$  = density difference of root

$d$  = average height,

$t$  = distance between average topographic surface and topographic root,

$\gamma$  = gravity constant,

$k$  = wave number ( $2\pi/\lambda$ ),

$\lambda$  = wave length

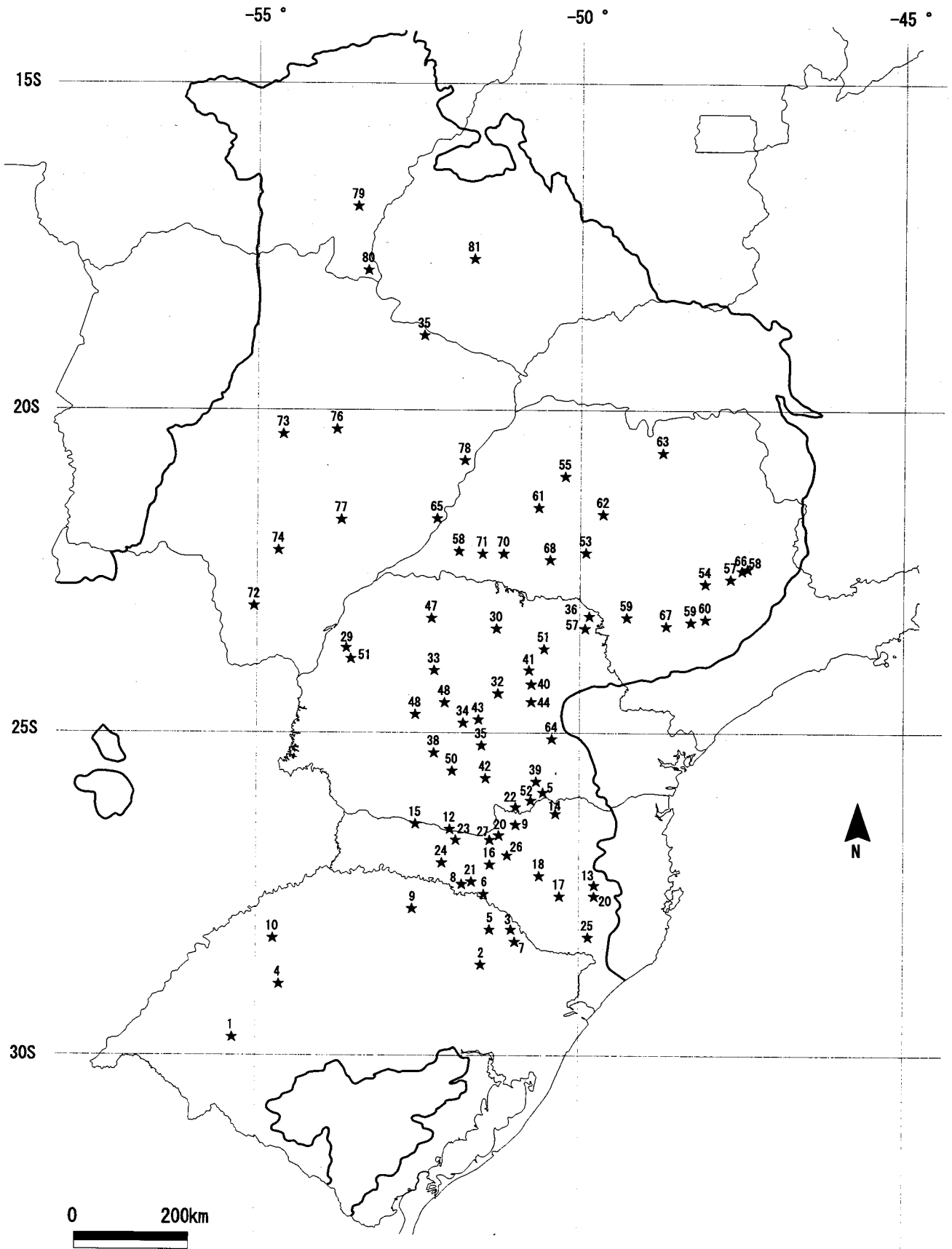


Fig. II-1-4-18. Locations of drilling holes used by M.C.L.Quintas (1995).

**Table II-1-4-2 Locations of drilling holes (M.C.L. Quintas, 1995)**

Name	City	#	Prillory	LATITUDE (°)	LONGITUDE (°)
Alegrete	Alegrete	1	2-AL-1	-29,80216	-55,76664
Atanásio	Nova Prata	2	2-AO-1	-28,70143	-51,66456
Esmeralda	Esmeralda	3	1-ES-1	-28,17864	-51,17861
Itacurubi	Santiago	4	2-IT-1	-29,01666	-54,99165
Lagoa Vermelha	Lagoa Vermelha	5	2-LV-1	-28,16354	-51,50276
Machadinho	Machadinho	6	1-MA-1	-27,58679	-51,66314
Muitos Capões	Vacaria	7	1-MC-1	-28,35206	-51,11268
Marcelino Ramos	Marcelino Ramos	8	2-MR-1	-27,50741	-51,90275
Ronda Alta	Ronda Alta	9	2-RD-1	-27,83906	-52,76718
Rio Ijuí	Rio Ijuí	10	2-RI-1	-28,29998	-55,04998
Torres	Torres	11	2-TO-1	-29,32604	-49,79139
Abelardo Luz	Abelardo Luz	12	2-AL-1	-26,45031	-52,18131
Barra Nova	Barra Nova	13	1-BN-1	-27,51242	-49,75526
Canoinhas	Canoinhas	14	2-CN-1	-26,26890	-50,51927
Galvão	Galvão	15	1-GO-1	-26,38268	-52,70943
Herval Velho	Herval Velho	16	1-HV-1	-27,21578	-51,46365
Lajes	Lajes	17	2-LA-1	-27,62966	-50,39526
Marambas	Curitibanos	18	1-MB-1	-27,32490	-50,73741
Matos Costa	Matos Costa	19	1-MC-2	-26,53240	-51,16127
Petrolândia	Petrolândia	20	1-PA-1	-27,59428	-49,73251
Piratuba	Piratuba	21	2-PI-1	-27,42579	-51,78401
Porto União	Porto União	22	2-PU-1	-26,26654	-51,05752
Rio Chapecó	Ponte Serrada	23	1-RCH-1	-26,65456	-52,04381
Seara	Seara	24	1-SE-1	-27,14331	-52,29831
São Joaquim	São Joaquim	25	1-SJQ-1	-28,27128	-49,91664
Tangará	Tangará	26	2-TG-1	-27,09529	-51,24427
Três Pinheiros	Água Doce	27	1-TP-3	-26,78443	-51,47568
Taquara Verde	Caçador	28	2-TV-1	-26,74703	-51,31477
Altônia	Altônia	29	2-AN-1	-23,85456	-53,80681
Apucarana	Apucarana	30	2-AP-1	-23,49690	-51,42150
Alto Piquiri	Alto Piquiri	31	2-AP1-1	-24,00000	-53,71667
Cândido de Abreu	Cândido de Abreu	32	1-CA-1	-24,52191	-51,38116
Campo Mourão	Campo Mourão	33	2-CM-1	-24,14190	-52,41140
Chapéu do Sol	Pitanga	34	2-CS-1	-24,96406	-51,96473
Guarapuava	Guarapuava	35	2-GP-1	-25,30543	-51,65681
Jacarezinho	Jacarezinho	36	1-J-1	-23,22889	-49,95227
Joaquim Távora	Joaquim Távora	37	1-JT-1	-23,46803	-49,94966
Laranjeiras do Sul	Laranjeiras do Sul	38	2-LS-1	-25,40080	-52,41102
Mallet	Mallet	39	1-M-1	-25,86915	-50,78576
Monjolinho	Monjolinho	40	1-MO-1	-24,37329	-50,87615
Ortigueira	Ortigueira	41	2-O-1	-24,18103	-50,88900

Name	City	#	Prillory	LATITUDE (°)	LONGITUDE (°)
Pinhão	Pinhão	42	1-PH-1	-25,82482	-51,59075
Pitanga	Pitanga	43	1-PT-1	-24,93268	-51,75518
Reserva	Reserva	44	1-R-1	-24,62266	-50,88491
Rio Claro do Sul	Rio Claro do Sul	45	1-RC-1	-26,01330	-50,70451
Rio do Canto	Alto Paraná	46	1-RCA-1	-24,82831	-52,70100
Rio Ivai	São Caetano do Ivai	47	2-RI-1	-23,33131	-52,45518
Roncador	Roncador	48	1-RO-1	-24,61206	-52,24856
Rio Piquiri	Palmital	49	2-RP-1	-24,82831	-52,70131
Rio Segredo	Mangueirinha	50	1-RS-1	-25,70581	-52,11668
PRS. Jerônimo da Serra	PRS. Jerônimo da Serra	51	1-SJ-1	-23,78260	-50,66413
União da Vitória	União da Vitória	52	2-UV-1	-26,17903	-50,92866
Amadeu Amarel	Marília	53	2-AA-1	-22,30243	-50,04193
Anhembí	Piracicaba	54	2-AB-1	-22,77853	-48,18202
Araçatuba	Araçatuba	55	2-AR-1	-21,12818	-50,37406
Assistência	Assistência	56	2-AS-1	-22,51690	-47,58190
Artemis	Artemis	57	1-AT-1	-22,66778	-47,80491
Cuiabá Paulista	Cuiabá Paulista	58	1-CB-1	-22,30331	-52,03931
Carlota Prenz	Angatuba	59	1-CP-1	-23,37153	-48,38751
Guareí	Guareí	60	2-GU-3	-23,34254	-48,20576
Lagoa Azul	Oswaldo Cruz	61	2-LA-1	-21,65418	-50,79318
Lins	Lins	62	2-LI-1	-21,69227	-49,75616
Olímpia	Olímpia	63	2-OL-1	-20,68754	-48,92776
Piratininga	Piratininga	64	1-PA-1	-25,17368	49,11356
Presidente Epitácio	Presidente Epitácio	65	2-PE-1	-21,75842	-52,10189
Piracicaba	Fazenda Pitanga	66	1-PG-1	-22,54449	-47,64022
Paranapanema	Paranapanema	67	2-PN-1	-23,45281	-48,77431
Paraguaçu Paulista	Paraguaçu Paulista	68	2-PP-1	-22,41828	-50,60464
Sarutaiá	Sarutaiá	69	1-SA-1	-23,28206	-49,42643
Taciba	Taciba	70	2-TB-1	-22,33381	-51,34668
Tarabáí	Tarabáí	71	1-TI-1	-22,5331	-51,67318
Amambai	Amambai	72	2-AM-1	-23,10990	-55,23664
Campo Grande	Campo Grande	73	2-CG-1	-20,48579	-54,71914
Dourados	Dourados	74	2-DO-1	-22,26803	-54,81275
Rio Aporé	Cassilândia	75	2-RA-1	-18,83568	-52,36043
Ribas do Rio Pardo	Ribas do Rio Pardo	76	2-RP-1	-20,42079	-53,87242
São Domingos	São Domingos	77	2-SD-1	-21,82778	-53,81565
Três Lagoas	Três Lagoas	78	2-TL-1	-20,87916	-51,75000
Alto do Garças	Alto do Garças	79	1-AG-1	-16,96066	-53,52491
Taquari	Alto Araguaia	80	2-TQ-1	-17,88166	-53,27465
Jataí	Jataí	81	2-JA-1	-17,80656	-51,78718

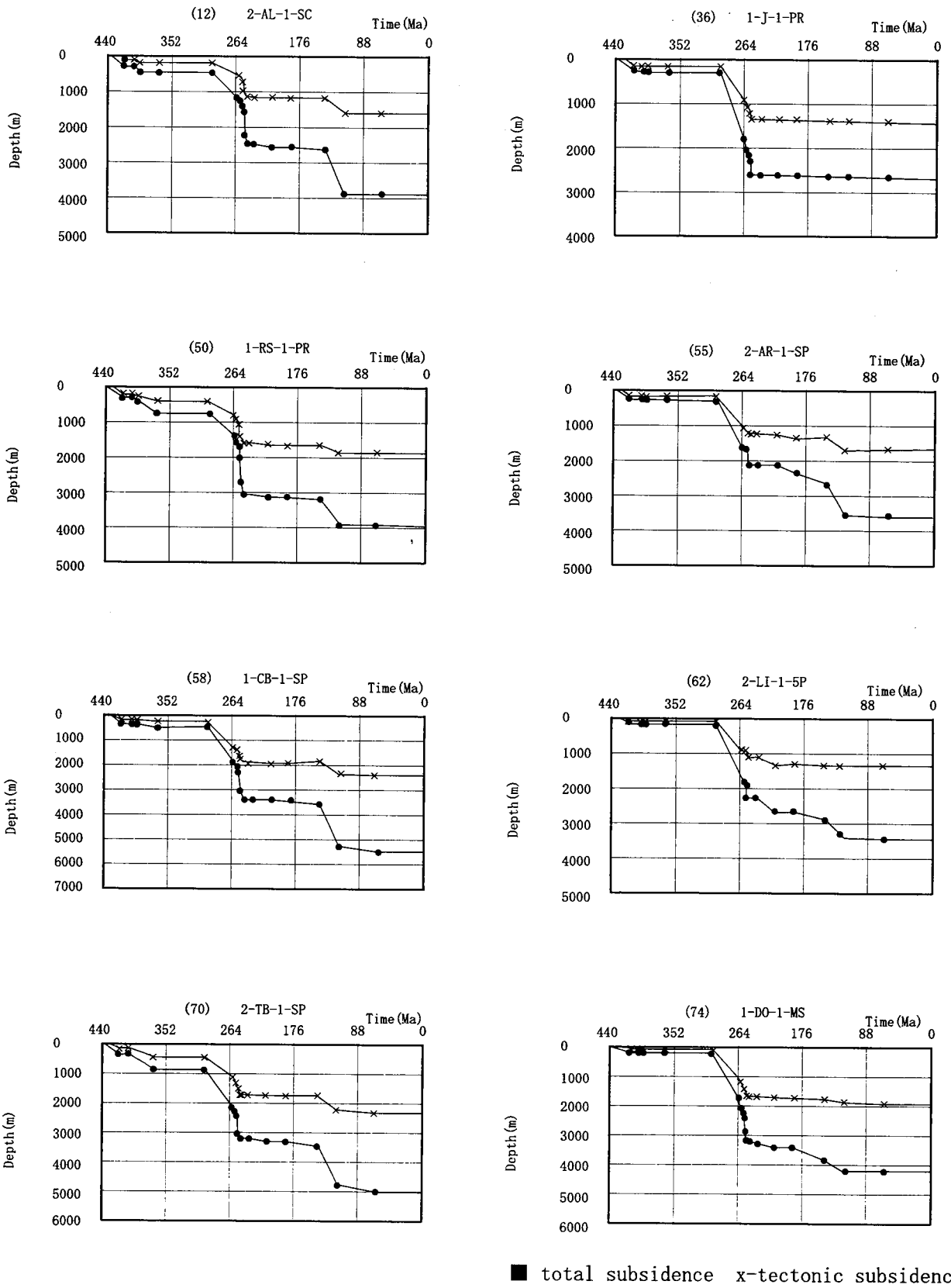


Fig. II-1-4-19. Calculated tectonic subsidences (backstripping method). Drilling 12,36,50,55,58,82,70 e 74 (M.C.L. Quintas 1995)

**Table II-1-4-3 Basic Parameters used in thermomechanic model (M.C.L. Quintas, 1995)**

parameter	value
Density of water	1.03 g/cm <sup>3</sup>
Density of crust	2.80 g/cm <sup>3</sup>
Density of mantle	3.33 g/cm <sup>3</sup>
average density of lithosphere	2.8 g/cm <sup>3</sup>
Temperature on the base of lithosphere	1.350 °C
Thermal diffusion of lithosphere	8.0 10 <sup>-3</sup> cm <sup>2</sup> s <sup>-1</sup>
Average thermal conductivity of lithosphere	7.5 10 <sup>-3</sup> cat cm <sup>-1</sup> °C <sup>-1</sup> s <sup>-1</sup>
Thermal conductivity of water	1.35 10 <sup>-3</sup> cat cm <sup>-1</sup> °C <sup>-1</sup> s <sup>-1</sup>

**Table II-1-4-4 Ratios of tectonic subsidence and total subsidence with the time**  
with the time. The values in the parenthesis correspond to the averages for the time (M. C. L. Quintas, 1995).

Formations or Groups	S <sub>tectonic</sub> / time	S <sub>total</sub> / time
Grupo Rio Ivai	7	13
Furnas	13	19
Ponta Grossa	6	14
Itararé	14	26
Rio Bonito	17	39
Palermo	30	71
Irati	33	58
Teresina	42	178
Rio do Rasto	92	137
Pirambóia	3	6
Botucatu	1	3
Serra Geral	5	26
Bauru	1	2



### (3) Data

The drilling data for petroleum prospecting of the DEPEX-PETROBRAS Corporation and the gravity data of the Research Institutes of IAG/USP, IBGE, ON and CPRM & UFPR were used. PETROBRAS Corporation and PETEROPAULI Corporation carried out 73 drillings and 33 drillings respectively until 1985. M.C.L. Quintas (1995) used 81 of these drilling data. The drilling locations are shown in Fig.II-1-4-18, Table II-1-4-2). The La Costa & Romberg G gravimeter was used for gravitation measurement. The Bouguer anomaly was corrected International Gravimetric Formula (1967) and average density  $2.670 \text{ kg/m}^3$ . Topographic reduction was not carried out because of the flat topography of the Parana region. Thermal conductivity (K), porosity ( $\phi$ ) and decreasing ratio (c) are used referring to the IPT Report.

### (4) Results of Analysis

#### a) Subsidence Curve by Backstripping Method

The depth of the basement was calculated using equation (10), classifying rock facies of sediments into five types (sandstone, crystalline schist, limestone, siltstone and basalt) and fixing each porosity ( $\phi$ ) and decreasing ratio (c) (Fig.II-1-4-19, Table II-1-4-3).

Presuming the total formative period of the basin to be 440 Ma and total thickness of the sediments to be 6,000 meters as the preconditions, the average subsiding ratio of the basement becomes 13.6m/Ma. The sedimentation periods are 414 – 410 Ma, 367 – 296 Ma, 248 – 238 Ma, 213 – 188 Ma, 65 – 0 Ma, totally 184 Ma by subsidence curve and geological data. Presuming the 10 percent erosion ratio of sediments, 600 meters of sediments are eroded in 184 Ma and a 3.3m/Ma of erosion ratio is obtained. Therefore, the average subsiding ratio of the basement is 16.9m / Ma as the erosion correction.

Remarkable subsidence is observed in the period from the Palermo Formation to the Rio do Rast Formation (248 – 238 Ma). During this period, the structural subsiding and total subsiding ratios are 49m/Ma and 111m/Ma, respectively. This marked subsidence (sedimentation) is a common phenomenon in the rift basin which occurred worldwide after the Hercynian orogenic movement in the Permian to Triassic. In the case of Serra Geral Formation (Parana flood basalt: early Cretaceous), the structural subsidence (5m/Ma) is approximately 20 percent of total subsidence (26m/Ma) and is lower than those of other sedimentary rocks. The reason is considered to be that the load of the Parana flood basalt being high density markedly affected the total subsiding ratio.

#### b) Attenuation Ratio by Thermodynamic Model ( $\epsilon$ )

The attenuation ratios of the upper part  $\beta$ , the lower part  $\delta$  of the lithosphere and the

attenuation ratio  $\epsilon$  of the whole lithosphere were obtained comparing to the structural subsiding curves and theoretical subsiding curves that were obtained by using the thermodynamic model and the Backstripping method. The basic parameters that were used in the thermodynamic model are shown in Table II-1-4-4.

Three activities are defined by the subsiding curve. Those are: the first distensible period of activity: before the sedimentation of the Silurian to Devonian (before 440 Ma), the second distensible period of activity: before the sedimentation of the upper Carboniferous (before 296 Ma), the third distensible period of activity: before the eruption of the flood basalt of the Jurassic to Cretaceous (before 144 Ma). The attenuation ratio ( $\epsilon$ ) was calculated based on the crust thickness  $a = 45\text{km}$  by seismic data and the lithosphere thickness  $t_c = 150\text{km}$  (by D. E. James et al. (1994)). M.C.L. Quintas (1995) confirmed that the thermodynamic model by Royden and Keen (1980) was more accurate than the model by McKenzie (1978) and used the former model.

**The first distensible activity:**  $\epsilon$  is 1.01 to 1.32 (Fig.II-1-4-20). The high  $\epsilon$  zone is observed in the western part to north-western part of Parana Province near the eastern border of Paraguay in the NE – SW direction. This suggests that the western part to north-western part of Parana Province was the thinner part of the lithosphere during this period in the NE – SW direction. The corresponding expanding stress field is presumed in the NW – SE direction. Furthermore, the high  $\epsilon$  zone corresponds to the area where a large amount of sills and dykes intrude (Fig.II-1-4-21).

The high  $\epsilon$  zone (approximately 1.16) is also recognized along  $W52^\circ$  meridian in Mato Grosso do Sul extending in the direction of N – S. These results coincide with the results of Fig.II-1-4-9, Fig.II-1-4-10). By these facts, the sedimentation of the Rio Ivai Supersequence and Parana Supersequence is assumed to begin in this part after the first distensible period of activity.

**The second distensible activity:**  $\epsilon$  is 1.06 to 1.61 (Fig.II-1-4-22). The high  $\epsilon$  zone ( $S23^\circ 8' - S22^\circ 3'$ ,  $W53^\circ 8' - W52^\circ 0'$ ) observed from the western part of Parana Province to the south-western end of Sao Paulo Province along the Parana River in the NE – SW direction. The distensible stress field in the same direction as the first expanding activity is considered to continue. However, the high  $\epsilon$  zone in the south-western end of Sao Paulo Province could not be observed in the first period.

Although the absolute value of  $\epsilon$  is not so big as the former, the high  $\epsilon$  zone in the NW – SE direction which was not observed during the first activity can be observed. This high  $\epsilon$  zone extends from the central part of Mato Grosso do Sul Province to the southern part of Parana Province. In the high  $\epsilon$  zone, the thickest sill is observed in the drilling and it is also observed on the isopach map of sill in Fig.II-1-4-21. Turner et al. (1994) concluded that the expanding stress field involved the rapture of the South American Continent with clockwise rotation for

Gondwana continent and the rupture of continent progressed from the south to the north. The high  $\epsilon$  zone along fracture zone or the marginal basin in the NW – SE direction was formed by the expanding stress field in the NE – SW direction (Fig.II-1-4-23). The other high  $\epsilon$  zone with a value more than  $\epsilon = 1.42$  can be observed in the northern end of Rio Grande do Sul Province.

**The third distensible activity:**  $\epsilon$  is from 1.01 to 1.26 (Fig.II-1-4-24). The mechanism of the third distensible activity differs from that of the former two activities, because the third distensible activity is due to the eruption of Parana flood basalt (Serra Geral Formation). The high  $\epsilon$  zone is located in the south-western end of Sao Paulo Province (drilling points: 2-CB-1-SP, 2-TB-1-SP, 1-TI-1-SP, 2-PE-1-SP) and this high  $\epsilon$  zone corresponds to the highest  $\epsilon$  zone of the second distensible activity. However, the high  $\epsilon$  zone of the western to north-western part of Parana Province near the border of Paraguay disappears in the third distensible activity.

The magma activity of the Parana flood basalt just after the third expanding activity is closely related to the expanding activity of the lithosphere (high  $\epsilon$  zone). The high  $\epsilon$  zone is observed from the western part of Parana Province to the south-western end of Sao Paulo Province. Parana flood basalt magma is presumed to erupt or intrude from the high  $\epsilon$  zone as the feeder. As a fact, at the drilling point of 2-CB-1-SP, the thickness of the basalt layer shows the thickest as 1,723 meters in the Parana basin. The  $\epsilon$  is 1.26 which shows the highest in the third expanding activity. The high  $\epsilon$  zone of the north-western part of Parana Province in the first expanding activity corresponds to the region where dykes and sills intruded the thickest.

### c) Residual Gravity Anomaly by Isostasy Model

The Bouguer anomaly is shown in Fig.II-1-4-25. The isostasy model was calculated by using the following density values. Average density of the crust is  $2.80\text{kg/m}^3$  (the value of the uppermost:  $2.75\text{kg/m}^3$ , in the middle:  $2.80\text{kg/m}^3$ , in the lowermost:  $2.85\text{kg/m}^3$ ) and upper mantle:  $3.33\text{kg/m}^3$ . Here, the density of the sedimentary layer within the basin is  $2.55\text{kg/m}^3$ , the density of flood basalt is  $2.87\text{kg/m}^3$  and the corrected Bouguer density is  $2.67\text{kg/m}^3$  as the preconditions. The layers of the lower basin is bent downward by isostasy and the lower crust is rooted to the mantle, which causes a minus Bouguer anomaly. The thickness of the root is determined by the rigidity  $D$  of the lithosphere, and is indicated by effective elasticity thickness  $T_e$ . In this part, because the root of the crust is presumed to be supported by isostasy,  $D=0$  was given. Under these preconditions, the isostasy gravity anomaly was calculated (Fig.II-1-4-26). The Gravimetric trend anomaly was calculated by using the second order polynomial equation (Fig.II-1-4-27). Finally, the residual gravity anomaly was calculated (Fig.II-1-4-27).

#### 1) Residual Gravity Anomaly and High $\epsilon$ Zone

Low gravity anomalies are limited in the Ribeira belt in the south-eastern part of the basin,

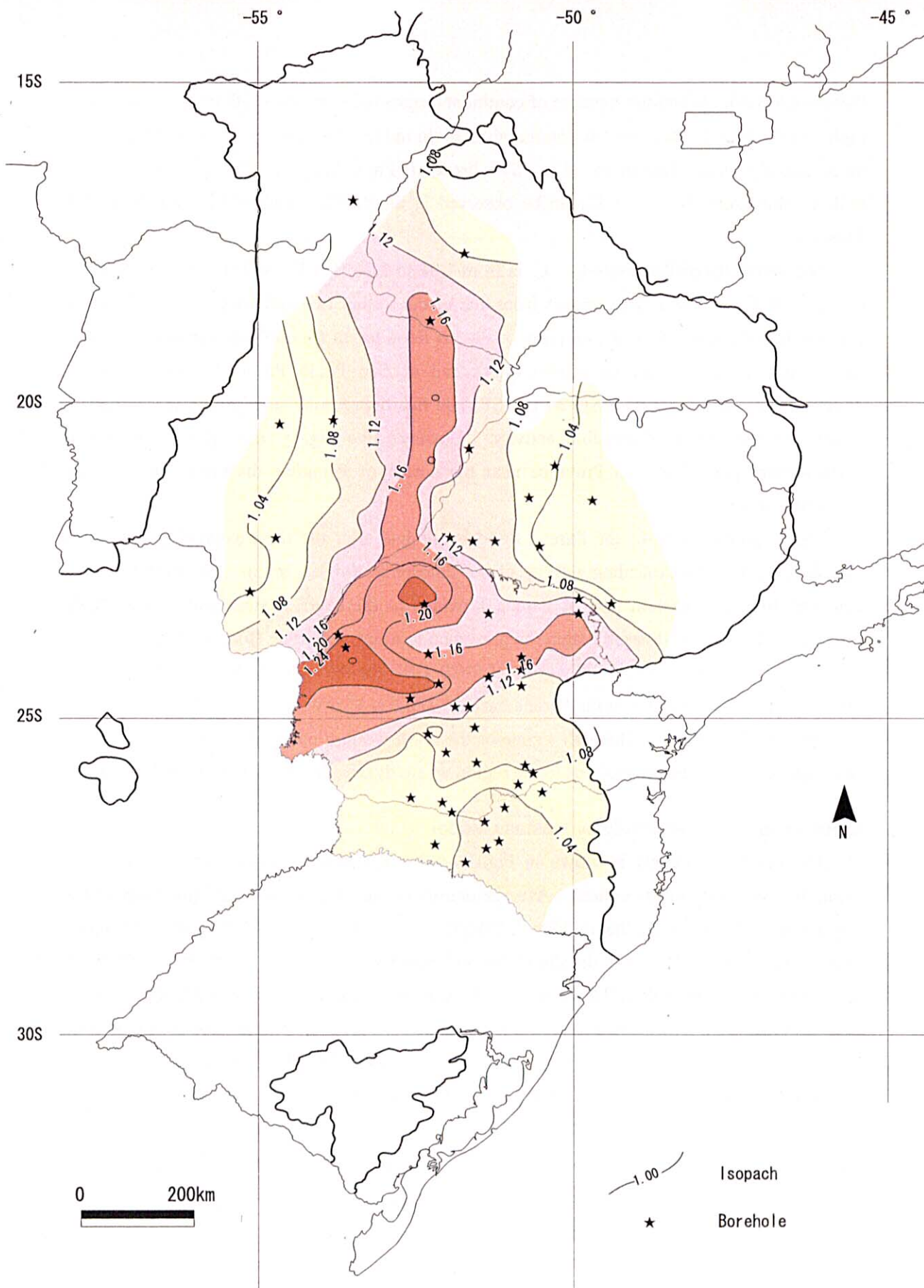


Fig. II -1-4-20. Iso-attenuation map of the first distensible event (440 Ma). (M.L. C. Quintas, 1995).

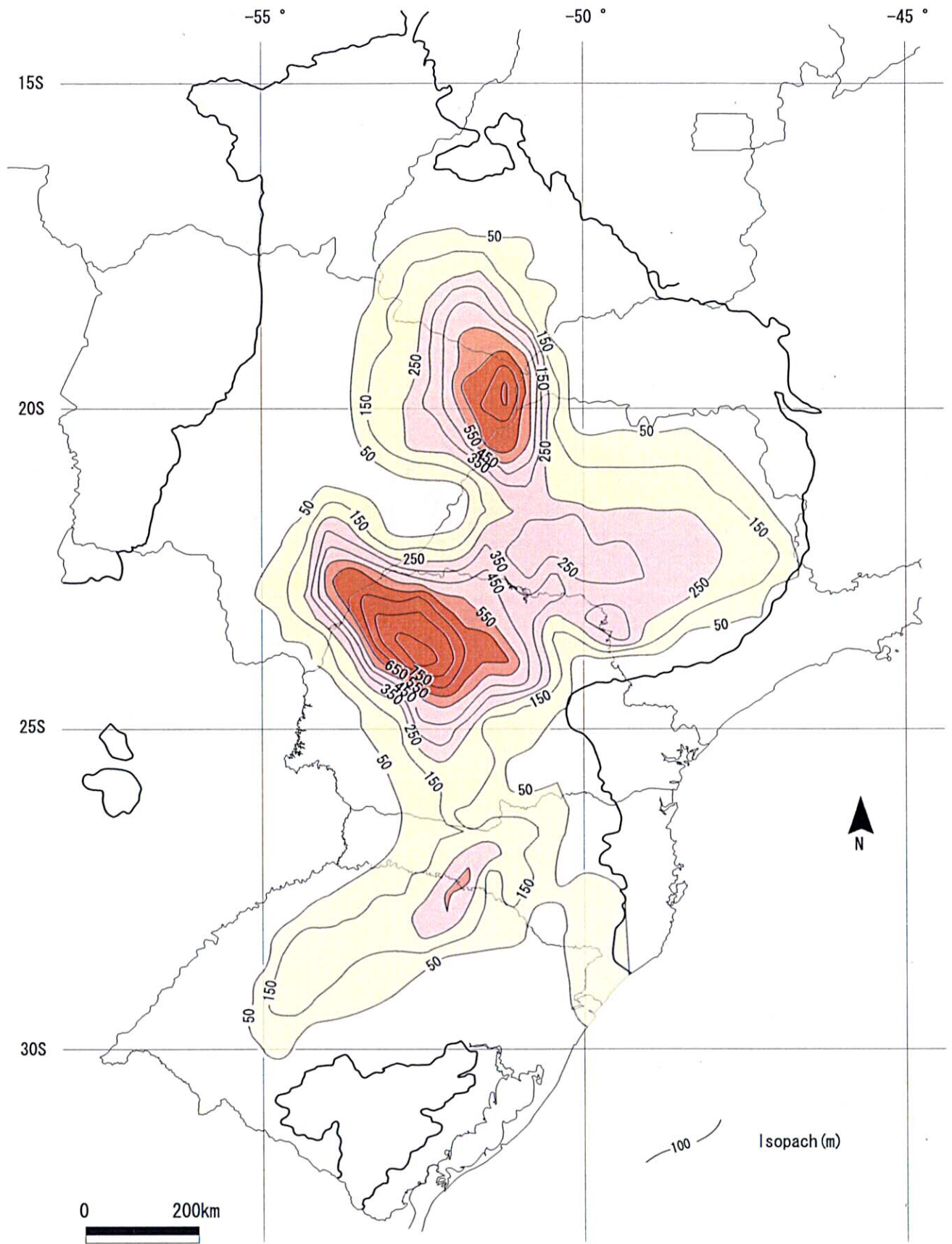


Fig. II -1-4-21. Accumulated thickness of sills, modified from Zalan et al, (1986).(M. C. L. Quintas, 1995).



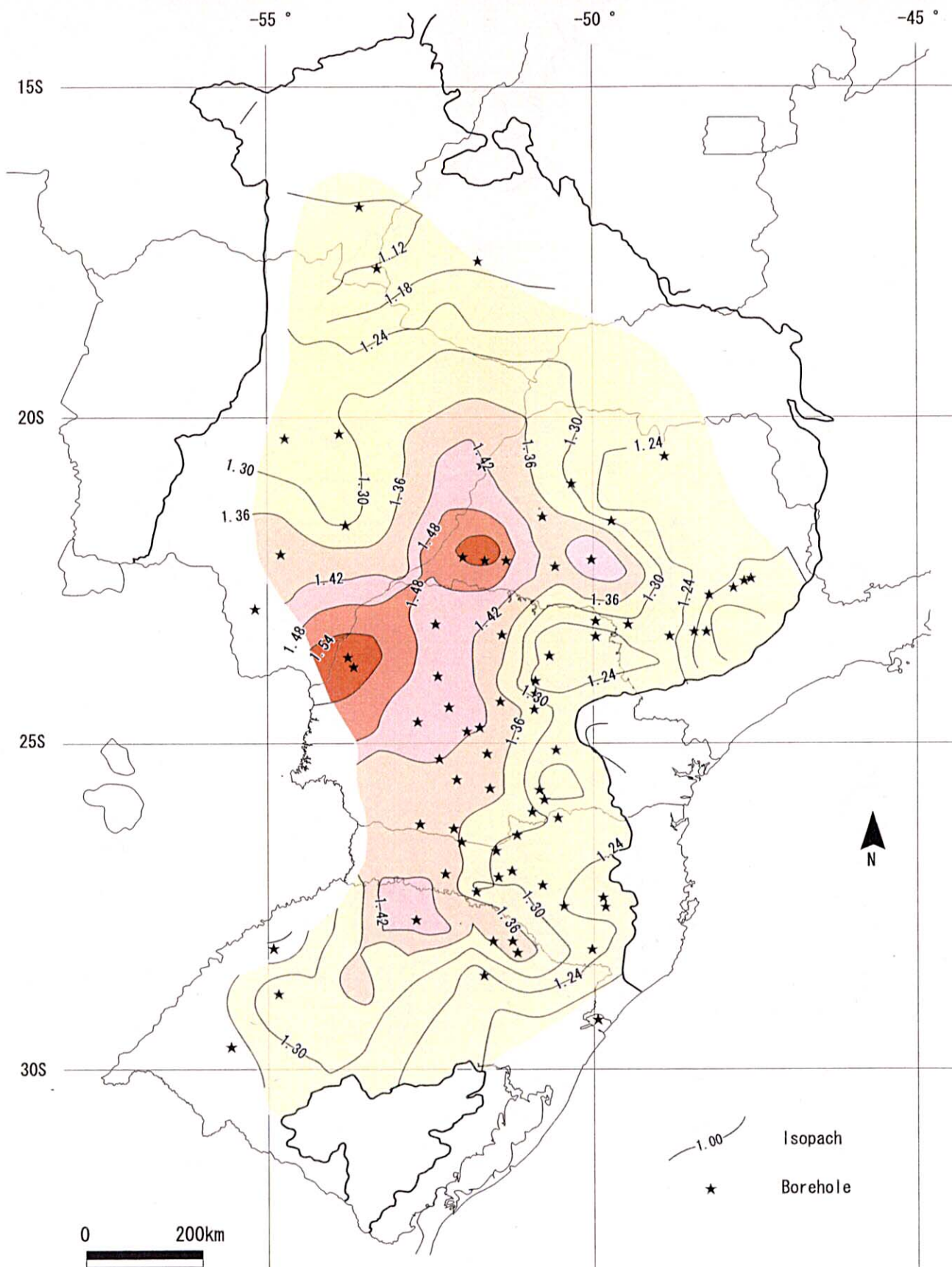


Fig. II-1-4-22. Iso-attenuation map of the second distensible event after the simulation of erosion (296 Ma). (M. C. L. Quintas, 1995).

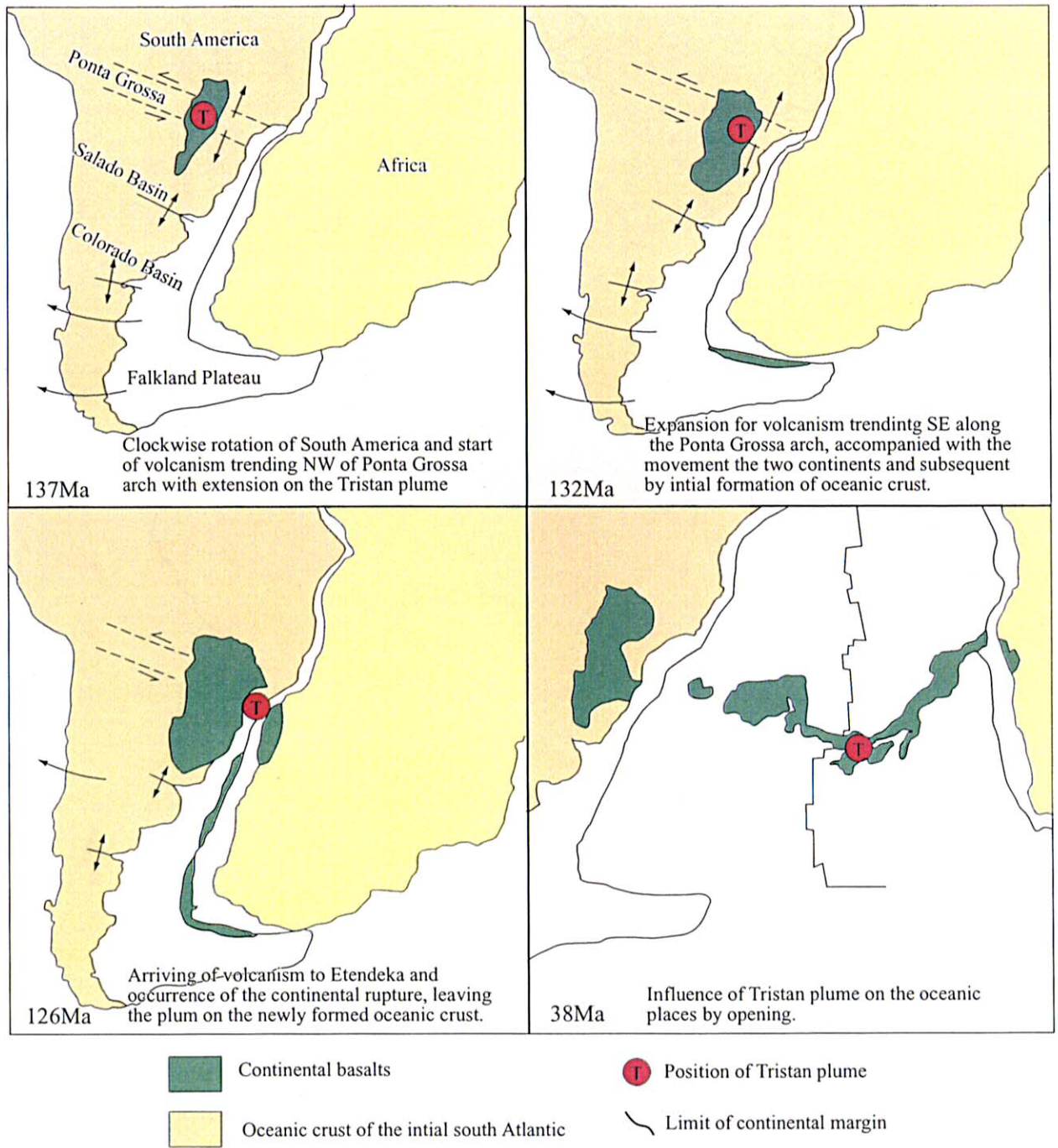


Figure II -1-4-23. Sense of rupture of Gondwana (Turner et al.,1994)



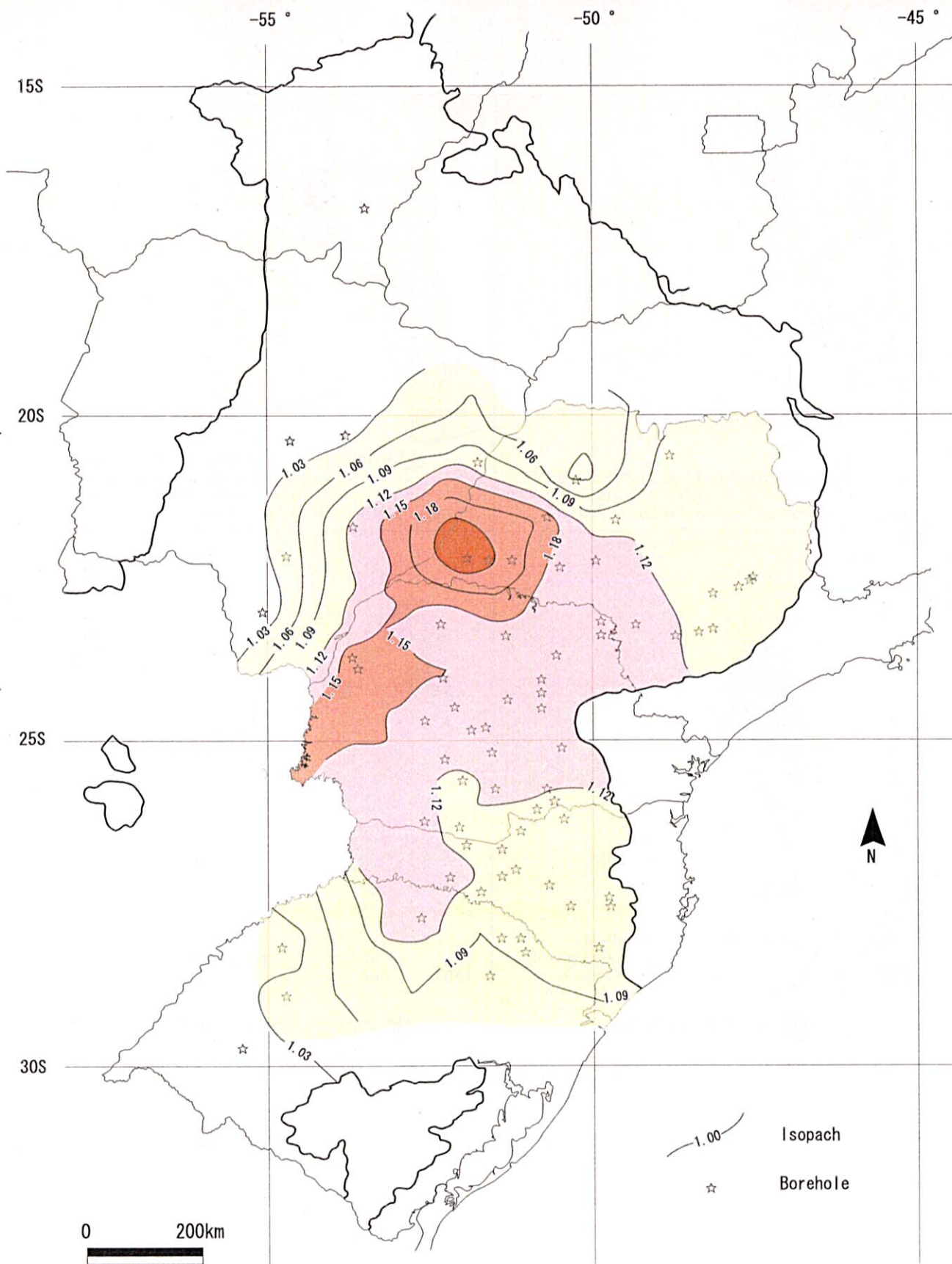


Fig. II-1-4-24. Iso-attenuation map of the third distensible event after the simulation of erosion (144 Ma). (M. C. L. Quintas, 1995).



in the Brazilian belt in the north-eastern part of the basin and in the Paraguay belt in the north and the north-western part of the basin. High gravity anomalies are observed in the eastern part of Mato Grosso do Sul along the Parana river from eastern Paraguay to the western part of Parana Province, in the central part of Sao Paulo Province and in the north-western part of Rio Grande do Sul Province.

Comparing the residual gravity anomaly map (Fig.II-1-4-28) and attenuation( $\epsilon$ ) map, in the case of the first expanding activity (Fig.II-1-4-20), the high gravity anomalies which are distributed along the Parana river from east Paraguay to the western part of Parana Province (in the NE – SW direction) and in the eastern part of Mato Grosso do Sul Province (in the N-S direction) correspond to the high  $\epsilon$  zones. In the case of the second expanding activity (Fig.II-1-4-22), the high gravity anomalies which are distributed along the Parana river from east Paraguay to the western part of Parana Province, in the central part of Sao Paulo Province (in the NW – SE direction) and in the northern part of Rio Grande do Sul Province (in the NW – SE direction) correspond to the high  $\epsilon$  zones. However, the high  $\epsilon$  zones which are observed in the second expanding activity, that are distributed in the central part of Mato Grosso do Sul Province to the southern part of Parana Province (in the NW – SE direction) do not reflect in the gravity anomaly. In the case of the third expanding activity (Fig.II-1-4-24), big high  $\epsilon$  zones, which are distributed in the south-western part of Sao Paulo Province, correspond to the high gravity anomaly.

As the result of the analysis of the basement structure of the Parana basin by using the thermodynamic model by Royden & Keen (1980) and the isostasy model, residual gravity anomaly and  $\epsilon$  can obtain almost the same results.

## 2) Residual Gravity Anomaly and Geological Structure Province

The Paraguay belt corresponds to the low residual gravity anomaly which extends from the north to the south with long length and narrow width. Remarkable low gravity anomaly (Goiania flexure) is observed in the north-eastern part of the basin. This gravity anomaly is a part of the Brazilia belt and suggests the existence of the suture line to Goias massif. Goias massif, Amazon craton and Rio de la Plata craton are presumed to be formed by multi-collision in the subsidence zone (Fig.II-1-4-29). The low gravity anomalies are parallel in the NE–SW direction in the north-western part, in the central part and in the eastern part of Parana basin. These low gravity anomalies can be considered as the segments of crust, with 150 km to 400km in length, which are formed with the progress of collisions. As mentioned above, the process of the basement markedly influenced the genesis of the Parana Basin that is caused by expansion and cooling of mantle.

The high gravity anomaly in the central part of the Parana basin (high  $\epsilon$  zone of the second distensible activity) is located in the south-western part of the Brazilian belt whose direction corresponds to the direction of the Tiete tectonic line in the NW – SE direction, and is presumed

to be one of the feeders of flood basalt. Since the direction of the Tiete tectonic line corresponds to the direction of the south-western margin of the Goiania flexure, this high gravity anomaly is presumed to be the structural influence from the Brazilia Belt.

The Paranapanema block of the central part of the Parana basin is bounded on the south-east by the Jakchinga fault, in the north-east by the Goiania flexure and on the north-west by the Oeste de Goias arch. This block is considered to be a segment of the crust in the middle to late Proterozoic.

The Ribeira belt is located in the eastern marginal part of the Parana basin. The belt is exposed in the ENE–WSW direction and is bounded on the south by the Jacutinga fault and on the north by Lancinha fault. Concerning the gravity anomaly, the unstable low anomaly extends in the ENE–WSW direction. It disappears around the north-western part of Rio Grande do Sul Province near latitude 28° S where the high gravity anomaly zone is. The Ribeira belt is confirmed by seismic prospecting. The low gravity anomaly with big round shapes on the south-eastern part of the Ribeira belt was caused by acid volcanic rocks, which consist of part of the Parana flood basalt.

The high gravity anomaly (high  $\epsilon$  zone) near the north-western part of Rio Grande do Sul Province (latitude 28° S) in the WNW–ESE direction is located in the area where the Ribeira belt, the Paranapanema craton and the Rio de La Plata Craton meet. The Toles Posadas tectonic line (Reintz, 1949) pass through the area in the WNW–ESE. It is possible that the high gravity anomaly could be the junction of the three tectonic provinces mentioned above. The porous basalt lava flows are distributed there accompanied with native copper mineralization. The area assumed to have been one of the eruption center of the flood basalt magmatism. The Ponta Grossa arch only shows a small gravity anomaly. The  $\beta$  value also is a small value (1.11 - 1.25).

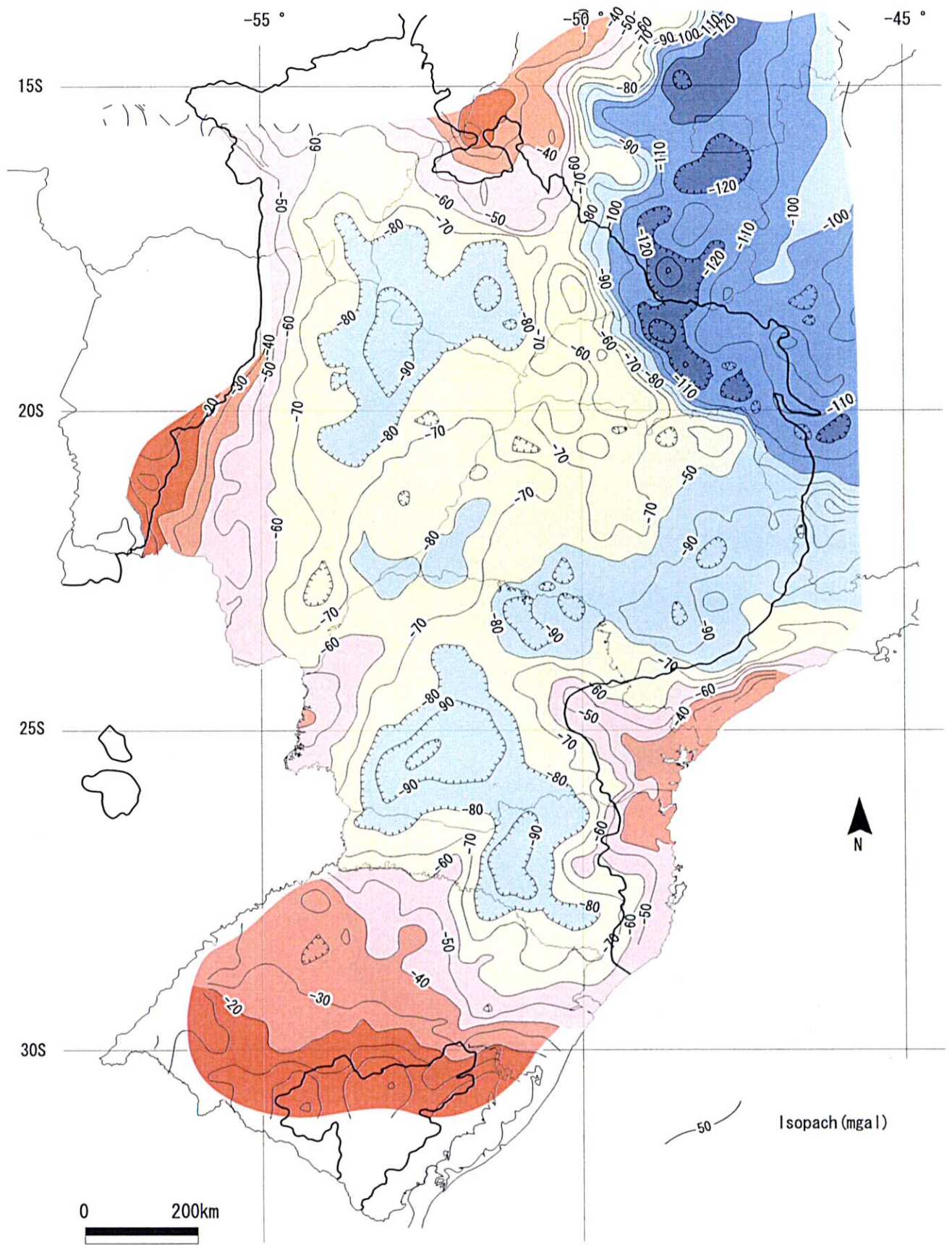


Fig. II-1-4-25. Bougure anomaly calculated from observed data (M. C. L. Quintas, 1995).



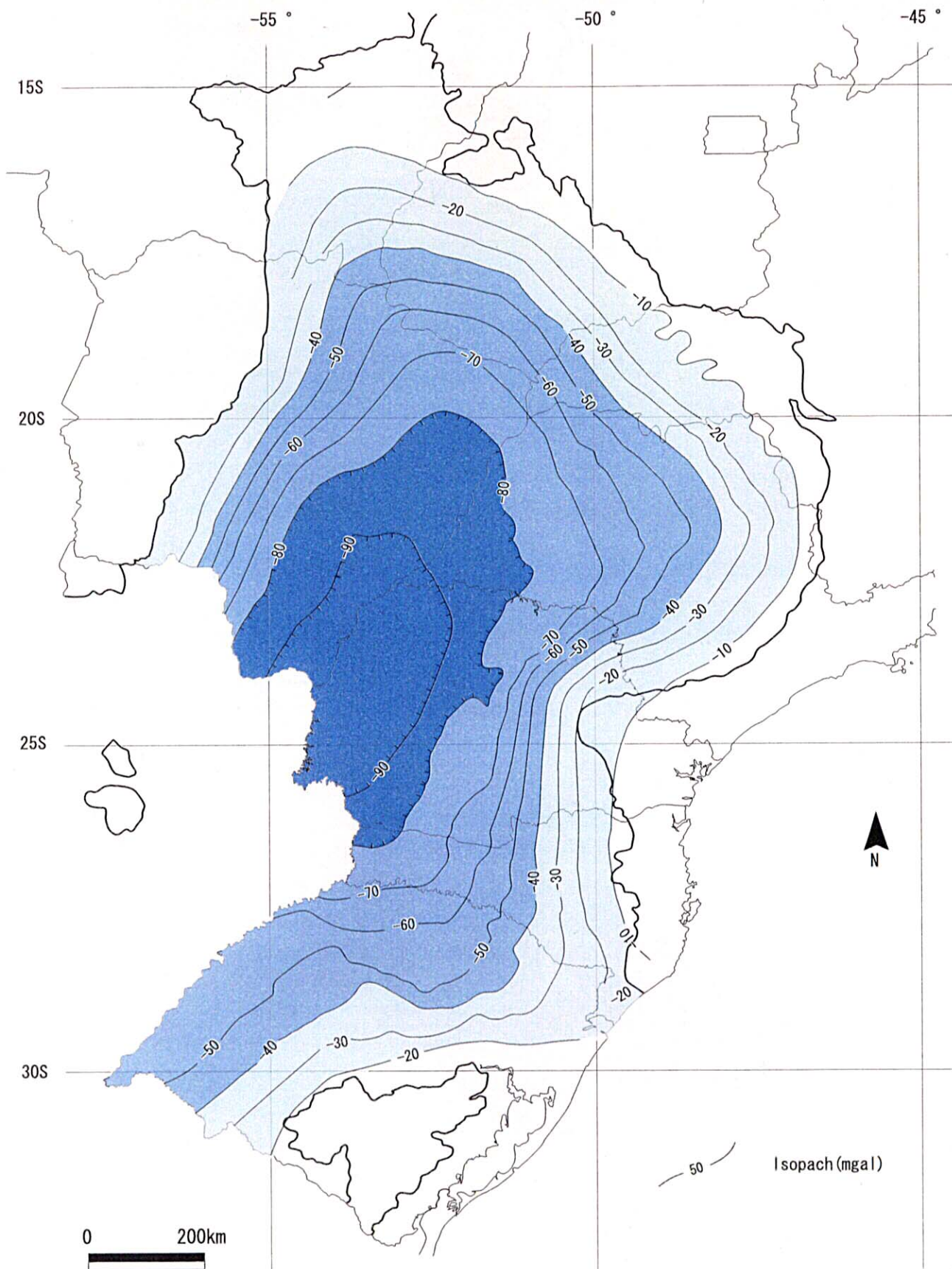


Fig. II-1-4-26. Anomaly calculated due to the Parana basin, considering anomalies generated by sediments, igneous rocks, sillis and "root" (M. C. L. Quintas, 1995).

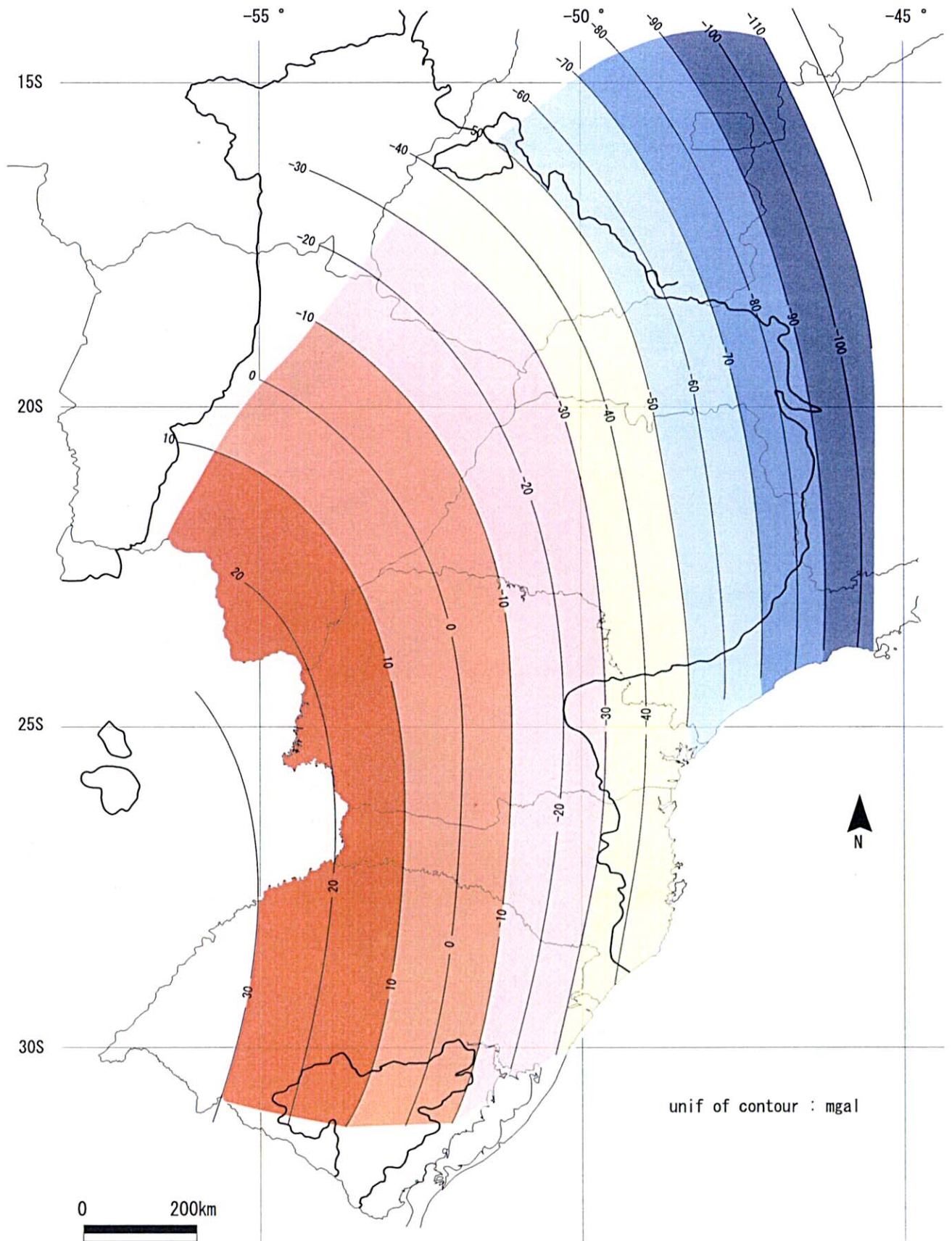


Fig. II-1-4-27. Gravimetric trend anomaly generated by the second order polynomial, (M. C. L. Quintas, 1995).



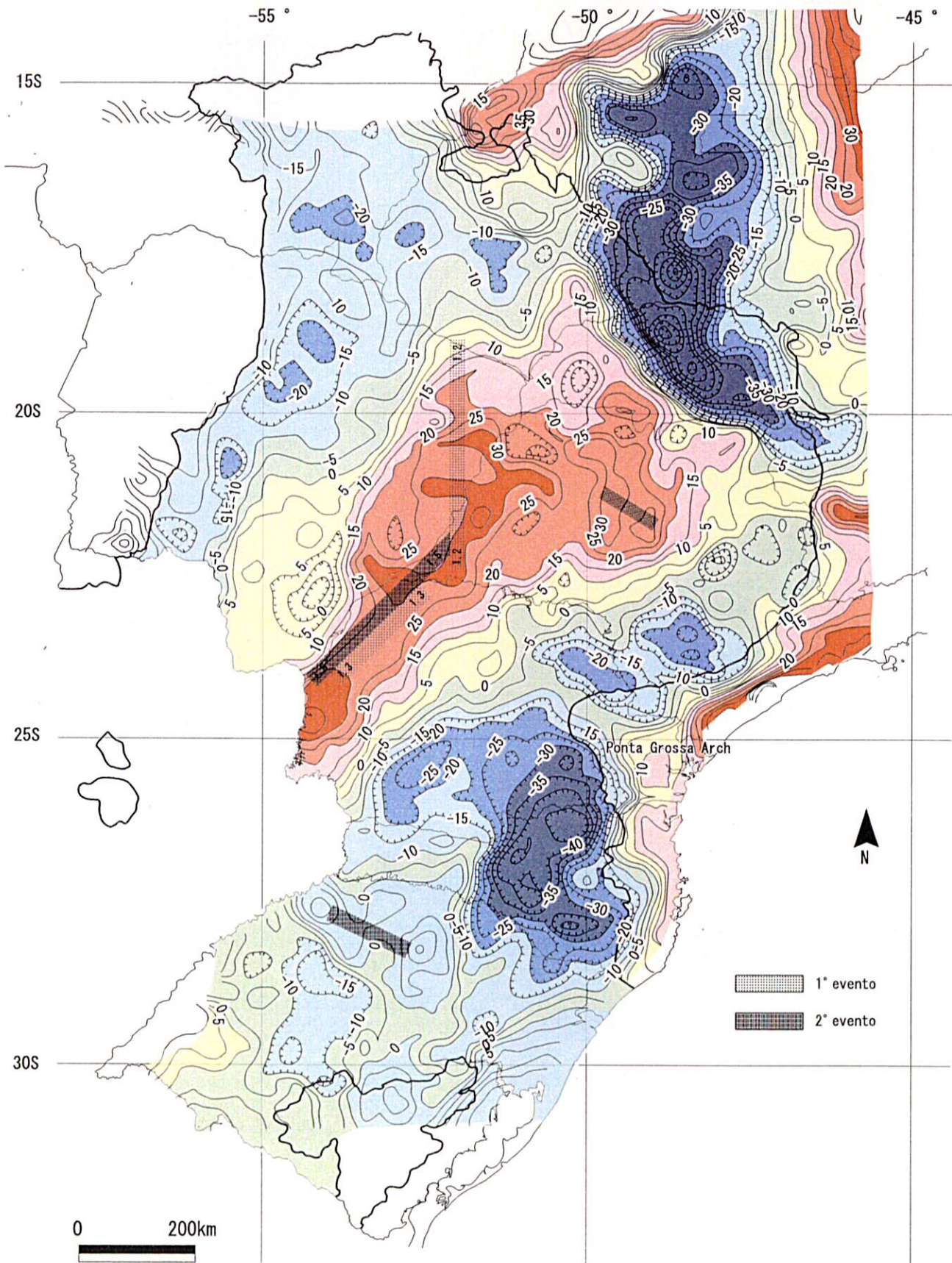
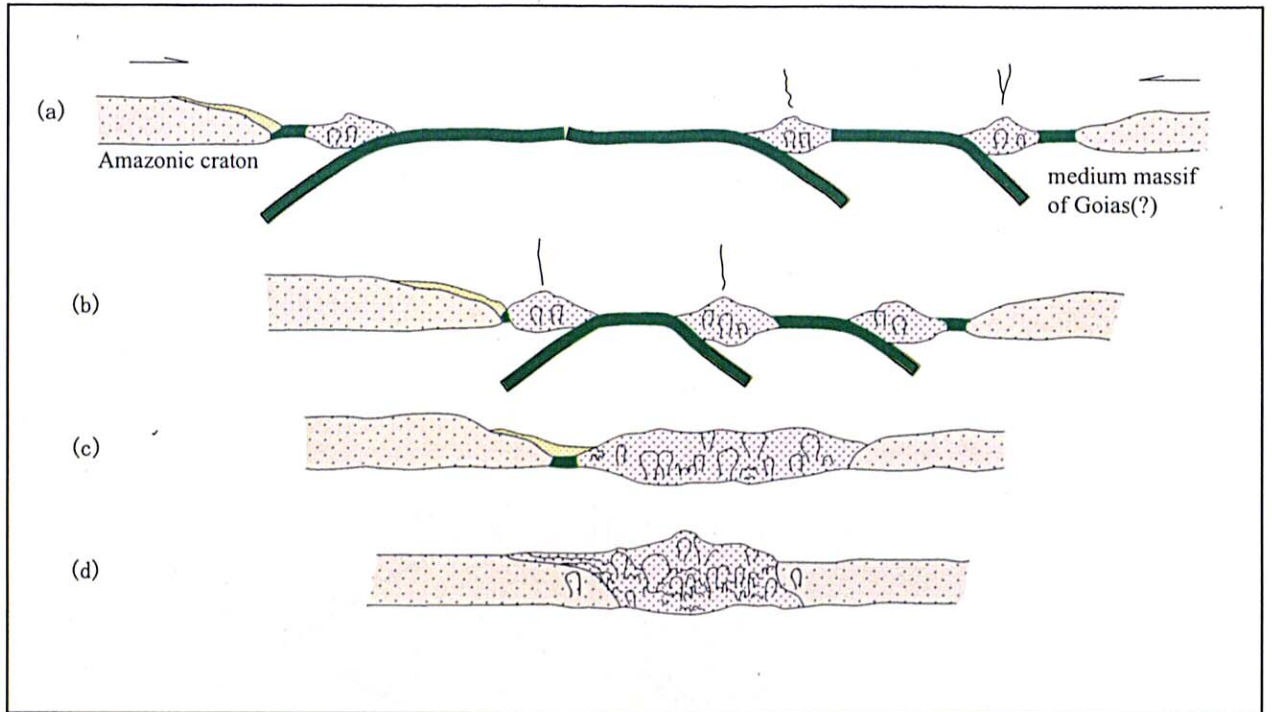


Fig. II-1-4-28. Residual anomaly subtracted the second order trend anomaly from the Bonguer anomaly indicating zones of major attenuations related with two distensible events. (M. C. L. Quintas, 1995).



**Figure II-1-4-29. Hypothetical model for geotectonic evolution of segments adjacent to Paraguay belt, inferred by geological observations in south western Goiás region(extracted from Pimentel and Fuck,1987).**

This evolution can be subdivided into 4 stages: (a) establishment of volcanic arches with the extrusions of tholeiitic basalts and subsequent by intrusions of gabbroic-dioritic bodies; (b) extrusion of calc-alkalic volcanic sequences and intrusions of small bodies equivalent to the compositions; (c) Joining of two arches with intrusions of granitic and basaltic bodies; (d) Collision and joining continental masses and



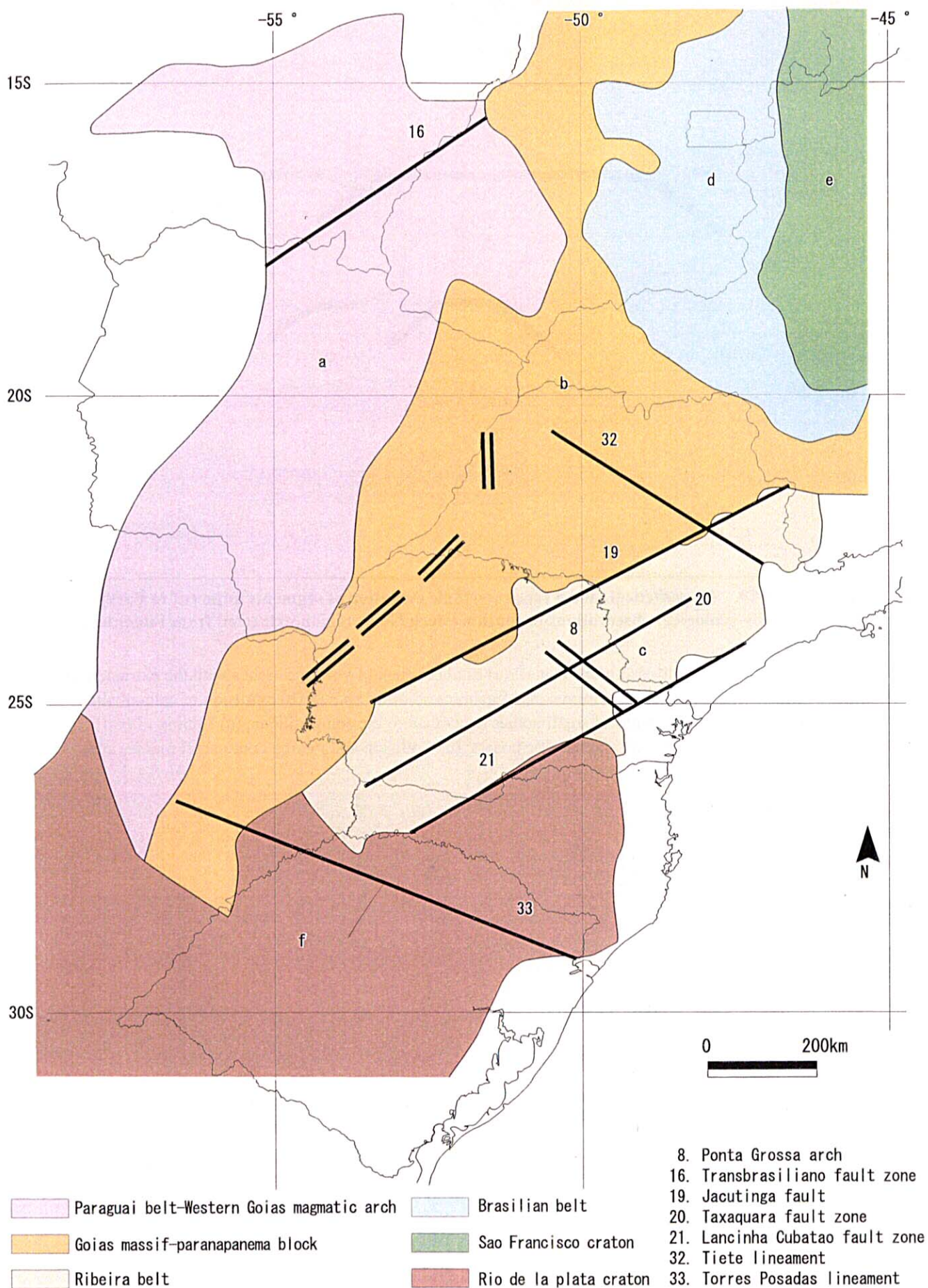


Fig. II-1-4-30. Tectonic provinces of basement rocks and lineaments inferred from residual gravimetric anomalies(M. C. L. Quintas, 1995).

## 1-5 Geology and Geological Structure of Central Parana Basin

As stated in section 1-4, ① the central Parana Basin has a region where many faults, including the Rio Alonzo Fault and Guapiara Fault etc.al., are concentrated in the NW-SE direction. ② The region is intruded by many dykes and sills. ③ The residual gravity anomaly, attenuation ratio ( $\epsilon$ ) are higher along Rio Parana in the NE-SW direction. These mean that the central Parana Basin is a region where was the largest magma activities in the Parana Basin. For instance, the Noril'sk deposit is considered to have been formed along large faults leading to the mantle and in the central area of the magma activities. Based on these facts, we estimate that the highest possibility of occurrence of deposits is found in the central Parana Basin. In order to have a full understanding of the geology and the geological structure of the central Basin, we analyzed aeromagnetic anomaly maps and satellite TM images by comparing them with existing data.

### 1-5-1 Geology and Geological Structure

Fig.II-1-5-1 is a geological map of the central Parana Basin which is excerpted from Mapa Geologico do Brasil (1:2,500,000). The Precambrian basement rocks such as the Ribeira belt and the Curitiba massif (Section 1-4-2) bounded by faults in the NE-SW direction are distributed in the southeastern area of the central Basin (Fig.II-1-5-2: Photos 1 to 4). The Paleozoic sedimentary rocks are distributed in west sides and north sides of basement rocks area (Photos 5 to 8). The southwestern area of the central Parana Basin is covered with basaltic lava (Serra Geral formation), while the northern area of the central basin is covered with basaltic lava and Bauru formation with a thickness of 100-200m (Section 1-4-3, Photos 9 to 18).

The faults in the NW-SE, NE-SW, and E-W directions (Fig.II-1-5-3) are predominant. The faults in the NW-SE direction cut the structure of basement rocks at the right angle to high angles; faults in the NE-SW direction are almost parallel with the structure of basement rock and a part of the faults consists of high-angle reverse faults. Two E-W direction faults are recognized in the central zone and they seem poor in continuity.

A continuous upheaval structure which is called the Ponta Grossa arch, is observed toward the NW-SE direction from the southeastern of this area. A large amount of dykes and sills in the NW-SE direction intrude into the basement rocks, Paleozoic sedimentary rocks, and flood basalt lava in the arch. Fig.II-1-5-4 indicates a distribution of faults, sillas and dykes of the Ponta Grossa arch (Ferreira et al.,1981). The dykes and sills mainly intrude along faults in the NW-SE and NE-SW directions between Rio Alfonzo fault and Guapiara fault. J. P. P. Pinese (1989) concluded that faults in the NW-SE direction of the Ponta Grossa arch were formed when the arch upheaved. Meanwhile, Ferreira et al. (1981) estimated that they were formed in relation with an aulacogene in the NW-SE direction since Early Paleozoic, because they are



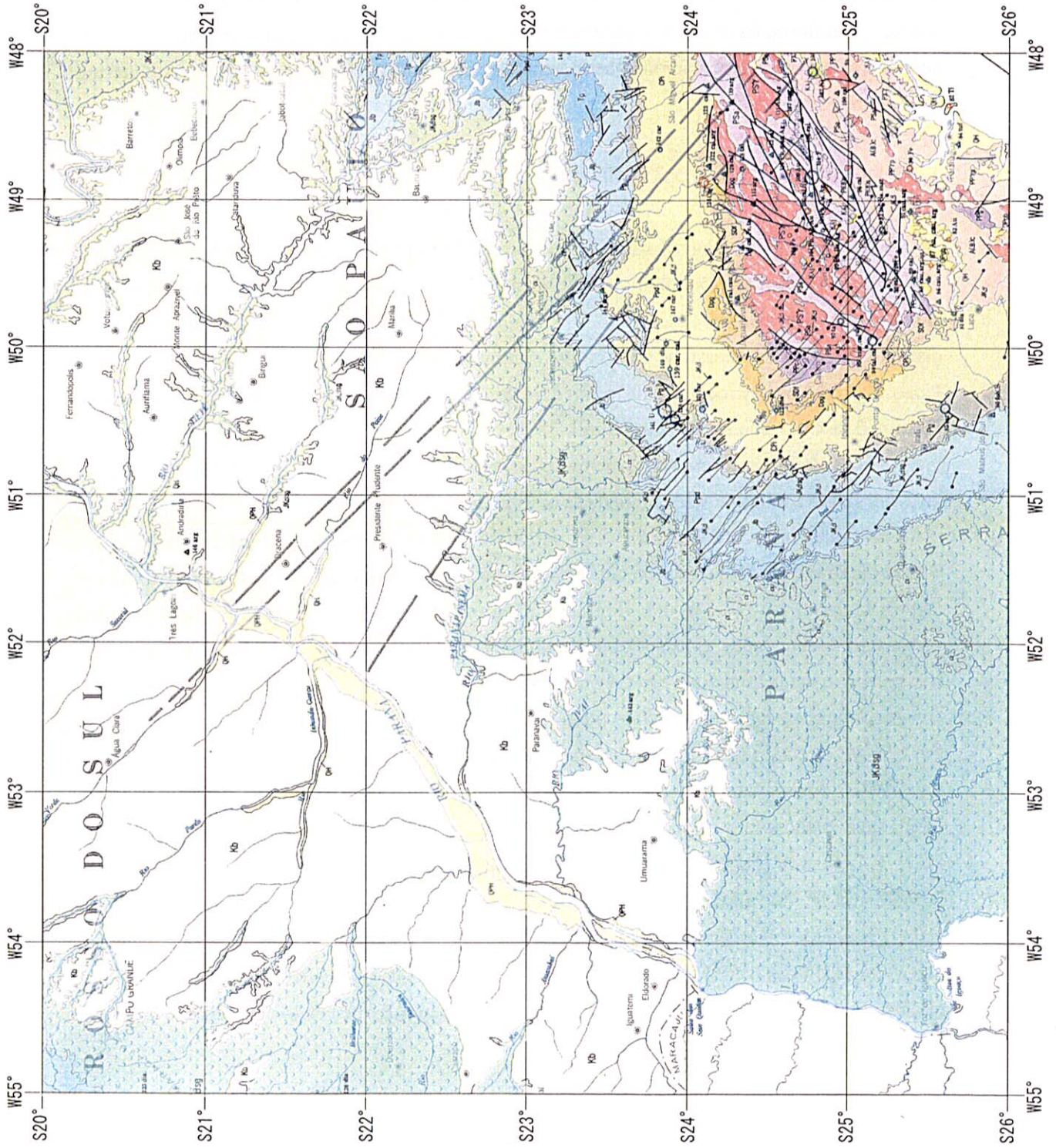
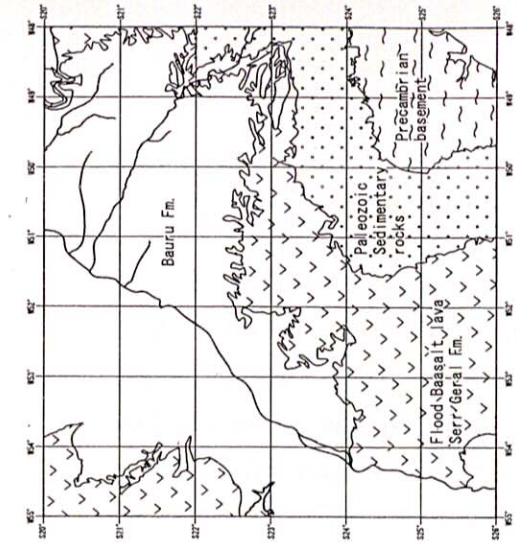


Fig. II -1-5-1.  
Geological Map of Central Parana Basin



## Precambrian Basement rocks



49° 45' 38.9" W, 25° 00' 36.5" S.

Photo-1 : Steep topography of basement rocks in the NE-SW direction.



49° 46' 31.7" W, 24° 59' 56.0" S (KN135).

Photo-2 : Pelitic schist. N45E, 73SE trending Schistosity.  $\kappa = 0.19$  (Susceptibility  $\times 10^{-3}$  emu/cc).



49° 45' 38.9" W, 25° 00' 36.5" S (KN136).

Photo-3 : Granodiorite (K-Ar 610Ma).  $\kappa = 11.0$



49° 46' 31.7" W, 24° 59' 56.0" S (KN132).

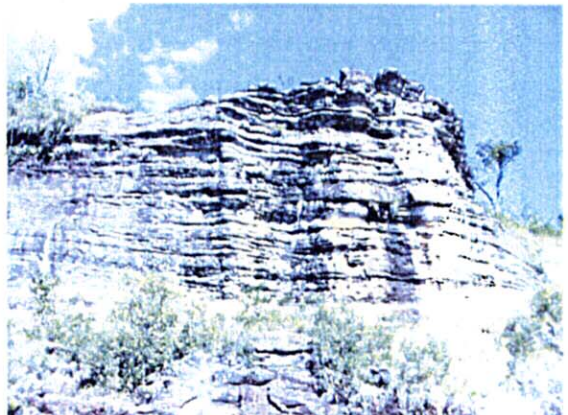
Photo-4 : Limestone in Abapa quarry (Proterozoic) N50E, 52SE.  $\kappa = 0.63$ .

## Paleozoic sedimentary rocks



49° 46' 31.7" W, 24° 59' 56.0" S (KN129A).

Photo-5 : Castro Fm. (Ordovician). Weak altered tuff breccia.  $\kappa = 0.59$ .



50° 26' 43.2" W, 24° 30' 02.9" S (KN103).

Foto-6 : Furnas Fm. (Devonian). Siltstone. Horizontal bedding.  $\kappa = 0.10$ .

**Fig. II-1-5-2 (a) Photos of igneous and sedimentary rocks in central Paraná basin**



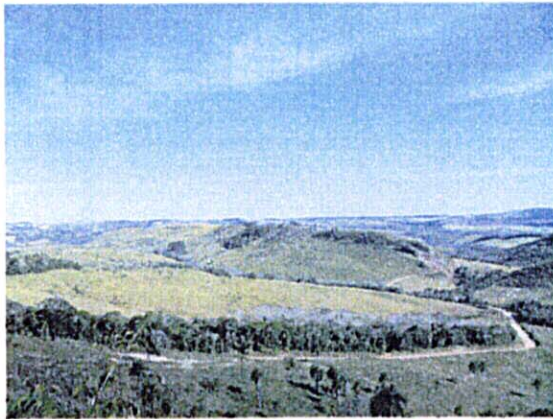


50° 20' 50.4" W, 24° 05' 57.1" S (KN127).  
 Photo-7 : Itarare Fm. (Carboniferous) .  
 Siltstone.  $\kappa = 0.10$ .



50° 37' 25.0" W, 23° 50' 25.0" S (KN116).  
 Photo-8 : Rio do Rasto Fm. (Permian) .  
 Horizontal bedding.  $\kappa = 0.14$ .

### Early Cretaceous Flood Basaltic rocks



50° 42' 04.3" W, 23° 58' 04.3" S.  
 Photo-9 : Dyke forms long and narrow hill in  
 the N60W direction. (from central part of photo).



50° 52' 04.7" W, 24° 18' 29.9" S (KN123).  
 Photo-10 : Boulders of dykes scattered at top of hill  
 (N32W) . Pd 24.2ppb, Pt 3.9ppb.  $\kappa = 19.8$ .



50° 32' 18.2" W, 24° 28' 01.9" S (KN104).  
 Photo-11 : Dyke of the highest PGE grade (N55W  
 78NE, w 10m<) . Pd 134ppb, Pt 18.7ppb.  $\kappa = 21.0$



49° 21' 13.1" W, 23° 27' 42.5" S (KN149).  
 Photo-12 : Joints of dyke have in three directions  
 of dyke. Pd 16.6ppb, Pt 8.8ppb.  $\kappa = 21.2$ .

**Fig. II-1-5-2 (b) Photos of igneous and sedimentary rocks in central Paraná basin**





50° 51' 48.2" W, 24° 38' 05.4" S (AS014).  
 Photo-13 : Sill crops out trapezoidally.  
 Pd <0.2ppb, Pt <0.2ppb.  $\kappa$  =37.3.



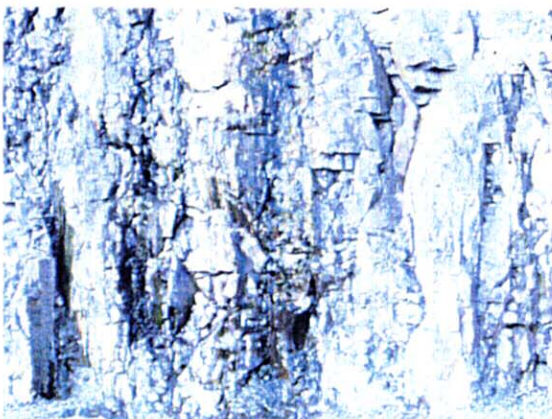
51° 05' 06.8" W, 23° 59' 53.2" S. (KN110).  
 Photo-14 : Sill intruded into siltston.  
 Pd 43.4ppb, Pt 16.5 ppb.  $\kappa$  =60.5.



50° 35' 10.5" W, 24° 25' 26.0" S (KN105).  
 Photo-15 : Typical lithoface of sill or dyke. Width = 50m(<). Pd 35.7ppb Pt 6.0ppb.  $\kappa$  =23.2.



50° 36' 54.0" W, 23° 55' 12.0" S (KN167).  
 Photo-16 : Pegmatitic gabbroic dyke  
 Pd <0.2ppb, Pt 0.7ppb.  $\kappa$  =47.3.



50° 29' 28.2" W, 22° 36' 17.7" S (KN157).  
 Photo-17 : Quarry of basaltic lava.  
 Pd 17.0ppb, Pt 8.7ppb.  $\kappa$  =34.5.



52° 49.0' 06.6" W, 26° 18.0' 07.6" S (KN017).  
 Photo-18 : fine grained, massive and homogeneous tholeiitic basalt lava. Pd 12.2 ppb, 18.1 ppb.

**Fig. II-1-5-2 (c) Photos of igneous and sedimentary rocks in central Paraná basin**

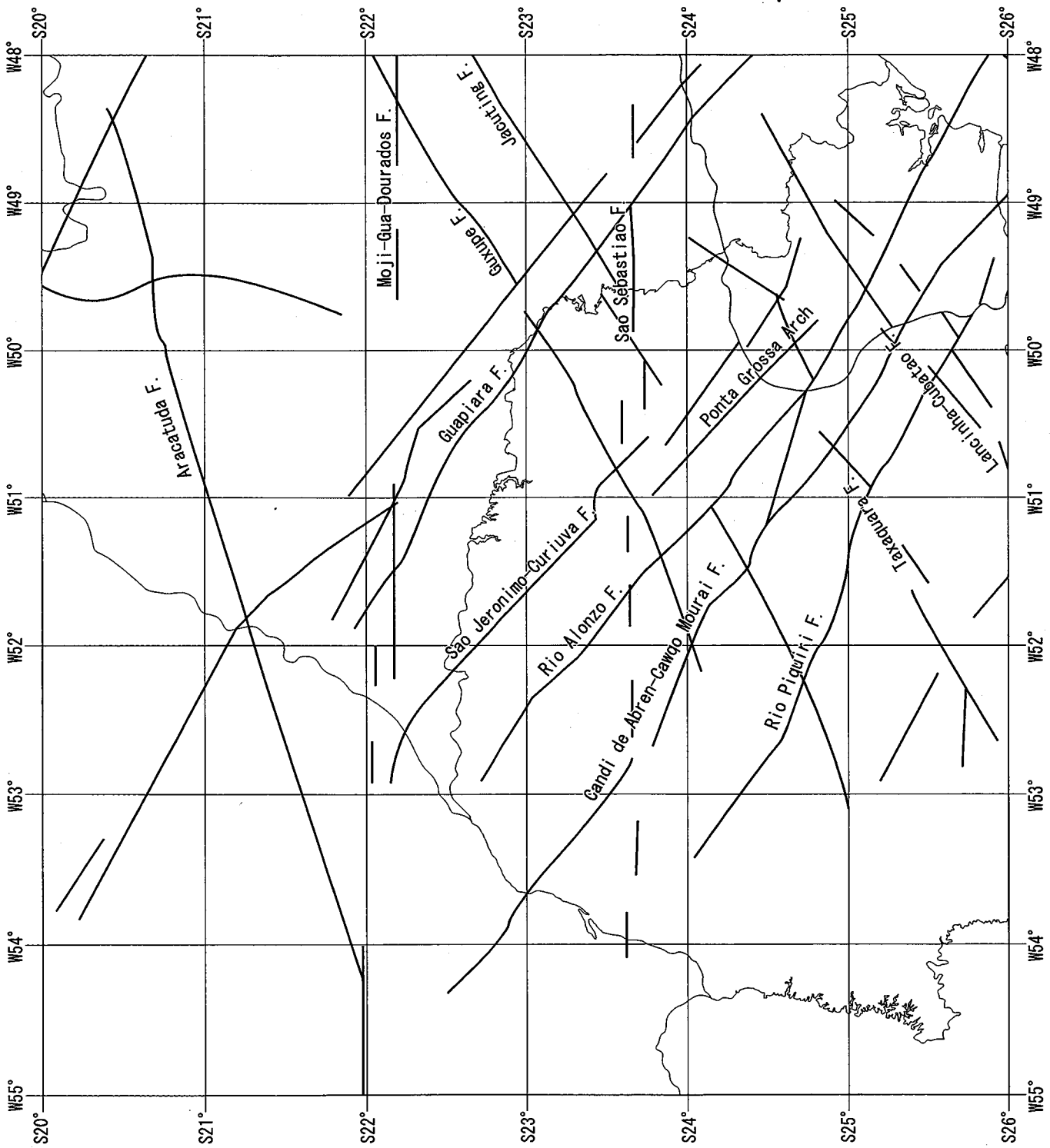


Fig. II -1-5-3. Principal arch faults in the central Parana Basin (M.C.L. Quintas, 1995)



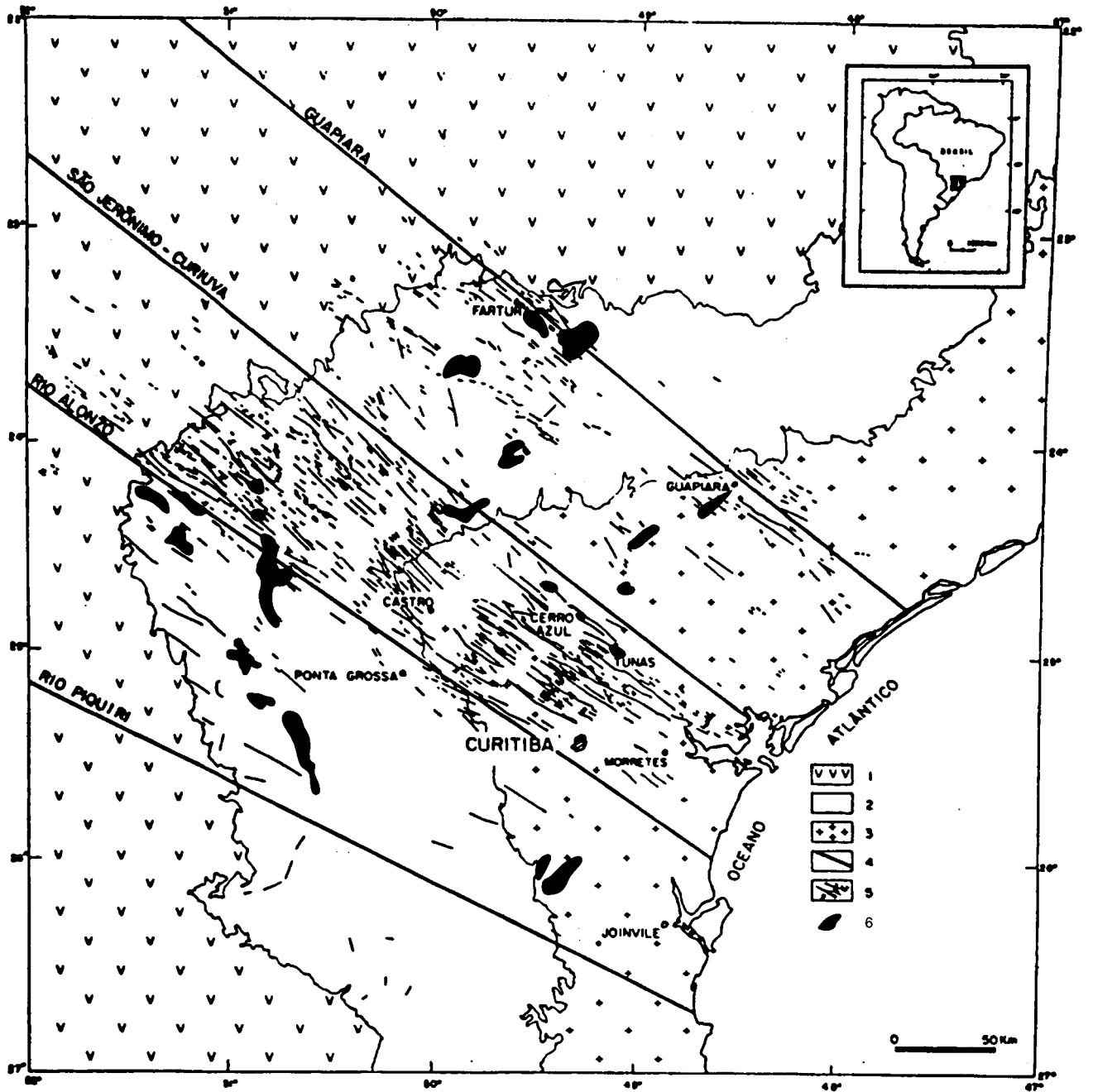
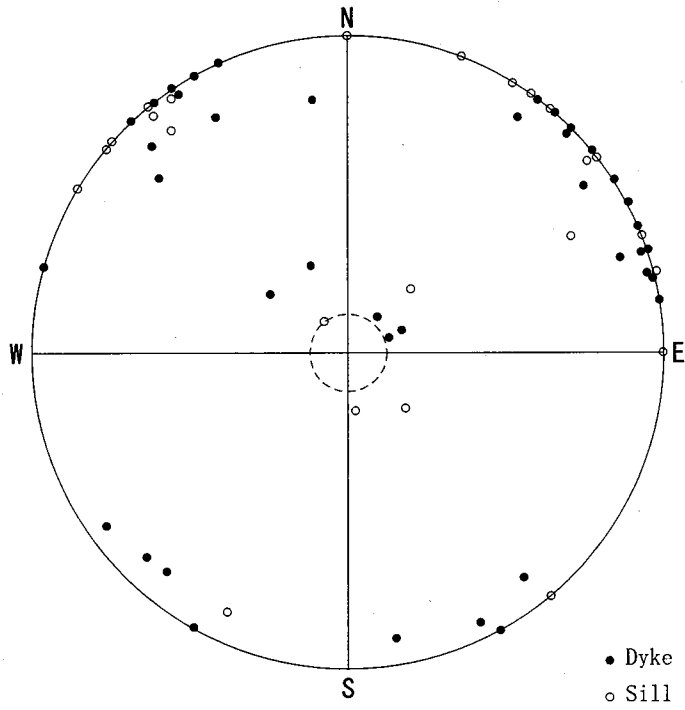


Fig. II-1-5-4. Dyke swarn of the Ponta Grossa Arch

1: Parana flood basalt lava , 2: Paleozoic sediment , 3: Crystallized basement , 4: Magnetic structures , 5: Dykes based on geologic , aeromagnetic and remote sensing data . (modified from A.J.Melf et al ., 1988)



**Fig. II -1-5-5. Poles of joints of basalt dykes in the central area. Plotted on lower hemisphere.**

almost perpendicular to the directions of basement rocks in Precambrian. The dykes on the ground surface form long and narrow hills in the NW-SE direction (Fig.II-1-5-2: Photo 9). Meanwhile, sills tend to form gentle inclined plateau landforms (Fig.II-1-5-2: Photos 13 to 14). The dykes range in width from 10m to 50m, and some have a continual length of several hundred kilometers. Although most of the dykes are in the NW-SE direction, some of them intrude along faults in the NE-SW direction like the dyke along the Jacuting fault. Some lengthy sills (several kilometers  $\times$  several 10km) are observed along faults while other sills (diameter: 10 to 40km) like a circle are observed at a cross of faults. Most of the sills range several tens of meters in thickness. According to coal drilling core data of CPRM, sills with a thickness of 100m or more are observed only at three sites, namely Saponema, Reserva, and Pien (Fig.II-1-5-4).

An intrusion direction of dyke can sometimes be estimated from its geography on the ground surface. Furthermore, it can also be estimated from the cooling joints. Fig.II-1-5-5 is a stereo projection of directions of dykes and sills which intruded into the Paleozoic in the central Basin. According to the stereo projection, directions of joints are concentrated in the following three directions. ① N60W to N10W, average N35W, inclination  $90 \pm 10$ , ② N45E to N65E, average N55E, inclination  $90 \pm 10$ , ③ Inclinations of joints are close to horizontal levels of 0 to 20. The joints in the N35W direction and the joints in the N55E direction are cross at the right angle. The N35W direction coincide with direction of intrusion of dyke. The joints in the N55E direction and those close to horizontal levels are perpendicular to the intrusion direction. These joints are formed associated with cooling of magma in the underground.

## 1-5-2 Aeromagnetic Anomaly Maps

### (1) Outline

In order to reveal the geological structure at depth in the underground of the central Basin, we purchased a set of aeromagnetic anomaly maps with a scale of 1:1,000,000 and in 1:3,000,000 from GETECH Corporation (United Kingdom), namely eight kinds of maps for two projection methods. We also purchased an Geotif image CD (tmi.tif) for Acc View of the total magnetic anomaly map and flight line location map. Concerning the projection methods, we adopted the UTM method and the linear longitude/latitude method. The maps of linear longitude / latitude method are put on this report. The specifications of the UTM projection are Transverse Meractor, Spheroid WGS 84, Central Meridian 51 °W, Scale Factor 0.9996, Latitude of Origin 0°, False Easting 500 km and False Northing 10,000 km. The specifications of the linear longitude/latitude method are 1°= 111.1 km and longitude 1°= 102.3 km.

**Flight line locations:** Since survey data of a southern area were unavailable, we could not cover the area (Fig.II-1-5-6).

**Total magnetic intensity:** Grid data of different surveys were compiled and calculated in 1km grids at an aerial point of 1 km above the ground surface. IGRF (International Geomagnetic Reference Field) at the time of the data acquisition was already subtracted (Fig.II-1-5-7).

**Second vertical derivative of total magnetic intensity:** The vertical derivative measures the rate of change in the Z field. The filter function is represented by a quadratic curve  $F(u, v) = u^2 + v^2$ , and short wavelength ranges are amplified. This anomaly is effective to grasp fault directions and geological structure, especially to amplified anomalies near the ground surface (Fig.II-1-5-8).

**Total horizontal derivative of the total magnetic intensity:** The total horizontal derivative measures the rate of change of the field in the X and Y directions (Fig.II-1-5-9). Such anomalies are effective to estimate the existence of faults and geological structure.

**Total horizontal derivative of pseudogravity:** The total horizontal derivative measures the rate of change of the field in the X and Y directions (Fig.II-1-5-10). Such anomalies are also effective to estimate the existence of faults and geological structure.

**Analytical signal:** The analytical signal is sometimes termed the total derivative and is the Pythagorean sum of the X, Y, and Z derivatives (Fig.II-1-5-11).

**Reduced to the pole magnetic anomaly:** The reduction to the pole operation transforms a magnetic field to that which would arise from the same source placed at the magnetic pole i.e. It removes the bi-polar nature of the magnetic anomaly resulting in a signal anomaly directly over the causative body (Fig.II-1-5-12). The transformation for this area was based on a magnetic inclination of  $-22.47^\circ$  and declination to  $-13.50^\circ$ .

**Pseudogravity:** The pseudogravity operation is the vertical integration of the reduced to the pole magnetic anomaly and has the effect of transforming the dipole magnetic anomaly into a monopole anomaly. Therefore, pseudogravity is a filter to amplitude long wavelengths in reduction to the pole magnetic anomaly (Fig.II-1-5-13). Gravity field and magnetic field have the following relations. When a rock body that brings about magnetic anomaly is assumed as  $v$ , gravity potential U and magnetic potential V in aerial point p are expressed in the following formulas.

$$U(\vec{r}) = -G \iiint_v \frac{\rho(\vec{r}_0)}{(\vec{r} - \vec{r}_0)} dV$$

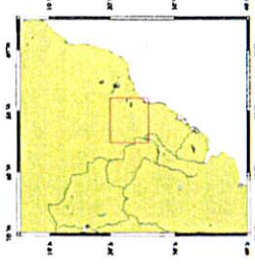
$$V(\vec{r}) = -\iiint_v \frac{\text{grad} \cdot \vec{J}(\vec{r}_0)}{(\vec{r} - \vec{r}_0)} dV$$

$\rho$  = Density of rock body

$\vec{J}$  = Intensity of magnetization of rock body

G = Gravitational constant ( $6.67 \times 10^{-8}$  c.g.s)

Location Map



Technical Specifications

The map shows aeromagnetic flightlines. GETECH has compiled, reproduced and merged aeromagnetic data from a variety of sources into a unified line grid at 1 km mean terrain clearance.



Projection: UTM  
 Datum: WGS 84  
 Zone: 18 S  
 Units: Meters

GETECH (Geophysical Exploration Technology)  
 Southern Brazil Aeromagnetic Data  
 Aeromagnetic Flight Line Locations

Scale - 1:100,000 Map 8 of 8 Date - August 2002  
 GETECH Corporation 4000 Highway 100  
 Houston, Texas 77058 USA  
 Phone: +1 281 280 1000  
 Fax: +1 281 280 1001  
 E-mail: info@getech.com  
 Website: www.getech.com

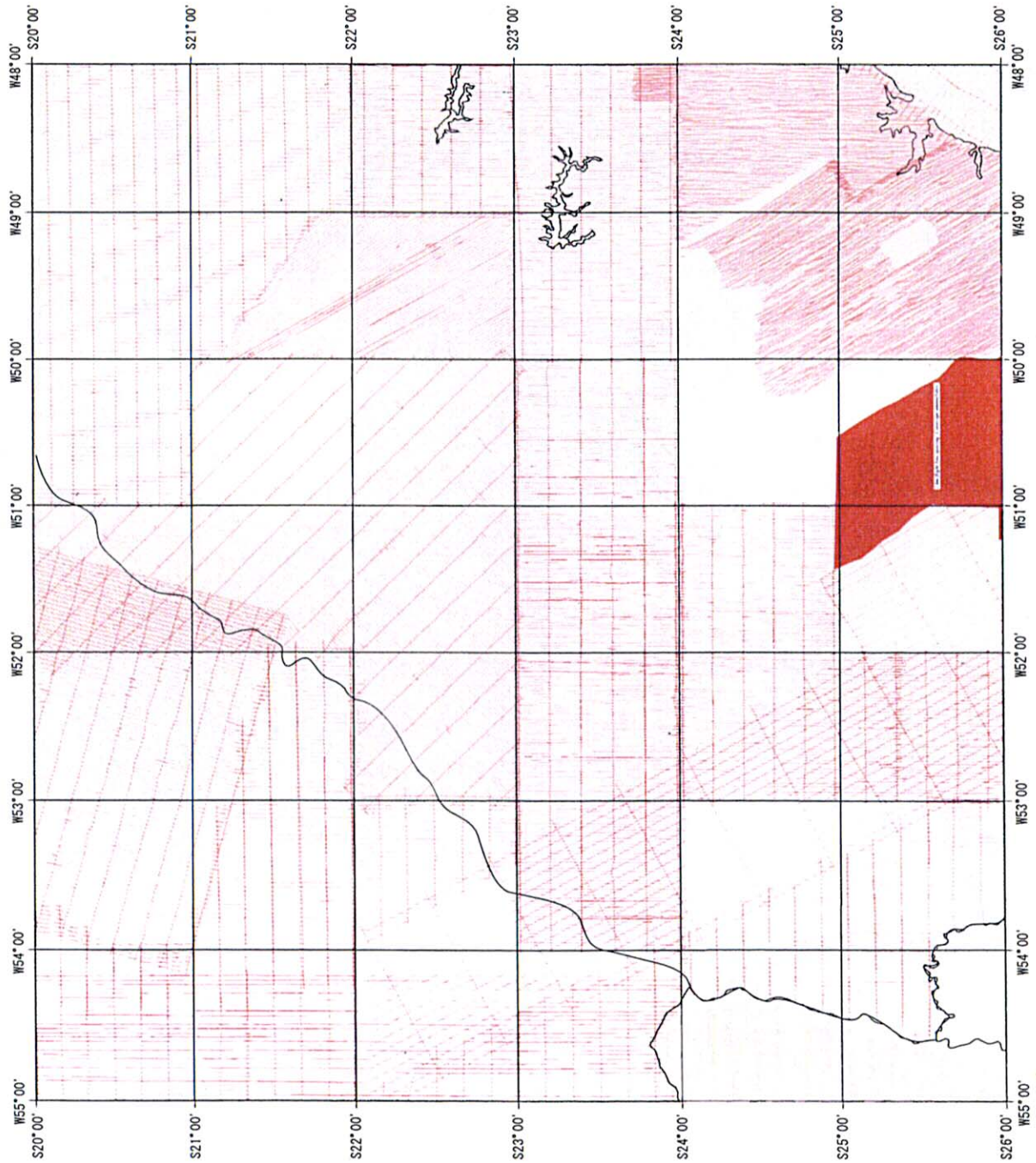
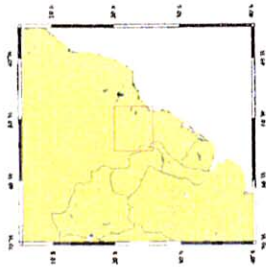


Fig. II-1-5-6 Flight line locations of aeromagnetic data in central Paraná basin

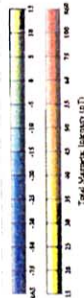


Location Map



**Technical Specifications**

This map shows total magnetic intensity (TMI) data compiled, reprocessed and merged aeromagnetic data from a variety of sources into a unified 1km grid at 1km mean terrain altitude. Flight line coverage is shown on a separate map (OBR/BCBR for east or acquisition reserved).



GETECH (Geophysical Exploration Technology)

Southern Brazil Aeromagnetic Data

Total Magnetic Intensity

Contour Interval: 5 nT

Shading from north

Map 1 of 8

Scale: 1:100,000

Date: August 2002

GETECH (Geophysical Exploration Technology) Ltd.

Geophysical Exploration Technology Ltd. is a registered company in the United Kingdom. The company is a subsidiary of Geophysical Exploration Technology Ltd.



Copyright © 2002 Geophysical Exploration Technology Ltd. All rights reserved. This map is a reproduction of the original data and is not to be used for any other purpose without the written consent of Geophysical Exploration Technology Ltd.

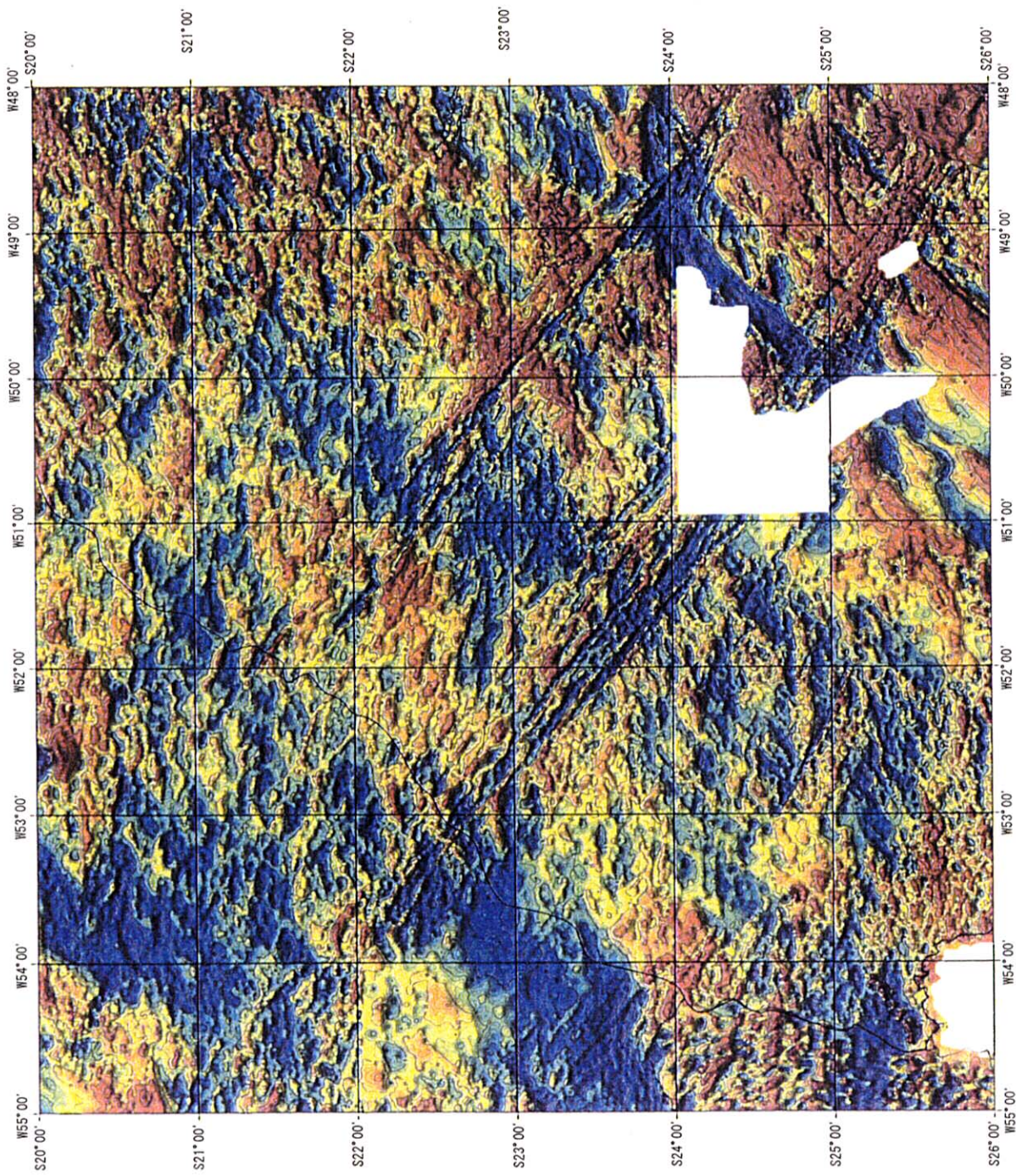
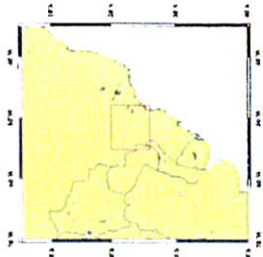


**Fig. II-1-5-7 Total magnetic intensity of aeromagnetic data in central Paraná basin**



Location Map



Technical Specifications

This map shows the 2nd vertical derivative of the total magnetic intensity (VTD) for aeromagnetic data collected in the area shown. The data were collected in 1997 and 1998. The map was prepared using the software package GEOTECH (Geophysical Exploration Technology) and the data were processed using the 2nd Vertical Derivative (VTD) filter. The map was prepared using the software package GEOTECH (Geophysical Exploration Technology) and the data were processed using the 2nd Vertical Derivative (VTD) filter.



GEOTECH (Geophysical Exploration Technology)  
Southern Brazil Aeromagnetic Data

2nd Vertical Derivative of Total Magnetic Intensity

Contour Interval: 0.005 nT/km  
Shading from north  
Scale: 1:1,000,000 Map 7 of 8 Date: August 2002

© 2002 Geophysical Exploration Technology Ltd.  
Geophysical Exploration Technology Ltd.  
1000 Lakeshore Blvd. West  
Richmond Hill, Ontario L4B 1N1, Canada  
Tel: (905) 882-2222 Fax: (905) 882-2223  
E-mail: info@getech.com

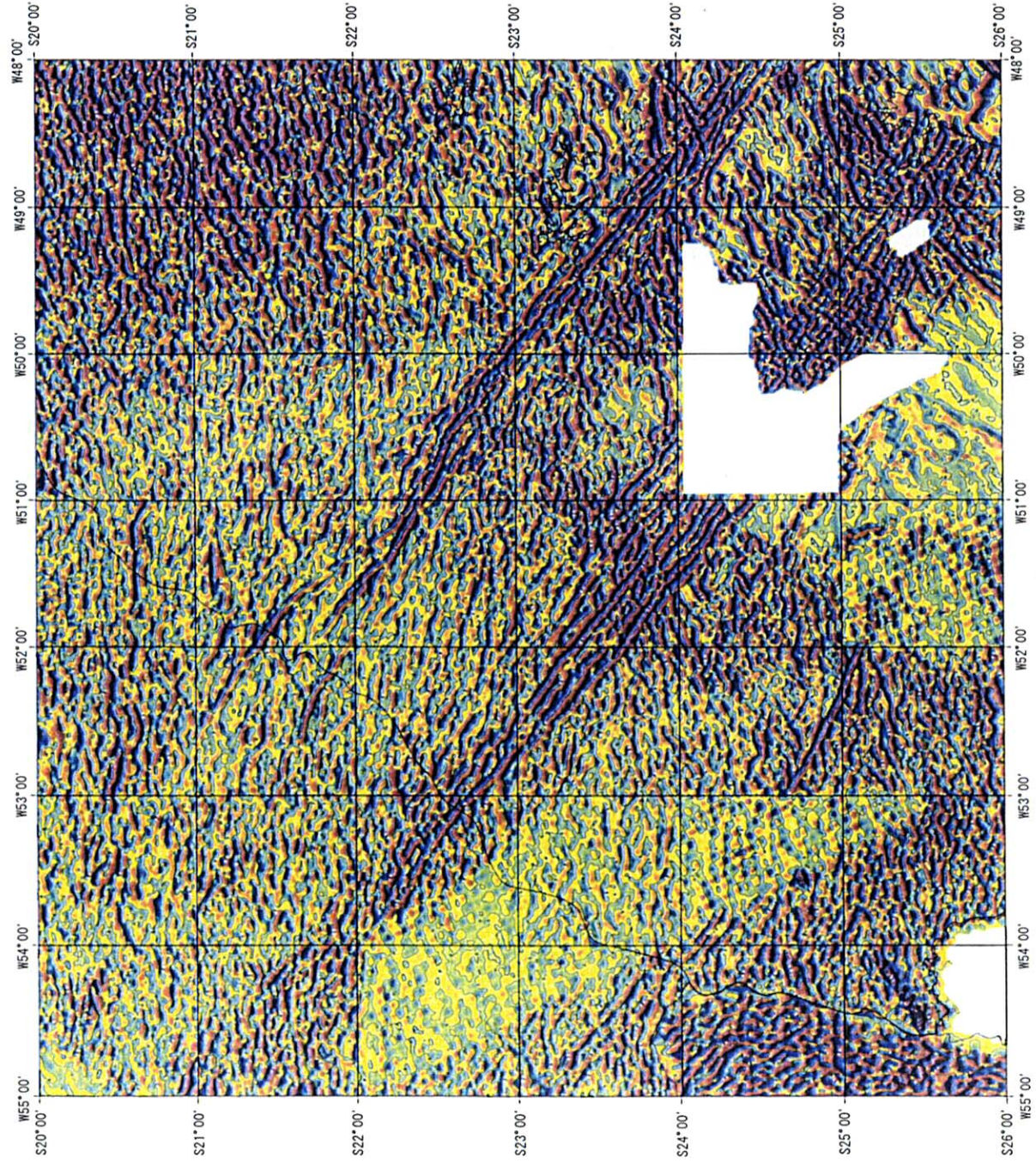
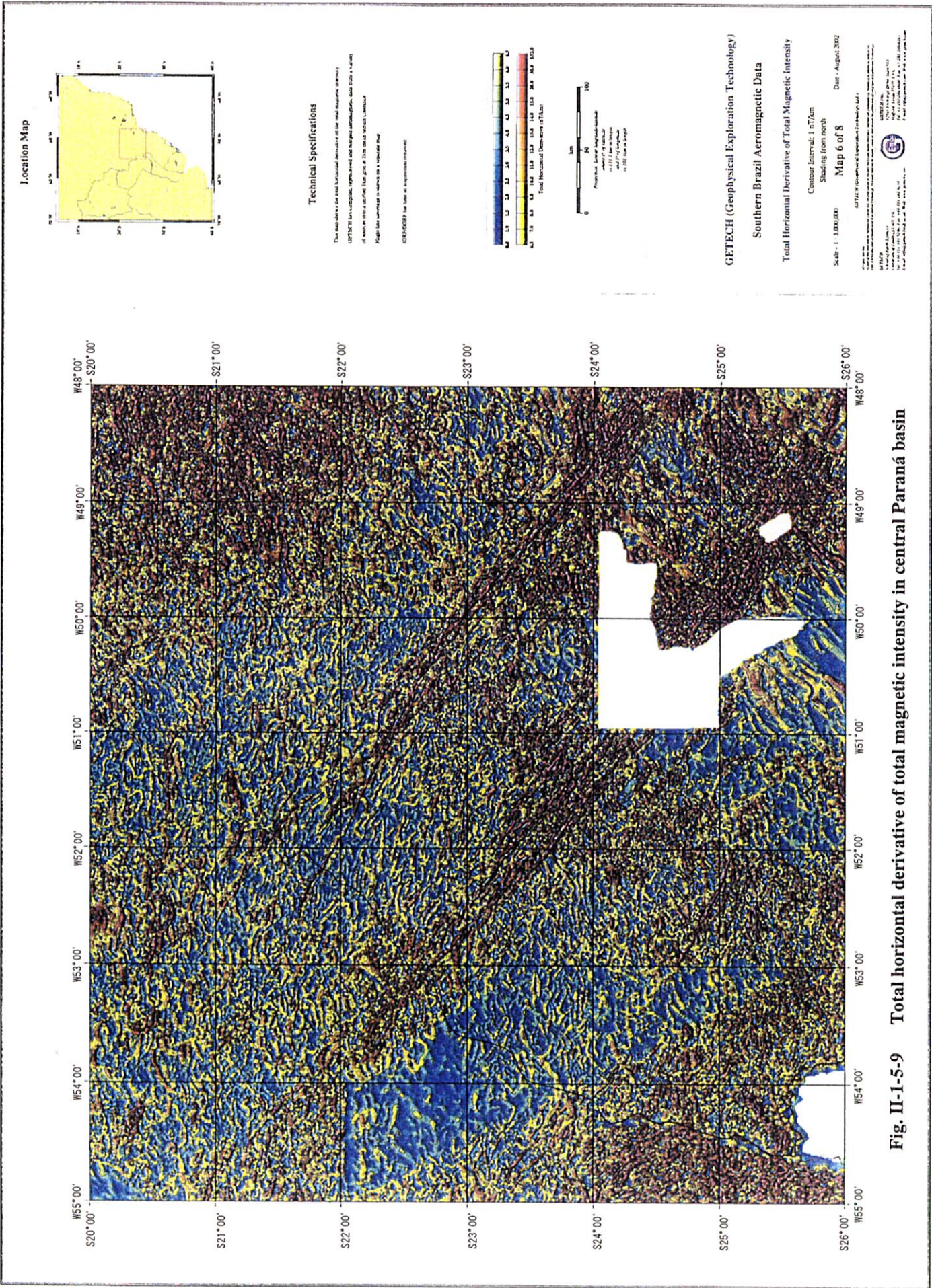


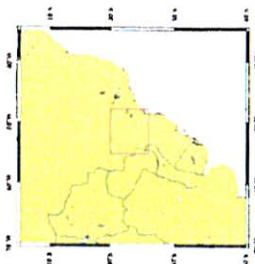
Fig. II-1-5-8 2nd vertical derivative of total magnetic intensity in central Paraná basin







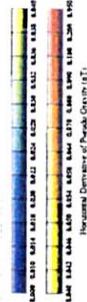
Location Map



Technical Specifications

This map shows the total horizontal derivative of pseudo-gravity. Pseudo-gravity is calculated by adding the vertical integration of the observed to the predicted magnetic intensity, including a relationship factor between magnetic intensity and magnetic susceptibility, a relationship factor between magnetic intensity and density contrast.

Magnetic Anomaly: 22-472-00, scale: 1:50



GETECH (Geophysical Exploration Technology)

Southern Brazil Aeromagnetic Data

Total Horizontal Derivative of Pseudo Gravity

Contour Interval: 100 nT  
Shading from north

Scale: 1:300,000 Map 4 of 8 Date: August 2002

GETECH (Geophysical Exploration Technology) Ltd.  
1111 17th Street, Suite 100  
Calgary, Alberta T2M 4K6, Canada  
Phone: (403) 243-1111  
Fax: (403) 243-1112  
E-mail: info@getech.com  
www.getech.com

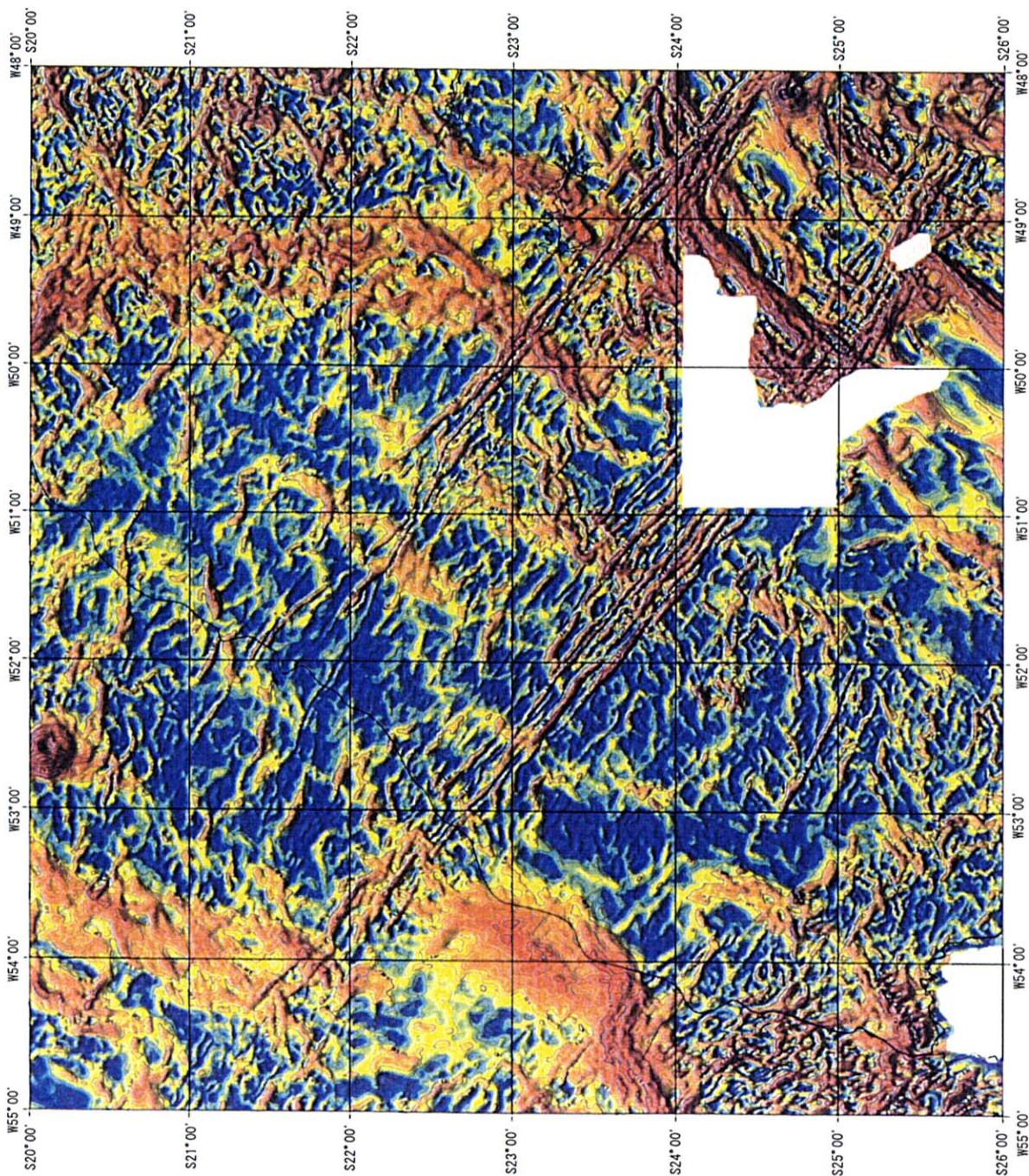
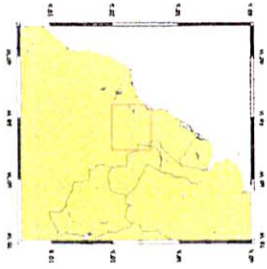


Fig. II-1-5-10 Total horizontal derivative of pseudo-gravity in central Paraná basin

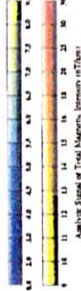


Location Map



Technical Specifications

This map shows the results of the aeromagnetic survey (AMT) for the study area. The aeromagnetic data were collected using a magnetometer mounted on a low-altitude aircraft. The data were processed and converted into a digital format. The map shows the aeromagnetic intensity in nT/km. The map is a contour map with a contour interval of 1 nT/km. The map is shaded from north to south. The map is a contour map with a contour interval of 1 nT/km. The map is shaded from north to south.



GETECH (Geophysical Exploration Technology)

Southern Brazil Aeromagnetic Data

Analytic Signal of Total Magnetic Intensity

Contour Interval: 1 nT/km  
Shading from north  
Scale: 1:3,000,000  
Map 5 of 8  
Date: August 2002

© 2002 by Geophysical Exploration Technology, Ltd.  
All rights reserved. This map is a technical drawing and is not to be used for any other purpose without the written consent of Geophysical Exploration Technology, Ltd.  
Geophysical Exploration Technology, Ltd.  
10000 Highway 100, Suite 100  
Calgary, Alberta T2C 1A8, Canada  
Tel: (403) 243-2222  
Fax: (403) 243-2222  
E-mail: info@getech.com

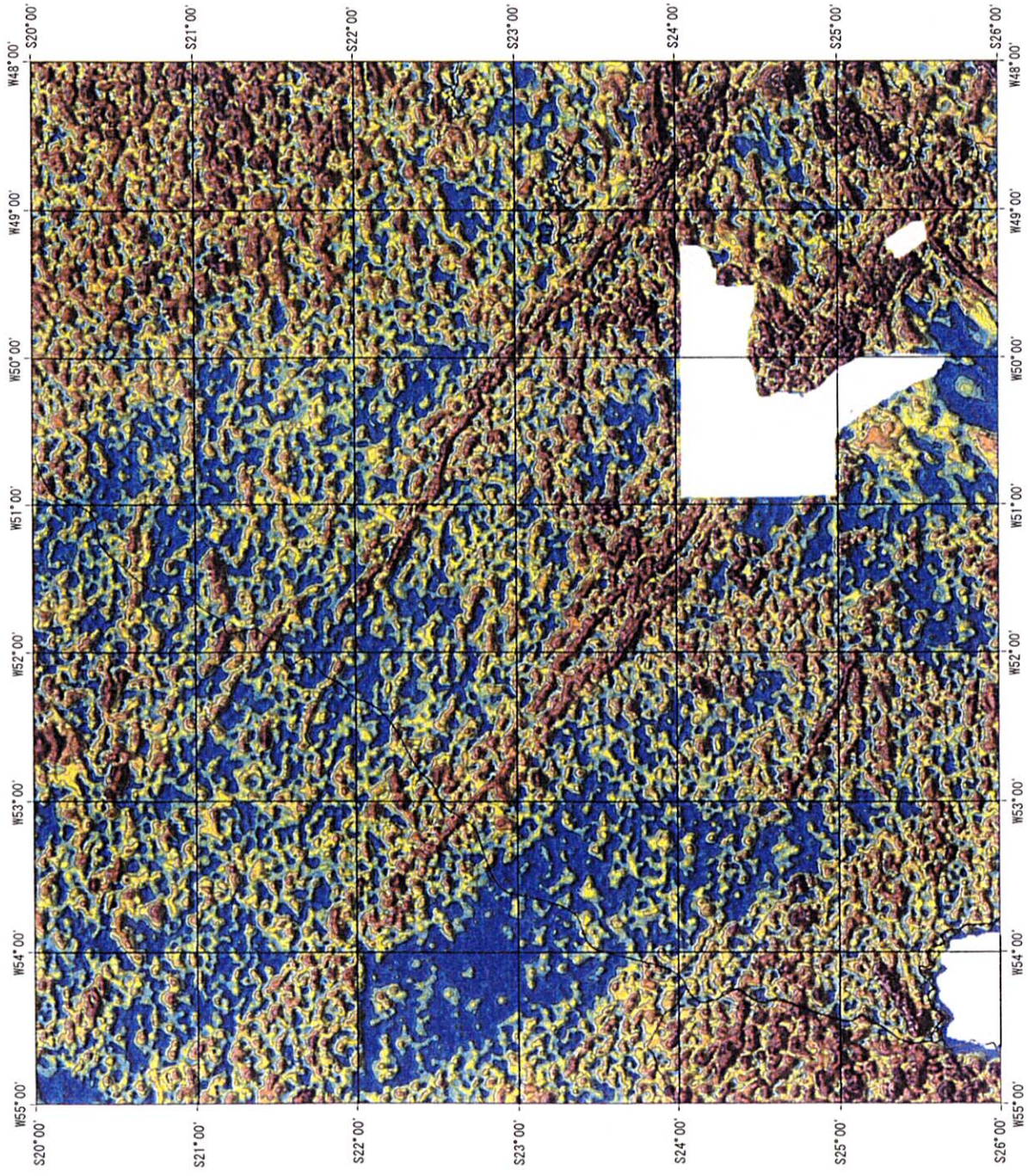
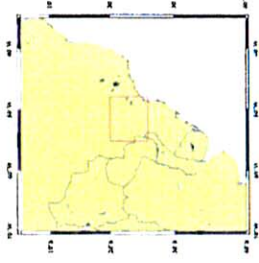


Fig. II-1-5-11 Analytic signal of total magnetic intensity in central Paraná basin



Location Map



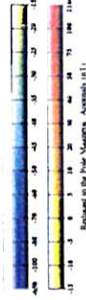
Technical Specifications

This map shows the magnetic field measured by the pole magnetic (Pole) system. The magnetic field is represented by the color scale. The color scale is based on the magnetic field intensity. The color scale is based on the magnetic field intensity. The color scale is based on the magnetic field intensity.

Scale: 1:100,000

Map 2 of 8

Date: August 2002



GETECH (Geophysical Exploration Technology)  
 Southern Brazil Aeromagnetic Data  
 Reduced to the Pole Magnetic Anomaly

Contour Interval: 5 nT  
 Shading from north

Scale: 1:100,000 Map 2 of 8 Date: August 2002

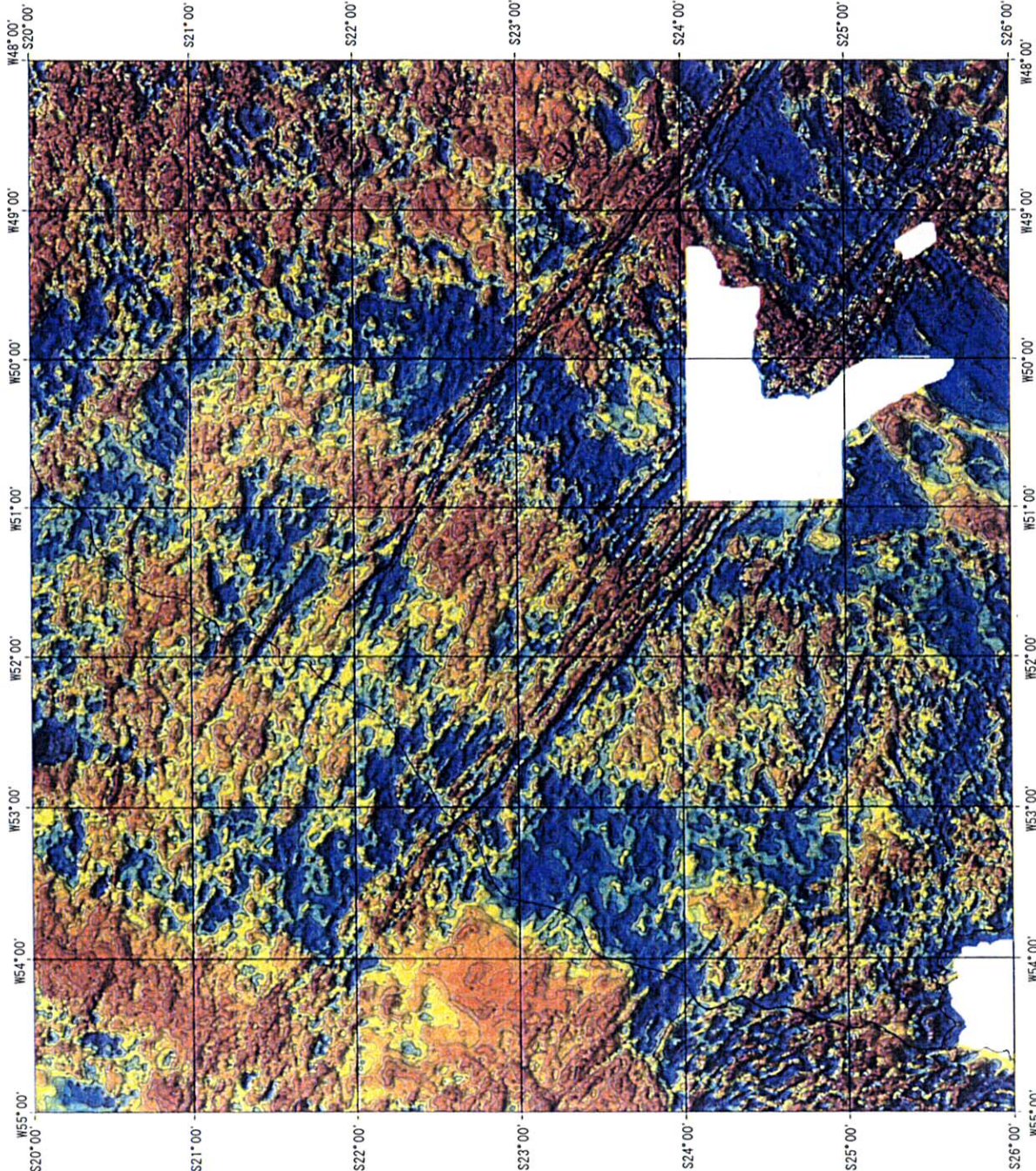
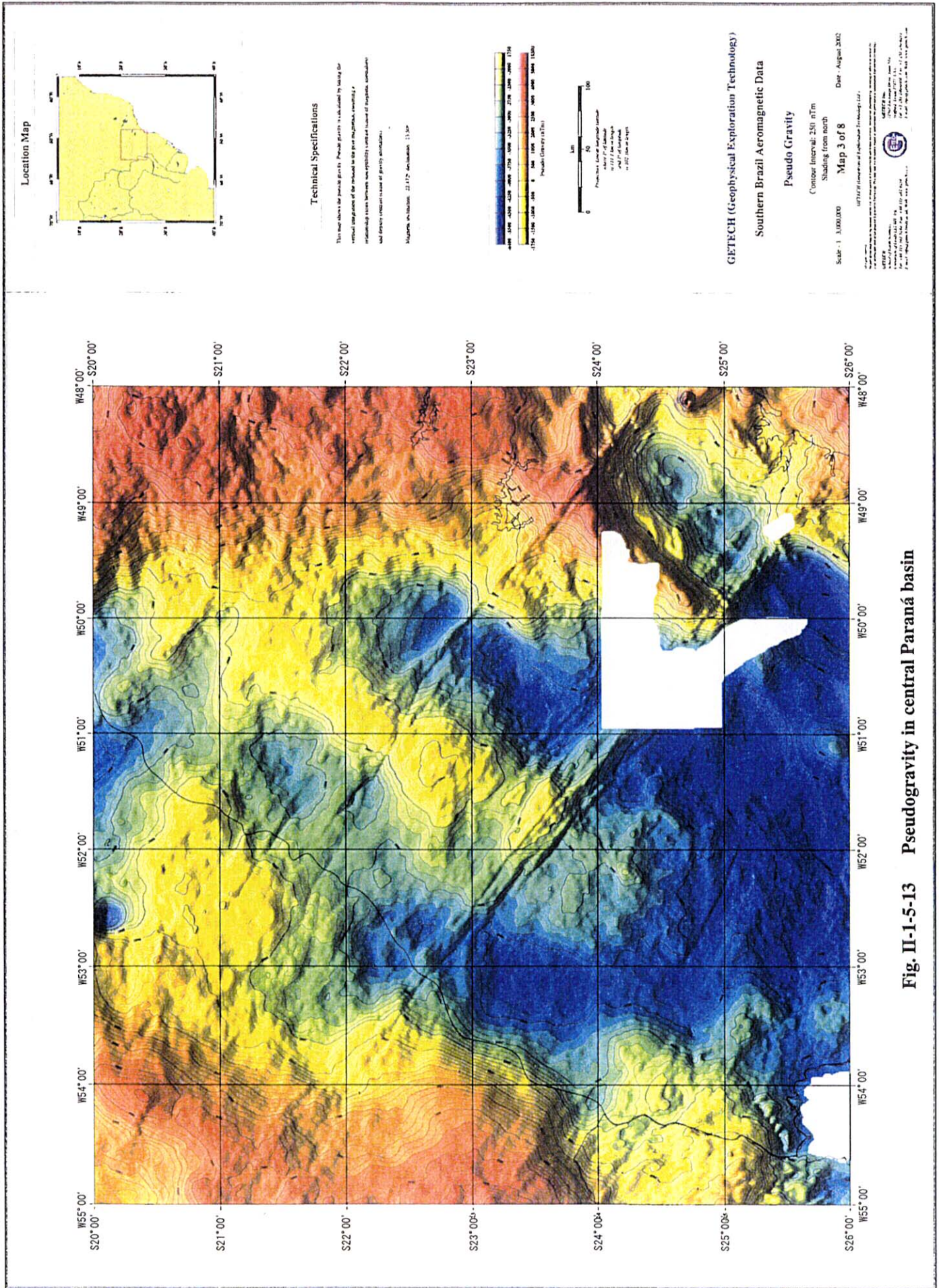


Fig. II-1-5-12 Reduced to the pole magnetic anomaly in central Paraná basin





**Fig. II-1-5-13 Pseudogravity in central Paraná basin**



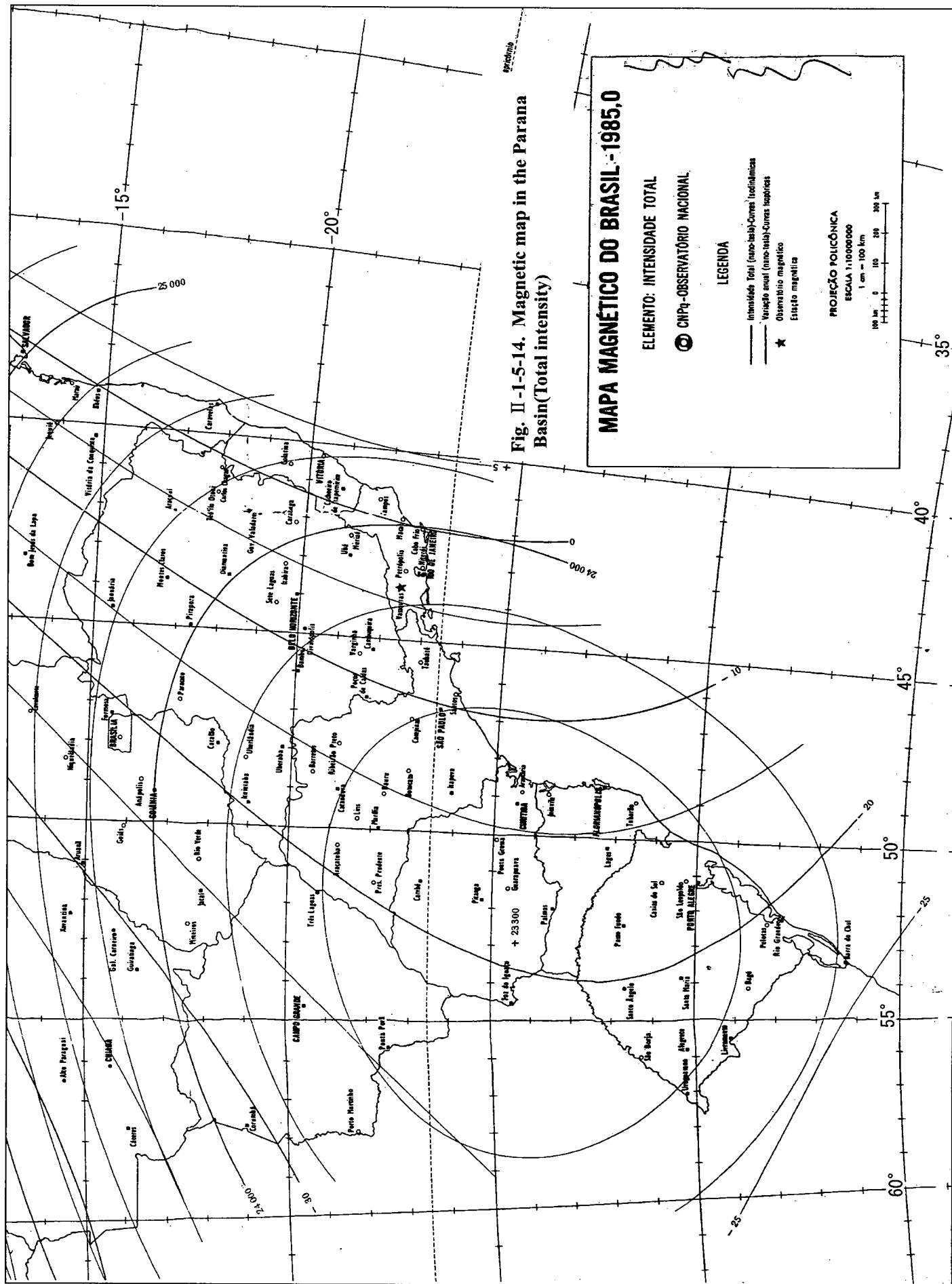


Fig. II-1-5-14. Magnetic map in the Parana Basin (Total intensity)

**MAPA MAGNÉTICO DO BRASIL - 1985,0**

ELEMENTO: INTENSIDADE TOTAL

● CNPq-OBSERVATÓRIO NACIONAL

LEGENDA

- Intensidade Total (nano-tesla)-Curvas Isointensiticas
- Variação anual (nano-tesla)-Curvas Isovariaticas
- ★ Observatório magnético
- Isoclinas magnéticas

PROJEÇÃO POLICÔNICA  
 ESCALA 1:100000000  
 1 cm = 100 km

100 km 0 100 200 300 km

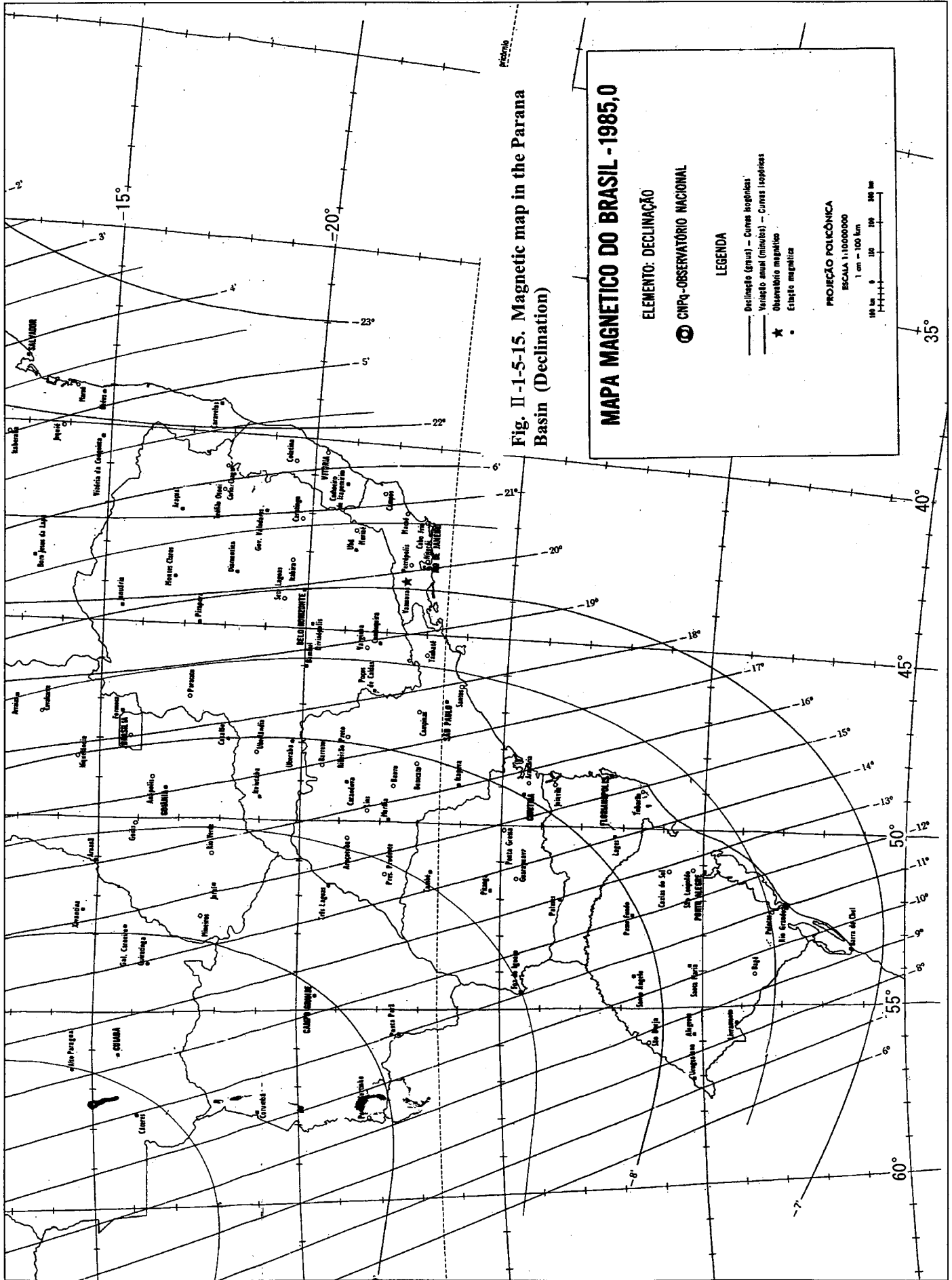


Fig. II-1-5-15. Magnetic map in the Parana Basin (Declination)

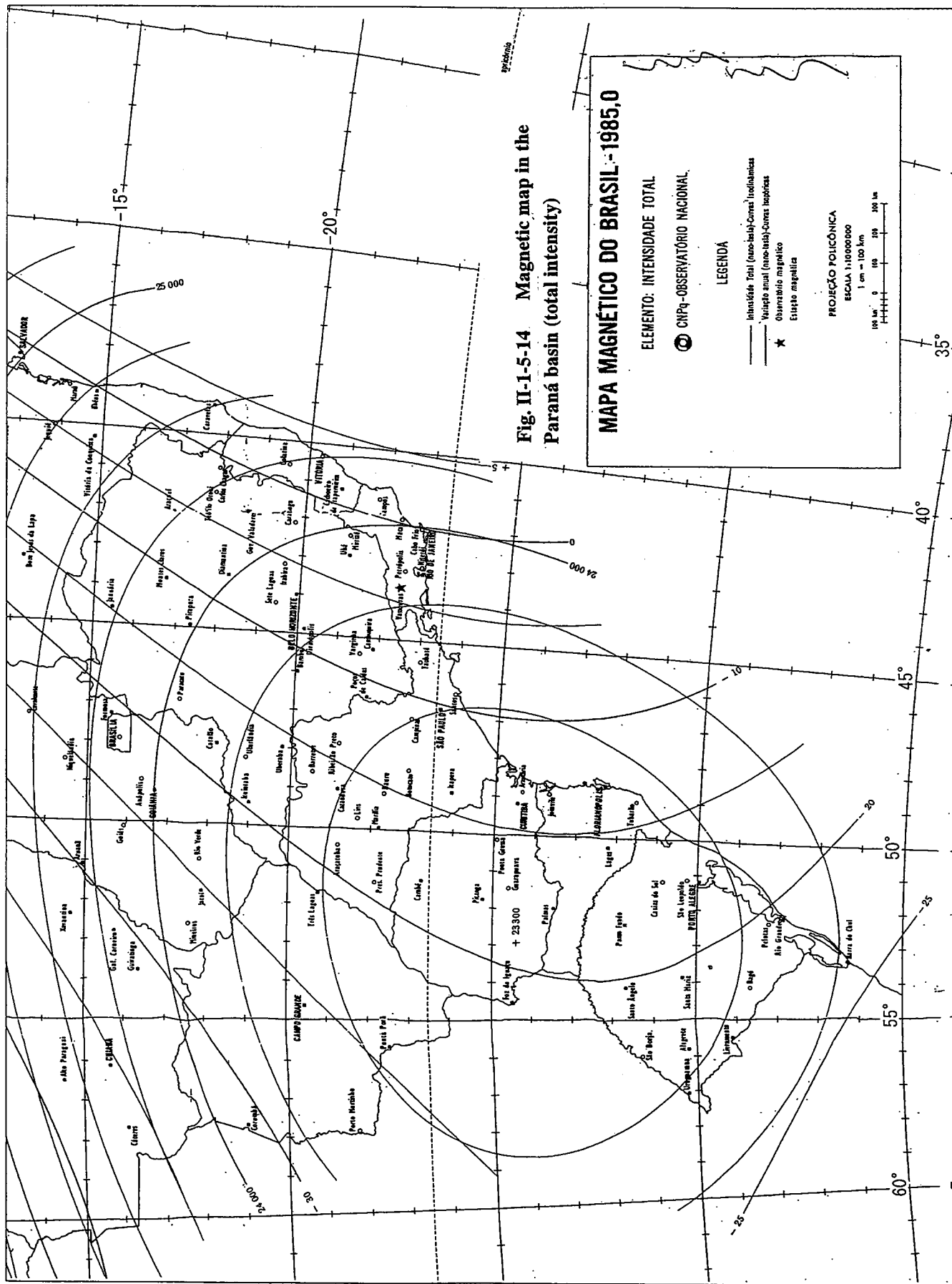


Fig. II-1-5-14 Magnetic map in the Paraná basin (total intensity)

**MAPA MAGNÉTICO DO BRASIL - 1985,0**

ELEMENTO: INTENSIDADE TOTAL

CNPq - OBSERVATÓRIO NACIONAL

LEGENDA

- Isointensidade Total (Auto-baily-Cornat) Irregularidades
- Isopleta anual (Auto-baily-Cornat) Irregularidades
- ★ Observatório magnético
- Estação magnética

PROJEÇÃO POLICÔNICA

ESCALA 1:1.000.000

1 cm = 100 km

100 km 0 100 200 300 km

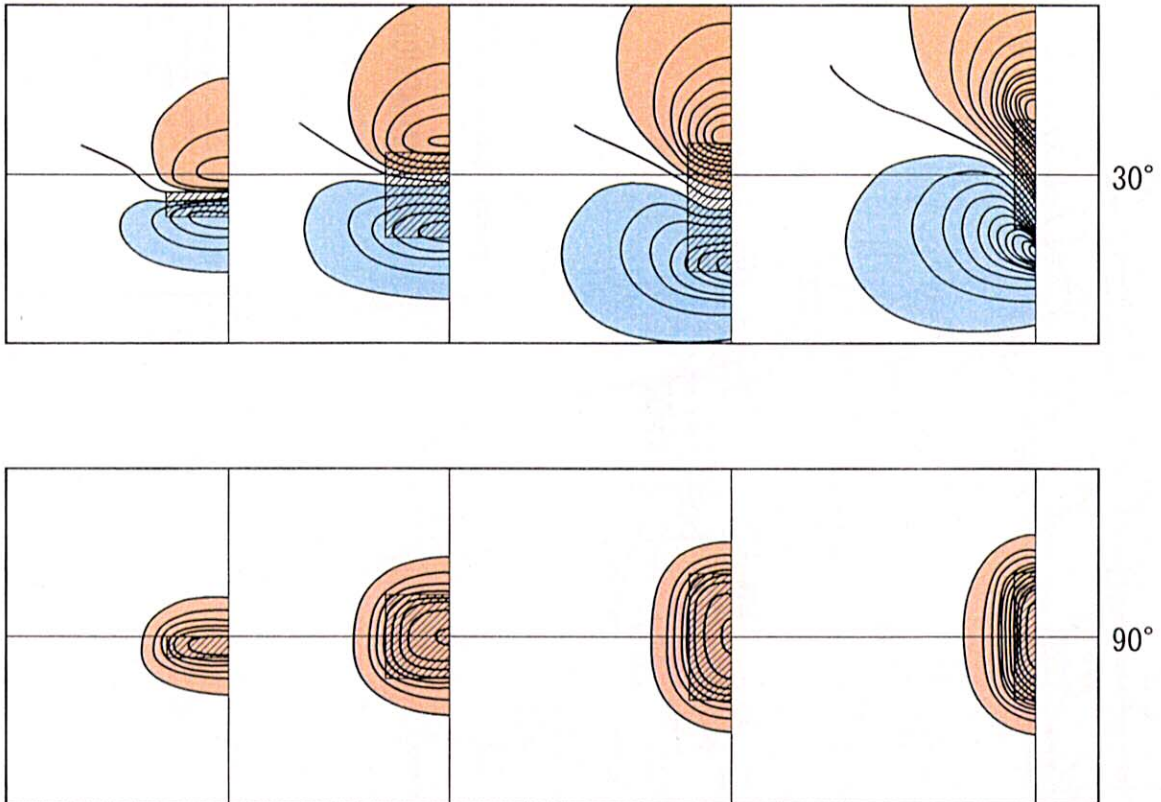


**Fig. II -1-5-17. Magnetic anomalies occurred by uniformly magnetized bodies in the southern hemisphere (Geodesy and Geophysics , 1969).**

Oblique line : magnetized body , Red : positive anomaly , Blue : negative anomaly.

$\vec{r}_0$  = Distance between the coordinate origin and rock body

$\vec{r}$  = Distance between the coordinate origin and aerial point p

Provided that  $\rho$  and  $\vec{J}$  are constant inside the rock body, the relation formula stated below is established between  $U(\vec{r})$  and  $V(\vec{r})$  (Poisson's formula). Poisson's formula combines gravitational field  $g$  and magnetic field  $f$ . The formula leads to calculating pseudogravity from magnetic anomaly.

$$V(\vec{r}) = \frac{1}{G\rho} \text{grad}U(\vec{r}) \cdot \vec{J}$$

## (2) Geomagnetic field of the central Parana Basin

When we analyze magnetic anomaly maps, we have to know the declination and the inclination of geomagnetic field in the area. They were excerpted from MAPA MAGNETICO DO BRASIL (1985) (Fig.II-1-5-14, Fig.II-1-5-15, Fig.II-1-5-16). The total intensity around Pitanga city in the central Parana Basin is the lowest (approx./ 24,000 nT). The inclination around Pitanga city is 26°S and the declination 14°W. As the references, Fig.II-1-5-17 shows the magnetic anomalies in the southern hemisphere (30° S and 90° ). The average inclination and declination of geomagnetic field in the central Parana Basin are 26°S and 14°W of respectively.

### 1-5-3 Measuring the Magnetism of Rocks

#### (1) Magnetic susceptibility

We used a Kappameter KT-6, made by GEOFYZIKA Corporation, to measure magnetic susceptibilities of rocks on the ground surface for analyzing magnetic anomaly maps. For measurement specimens, we collected flood basaltic lava, dykes and sills, sedimentary rocks in the Paleozoic, and sedimentary rocks and igneous rocks in the Precambrian, in the eastern area of Parana Province and in the southeastern area of San Paulo Province. In total, 84 specimens were measured (Fig.II-1-5-18).

We classified rocks and checked the magnetic susceptibilities. The lava of the flood basalt had 25.8 of average susceptibility (unit:  $\times 10^{-3}$  SI), gabbro 29.8, and the average of these rocks 28.7, a fairly high Fig.. The sedimentary rocks in the Paleozoic had 0.18 of average susceptibility, a very low figure. The igneous rocks in the Precambrian had 7.0 of average susceptibility, a rather high figure. The sedimentary rocks in the Precambrian had 0.33 of average susceptibility, a low figure. They indicate that the lava and intrusive rock in the flood basalt and igneous rock in the Precambrian cause magnetic anomalies.

Major basement rocks before the Cambrian consist of greenstone, dolomite, limestone,



schist, granite to syenite, diorite, gneiss, and basic to ultrabasic rocks in the Cambrian to the Archean. Of these basement rocks, diorite, gneiss, and basic to ultra-basic rock had a high susceptibility while sedimentary rocks such as dolomite, limestone, and schist had a low susceptibility.

## (2) Natural Remanent Magnetization (NRM)

### a) Preparation of specimens and measurements

We measured the NRM of seven specimens of lava and 18 specimens of sills and dykes of flood basalt in this area. We used a clinometer to collect specimens in the oriented block sampling method that measures the strike and dip of the smooth surface. In principle, we cut out three column-shaped specimens with a 30mm diameter and a 30mm height for measurement.

We used the Ringcore Fluxgate Spinner Magnetometer to measure the NRM of the specimens. Before measurement, we had conducted 20mT alternating field demagnetization to eliminate the influences of secondary magnetization such as viscous magnetization.

In order to confirm dispersions of data, we used Fisher statistics (Fisher, 1953) to calculate the  $\alpha_{95}$  and k values. The  $\alpha_{95}$  value is an index which was devised to indicate dispersions of the data and indicates the vertical angle of a cone in which 95% of the data is included. Therefore, smaller  $\alpha_{95}$  values indicate that the measurement values are more concentrated. The k value is called an accuracy parameter. When this value is greater, the accuracy is also higher. TableII-1-5-1 lists the results of NRM measurements. Fig.II-1-5-19 indicates a part of stereo projection charts of NRM measurements. However, we did not include KN159 because the result seemed to indicate that a mistake had taken place at the stage of shaping the specimen.

### b) Magnetization intensity

The specimen KN160 ( $1.74 \times 10^{-1}$  kA/m) had a high magnetization intensity, but most of the specimens had magnetization intensities within the range of  $10^{-2}$  to  $10^{-3}$  kA/m. The average value except for KN160 was  $4.7 \times 10^{-3}$  kA/m.

### c) Konigsberger value

The magnetization intensity of magnetic rock body (J) that brings about magnetic anomaly is the sum of inductive magnetization strength of geomagnetic field ( $\kappa H$ ) and natural remnant magnetization strength (Jr). The ratio of inductive magnetization strength ( $\kappa H$ ) and natural remnant magnetization strength (Jr) is called the Konigsberger value (Q-ratio), which indicates  $Q > 1$  in general. The Q value of some volcanic rocks may indicate 2 to 10 while the Q value of

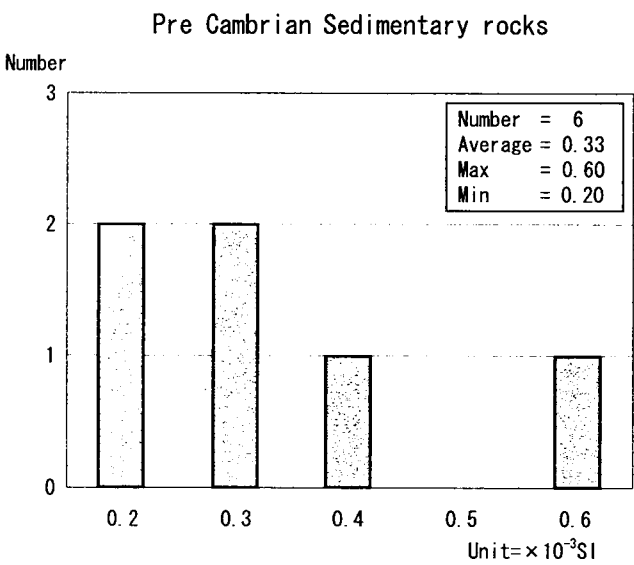
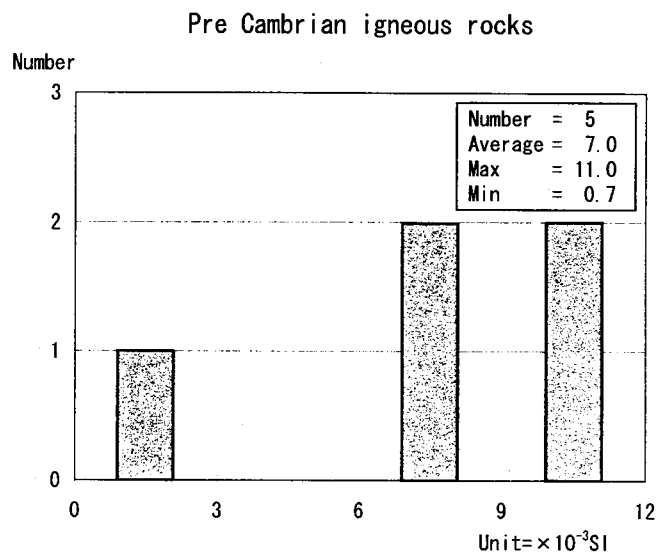
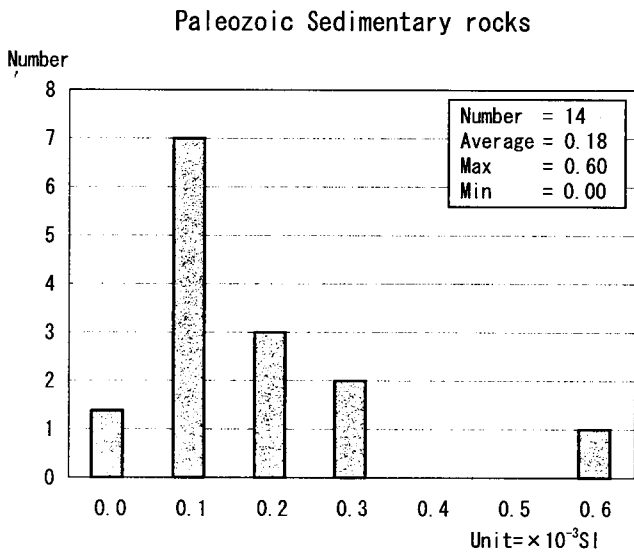
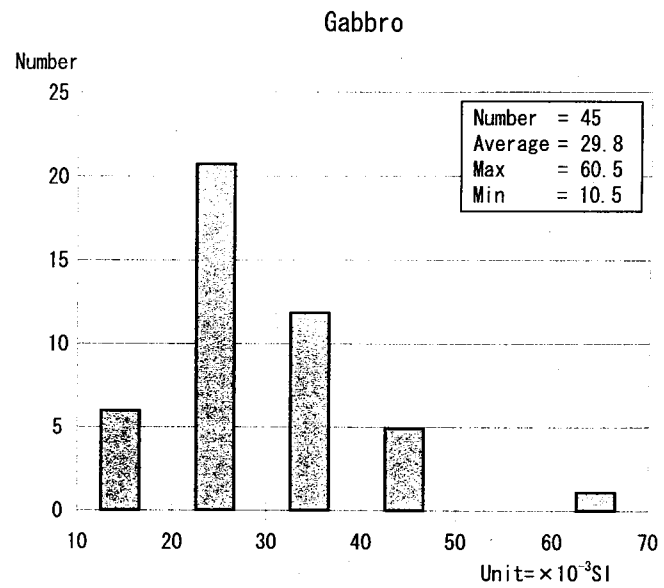
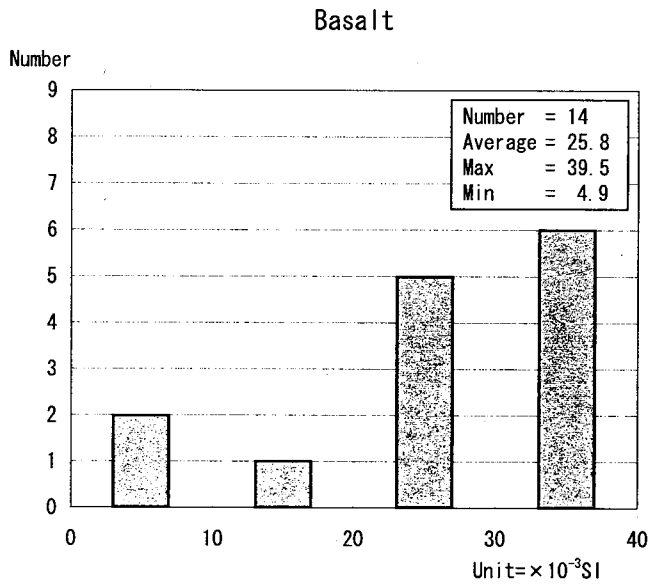
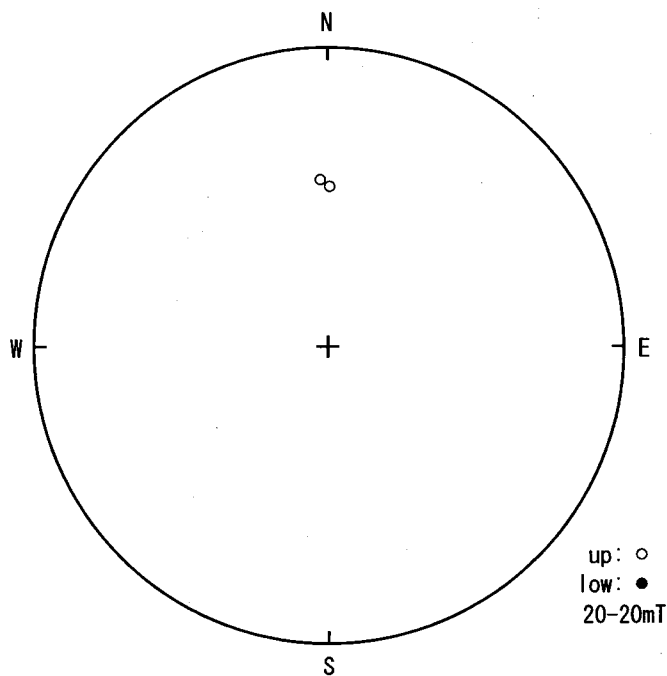


Fig. II-1-5-18 Susceptibilities classified by rock types

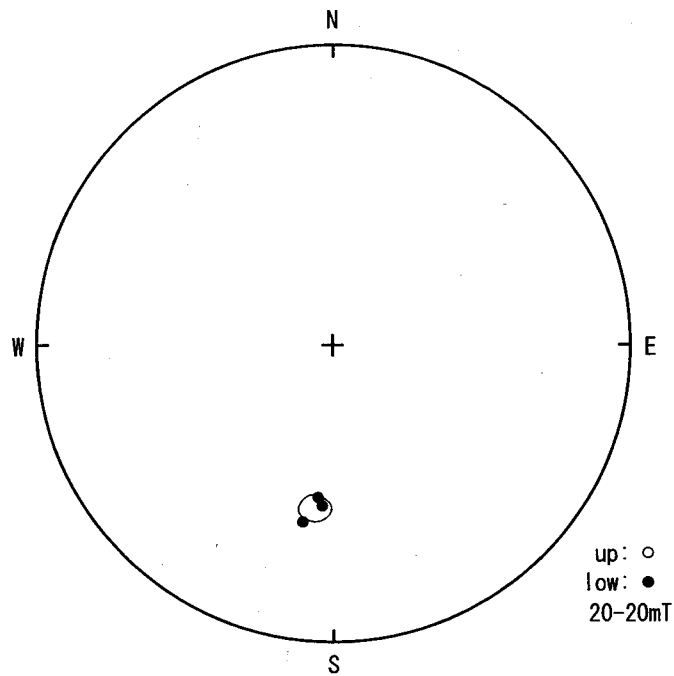
**Table II-1-5-1 Natural remanent magnetizations (NRM) and susceptibility of basalt lavas and gabbro sills in the central area of the Paraná basin**

Sample Name	Lava, Dyke or Sill	Basaltic Magma type	NRM before		NRM after demagnetization by alternating current (20mT)				$\alpha_{95}$
			Demag. AC ( $10^{-4}$ kA/m)	Intensity ( $10^{-4}$ kA/m)	Declination	Inclination	Magnetic Pole	k-value	
AS014	Sill	Undefined	94.4	5.48	10.29	1.48	Normal	32.0	14.30
KM106	Lava	P	38.4	33.1	134.56	-29.84	Reverse	6.0	33.08
KM117	Lava	PP	1.69	0.936	129.80	17.82	Reverse	7.6	29.24
KM126	Lava	PP·R	34.8	21.7	190.41	-37.85	Reverse	50.9	11.33
KM148	Lava	P	8.21	7.66	359.36	-44.57	Normal	1643.2	0.00
KM153	Lava	P	14.1	11.0	182.45	45.14	Reverse	327.9	4.46
KN035A	Sill	PP·R	20.6	19.9	158.46	47.28	Reverse	101.2	8.03
KN105A	Dyke	PP·R	30.6	15.7	5.46	-48.60	Normal	63.3	10.16
KN106	Dyke	PP·R	6.50	2.33	194.47	16.88	Reverse	38.3	13.07
KN110A	Sill	PP	74.6	57.0	191.44	45.38	Reverse	107.4	7.80
KN112	Dyke	PP·R	30.1	12.7	353.29	-39.36	Normal	119.2	7.40
KN117	Sill	PP	47.6	35.6	355.48	-22.51	Normal	142.5	6.77
KN119	Sill	PP	112	19.9	44.27	-44.13	Normal	34.4	13.78
KN121	Dyke	P	26.4	21.1	0.65	-41.70	Normal	106.8	7.82
KN126A	Dyke	PP·R	22.0	13.4	136.27	61.14	Reverse	266.0	4.96
KN146	Sill	P	16.9	8.78	176.29	-3.32	Reverse	148.1	6.64
KN148	Dyke	R	80.5	18.4	346.30	-46.85	Normal	314.9	4.55
KN150	Sill	P	24.1	15.8	357.83	-3.25	Normal	251.5	5.10
KN157	Lava	PP	16.6	13.7	158.40	43.88	Reverse	2.5	51.21
KN160	Dyke	P	2390	1740	350.14	-63.40	Normal	128.4	7.13
KN163	Dyke	P	13.0	0.768	158.07	42.72	Reverse	22.9	16.89
KN167A	Dyke	P	1360	430	180.17	21.10	Reverse	32.7	14.12
KN170	Sill	PP	632	307	315.55	12.83	Normal	127.1	7.17
KN174A	Sill	E	13.4	6.92	165.33	-24.85	Reverse	142.1	6.78

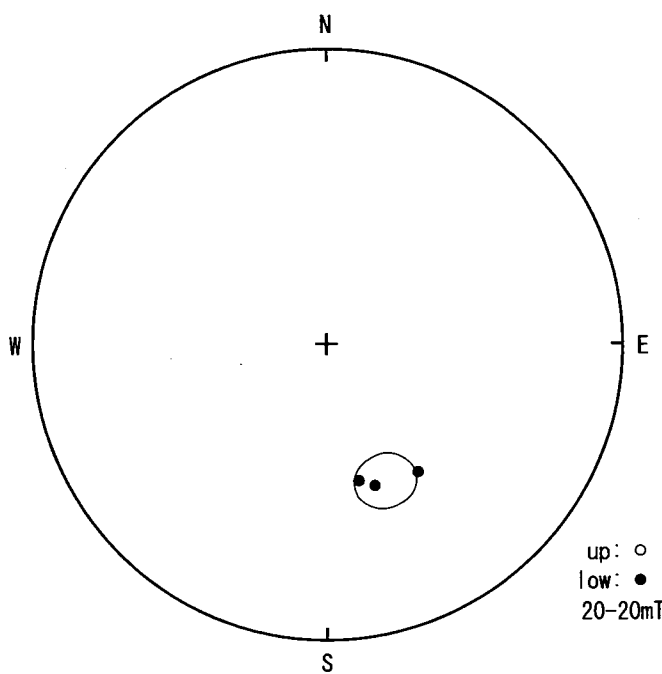
kA/m= $10^3$ A/m, Basaltic Magma types (P: Pitanga, PP: paranapameara, R: Riviera, PP·R: Paranapamera·Riviera, E: Esmeralda)



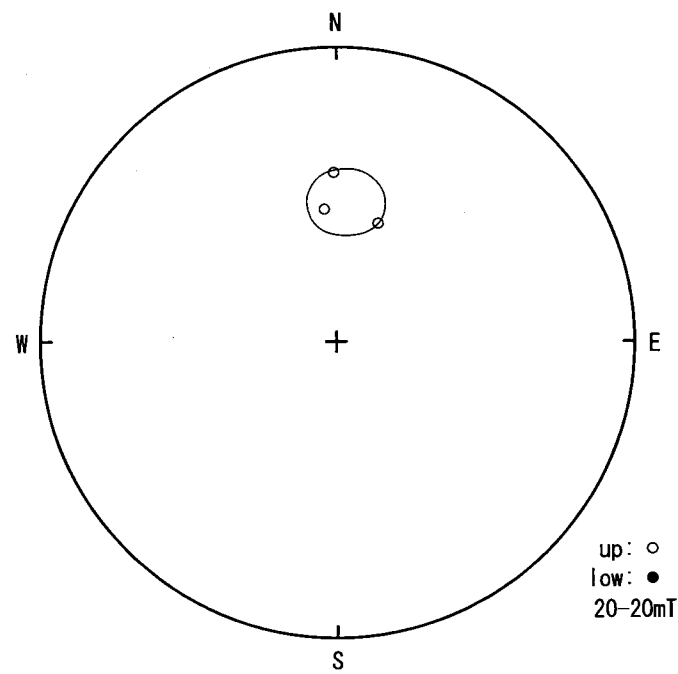
KM148(D=359.36 , I=44.57 , k=1643.2 ,  $\alpha_{95}$ =0.00)



KM153(D=182.45 , I=45.14 , k=327.9 ,  $\alpha_{95}$ =4.46)



KN035A(D=158.46 , I=47.28 , k=101.2 ,  $\alpha_{95}$ =8.03)



KN105A(D=5.46 , I=48.60 , k=63.3 ,  $\alpha_{95}$ =10.16)

**Fig. II -1-5-19. Examples of stereo-projection of NRM after 20mT demagnetization by alternating current.**

D : declination , I : inclination , K : susceptibility ,  $\alpha_{95}$  : confidence circle

basic to ultra -basic rock, such as basalt, may indicate higher than 100 (T. Nagata, 1961). The values of magnetization strength, namely  $J$ , and the  $Q$  value of magnetic rock body, are expressed in the formulas stated below. The  $Q$  value of flood basalt in the Parana Basin is 8.6 (the geomagnetic field strength  $H$ : 24,000nT). In other words, most of magnetic anomalies derive from NRM.

#### d) Magnetic pole

We could say that the reliability of our measurement values, except for KN157, KM106, and KM117, are high because the values indicate good statistic values. Of the 25 specimens, 11 specimens indicated normal polarity while 13 specimens indicated reverse polarity. When we checked directions of NRM by magma type, a half of the specimens indicated normal polarity while the remaining half of the specimens indicated reverse polarity. Based on these facts, we estimate that for a short period of Early Cretaceous when the flood basalt magma erupted, the geomagnetic poles is considered to have repeated normal and reverse.

M. ERNESTO and I.G. PACCA (1988) measured many NRMs of flood basalt. Their measurement values also indicate that the geomagnetic poles often reversed during activities of the flood basalt magma, as our result indicated. The reversal of geomagnetic pole tends to has intervals of several hundreds of thousands of years (Nikkei Science, 2003). The maximum reversal term is 50 million years.

#### 1-5-4 Analysis of Magnetic Anomaly Maps

G. G. Rompel (1994) eliminated the total magnetic intensity due to basalt lava near the ground surface and then simulate the depth and thickness of sills which are associated with the Noril'sk ore deposit by model calculation. However, it is very difficult to eliminate the total magnetic intensity due to basalt lava because the basalt lava has a thickness of more than 1,000m and the reversal of the geomagnetic field had often occurred in this area. Accordingly, this report only examines magnetic lineaments, which have been brought about mainly by basement structure and faults.

##### (1) Total magnetic intensity

High anomaly zone was observed in the NE-SW direction along the right-side bank on Parana River although the boundary was uncertain. A high residual gravity anomaly, high attenuation ratio, and thick basalt lava suite were present in the area. The area where basement rocks are dirtibuted near Curitiba also indicated a few strong high and low anomaly zone in the same direction. These anomaly zones in the NE-SW direction are inferred to related with the structure of basement rocks.



The northeastern side and southwestern side of the Ponta Grossa arch have two continuous sharp magnetic linearments in the NW-SE direction. The magnetic linearments on the northeastern side correspond to the Guapara Fault, while the magnetic lineaments on the southern side correspond to the Rio Alonzo Fault. Many dykes and sills intrude into areas along these faults and the surroundings. Besides them, a number of sharp magnetic lineaments are observed in the NW-SE direction although they are short.

**(2) Second vertical derivative, Total horizontal derivative of the total intensity, Total horizontal derivative of pseudogravity, and Analytical signal**

The Guapara Fault and the Rio Alonzo Fault, both of which are on the border of the Ponta Grossa arch, are indicated as sharp magnetic lineaments with high continuity in the NW-SE direction on all these maps. The basement structures in the NE-SW direction are found as a marked high anomaly on the total horizontal derivative of pseudogravity. Magnetic lineaments in the range of  $W51-52^{\circ}$  and  $S21-22^{\circ}$ , seem to be lateral secondary shear faults on the second vertical derivative of the total intensity and the total horizontal derivative of pseudogravity.

**(3) Reduced to the pole magnetic anomaly**

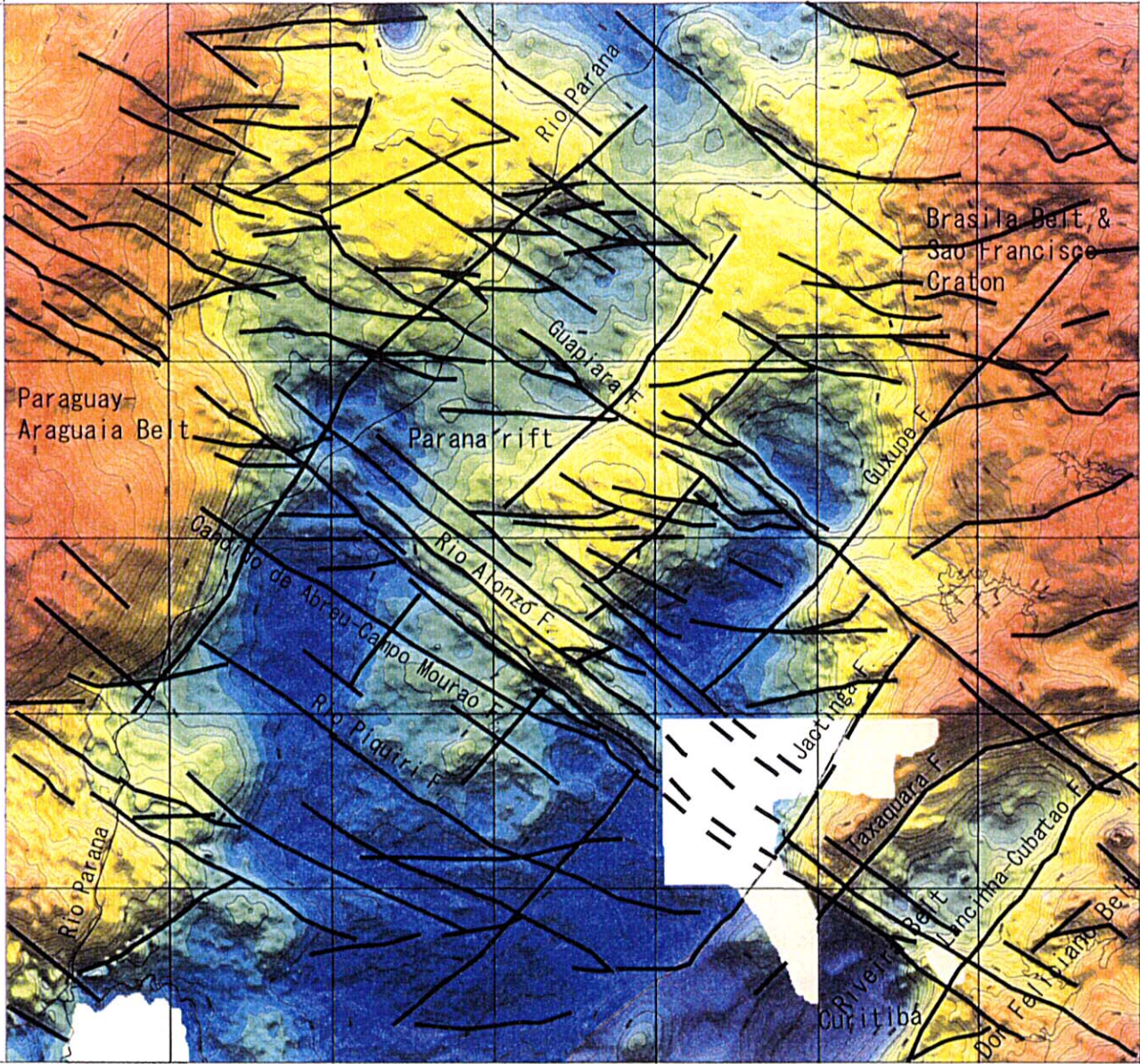
The reduced to the pole magnetic anomaly is direct above the magnetic body, as is shown in Fig.II-1-5-17. A high anomaly zone of total magnetic intensity along the right-side bank of Parana River in the NE-SW directions dislocated several tens of kilometers to the south. As the result, A zone of high residual gravity anomaly and high attenuation ratio along the right-side bank of Parana River indicated a low reduced to the pole magnetic anomaly. A marked magnetic lineaments in the NW-SE direction are also observed in areas to the south than those of total magnetic intensity. Large scale high anomaly zones the N-S directions are present in the eastern and western ends of the central Basin.

**(4) Pseudogravity anomaly map**

Pseudogravity anomaly map is what long wavelength anomalies are amplified, and what basement structures become more clear (Fig.II-1-5-13, Fig.II-1-5-20). Large high anomaly zones are observed in the N-S direction in the eastern and western parts of central Basin. Meanwhile, a low anomaly zone is observed in the central part of central Basin. The former are considered to be located in relatively shallow areas of basement rocks in the Parana Basin and the latter in an area that basement rocks collapsed due to the flood basalt magmatism. The high anomaly zone in the western part is estimated to be due to the latent Paraguay-Araguay belt. The Paraguay-Araguay belt was formed in the Early Proterozoic to the Cambrian at the southeastern end of the Amazon craton (Fig.II-1-4-30). The high

W55° 00'  
S20° 00'

W48° 00'  
S20° 00'



S26° 00'  
W55° 00'

S26° 00'  
W48° 00'

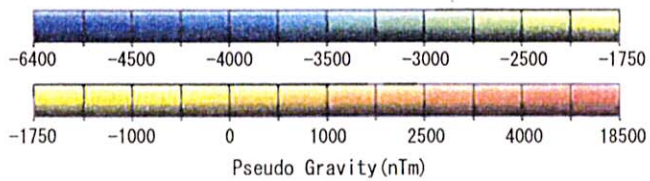


**Fig. II-1-5-20 Analyzed map of pseudogravity**

Thick solid line : lineament (fault) , Projection : linear longitudel latitude , Contour interval : 250 ntm shading from north , Magnetic inclination :  $22.472^\circ$  , declination :  $13.50^\circ$

anomaly zone in the eastern part has is estimated to be due to the Brasilia belt and the Sao Francisco craton in the N-S direction.

In the southern side of the high anomaly zone in the N-S direction in the eastern part, high anomaly zone and low anomaly zone in the NE-SW direction are also due to granites and metamorphic rocks of the Ribiera belt and Curitiba massif.

Two low anomaly zones and one small high anomaly zone are observed in NE-SW direction are in the central part of the central Basin. The low anomaly zone along the right side bank of the Parana River coincides with the high residual gravity anomaly, high attenuation ratio, and thick basalt lava suite. The small high anomaly zone is estimated to be a relatively shallow zone of basement rocks. The low anomaly zone in the NE-SW direction along Parana River could be a rift zone formed under the extensional stress field in the NW-SE direction.

The pseudogravity map also allows to have clear traces of magnetic lineaments. The magnetic lineaments are located mainly in the NW-SE direction, NE-SW direction and E-W direction. These lineaments coincide with faults of Fig.II-1-5-3. The magnetic lineaments in the NW-SE direction are estimated to be continuous faults with a sharp boundary. The basement block in southwestern side of the Rio Alfonzo fault has a large subsidence like a normal fault. However, no major collapses are observed in other faults in the NW-SE direction. The faults in the E-W direction are poor in continuity, and most of the faults look like secondary shearing faults of the faults in the NW-SE direction. Faults in the NW-SE direction and E-W direction considered to be a series of faults which were formed by left-lateral movements with sinistral rotation.

#### 1-5-5 TM Image Analysis

We analyzed TM false color images of the central Parana Basin (RGB=234; Fig.II-1-5-21). We delineated geological boundaries into flood basalt lava, Paleozoic formation, and basement rocks in the Precambrian, based on their erosion resistance of geological layers, vegetation, and geography while referring to Mapa Geologico do Brasil (1:2,500,000, Fig.II-1-5-1).

Faults in basement rocks such as Jactinga fault and Taxaquara fault in the NE-SW direction, and faults in the E-W directions were recognized. As is shown in the images, the Parana River also is located in the NE-SW direction.

Around the Ponta Grossa arch and Xavantes Lake, gabbroic dyke swarm was formed in the NW-SE direction. They appear as long and narrow hills on the ground surface (Fig.II-1-5-1, Photo 9), which is taken as an image of an elevated lengthy cordlike geography. Most of dykes are highly continuous in the Paleozoic formation and basalt lava, but they become hollow linear geography in Precambrian basement rocks. Outcrops and boulder of dykes in the



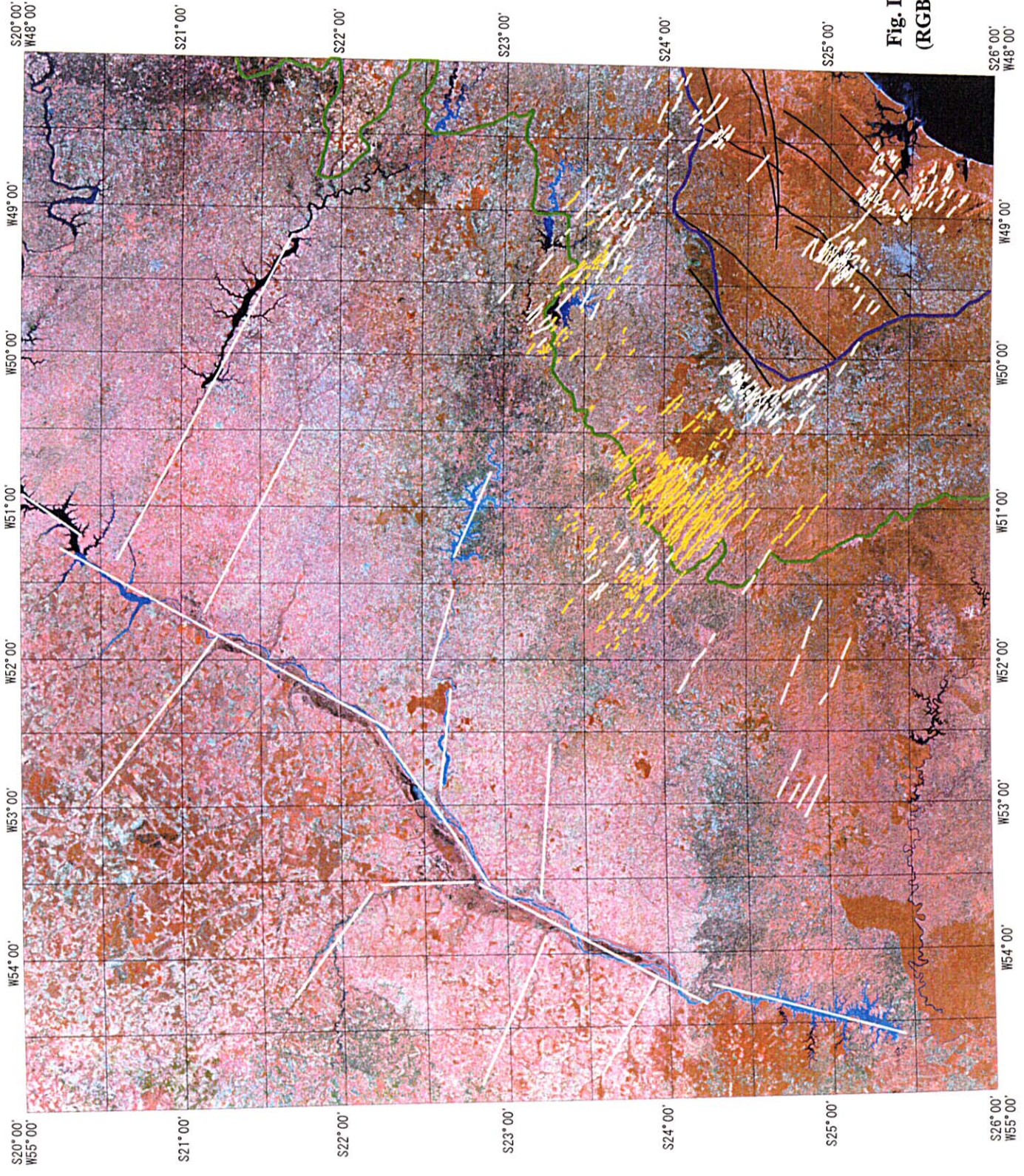


Fig. II-1-5-21 TM image (RGB=234) of the central Paraná basin



basement rocks are very few. Parana River has a number of branches in the NW-SE direction. These branches may represent parts of faults in the NW-SE direction.

## 1-6 Tectonics of Ni- Cu-PGE Ore Deposit associated with Flood Basalt

In the Ni- Cu- PGE ore deposit associated with flood basalt, Noril'sk ore deposit in Russia (555Mt, Ni 2.7%, Cu 2.06%) and Jinchuan ore deposit in China (515Mt, Ni 1.06%, Cu 0.67%) have the world second and third ore reserves of nickel. At present, the both ore deposits are in operation. Besides the above two ore deposits, there are Duluth ore deposit in Minnesota, USA (4,000Mt, Ni 0.2%, Cu 0.66%), Great Lake ore deposit in Canada (45.6Mt, Ni 1.2%, Cu 0.34%) and Disko Bugt ore deposit in Greenland as the same origin ore deposits. The development of these three ore deposits have not carried out yet. In this chapter, based on some papers, it is discussed how the Duluth ore deposit and the Noril'sk ore deposits are concerned to the tectonics. Furthermore, the tectonics of flood basalt magmatism in the South American Continent and the rupture of the Gondwana Continent is discussed. Finally, the possibility of the Cu- Ni- PGE ore deposit in the Parana Basin is discussed mainly from the viewpoint of Parana flood basalt magmatism and the tectonics.

### 1-6-1 Tectonics of Duluth Ore Deposit

The Duluth ore deposit is located in the Midcontinent Rift (MCR) of North America which has the extension of 2,300 kilometers from the central Kansas Province through the Lake Superior to the north, and runs through the south of Michigan Province to Ohio Province. The MCR that was formed in the middle Proterozoic (1,200 to 1,100 Ma) is the world biggest class continental rift. Rocks of the MCR are exposed only around the Lake Superior. In other part, they are overlain by the Paleozoic. The whole feature of the MCR can be only identified by the high gravity anomalies (Fig.II-1-6-1, Fig.II-1-6-2).

Weiblen and Morey (1980) discussed two possible models which are named triple junction model (Brooks, 1973) and transform fault model about a relation between the tectonics of MCR and the ore deposit, and concluded as the following.

The troctolitic to gabbroic intrusions of Duluth Complex were formed in the magma reservoir of semi-graben situation. The faults with the NE—SW and NW—SE direction occurred in the Duluth Complex and its surrounding. The former is the stair-step rift in the basement part of the magma reservoir and the latter transform faults across the magma reservoir. The basement of the semi-graben magma reservoir is considered to be the most potential zone of mineralization of copper, nickel and PGE (Fig.II-1-6-3).



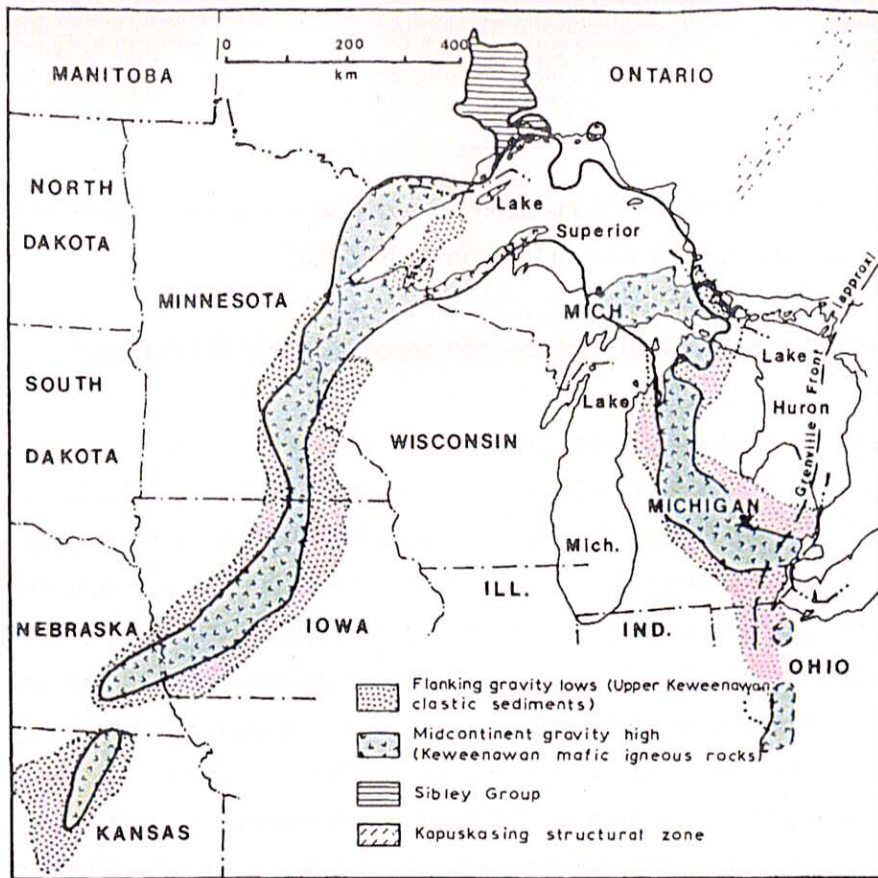


Fig. II-1-6-1 Generalized map of the Midcontinent rift of North America, after P.W. Weiblen (1980)

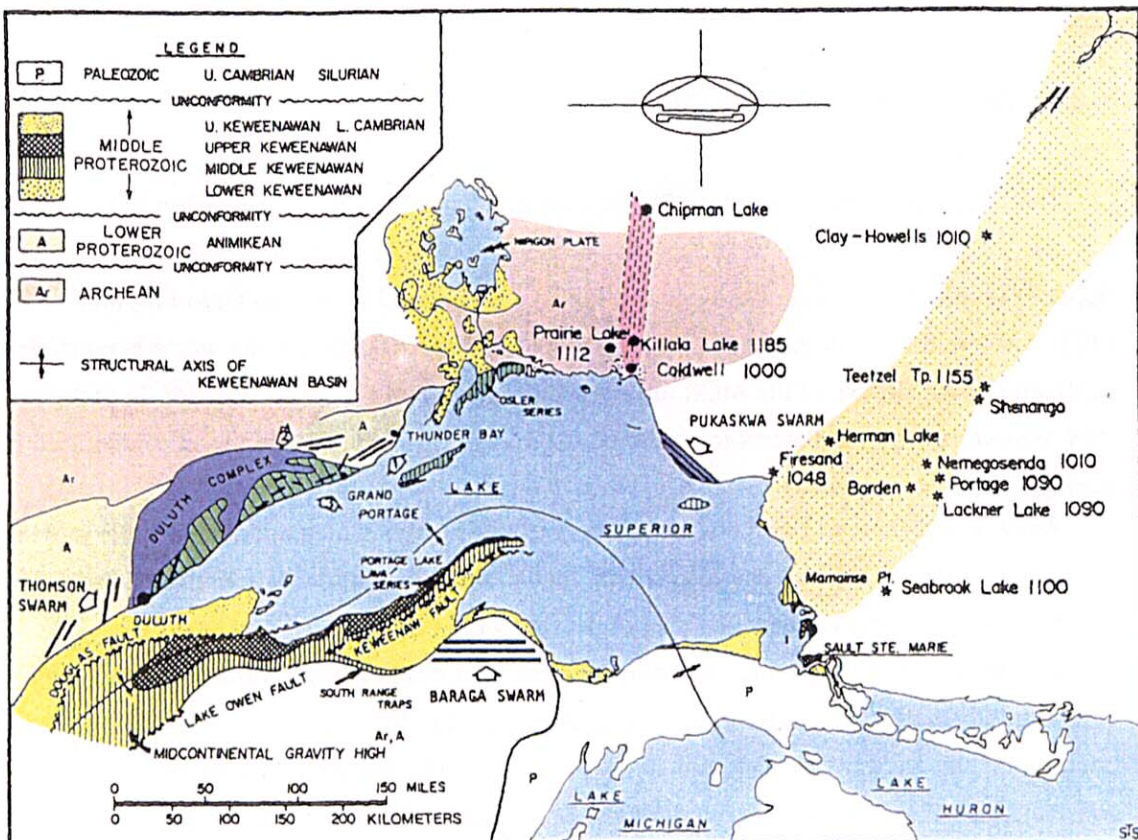
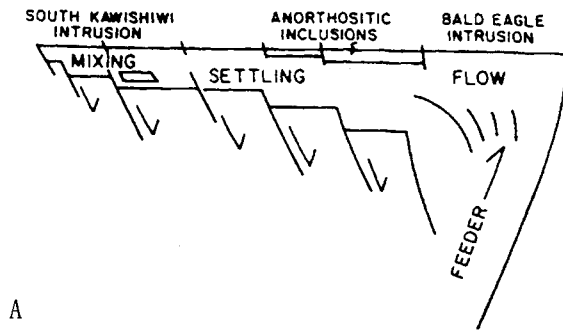
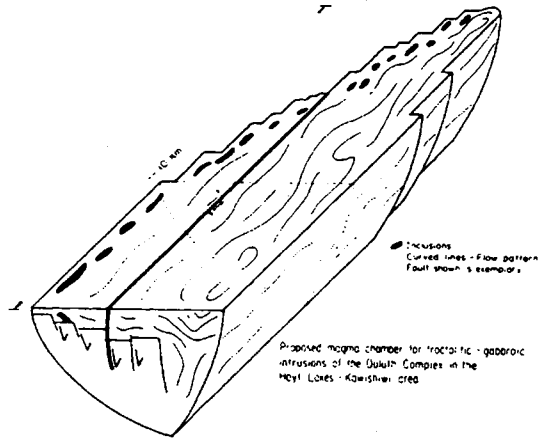


Fig. II-1-6-2 Generalized map of the Lake Superior region

Asterisks, nepheline-carbonatite complexes (K-Ar ages in m. y.) in the Kapuskasing Structural Zone (Gittens and others, 1967; Currie, 1976). Solid dots, alkaline intrusions in the Coldwell Alkaline Province (Currie, 1976). Diagonal lines, North Shore Volcanic Group. The "Nipigon Plate" refers to the patterned areas north of the Osler Series (Card and others, 1972). It includes the Sibley Group (checked pattern) (Franklin and others, 1980) and an extensive area of dip slope exposure of Keweenawan diabase sills (randomly slashed pattern). Keweenawan dike and sill swarms are indicated with heavy parallel lines. One, two, and three refer to the Thunder Bay, Gunflint, and Grand Portage swarms, respectively. The Mellen Complex is located in the area SW of the Keweenaw Fault. (P. W. Weiblen, 1982).



A



B

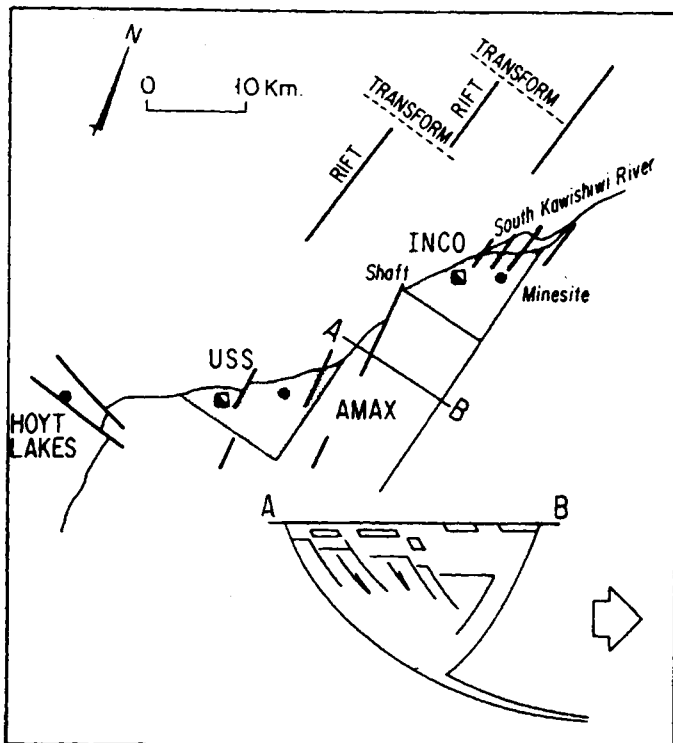


**Fig. II -1-6-3. Generalized map view of the Kawishiwi area of the Duluth Complex**

The faults (heavy lines) are suggested by coincidence of topographic, aeromagnetic, and gravity lineaments with joint density data (Cooper and others, 1981). The offsets in the basal contact could be generated by a small scale rift and transform fault system (inset) during evolution of magma chambers, as indicated in Fig. II -1-5-4 (B). The sites of most intensive (Cu-Ni) exploration by mining companies (USS, AMAX, and INCO) lie within areas that could represent extensive development of offsets. Such areas would be likely places to find a high proportion of country rock mixed with magma (P. W. Weiblen, 1982).

### (1) Triple Junction Model

The doming of hot spots in several points inside the continent initiated the formation of the triple junctions. Then, the triple junctions connected to form a rift system and brought about the continental rupture (Fig.II-1-6-4). Moreover, the evolution of magma from CO<sub>2</sub>-Alkali rich magma to tholeiitic magma depending on the generated depth, the reaction between the melt and the feeder, and the grade of fractional crystallization is recognized (Bailey, 1978). The examples of the above model are the Red Sea rift of Ethiopia, the North Atlantic rift of the eastern part of Greenland, and the present Mid-Atlantic rift. As the Keweenawan intrusive rocks of MCR are composed of alkaline rock bodies and tholeiitic rock bodies, this model can be applied. Comparing the Keweenawan intrusive rocks with the them of the North Atlantic Rift (the opening in Tertiary), the similar rift system can be considered (Fig.II-1-6-5). Anyone of Sibley graben, Codwell alkaline rock body or Kangerdlugssuaq alkaline rock body can become aulacogen (failed arm). The remaining two arms correspond to the direction of the axis of rift and are connected to the other triple junctions. Flood basalt is distributed in the axis of this arm. The Lake Superior and Faeroes are considered to be the triple junction. They were considered to be the center of the magma activities.

### (2) Transform Fault Model

The transform fault model explains the forming of the rift and the transform fault by lateral movement. The simple shear fracture occurs with lateral movement in isotropic homogeneous medium (Fig.II-1-6-6, A- E). If there are existing fractures in the medium, the directions of the shear fractures change (Fig.II-1-6-6, D- E). As the lateral movement progresses, the conjugate shear fractures (R, R') change angles to the direction of the lateral movement. The low angle shear fracture (R) becomes the lower angle shear fracture, and the high angle fracture (R') the higher angle extensional fracture (Fig.II-1-6-6, G). When the lateral movement progresses further, the low angle shear fracture develops to the transform fault and the high angle extensional fracture to the rift (Fig.II-1-6-7).

Norman (1978) says that the distribution of Keweenawan Complex can be explained by the model of transform fault (Fig.II-1-6-5). Chase and Gilmer (1973) presume the transform fault in the rift. For example, the dykes of Gunflint, Thomson, Duluth Complex and MCR can be applied to this model. MCR is divided into several segments estimated by the gravity anomaly (-20 mgal). These segments show the trends of NE – SW and NW – SE directions, which suggest the shear fracture and the transform fault, respectively (Fig.II-1-6-8, A). The airborne magnetic anomaly in the southern part of MCR (Fig.II-1-6-8, B) suggests the shear fracture and the extensional fracture of the same direction. Chase and Gilmer (1973) estimated that the rupture of the extensional fracture and the width of the rift were approximately 55 kilometers.

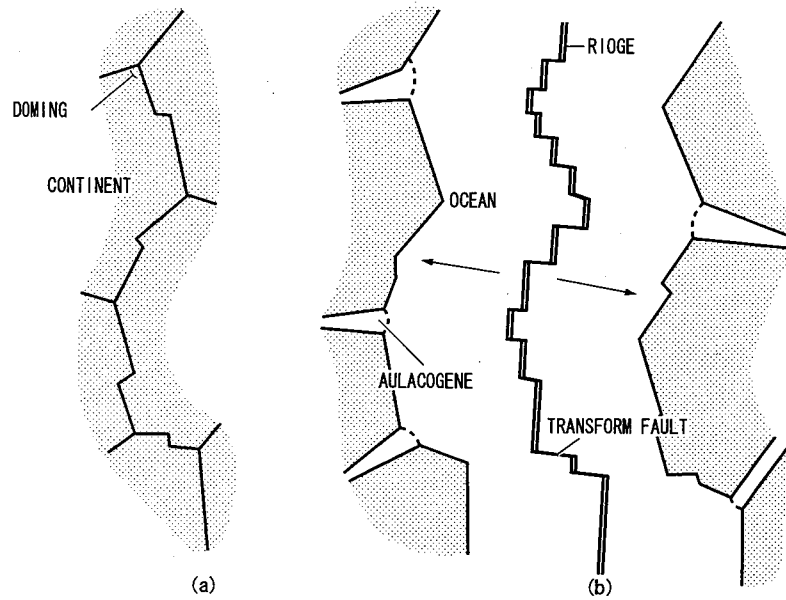


Fig. II -1-6-4. Formation of aulacogene (b) associated with the rapture of the continent (a) (S. Ueda, 1989).

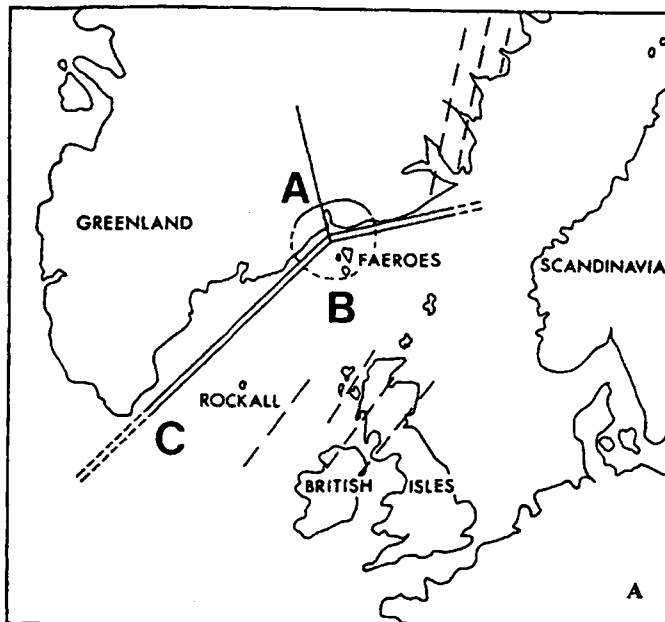
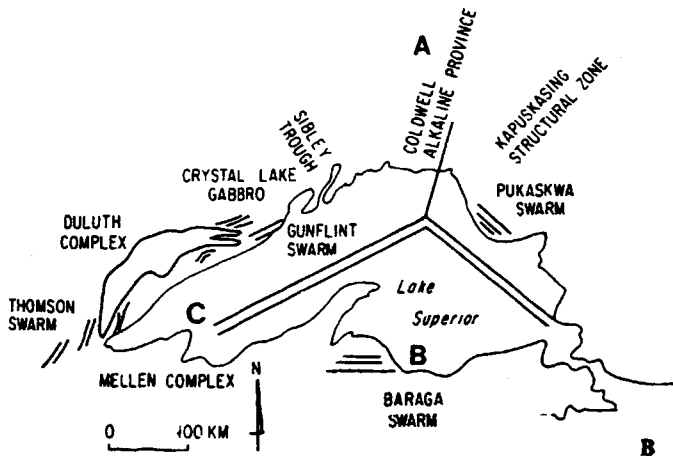
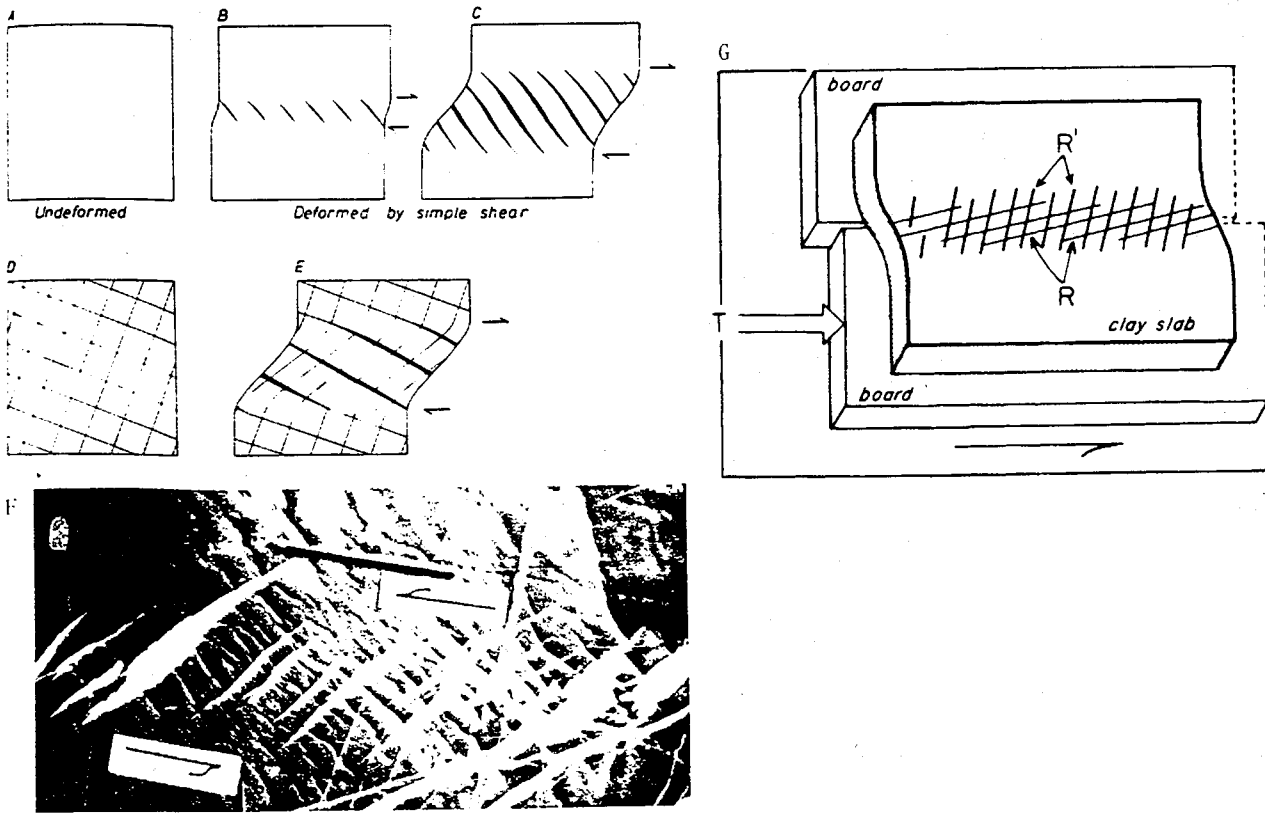


Fig. II -1-6-5. Possible analogies between the geometry of the igneous rocks associated with the Tertiary opening of the North Atlantic and those in the Midcontinent Rift System.

(A) Failed arm-rift relations in the North Atlantic (modified from Brooks, 1973); (a) Kangerdlugssuaq alkaline intrusion, (b) high-FeTi quartz tholeiite volcanism. (c) high-Al olivine tholeiite volcanism. (B) Analogous relations to (A) in the Lake Superior region of the Midcontinent Rift System; (a) Coldwell Alkaline Province, (b) quartz tholeiite dikes and sills, (c) olivine tholeiite dikes and sills. (P. W. Weiblen, 1982).



Transform Fault Model



**Fig. II-1-6-6. Shear mechanisms for producing extensional features in rocks.**

A-F, simple shear from Ramsay (1967, p. 88-89). A-C illustrate structures that are likely to develop with shear in an isotropic rock. Note the curvature in the tension gashes that develops with progressive shear (B-C). D and E illustrate structures that might form in a previously jointed rock. F illustrates zone of en echelon quartz-filled tension gashes produced in graywacke by simple shear, Note the similarity in the shape of the large gash on the left and the map pattern of the Duluth Complex (Fig. II -1-5-2,3,9) G, pattern of fractures in the Riedel shear experiment (Tschalenko, 1970). The primary shears (R) rotate to lower angles to the direction of movement as shearing progresses. The conjugate shears (R') are essentially the tension gashes in simple shear (B). The two shear directions are analogous to those depicted by Cloos (1955) for shear with rotation. (P. W. Weiblen, 1982).

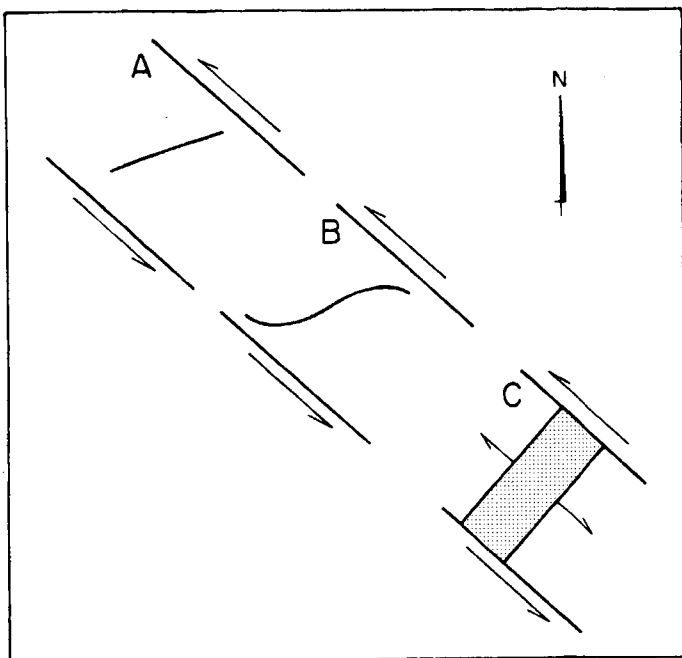


**Fig. II -1-6-7. Hypothetical transition in tectonic regimes proposed for the Midcontinent Rift System.**

(A) In an inirial stage, left lateral wrench faulting would produce simple shear or conjugate Riedel fractures at high angles to the shear directions (Fig. II -1-5-10). Intersection of these directions with preexisting zones of weakness would localize alkaline magmatism as found in the Kapuskasing Structural Zone and the Coldwell Alkaline Province. (B) Progressive shear would produce en echelon fractures as exemplified by the quartz tholeiite and olivine tholeiite dike and sill swarms (Fig. II -1-5-9). (C) The gravity model of Chase and Gilmer (1973) and the half-graben magma chamber model of Weiblen and Morey (Fig. II -1-5-4) suggest that wrench faulting did progress to actual rifting. (P. W. Weiblen, 1982).



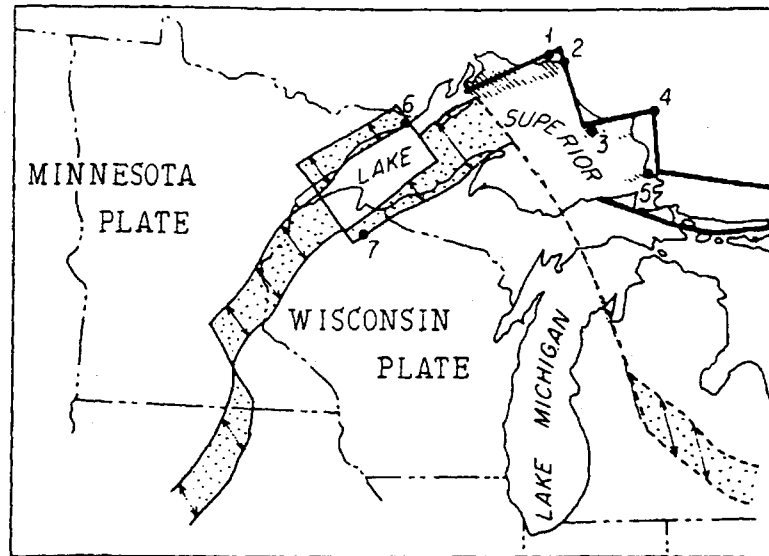


**Fig. II -1-6-8. Rifting models for the Midcontinent Rift System (from Norman,1978).**

Shaded area outlines Chase and Gilmer's (1973) model. Heavy lines outline rift and transform intersections proposed by Norman (1978) to explain locus of alkaline complexes and sites of extensive felsic magmatism. 1. Praire Lake Complex; 2. Coldwell Complex; 3. Michipicoten Island; 4. Firesand River Complex; 5. Batchawana area; 6. Hoveland, Minnesota; and 7. Mellen, Wisconsin. Gravity data do not indicate lithospheric separation north of Lake Superior. (P. W. Weiblen, 1982)

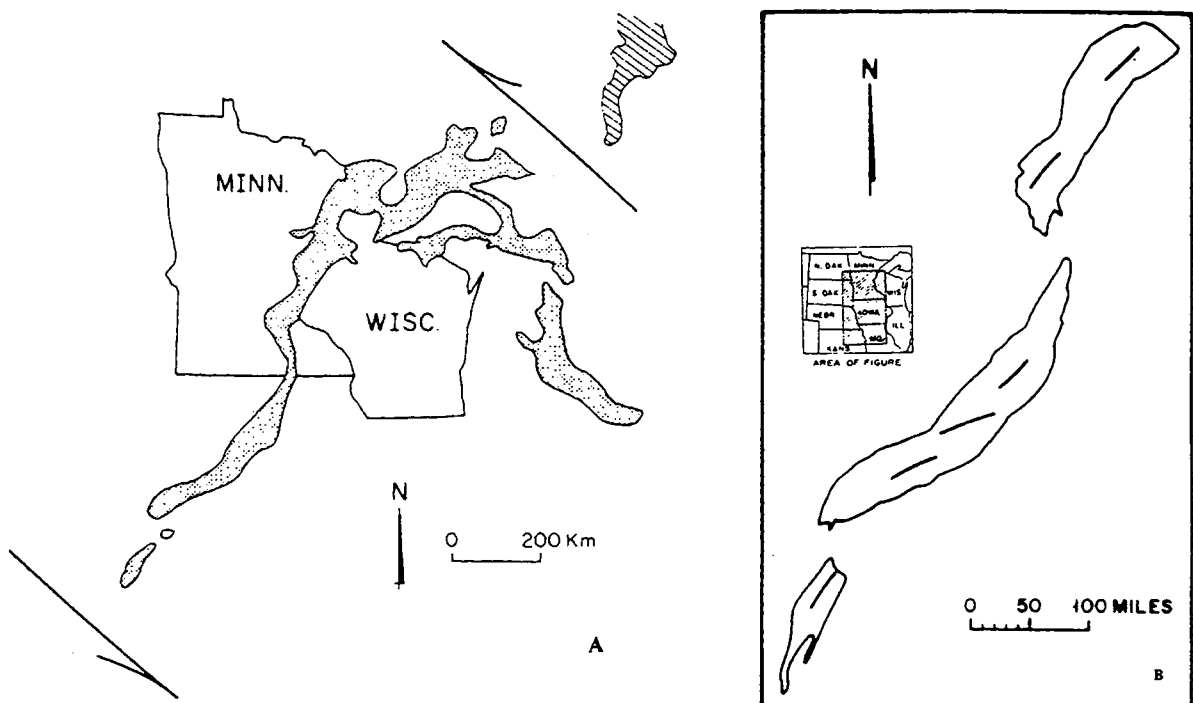


**Fig. II -1-6-9. Regional patterns of geophysical anomalies in the Midcontinent Rift System.**

(A) Outline (stippled area) of the -20 milligal Bouguer gravity anomaly of the Midcontinent Rift System (from Craddock, 1972). Trends of individual segments range from northeast to northwest. Possibly this range in orientation of segments and their sinuous continuity record a change in fracture patterns with time analogous to the two directions shown for a shear couple depicted in Fig. II -1-5-10. and Fig. II -1-5-11. (B) Outline of aeromagnetic anomalies in the southern part of the Midcontinent Rift System (from King and Zietz, 1971). As suggested for the northern part of the rift in (A), the sinuous pattern might also more closely reflect a change in fracture directions due to shear with time rather than a single rift- transform geometry.

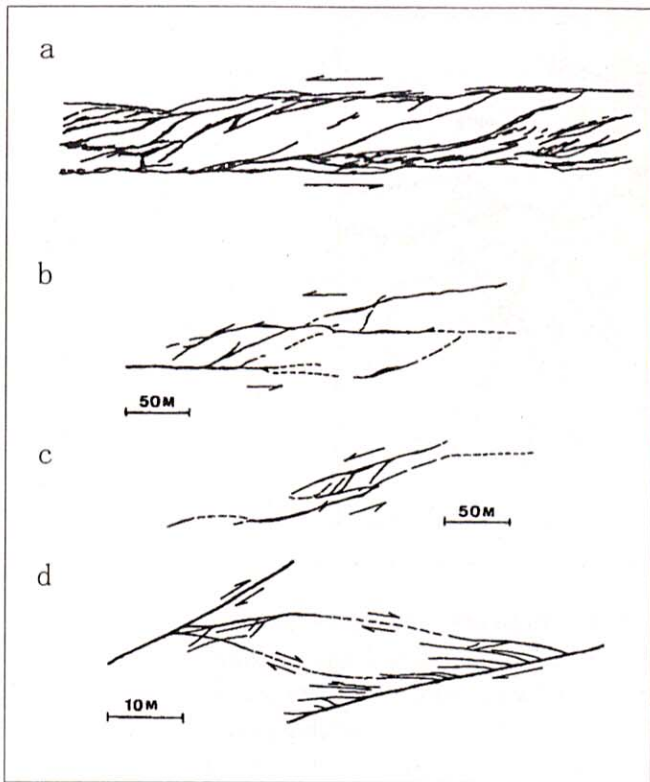


Fig. II-1-6-10. Interior structure of crush zone of the shear fracture formed by rock failure test(a) and those of vein(b~d)(K.Otsuki et al.,1991)

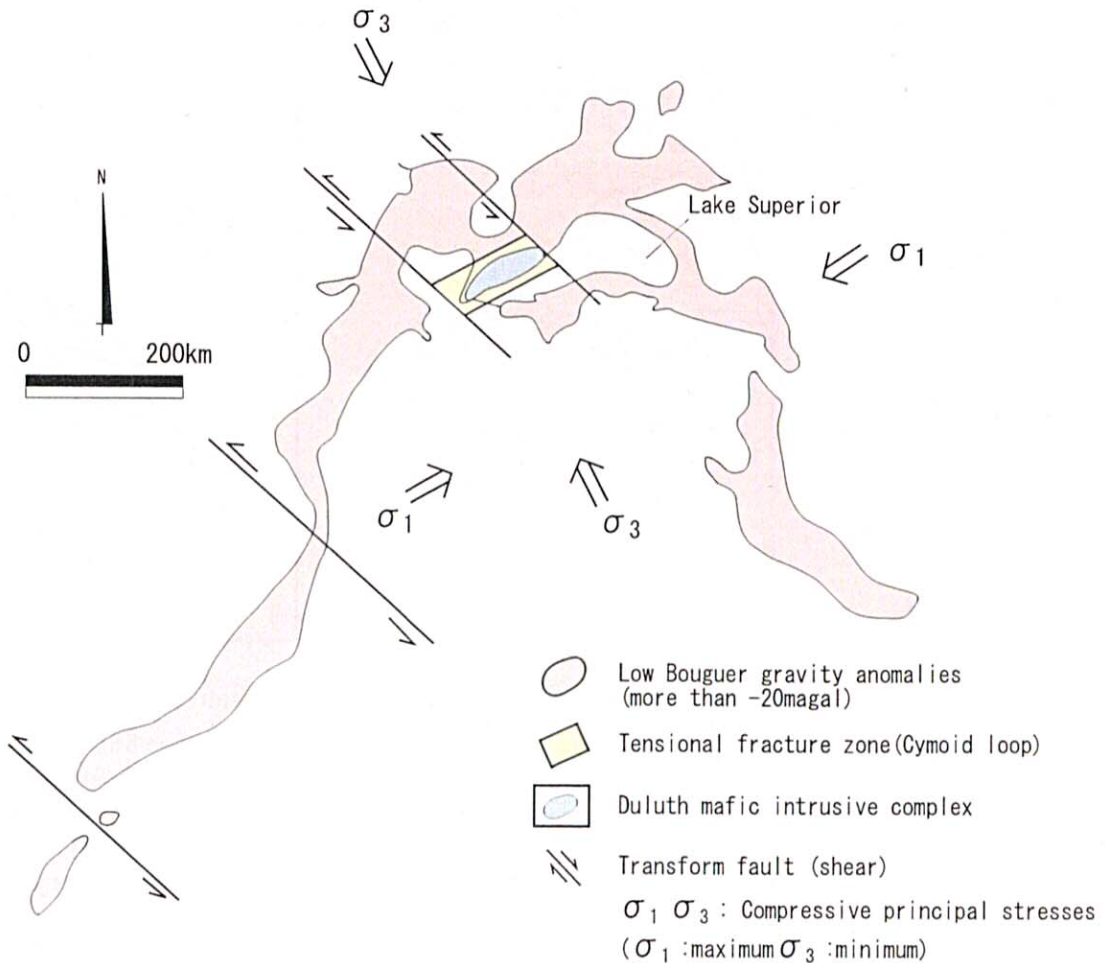


Fig. II-1-6-11. Formation model of Duluth mineralized intrusive complex.

It is well known that primary shear fractures form many diagonal echelon secondary shear fractures as the lateral movement progresses and the secondary shear fractures are connected each other to form a large tensional fracture called a cymoid loop (Byerlee et al., 1978, Fig. II-1-6-10). The Duluth ore deposit may be one of ore deposits inside cymoid loops.

Regarding a regional stress field which formed the Duluth ore deposit, assuming that the intermediate compressive principal stress axis ( $\sigma_2$ ) is perpendicular, the maximum compressive principal stress axis ( $\sigma_1$ ) has the same NE-SW direction as the MCR, and the minimum compressive principal stress axis ( $\sigma_3$ ) has the same NW-SE direction as the transform faults (Fig.II-1-6-11).

## 1-6-2 Tectonics of Noril'sk Ore Deposit

### (1) Tectonics of the Siberian Plate

Zonnenshain et al. (1990) have reconstructed a paleogeography during the Palaeozoic to the Mesozoic in the northern Eurasian Continent (Fig.II-1-6-12). The early Carboniferous (340Ma) to the late Permian: The plates of Euro-America, Siberia, and Kazakhstan converged into the Ural Sea as a subduction zone and involved the Ural orogenic belt. The orogenic movement had finished and formed the Laurasia plate. The convergence movement was linked with the Hercynian orogenic movement.

The late Permian (250Ma) to the early Triassic: These periods have changed from a compressive stress field to an extensional stress field. Since the end of the Permian period, the Laurasia plate ruptured as a starting point of the hot spot formed in the present Gydansk Peninsula and was divided into the Siberian plate of the eastern side and the East European plate of the western side (Fig.II-1-6-12). This continental drift is called the "Siberian continental drift" (Tamrazyan, 1962). The rupture of the Laurasia plate propagated from the north to the south, and formed the Gydansk-Omsk rift with a more than 1,000km length. The huge amount of the tholeiitic Siberian flood basalt erupted along the rift. According to  $^{40}\text{Ar}$ - $^{39}\text{Ar}$  radioactive dating, the Siberian flood basalt erupted during 600,000 years in the end of the Permian period ( $248.9 \pm 2.8\text{Ma}$ , Campbell et al., 1992). The early Triassic to the middle Tertiary period: The extensional stress field continued after igneous activities of the Siberian flood basalt, and the Siberian plate and the East European plate continued to drift further into the east and west directions. The West Siberian lowland was formed in the area where the crust was thinned.

According to seismic exploration data, the Mohorovicic discontinuity of the East European plate, Siberian plate, and southern Kazakhstan block are 40 to 50 km in depth and that of the West Siberian lowland is the 30 to 40 km in depth. Especially the Mohorovicic discontinuity of Gydansk Peninsula in the northern edge of the rift is less than 30 km in depth (Fig. II-1-6-14). The root of Gydansk Peninsula ( $N68^\circ$ ,  $E85^\circ$ ) is considered to be a triple junction with two

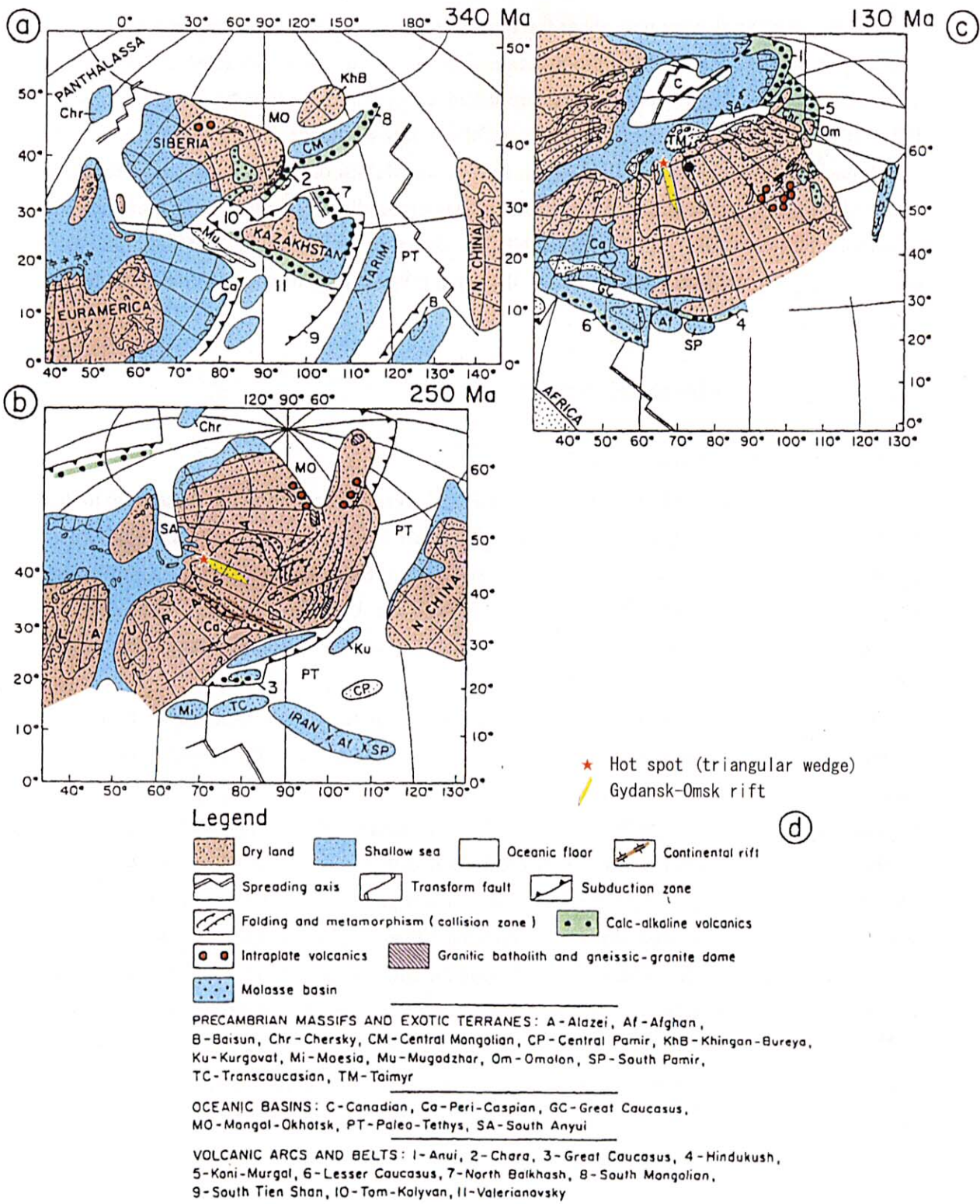


**Fig II-1-6-12. Reconstruction of the position of the American, European, Siberian, Kazakhstan, North China, and several smaller plates**

(a) the early Carboniferous 340 Ma; (b) the Late Permian, 250 Ma; and (c) the Early Cretaceous. Within the larger plates, lines of latitude and longitude refer to their present-day positions. The position of the plates in each diagram refers to their absolute positions during the period in question (drawn after Zonnenshain et al., 1990).



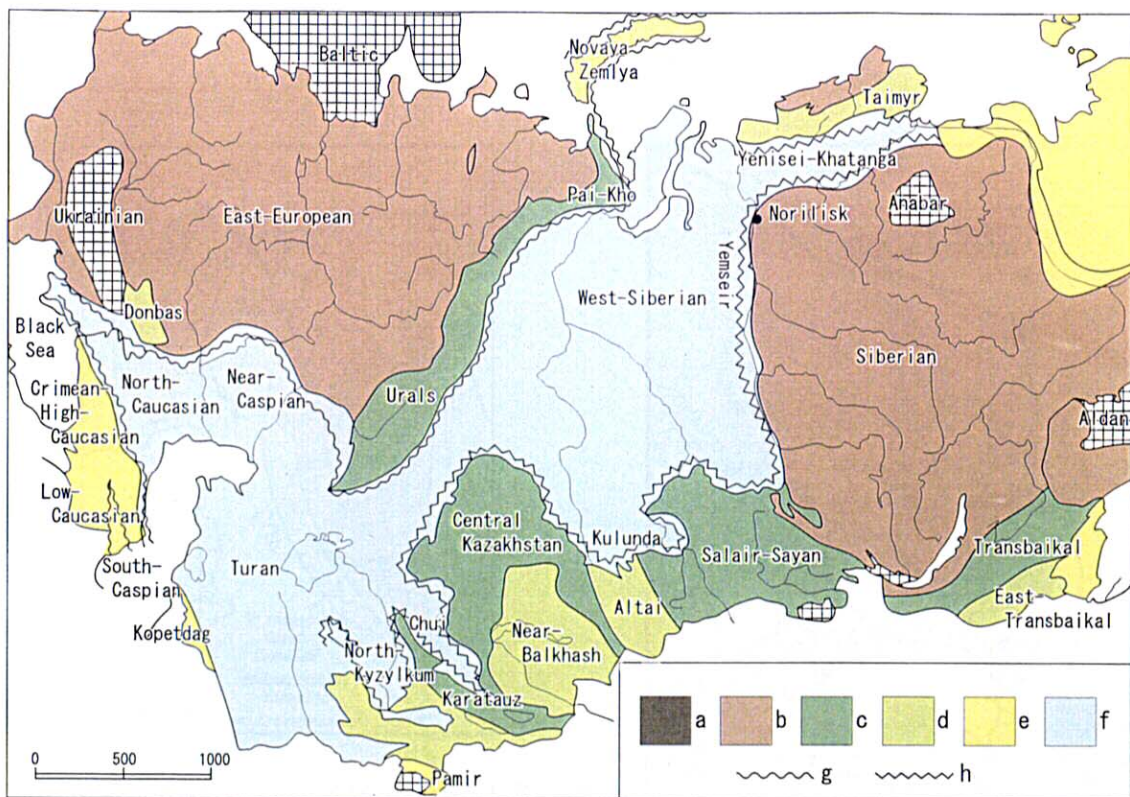


**Fig. II -1-6-13. Diagram of geological geotectonic zoning and the Siberian Continental drift.**  
 a: ancient shields (archean and proterozoic), b: ancient platforms (Paleozoic), c: regions of Caledonian foldings (Early and Middle Paleozoic), d: regions of Hercynian foldings (Late Paleozoic), e: the Alpine fold regions in the South of the U.S.S.R. (Mesozoic, Cenozoic), f: troughs on the Precambrian folded base (Mesozoic, Cenozoic), g&h: western edge and eastern edge of the Siberian fractural suture. (G.P. Tama ra zyan, 1971).

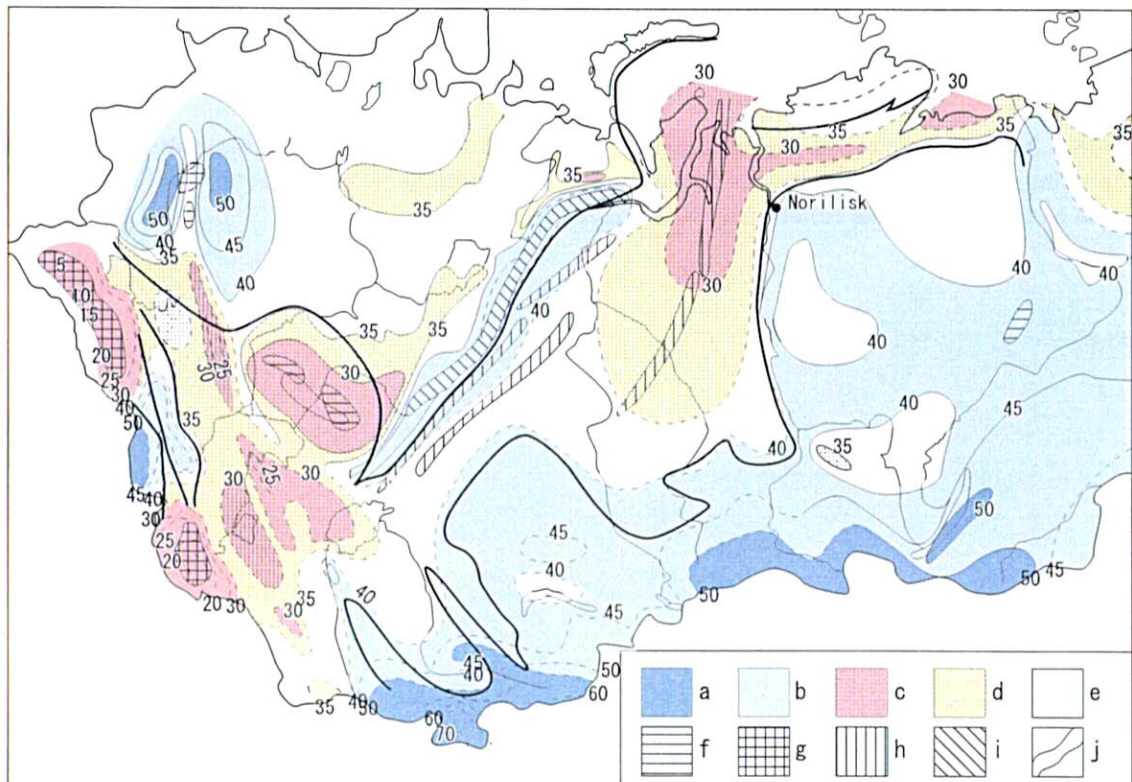


**Fig. II -1-6-14. Isopach map of thickness of crust, limited by the surface of Mohorovicic and that of the Paleozoic (and is some places Meozoic) foundation.**

Thickness of consolidated crust ; a: more than 50km; b: 40-50km c: less than 30 km; d: 30-50 km ; e: 35-40 km ; f: projections of basalt layer, g: zones of cilandseas with no granite layers (intracrotoric basin), h: crushing foundering and down warping bands (bands of positive gravity aromalies and magnetic maxima, i: bands of intensive basalti fication of granite layers in continental crust region (the Urals), j: edges of the Siberian fractural suture. (G.P. Tamarazyan, 1971).



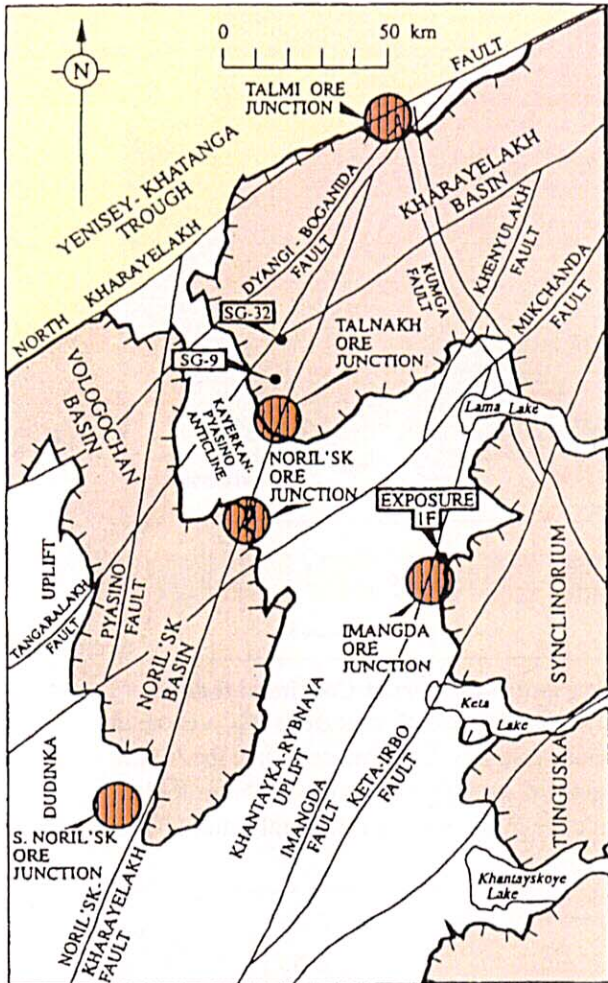


Fig. II -1-6-15. Map of the Noril'sk region showing the outcrop of the lavas (areas surrounded by lines with attached hatching), main tectonic elements and principal ore junctions (from Naldrett et al., 1992). Map compiled on the basis of data collected by NKGRE and TsNIGRI.

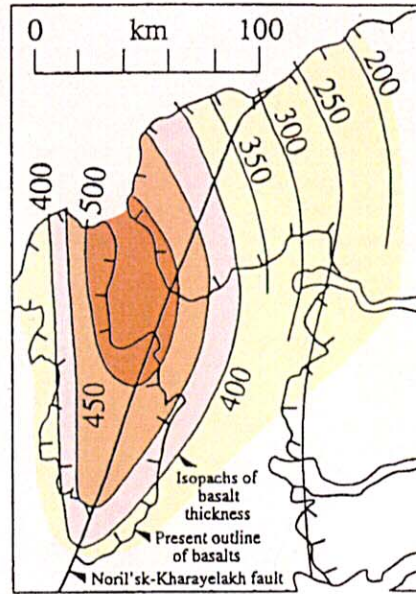


Fig. II -1-6-16. Thickness of the Nadezhinsky formation (lower+middle+upper)suite which illustrates the basin into which lavas were accumulating at the time of eruption (after Naldrett et al.,1992)

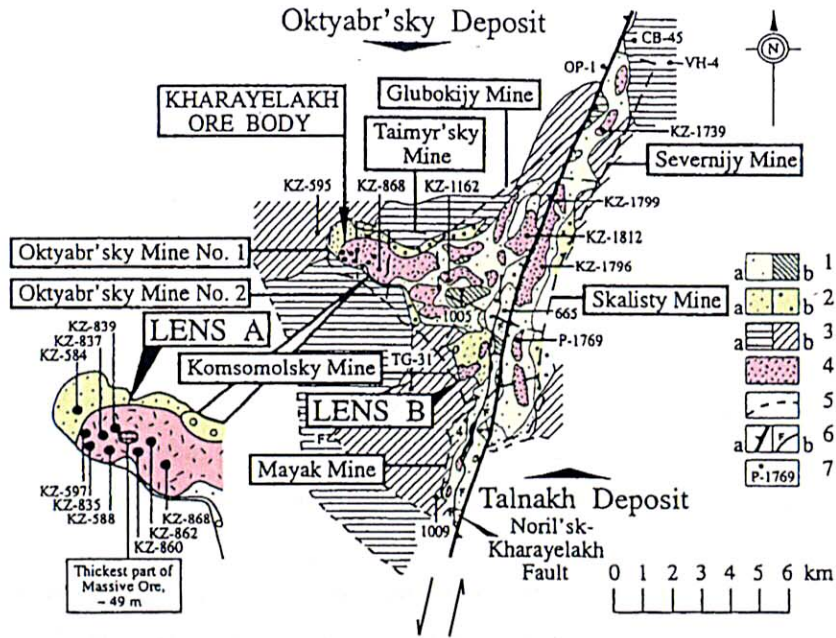


Fig. II-1-6-17. Plan showing the outline of the Northwest Talnakh intrusions. showing the distribution of lenses of massive sulfide.

1=outline of ore-bearing intrusions. 2= the intrusions that are thought to represent the intruding mass of magma. 3=Differentiated apophyses(sills) of the ore-bearing intrusions. 4= massive sulfides underlying the intrusions. 5= erosional boundaries of intrusions: 6= faults, (a) the Noril'sk Kharayelakh faults; 7= drill holes. (after Naldrett et al., 1996)

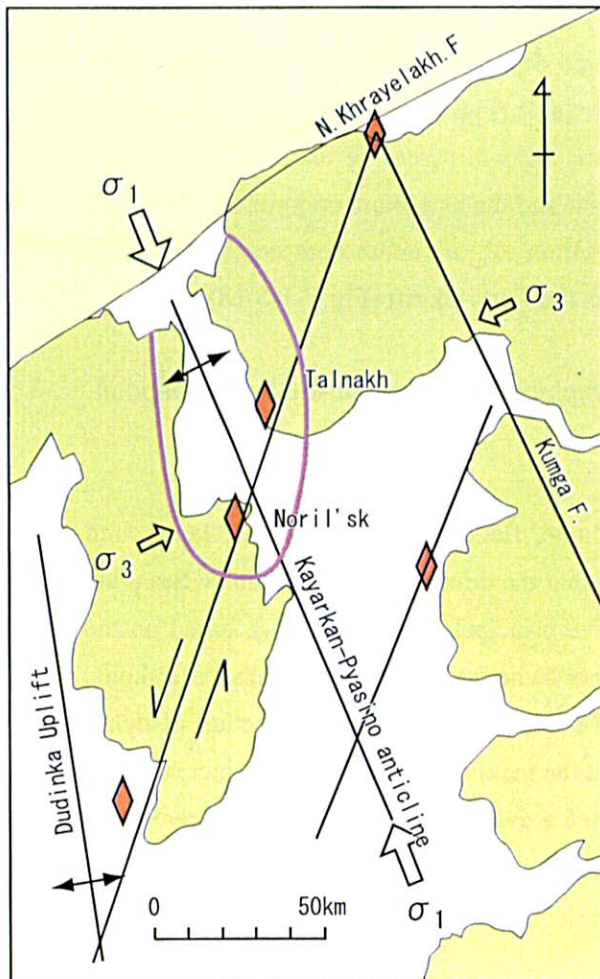


Fig. II-1-6-18. Formation model of Noril'sk ore deposit

- Sedimentary rocks of the Jurassic to the Cretaceous
- Siberian flood basalt
- Sedimentary rocks of the Paleozoic
- Faults and lateral movement
- Uplifts
- Tensional Fracture Zone(ore deposits)
- $\sigma_1, \sigma_3$  Compressive Principal Stresses ( $\sigma_1$ :maximum,  $\sigma_3$ :minimum)
- Volcanic center of Nadezhinsky lava unit more than 500meters in thickness.

arms, namely the Gydansk-Omsk rift (N-S length: 2,000km, width 30-50km) and the Khatanga rift. The Noril'sk ore deposit is inferred to have been formed by a mantle plume ascending along the triple junction. The Noril'sk ore deposit is now dislocated approx. 300 km away from the triple junction due to the movement of the plates (Nalrett et al. (1992), D. Schissel (2001)).

## (2) Geological Structure around the Noril'sk Ore Deposit

The Noril'sk ore deposit is located in the northwestern part of the Tunguska basin in the Siberian plate; the West Siberian lowland is located on the western side of the deposit, which overlooks the Khatanga graben, consisting of sediments of the Jurassic to the Cretaceous, in the northern side (Fig. II-1-6-15).

The Noril'sk ore deposit consists of the South Noril'sk ore deposit, the Noril'sk ore deposit, the Talnakh ore deposit, and the Talmi ore deposit. The Noril'sk ore deposit and the Talnakh ore deposit which are very important economically, are present along the Noril'sk-Kharayelakh fault in the NNE-SSW direction around the Kharayelakh basin and Noril'sk basin. The area where is caught by both basins is the Khantayka-Rybnaya anticline in the NNE-SSW direction. The Noril'sk and Talnakh ore deposits are located in the thickest part of the Nadezhinsky basalt lava unit what played an important role on the generation of the ore deposits. That to say, both ore deposits are inferred to have occurred at the eruption feeder of the basalt lava unit (Fig. II-1-6-16).

A relation between a bonanza of the Talnakh ore deposit and Noril'sk- Karayelakh fault suggests that the fault is a sinistral strike-slip shear fault (Fig. II-1-6-17). According to the regional stress field associated with the Noril'sk ore deposit, assuming that the intermediate compressive principal stress axis ( $\sigma_2$ ) is perpendicular and the maximum compressive principal stress axis ( $\sigma_1$ ) coincides with the NNW-SSE direction, the minimum compressive principal stress axis ( $\sigma_3$ ) has the same ENE-WSW direction as the Gydansk rift (Fig. II-1-6-18).

## 1-6-3 Tectonics of Parana Flood Basalt and Emplacement of Ni-Cu-PGE Ore Deposit

### (1) Tectonics of Flood Basalt

Concerning the relations among the mantle plume, flood basalt lava, dykes, faults, and regional stress field, K. Nakamura (1995) concluded that the direction of the Phillipine Sea plate subduction coincides with the maximum compressive principal stress axis ( $\sigma_1$ ), based on the directions of distribution of volcanos and movements of active transcurrent faults on Hakone, Izu Peninsula, Izu-oshima Island, etc. Regarding the relations between the direction of dykes and the regional stress field, Nakamura indicated that the maximum compressive principal stress axis coincides with the direction of the intrusion when a dyke intrudes into a transcurrent fault,

and with the vertical direction when a dyke intrudes into a normal fault which is parallel to the dyke. The minimum compressive principal stress axis coincides in both the cases, with the direction of crossing with the dyke at a right angle. R.E.Ernst et al. (2001) and D.Mege (2001) come to conclusions similar to those of K.Nakamura (1995) about the relations among lavas and dyke swarm of flood basalt and surrounding fold structures and regional stress fields of the Earth and Mars.

W. M. de Rezende (1972) considered the breakup of Gondwana continent and the tectonic movement of South-American continent as follows (Fig. II-1-6-19), referring to basic igneous activities and faults that occurred in Post-Paleozoic in the South-American continent. (1) The craton of the South-American side on Gondwana continent broke up into some blocks in the Paleozoic and the Amazon, Parnaiba, and Parana intracontinental basins were emplaced at the boundary of breakup of craton. The breakups of South-American continent started both in Amazon in the north and in Parana in the south and spread gradually to their surrounding areas. (2) The breakup movements caused roto-translatory movements between South-American and African continents, resulting in rifts and regional transcurrent faults crossing the rifts at right angles. The faults around the Ponta Grossa Arch are sinistral transcurrent faults. The directions of rotations took place counterclockwise in both the Amazon and Parnaiba basins, and clockwise in the Parana basin. (3) A large volume of tholeiitic flood basalt extruded through the rifts and transcurrent faults. Flood basaltic lavas and / or dykes was dated as 220 Ma in Guiana craton, 181-170 Ma in Amazon basin, 130-120 Ma in Parnaiba basin, and 140-130 Ma in Parana basin. (4) The transcurrent faults continued to be formed from the Mesozoic to the Tertiary, and resulte in influencing tectonics of the Andean orogenic belt, such as Huancabamba deflection line and Santa Cruz tectonic deflection line.

Turner et al. (1994) concluded that South-Ameican continent broke up clockwise from the south of Gondwana continent, and the Ponta Grossa dyke swarm intruded and flood basalt lava extruded along the sinistral transcurrent faults in maximum compressive principal stress field in the NW-SE direction (Fig. II-1-4-23).

## (2) Rift Zone and Promising Areas of Emplacements of Ni-Cu-PGE Ore Deposits

Based on our survey results stated in Section 1-4 through Section 1-6, we will present a comprehensive explanation of Precambrian basement rocks, sedimentary rocks and flood basalts in Post- Early Paleozoic, and faults in the Parana Basin and consider the relation among the rift zone and the regional stress field and promising areas of emplacement of Noril'sk-type Cu-Ni-PGE ore deposit.

It is estimated that the structure of the basement in Parana Basin almost fixed in the Early Paleozoic when Gondwana land consolidated. After the Early Paleozoic, the Lithosphere in the Parana Basin repeated dilation and contractions due to the activities of Mantle plume, and



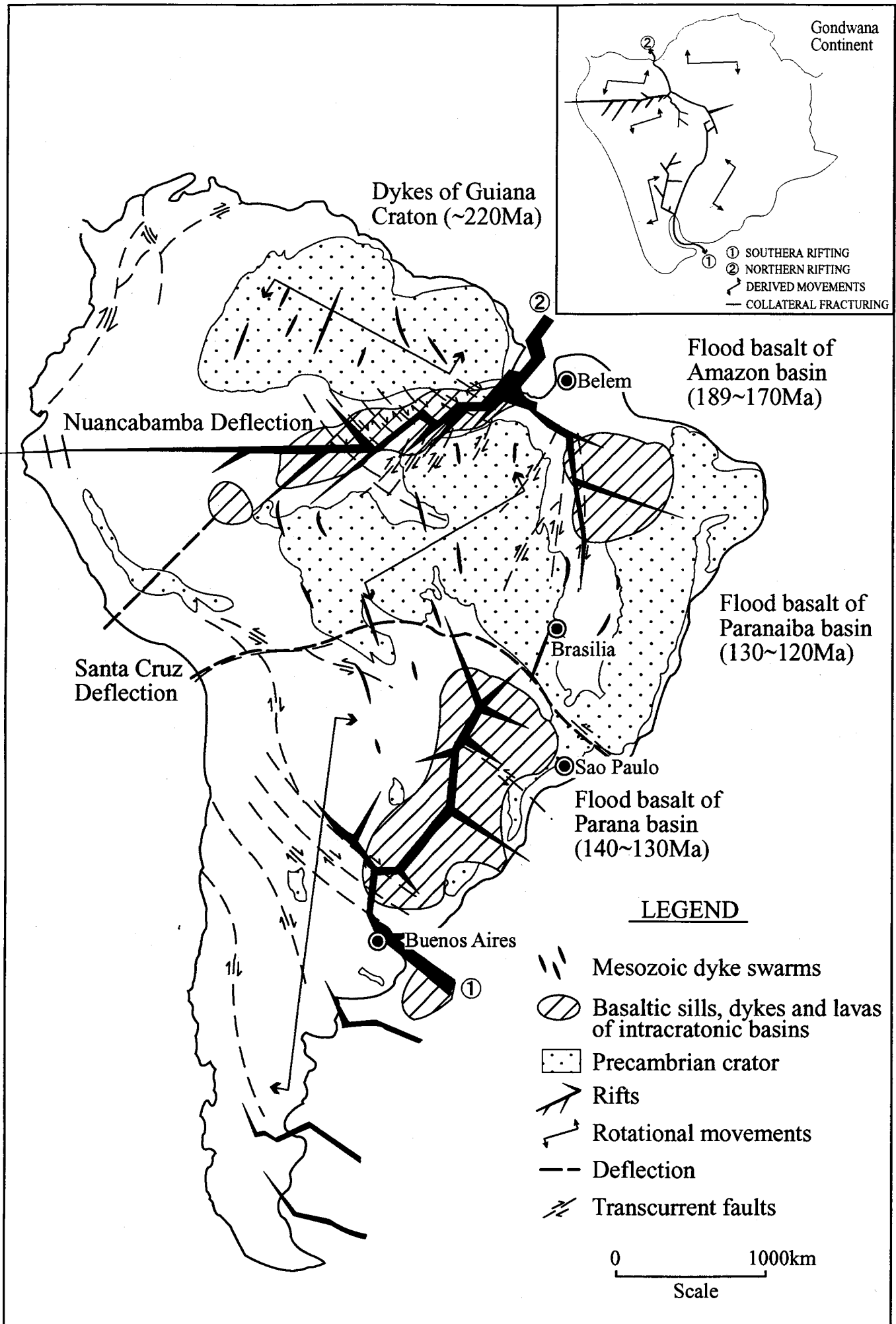


Fig. II-1-6-19 Post-Paleozoic geotectonics of South America  
(Modified from W.M. de Rezende, 1972; et al.)



the Rio Ivai Supersequences to Gondwana II Supersequence deposited along the Parana River in the NE-SW directions. The mantle plume was most active in the Early Cretaceous and a large quantity of flood basalt (Serra Geral Fm.) extruded in the Basin. A large low anomaly zone in the central part of the pseudogravity anomaly map (Fig. II-1-5-20) overlaps with a zone where sedimentary sequence and flood basalt lava are thick, with a zone where a large quantity of sills and dykes intruded, with a high residual gravity anomaly zone, and with a high attenuation factor zone. Based on these facts, it is concluded that the large low anomaly zone in the central part of the pseudogravity was rift zone at the time when flood basalt extruded (Fig. II-1-5-25).

The direction of the rift zone extends in the N-S directions in the northern Basin; in the NE-SW directions the central Basin, and in the NE-SW and NW-SE directions in the southern Rio Alfonzo fault based. The inside of the rift zone has repetitions of high anomaly zones and low anomaly zones in the NE-SW directions (Fig. II-1-5-20). These anomaly zones in the NE-SW directions were formed by stair-step normal faults (vertical direction: maximum compressive principal stress axis  $\sigma_1$ ) in the extensional stress in the NW-SE directions field (minimum compressive principal stress axis  $\sigma_3$ ).

The following four areas in the rift zone have thick flood basalt lava pile, thick accumulated intrusive rocks, high residual gravity anomaly high attenuation factor and low pseudogravity anomaly. (1) The area where the Tiete structural line in the NW-SE direction crosses through Parana River (2) The area where the Guapiara fault in the NW-SE direction crosses through Parana River. (3) The area where Rio Alfonzo fault in the NW-SE direction crosses through Parana River. (4) The western Torres Posadas fault area. All of these areas are estimated to have been the volcano-center of flood basalt magmas. The largest volcano-center is found in the area (3) where the Rio Alfonzo fault crosses through Parana River. The thickest accumulated sills and dykes intruded at the location.

The intrusive rocks in the area where the Rio Alfonzo fault crosses through Parana River directs the NW-SE directions in succession to the southeastern Ponta Grossa Arch. They intruded along the several faults in the NW-SE directions which identified by the magnetic lineaments on the aeromagnetic maps. The faults in the NW-SE directions are estimated to be sinistral transcurrent faults because they have sharp boundaries and are accompanied with many secondary shear faults in E-W directions. The unclockwise rotations of them coincides with those mentioned by Turner et al. (1994) and W.M. de Rezende (1972).

As mentioned above, the rift zone was formed in the N-S direction to NE-SW direction along the structural direction of the basement rock. Flood basalt magmas extruded along the rift zone. In particular, flood basalt magmas extruded most intensely at the area where the rift zone in NE-SW direction crosses through the transcurrent faults in the NW-SE directions. It is estimated to have been attributable to the formation of Cymoid Loop-like tensional fractures

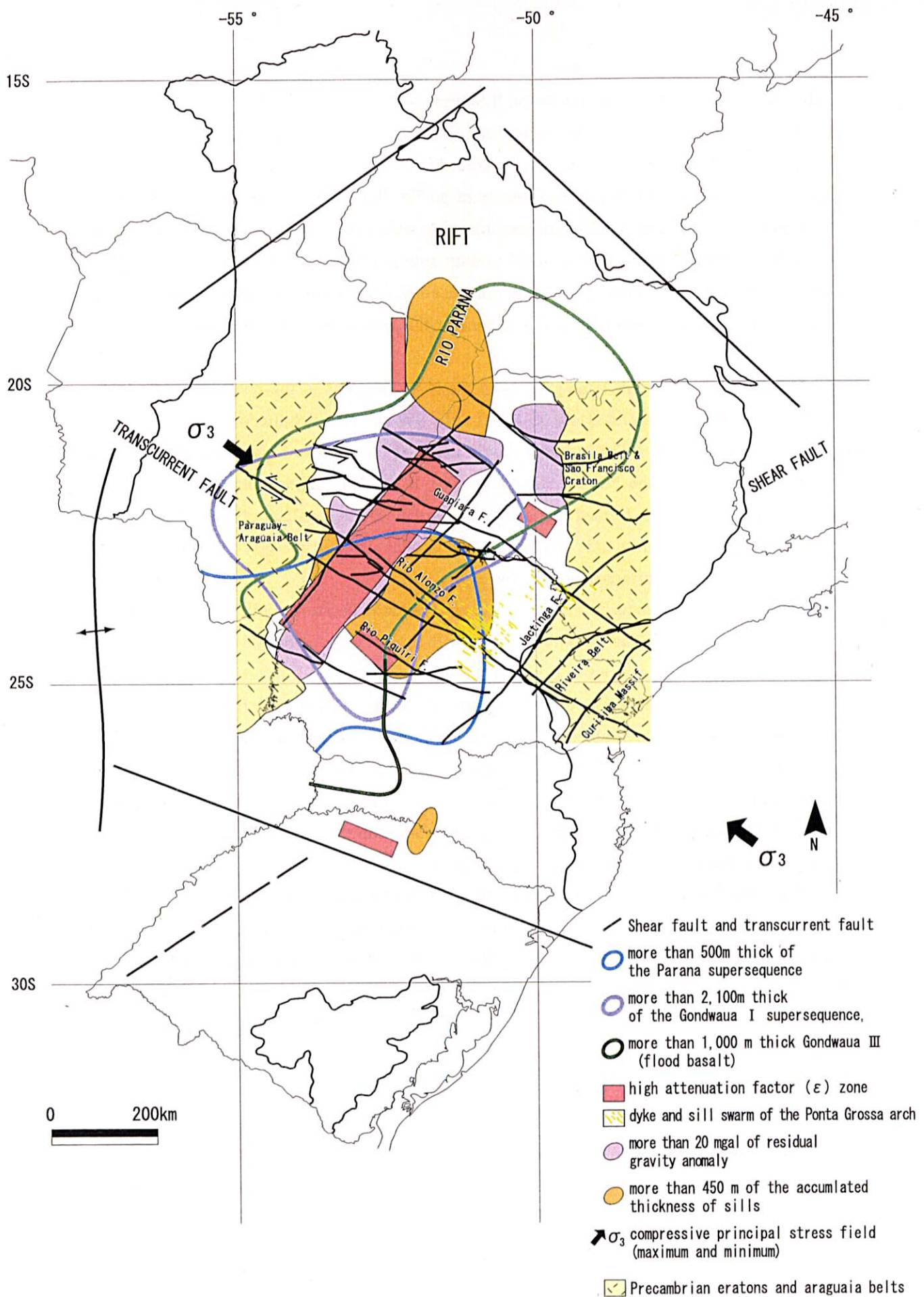


Fig. II-1-6-20. Comprehensive analysis map among the basement structure, basin sediment, gravity anomaly and regional stress field in the Parana basin.

originated from many secondary shear faults, such as the Duluth ore deposit (P.W. Weiblen, 1982).

The Noril'sk ore deposit was formed in the volcano-center where magma extruded most intensely in the Gydansk-Omsk rift zone (Tamrazyan, 1962). In the volcano-center, immiscible sulfide melts contacted most with large quantities of silicate melts containing Ni-Cu-PGE. As a result, the ore grade of Ni-Cu-PGE in the sulfide melts gradually improved and formed high graded ore deposits (A.J. Naldrett, 1992; R.R.Keays, 1997). Magma mixing, together with crustal contamination of magma, is estimated to be a major factor in the formation of orthomagmatic ore deposits.

We can present the following four areas as promising areas of emplacements of Ni-Cu-PGE ore deposits in the Parana Basin. (1) The area where the Tiete structural line in the NW-SE direction crosses through Parana River (2) The area where the Guapiara fault in the NW-SE direction crosses through Parana River. (3) The area where Rio Alfonzo fault in the NW-SE direction crosses through Parana River. (4) The western Torres Posadas fault area. Among four areas, we can propose that areas where the Guapiara fault and the Rio Alfonzo fault in the NW-SE directions cross through Parana River are the most promising area of emplacements of Ni-Cu-PGE ore deposits.

## **Chapter 2: Satellite Image Analysis**

### **2-1 Objectives**

The objectives of the survey are to produce a digital mosaic image using JERS-1/SAR data which cover the central part of the Paraná basin, make a photogeologic interpretation of the image to delineate geological structure, and study the supra-regional geological structure using Landsat TM image which cover the entire Paraná basin.

### **2-2 Processing and Production of JERS-1/SAR Image**

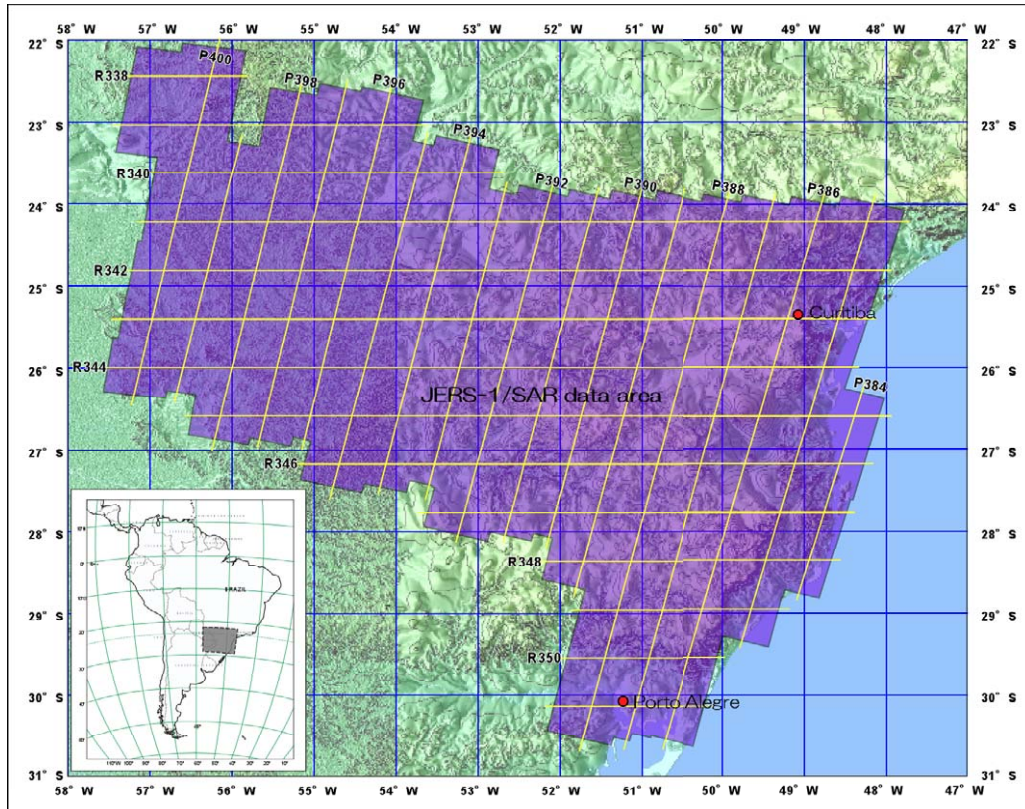
#### **2-2-1 Outline of the Survey Area**

Fig. II-2-2-1 shows the location of the survey area. The area is located in the center of the Paraná basin, ranging from 22° 00' to 30° 40' S latitude and from 57° 40' to 47° 45' W longitude, and has an area of about 500,000 km<sup>2</sup>. This area traverses the Paraná basin in the ESE-WNW direction and is widely covered with flood basalts erupted from the Jurassic to the Cretaceous. Also, sedimentary rocks of the Paleozoic and granites (the basement) are distributed in the northeastern part of the area (See Fig. I-3-1-1).

The survey area is steep near the coastal mountains in the east and the undulating hilly country spreads from the central part to the western inland area. The area is a maximum of 1,000 meters above sea level. Trees grow thick from the coast to the inland area. There are not many trees and grassland plants grow abundantly in the inland hilly country where cattle is raised.

#### **2-2-2 Satellite Data Used**

Table II-2-2-1 lists the data used. In the present survey, 131 scenes of JERS-1/SAR data were used.



**Fig.II-2-2-1 Location of JERS-1/SAR image analysis**



**Table II-2-2-1 List of JERS-1/SAR data**

No.	Path	Row	Date	No.	Path	Row	Date	No.	Path	Row	Date
1	400	338	1993/6/21	51	393	342	1994/5/31	101	387	346	1994/8/21
2	400	339	1993/6/21	52	393	343	1994/5/31	102	387	347	1994/8/21
3	400	340	1993/6/20	53	393	344	1994/5/31	103	387	348	1994/8/21
4	400	341	1993/6/20	54	393	345	1994/5/31	104	387	349	1994/8/21
5	400	342	1993/6/20	55	393	346	1994/5/31	105	387	350	1994/8/21
6	400	343	1993/6/20	56	392	341	1993/9/8	106	387	351	1994/8/21
7	400	344	1993/6/20	57	392	342	1993/9/8	107	386	341	1996/6/10
8	399	338	1993/6/20	58	392	343	1993/9/8	108	386	342	1996/6/10
9	399	339	1993/6/20	59	392	344	1993/9/8	109	386	343	1996/6/10
10	399	340	1995/4/10	60	392	345	1993/9/8	110	386	344	1996/6/10
11	399	341	1995/4/10	61	392	346	1993/9/8	111	386	345	1996/6/10
12	399	342	1995/4/10	62	392	347	1993/9/8	112	386	346	1996/6/10
13	399	343	1995/4/10	63	391	341	1994/8/25	113	386	347	1996/6/10
14	399	344	1995/4/10	64	391	342	1994/8/25	114	386	348	1995/11/3
15	398	339	1993/10/28	65	391	343	1994/8/25	115	386	349	1995/11/3
16	398	340	1993/10/28	66	391	344	1994/8/25	116	386	350	1995/11/3
17	398	341	1993/10/28	67	391	345	1994/8/25	117	386	351	1995/11/3
18	398	342	1993/10/28	68	391	346	1994/8/25	118	385	341	1993/9/1
19	398	343	1993/10/28	69	391	347	1994/8/25	119	385	342	1993/9/1
20	398	344	1993/10/28	70	390	341	1993/9/6	120	385	343	1993/9/1
21	398	345	1993/10/28	71	390	342	1993/9/6	121	385	344	1993/9/1
22	397	339	1992/5/17	72	390	343	1993/9/6	122	385	345	1993/9/1
23	397	340	1992/5/17	73	390	344	1993/9/6	123	385	346	1993/9/1
24	397	341	1992/5/17	74	390	345	1993/9/6	124	385	347	1993/9/1
25	397	342	1992/5/17	75	390	346	1993/9/6	125	385	348	1993/9/1
26	397	343	1992/5/17	76	390	347	1993/9/6	126	385	349	1993/9/1
27	397	344	1992/5/17	77	389	341	1995/12/20	127	384	344	1994/5/22
28	397	345	1995/1/10	78	389	342	1995/12/20	128	384	345	1994/5/22
29	396	339	1995/4/7	79	389	343	1995/12/20	129	384	346	1994/5/22
30	396	340	1995/4/7	80	389	344	1995/12/20	130	384	347	1994/5/22
31	396	341	1995/4/7	81	389	345	1995/12/20	131	384	348	1995/2/10
32	396	342	1995/4/7	82	389	346	1995/12/20				
33	396	343	1995/4/7	83	389	347	1995/12/20				
34	396	344	1995/4/7	84	389	348	1995/2/15				
35	396	345	1995/4/7	85	388	341	1993/9/4				
36	395	340	1993/6/15	86	388	342	1993/9/4				
37	395	341	1993/6/15	87	388	343	1993/9/4				
38	395	342	1993/6/15	88	388	344	1993/9/4				
39	395	343	1993/6/15	89	388	345	1993/9/4				
40	395	344	1993/6/15	90	388	346	1993/9/4				
41	395	345	1993/6/15	91	388	347	1993/9/4				
42	395	346	1993/6/15	92	388	348	1993/9/4				
43	394	340	1993/6/14	93	388	349	1993/9/4				
44	394	341	1993/6/14	94	388	350	1993/9/4				
45	394	342	1993/6/14	95	388	351	1993/9/4				
46	394	343	1993/6/14	96	387	341	1994/8/21				
47	394	344	1993/6/14	97	387	342	1994/8/21				
48	394	345	1993/6/14	98	387	343	1994/8/21				
49	394	346	1993/6/14	99	387	344	1994/8/21				
50	393	341	1994/5/31	100	387	345	1994/8/21				

### 2-2-3 Processing and Production of Image

#### (1) Procedures for Processing and Producing Image

Geomatica Prime ver. 7.0 manufactured by PCI Inc. in Canada was used to perform various types of image processing. The procedures for processing and producing image are as shown in Fig. II-2-2-2.

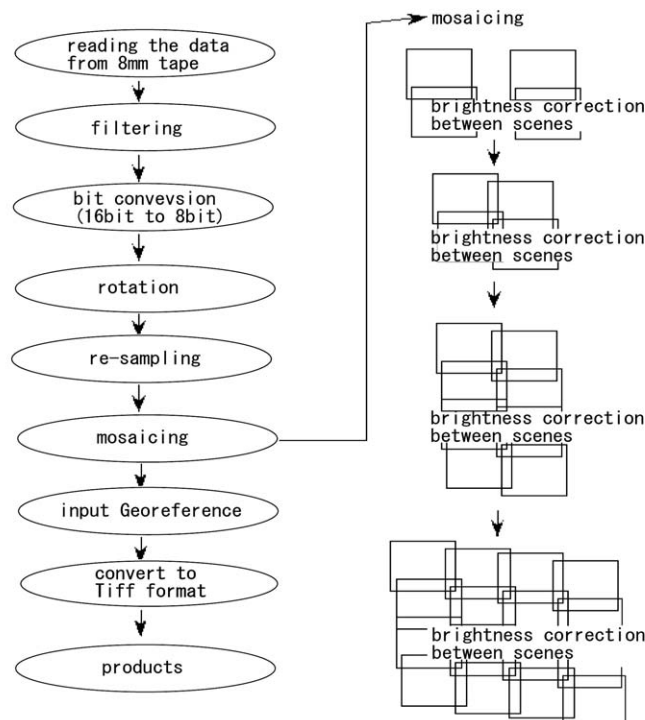


**Fig.II-2-2-2 Flow chart of producing JERS-1/SAR mosaic image**

#### (2) Image Processing Method

##### a) Filtering

A 3- by 3-pixel median filter was applied to the filtering. This application reduced black-and-white speckle noise.

##### b) Re-sampling

Raw data has an earth's surface resolution of 12.5 m per pixel. In order to enhance the processing speed, re-sampling was performed so that the image size could be 1/4. Consequently, the final image has an earth's surface resolution of 50 m per pixel.

#### c) Digital Mosaic Processing

In the digital mosaic processing, 20 to 200 GCPs were collected at each joint and the brightness among scenes was optimized to improve junction accuracy.

#### d) Inputting Georeference

A 1:500,000 scale TPC topographic map including the survey area was used to convert image data into georeference. About 100 GCPs were collected to enhance the georeference accuracy as much as possible.

#### e) Outputting Image

In the print-out, 1: 1,000,000 and 1: 500,000 scale images were output with titles, scales, and other information added. Mercator projection was adopted. Fig. II-2-2-3 shows the output example.

### 2-3 Interpretation and Analysis of the Image

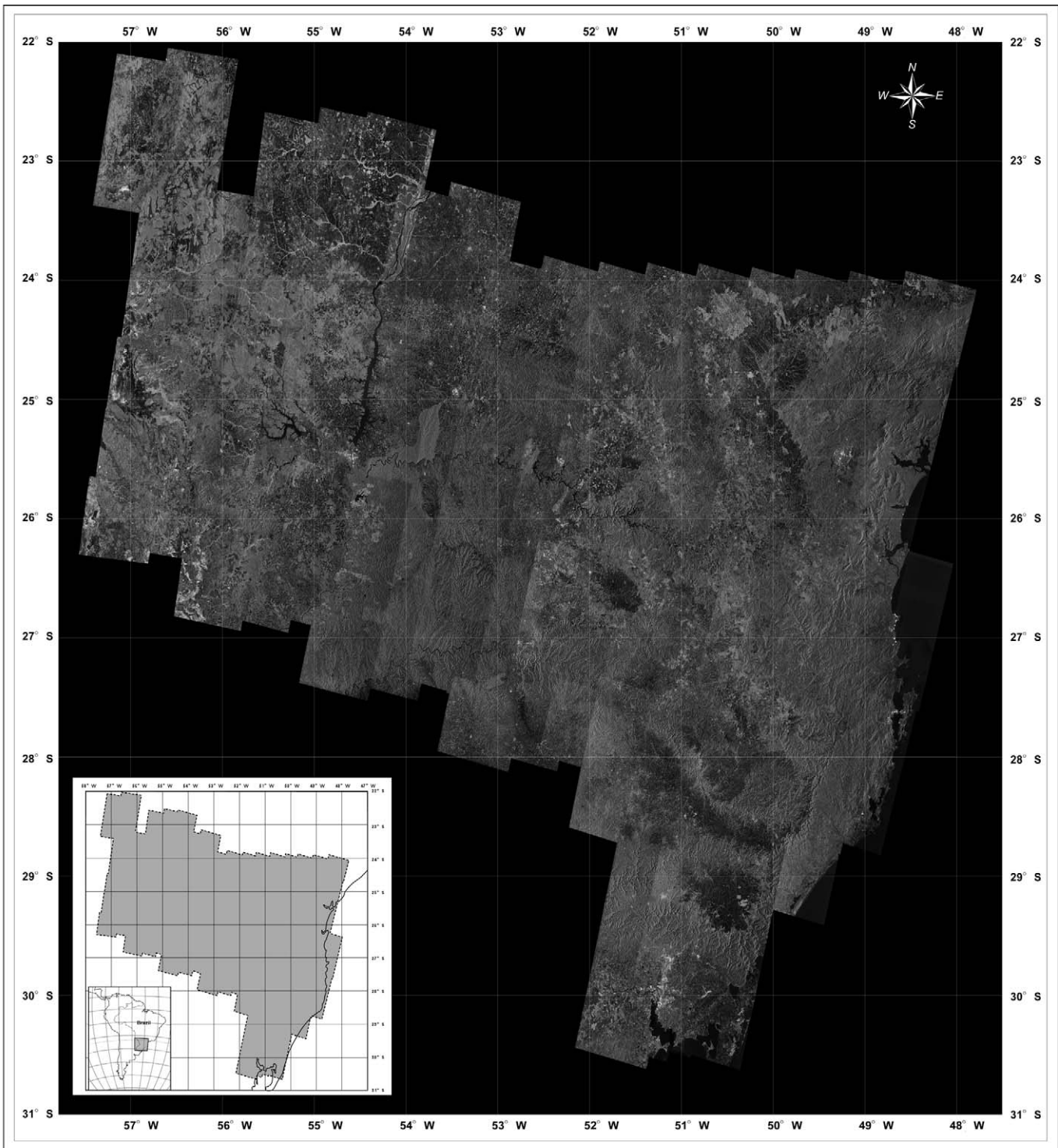
#### 2-3-1 JERS-1/SAR Image

A 1:500,000 printed-out mosaic image was used for interpretation and analysis. Lineaments and circular structures were extracted to interpret and analyze the geological structure. Lineaments that were confirmed as a fault on the existing geology and confirmed as a fault on the image are shown in the interpretation map (Fig. II-2-3-1). The extracted lineaments and circular structures were converted into ARC-VIEW-compatible digital data.

##### (1) Lineaments

In the Ponta Grossa Arch, the northeastern part of the survey area, some clear lineaments corresponding to faults on the existing geological map and many lineaments of the same system were extracted. In the Ponta Grossa Arch, sedimentary rocks of the Paleozoic and granitic basement rocks are distributed, and a great number of doleritic dikes considered to be feeders of flood basalts occur. The dikes have a strike extension of up to 80 km in the NW-SE direction. These dikes have been extracted as extremely clear lineaments on the image. This is attributable to the fact that a dike forms ridge-like continuous landform in sedimentary rocks which have little resistance to erosion. No dike that exists in granites of the basement has been extracted. This is due to the fact that a dike does not present a ridge-like landform because there is not much difference in resistivity to erosion between a dike and granites.

In the flood basalts area, a considerable amount of lineament groups in the NE-SW direction was extracted in the center of the survey area. These lineament groups, which have not been



Mosaic of JERS-1 SAR images for southern part of Brazil

1:1,000,000

**Fig.II-2-2-3 JERS-1/SAR mosaic image**



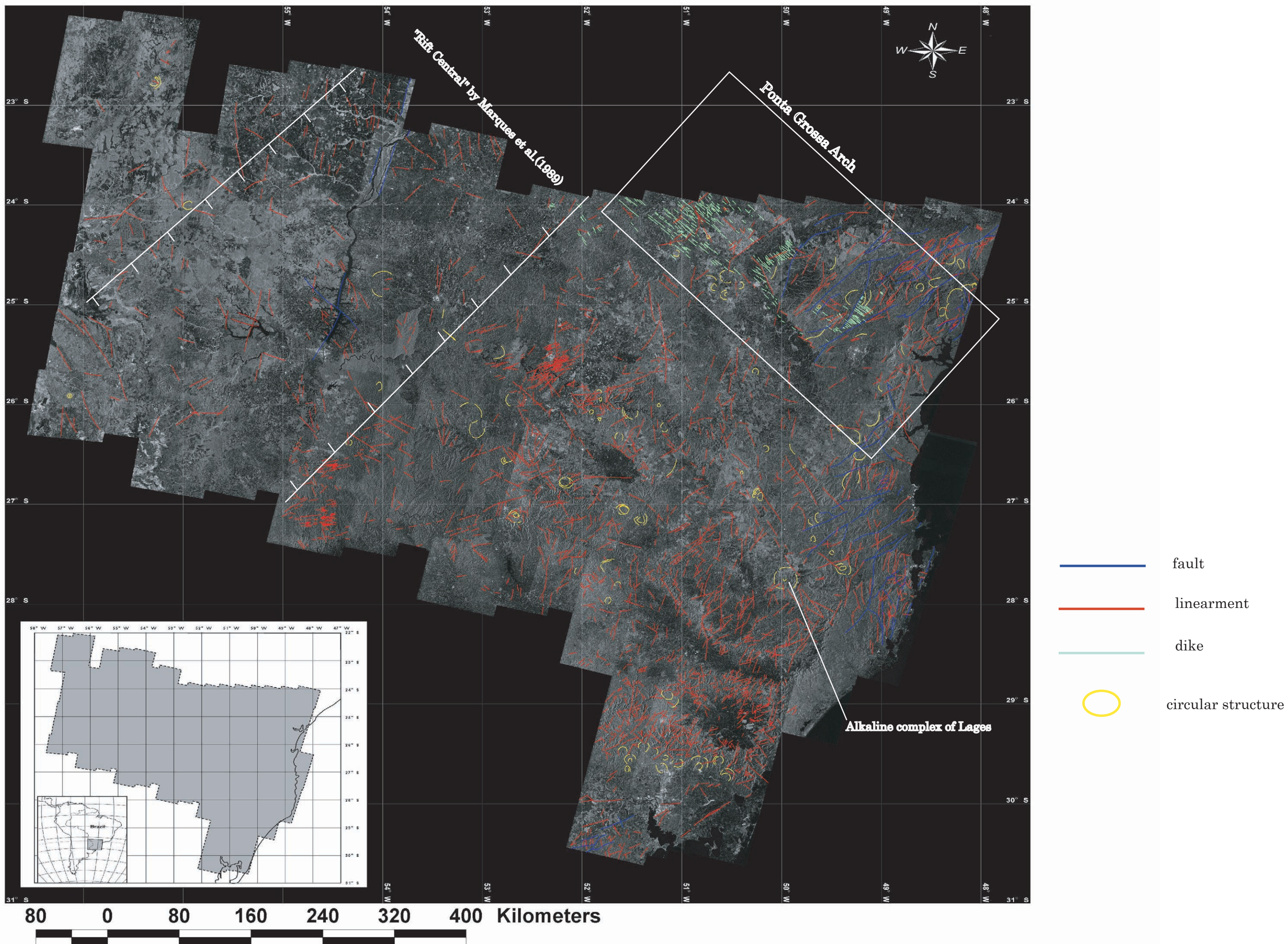


Fig.II-2-3-1 Interpretation map based on JERS-1/SAR mozaic imag



described on the existing geological map, are noteworthy.

The lineament density in the flood basalts distribution area, especially in the low land around the Paraná River, is far lower than that in the sedimentary rock area. This low land covers the “Central Lift” of Marques et al. (1989) in which horst and graben structure controlled by normal fault of NE-WS direction in the Ordovician to Silurian formations was assumed, and magnetic and gravity anomaly were extracted from airborne magnetic and gravity survey data; however, a lineament corresponding to it has not been extracted on the SAR image. This may indicate that the basement structure does not have a great tectonic influence upon the distribution of the flood basalts and there were no great tectonic movements in the present area since the flood basalts had been erupted.

## (2) Circular Structures

In the present area, many circular structures were extracted together with the lineaments. Among these, a circular structure in the Lages area has a clear correspondence to the geological circular structure. In the Lages area, a large-scale alkaline complex body, which intrudes into the Paleozoic formation exists, and this complex has been extracted as a clear circular structure. Also, in the flood basalts distribution area, some circular structures probably corresponding to a meteorite crater were extracted.

## 2-3-2 Landsat TM Image

The Landsat TM mosaic image composed of 74 scenes, which covers the entire Paraná basin, was purchased from GEOIMAGE Pty Ltd in Australia and was interpreted on a large scale of 1:2,500,000. The ground surface resolution was made as coarse as 200 m in order to compress the data capacity of the image. This resolution is sufficient for such a large-scale interpretation. The mosaic false color image of RGB = 345 was used for interpretation. The output example and interpretation map are shown in Fig. II-2-3-2 and Fig. II-2-3-3, respectively.

The Paraná basin shows very flat topography as a whole, and the lineament density is low. The dike swarm of the Ponta Grossa Arch was extracted as very clear lineaments similar to the case of the JERS-1/SAR image. This dike swarm is so large-scale that each dike can be extracted in the satellite image of 1:2,500,000 scale. The lineament density in the flood basalts distribution area is especially low. However, the Paraná River, which flows through the center of the basin, is very linear, and the lineaments of NNE-SSW direction along the Paraná River were extracted. Therefore, the Paraná River itself possible represents large-scale fracture zone. As a circular structure, A few alkaline complexes were extracted in the eastern margin of the Paraná basin.

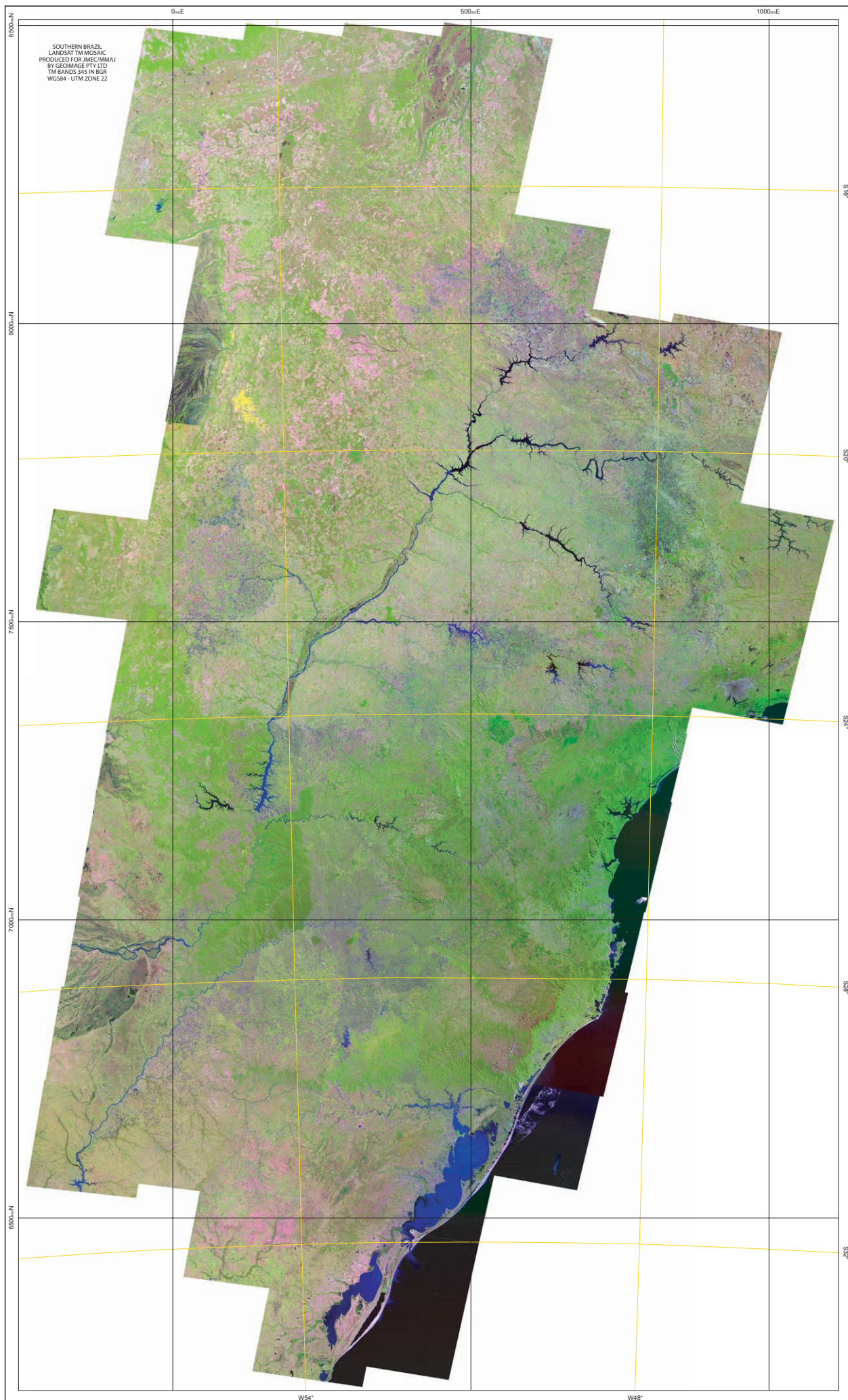


Fig.II-2-3-2 Landsat TM mosaic image  
 - 234 -



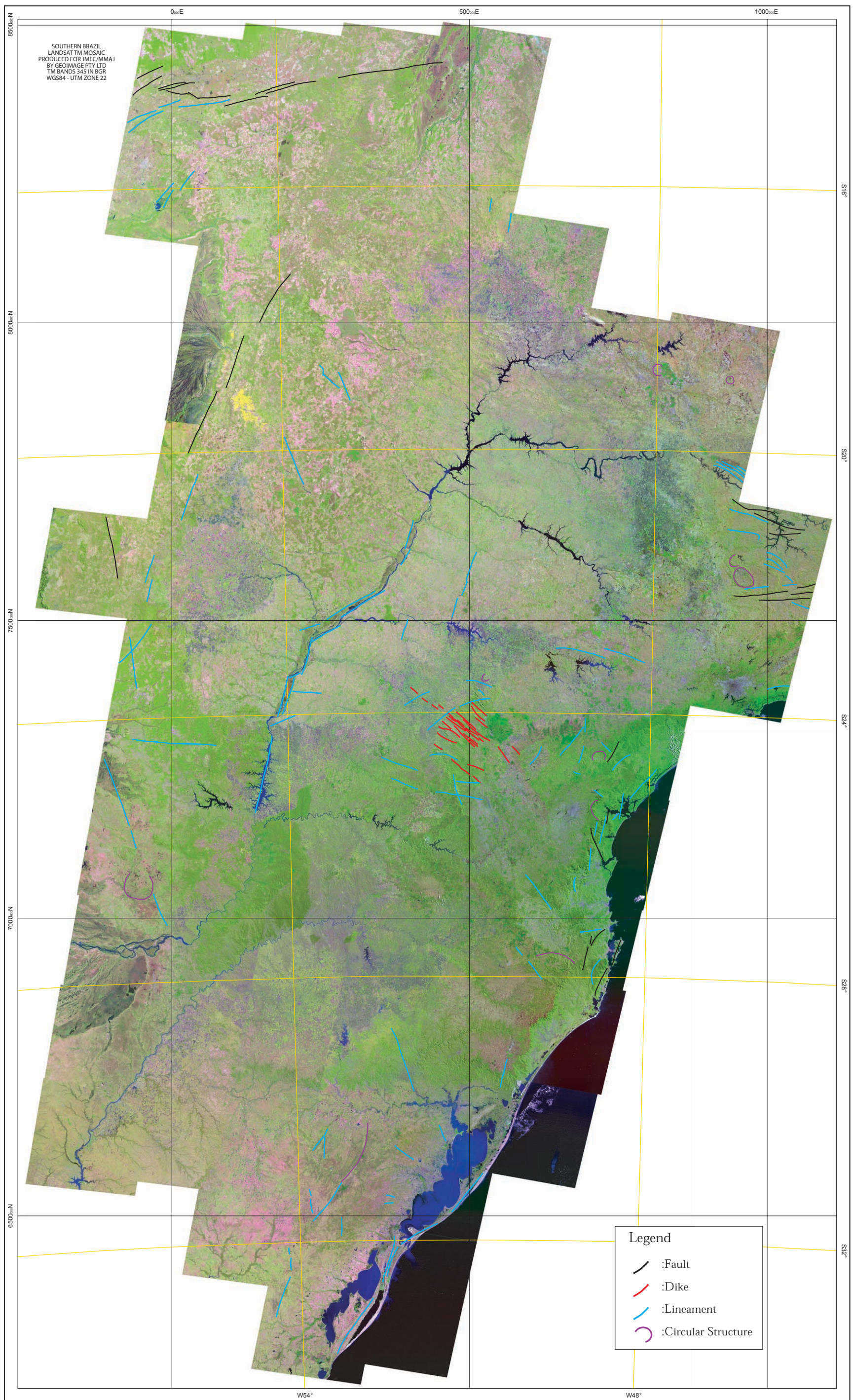


Fig.II-2-3-3 Interpretation map based on Landsat TM mosaic image